2010

Investigation of the sources and sinks of atmospheric methane

Christopher Lee Butenhoff
Portland State University

ABSTRACT

An abstract of the dissertation of Christopher Lee Butenhoff for the Doctor of Philosophy in Applied Physics presented June 11, 2010.

Title: Investigation of the Sources and Sinks of Atmospheric Methane

Methane (CH_4) is a potent greenhouse gas and its atmospheric abundance has nearly tripled since pre-industrial times. With a radiative forcing of 0.48 W m^{-2} it is second only to carbon dioxide in changing the radiative balance of the atmosphere. The behavior of CH_4 has been interesting in recent years. After nearly a century of rapid growth fueled by anthropogenic emissions from sources such as agricultural production and energy, in the past two to three decades the trend of CH_4 has declined to nearly zero, and its growth today is stalled. There is much interest in understanding why and how CH_4 changes on decadal time scales, not only to explain past behavior but more importantly to predict where CH_4 is heading in the future. This has implications not only for future climate change, but also for mitigation policies that aim to reduce emissions of greenhouse gases.

The work presented here represents a number of independent studies that investigated various components of the CH_4 budget, namely the sources and sinks. We used a chemical-tracer model and created unique long-term time series of atmospheric CH_4, carbon monoxide (CO), molecular hydrogen (H_2), and methylchloroform (CH_3CCl_3) measurements at marine background air to derive histories of atmospheric hydroxyl radical (OH) – the main chemical oxidant of CH_4, biomass burning – an

important source of CH_4 in the tropics, and emissions of CH_4 from rice paddies – one of the largest anthropogenic sources of CH_4, over decadal scales. Globally gridded inventories of CH_4 emissions from rice paddies and terrestrial vegetation were created by synthesizing greenhouse and field CH_4 fluxes, satellite-derived biophysical data, and terrestrial geospatial information.

Our main finding is that although global sources and sinks of CH_4 appear to be in balance now, as evidenced by stable levels of atmospheric CH_4, this is likely due to competing trends in individual sources and sinks. In particular we find good evidence that atmospheric OH levels have declined by 10-15% over the past few decades, with most of this change happening in the northern hemisphere. If so, this implies that global CH_4 emissions have fallen by about 50 Tg y^{-1} in the northern hemisphere. We find that this decrease is due in part to declining emissions of CH_4 from rice production in China driven by changes in agricultural practices there. In the southern tropics we find that biomass burning emissions have risen perhaps as much as 20%, though no significant change is observed in the northern tropics. Finally, if terrestrial vegetation is a source of CH_4, which recent reports indicate to be so, our work shows that it is potentially significant globally, up to 30 Tg y^{-1} as constrained by the ice core record. Emissions from this source could vary significantly on decadal scales due to pressures from climate and human activities such as land clearing and deforestation, and may balance the increase in emissisons from biomass burning. A dynamic picture of CH_4 emerges from this work. The near-constant global burden of CH_4 seen today hides the changing behavior of the sources and sinks beneath. Our findings will help us understand whether CH_4 levels will remain stable in the future.

Dedication

To my family ...

and TMZ.

ACKNOWLEDGEMENTS

As a child I never knew what a Ph.D. was or what scientists do. I only knew they wore white lab coats and peered inquisitively into bubbling beakers of colorful liquids (alas I do neither, which seriously calls into question whether I'm a real scientist!). But I had good teachers. Completion of this dissertation is the cap on my formal education that stretches back to Mrs. Beyers' morning kindergarten class at Minnesota City Elementary School in southeastern Minnesota, and continued there in the classrooms of Mrs. Taylor, Mrs. Fort, and Mrs. Poppe, in whose class I learned what a googol was before it could be googled. I thank all the teachers I had at Minnesota City and Goodview Elementary Schools, and Winona Junior and Senior High Schools. These teachers created a solid foundation for me to pursue higher education.

A good adviser does more than just advise, and this is certainly the case for my adviser, Aslam Khalil. Throughout my program, not only has Aslam been a guiding influence, but he has provide me opportunities to engage in the broader scientific community such as attending and organizing scientific conferences and meetings, and reviewing and contributing papers to books and other publications. Aslam is a world-class scientist and I have learned much under his guidance. But beyond that I've enjoyed our many long talks on politics, economics, human nature, religion, cycling, and any number of other topics completely unrelated to methane. I have sincerely enjoyed working with him and thank him for his support.

I would also like to thank the other members of my dissertation committee, Erik Bodegom (Physics), David Ervin (Economics), James Pankow (Chemistry and Civil & Environmental Engineering), and Andrew Rice (Physics). My journey through this program has been somewhat unorthodox and my committee members were very kind in their understanding and flexibility

Martha Shearer has been a constant member of our research group since I arrived. She manages all the day-to-day research activities and is the go-to person for everything from key requests to data sources, besides being a top-notch scientists to boot. She's invaluable to all work done in the group. Most importantly she ensures that our Friday research meetings (typically) end at a reasonable time.

There have been a number of students and post-docs who have passed through our group in the years I've been here, Kiren Bahm, Conrado Salas Cano, Aida Biberic, Zhengqin Xiong, Doug Parsons, Alec Sithole, Ellyne Kutsche, and Will Porter. Their friendship made this process much more bearable.

Additional thanks to James Pankow and Martha Shearer for their meticulous reading and editing of my dissertation. It is significantly better as a result.

Words can't fully convey my appreciation to my parents Ed and Nora Butenhoff. First for creating a home environment where academics and knowledge were valued which led to my pursuit of graduate education. But more importantly for always being there for me. My pursuit of a Ph.D. took me thousands of miles away from home, and yet they never once questioned my path. Even at that distance they've been my

Investigation of the Sources and Sinks of

Atmospheric Methane

by

Christopher Lee Butenhoff

A dissertation submitted in partial fulfillment of the
requirements for the degree of

Doctor of Philosophy
in
Applied Physics

Dissertation Committee:
M. Aslam K. Khalil, Chair
Erik Bodegom
David Ervin
James Pankow
Andrew Rice

Portland State University

Table of Contents

List of Tables

List of Figures

Chapter 1 — A Changing World: The Importance of Atmospheric Methane

1.1 Introduction

We have reached an important marker in the course of human development. Throughout our history, human impact on earth's biota and its supporting systems has been minimal in scope and scale and limited to local disruptions and disturbance. Though forests have been felled, fish stocks depleted, and waters and air polluted, these activities have had little global impact despite hardship to local biota and inhabitants. But population and industrial growth has led us into a new era. The waste products of our technological society now perturb global systems and affect regions far removed from pollution sources. For the past one hundred years or so our agricultural and industrial activities have dramatically altered the atmosphere's chemical composition and have disrupted the earth's radiative balance. The impacts of climate change are now widespread. Policy makers, planners, and indeed common citizens require a complete and accurate understanding of the life cycles of greenhouse gases (GHGs) to effectively and efficiently allot scant resources to climate change mitigation and adaptation.

The work presented here strives to better understand the behavior of a principal GHG, methane (CH_4), which has increased nearly threefold since pre-industrial times (*Ferretti et al., 2005*). The singular fact that CH_4 is over 20 times more potent on a per-

molecule basis than CO_2 (over a time horizon of 100 years) makes CH_4 an important gas to study (Table 1.1). The direct radiative forcing from CH_4 (calculated from 1750) is 0.48 W m^{-2}, which is 18% of the total long-lived greenhouse-gas forcing, and 49% of the non-CO_2 greenhouse-gas forcing *(Forster et al., 2007)*. If we include CH_4's contribution to tropospheric ozone and stratospheric water vapor, its radiative forcing is closer to 0.7 W m^{-2} *(Hansen et al., 2000)*. By some accounts, CH_4 contributes more to climate change than fossil fuel burning, since the negative forcing of the combustion aerosols offsets some of CO_2's positive forcing *(Hansen et al., 2000)*. Regardless, CH_4 plays an important role in Earth's radiative budget today and will continue to do so in the future.

Beyond its radiative properties, methane's impact on atmospheric chemistry is significant. It decreases the abundance of the hydroxyl radical (OH) through oxidation, which in turn increases the lifetime of hydrocarbons and other oxidized gas species, including the hydrofluorocarbons (HFCs) and hydrocholorofluorocarbons (HCFCs), the replacement compounds for the stratospheric ozone-destroying compounds, potent greenhouse gases themselves. In addition, transport of methane to the stratosphere and its subsequent oxidation there contributes 20-25% of the total water vapor flux to the stratosphere where it participates in the ozone-destroying HO_x cycle *(Warneck, 1999)*.

Table 1.1. Radiative properties of long-lived greenhouse gases.

Gas		Radiative forcing[a] W m^{-2}	Global Warming Potential[a] Time Horizon		
			20 yr	100 yr	500 yr
Carbon dioxide	CO_2	1.6	1	1	1
Methane	CH_4	0.48	62	23	7
Nitrous oxide	N_2O	0.16	275	296	156

[a] Data from IPCC 2007 *(Forster et al., 2007)*

Our awareness of the problem is recent. In the 1950s methane was identified as a "non-variable component of atmospheric air" (*Glueckauf, 1951*). Recognition of its increasing atmospheric burden dates back less than thirty years (*Rasmussen and Khalil, 1981*). Since then we've extended the evidentiary record backwards thousands of years using ice cores drilled from Greenland and Antarctica. For methane, the ice core record indicates that preindustrial Holocene background CH_4 was ~660 ppbv (parts per billion by volume, or nmol mol-1) (*Feretti et al., 2005*) and rose rapidly starting around the year 1750 to present-day global mean levels of about 1760 ppbv (*Dlugokencky et al., 2009*).

The behavior of atmospheric CH_4 is complex due to the diversity of its sources and sinks which individually respond to different pressures. Though the recent history of CH4 can be reconstructed from ice cores and direct atmospheric measurements, if we wish to go beyond explaining the past and project forward the path to the future, we must understand how current CH4 sources and sinks are changing today. This will allow us to predict future responses to a changed physical and human climate and chart a possible path to the mitigation of emissions.

Like any budget, the balance of methane in the atmosphere represents the net sum of its receipts and outlays. The receipts of atmospheric methane are source emissions released entirely at the surface and typically quantified as a flux in units of Tg CH_4 per year (1 Tg=10^{12} g). The sources of methane are many and varied, both

3

natural and anthropogenic (Table 1.2), but are dominated by anaerobic bacterial

production in soils and ruminants. In total, annual emissions of methane are estimated

Table 1.2. Sources and sinks of atmospheric CH_4. All values are Tg CH_4 y^{-1}. Adapted from *Lowe (2006)*.

Sources	Estimates	Range of estimates
Wetlands	145	92-237
Rice agriculture	60	40-100
Ruminants	93	80-115
Termites	20	2-22
Biomass burning	52	23-55
Energy generation	95	75-100
Landfills	50	35-73
Ocean	10	10-15
Hydrates	5	5-10
Vegetation	35	0-60
Total sources	**565**	**500-600**

Sinks	Estimates	Range of estimates
Tropospheric oxidation	507	450-510
Stratospheric loss	40	40-46
Soils	30	10-44
Total sinks	**577**	**460-580**

between 500-600 Tg CH_4 per year (*Denman et al. 2007*). Emissions from natural

wetlands are widely believed to be the largest of all sources, though a recent study

reported the controversial finding that aerobic emissions from plants may be larger

(*Keppler et al.* 2006). An assessment of the inventory for this source is part of the

current work. Emissions from anthropogenic sources such as ruminants and rice

agriculture have grown rapidly during the twentieth century (*Khalil and Shearer, 2000*).

The outlays of methane are its sinks, how it is removed from the atmosphere.

CH_4 is removed primarily by gas phase oxidation through its reaction with OH in the

troposphere. Smaller sinks include microbial uptake in soils, and an unknown but

4

presumably minor removal from ocean-produced chlorine atoms (*Gupta et al., 1997; Tyler et al., 2000; Platt et al., 2004; Allan et al., 2005*).

1.2 Mitigation Potential

CH_4 has properties that make it an attractive gas to trade under future climate mitigation policies. Most importantly, its large global warming potential allows economic actors to offset roughly 20 tons of CO_2 for every ton of CH_4 mitigated. CH_4's relatively short lifetime of 8-10 years means its mitigation today will have a real impact on climate in less than a decade. Compared to the relatively long lifetime of carbon dioxide, CH_4 becomes an attractive gas to target for rapid climate mitigation. Actors with the ability to reduce CH_4 emissions hold valuable assets that will significantly impact the overall trading price of carbon credits.

There is significant potential for GHG mitigation in agriculture as mitigation costs are typically cheaper for agriculture than for non-agricultural sources (*Smith et al., 2007*). *Caldeira et al (2004)* estimated that agricultural emissions of up to 5 Gt CO_2-eq y^{-1} (1 Gt = 1 gigaton = 10^{15} g, CO_2-eq is equivalent CO_2 emissions calculated using the GWP of GHGs) could be mitigated by 2030. For CH_4, mitigation potential is primarily via rice management and livestock. *Smith et al. (2007)* calculated that up to 500 Mt CO_2-eq y^{-1} could be mitigated through improvements in these practices by 2030.

The purpose of the work here is simple, to better understand the sources, sinks, and trends of atmospheric CH_4 in hopes of providing a firmer base on which we can predict its future behavior. Of course the future of CH_4 is not left to fate. We can alter its future through our decisions and policies. In this light, the proposed work also helps

5

to inform the debate on how best to manage methane emissions, and what sources are the best targets for mitigation.

1.3 Structure of dissertation

The logic of the following chapters is as follows. We start by using the global CH_4 record as a constraint to understand how emissions of CH_4 have changed over the past few decades. Whatever trends we find in individual sources and sinks should be consistent with this record. We find that the inversion permits no unique solution, as sources and sinks may be changing simultaneously. In Chapter 3 we investigate the main sink of CH_4, oxidation by OH, using a composite set of methylchloroform. (CH_3CCl_3) measurements as a proxy. Molecular hydrogen (H_2) and carbon monoxide (CO) are two other chemically important trace gases that are removed by OH. These gases are emitted from biomass burning and in Chapter 4 we use them to infer trends in the biomass burning strength. From this we can assess potential trends in CH_4 emissions from biomass burning.

Our focus next turns to one the largest sources of CH_4, rice production. Global inventories of rice emissions are ultimately based upon field studies of CH_4 flux from paddies using small static chambers. The low spatial and temporal frequency of measurement introduce uncertainty in seasonal averages. In Chapter 5 we perform Monte Carlo-style experiments to quantify how sampling uncertainty propagates into the seasonally-averaged CH_4 flux. This effort has practical implications. Not only can we retroactively assess uncertainty on past field studies, but our results are also useful in future work to strategically plan sampling campaigns. In Chapter 6 we outline one

such sampling campaign that was conducted simultaneously in greenhouses at Portland State University and in the field at Nanjing, China. We use the functional relations that were derived to connect CH_4 flux to its driving factors and construct globally-gridded maps of CH_4 emissions from rice paddies. This important study helps us to understand not only current emissions from rice agriculture, but in Chapter 7 we estimate trends of paddy emissions due to changes in agricultural management practices and climate. In Chapter 8, we investigate the potential of terrestrial vegetation as a globally significant source of CH_4. This work is based on a novel report (*Keppler et al., 2006*) that suggests CH_4 is emitted from plants in aerobic conditions. This finding is not consistent with the known mechanisms of CH_4 production. Finally we present our conclusions in Chapter 9.

1.4   Closing thoughts

In a somewhat more philosophical bent, perhaps we also study CH_4 not just out of concern for our future, but out of curiosity for our past as well. A snapshot of the CH_4 in the atmosphere records the natural and anthropogenic CH_4 activities of roughly the past ten years. From this view, we see the current CH_4 component of the atmosphere to be an echo of the very recent past. But though the present CH_4 may have a short history, the processes responsible for its emission and destruction are the chemical, physical, and biological products of hundreds, thousands, millions, even billions of years of evolutionary history. Microbial evolution, continental drift, mountain building, carbonaceous rock building, ancient plant decomposition, not to mention human

evolution, are all recorded today in this CH_4 snapshot. Thus the patterns of CH_4 in the atmosphere today, reflect not only the past ten years, but more importantly our ancestral past in all its varied meanings. Measuring the atmosphere in its current state is akin to receiving the ending to a story but not knowing the plotline that brought it there. Fortunately we are aided in this quest by an entire flipbook of snapshots that animates the record of CH_4 over thousands of years.

The seven studies reported in the following pages were each designed to improve our understanding of the CH_4 budget. The complexity of the methane cycle as mentioned makes these individual stories inherently disparate. Running throughout however, is a single thread, that binds the stories tightly, providing continuity. This thread is part of the larger fabric of a changing world and our changing role within it.

Chapter 2 — Inverse Modeling of Atmospheric Methane Mixing Ratios

2.1   Introduction

Atmospheric methane rose rapidly throughout much of the past century but its

rate of increase has slowed in recent years (*Khalil and Rasmussen, 1990; Khalil and*

Rasmussen, 1993; Dlugokencky et al., 1998; Karlsdottir and Isaksen, 2000;

Dlugokencky et al., 2003). A number of reasons for this decrease have been postulated

including declining emissions from the former Soviet Union (*Olivier and Berdowski,*

2001), a reduction in wetland emissions due to climate variability (*Bousquet et al.,*

2006), and increasing OH concentrations (*Karlsdottir and Isaksen, 2000*).

The behavior of CH_4 in the atmosphere is determined by changes in its sources

and sinks. As the budget of methane in the previous chapter shows (Table 1.2), the

sources of CH_4 are diverse, making it difficult to construct a temporal history of global

CH_4 emissions. An alternative approach is to invert the atmospheric measurements with

a chemical-transport model that can simulate the mass balance and transport of CH_4 in

the atmosphere.

Here we investigate what scenarios of sources and sinks are consistent with the

current behavior of methane. In particular, we look to understand the likelihood that the

declining rate of methane increase is driven by decreasing emissions. We extended this

analysis as far back as possible with available measurements. We created a unique time
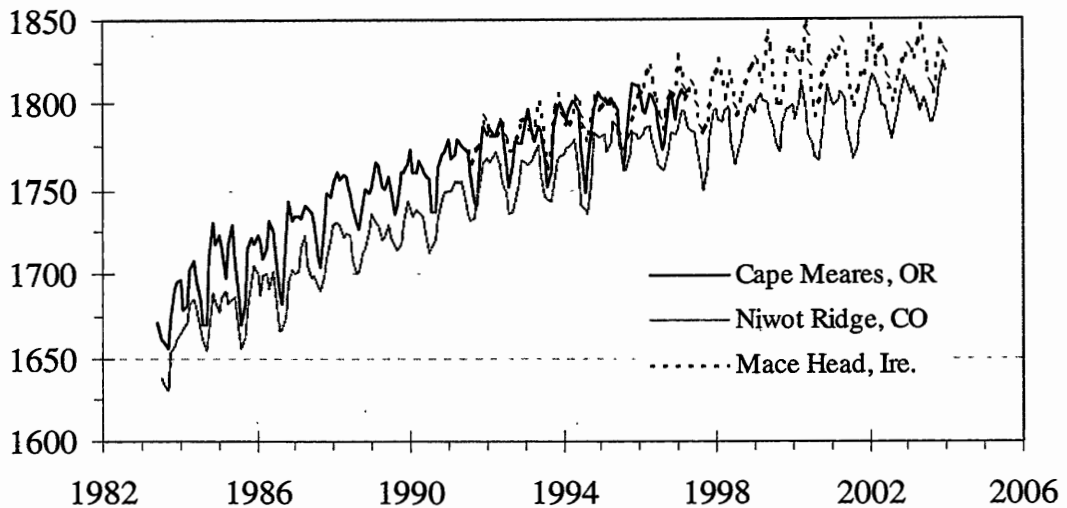
Figure 2.1. NOAA-GMD measurements of CH4 at northern mid-latitude sites. Here we see the record at Mace Head is in better agreement with the earlier record from Cape Meares. We chose Mace Head to extend the Cape Meares after sampling at Cape Meares finished.

series of methane measurements by joining together the data sets of two independent trace gas monitoring networks. We used a chemical transport model to invert the measurements and study the trend in the deconvoluted sources. As this is the first time the some of these measurements have been used in this way, our study will make valuable contributions to this question.

2.2   Composite CH$_4$ record

We used atmospheric CH$_4$ data from two trace gas monitoring networks to create a composite time series of measurements that span over twenty years, from 1981 to 2004. Data from the Oregon Graduate Institute (OGI) are available from eight sites worldwide (Barrow, Alaska 71.16N, 156.5W; Cape Meares, Oregon 45.5N, 124W; Mauna Loa 21.08N, 157.2W and Cape Kumukahi 19.3N, 154.5W, Hawaii; Samoa

14.1S,170.6W; Cape Grim, Tasmania 42S, 145E, Palmer Station, Antarctica, 64.46S, 64W and the South Pole 90S) between 1979 and 1997. These sites were chosen to sample clean background air from the major global air masses. Triplicate samples were taken weekly and analyzed using standard laboratory methods (gas chromatography/flame ionization detection). All samples were calibrated against a single standard. Details on the analytical method can be found in *Rasmussen and Khalil (1980, 1981)*.

Methane measurements are also available from the National Oceanic and Atmospheric Administration's Global Monitoring Division (*Dlugokencky et al., 2009*). Air was sampled at all of the same stations used by the OGI network. Sampling at most sites began in 1983 and continues today. The Cape Meares station was discontinued in 1997 with the ending of the OGI program and replaced with Niwot Ridge, Colorado (40.05N, 105.58W) and Mace Head, Ireland (53.33N, 9.90W). To extend the northern mid-latitude record past the record available from Cape Meares we used CH_4 measured at Mace Head, as this record is most consistent with Cape Meares in terms of absolute levels (Fig. 2.1). During times of overlap between the two stations (1991-1997), we took a latitudinally-weighted average of both station's CH_4.

To fill in short gaps (less than six months) in the data record, artificial data were constructed by adding an average seasonal cycle onto a linear interpolation across the time space of missing data. For longer gaps, we constructed data using the latitudinal gradients of neighboring sites. For this method we calculated the average latitudinal gradients between sites. The calculated gradients were BRW/CMO=1.011,

11

CMO/MLO=1.034, MLO/KUM=0.988, KUM/SMO=1.042, SMO/CGO=1.004, CGO/PSA=1.007, and PSA/SPO=1.003, where BRW=Barrow, AK, CMO=Cape Meares, OR, MLO=Mauna Loa, HI, KUM=Cape Kumukahi, HI, SMO=Samoa, CGO=Cape Grim, Tasmania, PSA=Palmer Station, Antarctica, and SPO=South Pole. With these gradients, the missing values were interpolated. If both neighboring sites had measurements, a simple average was taken of the two interpolated values.
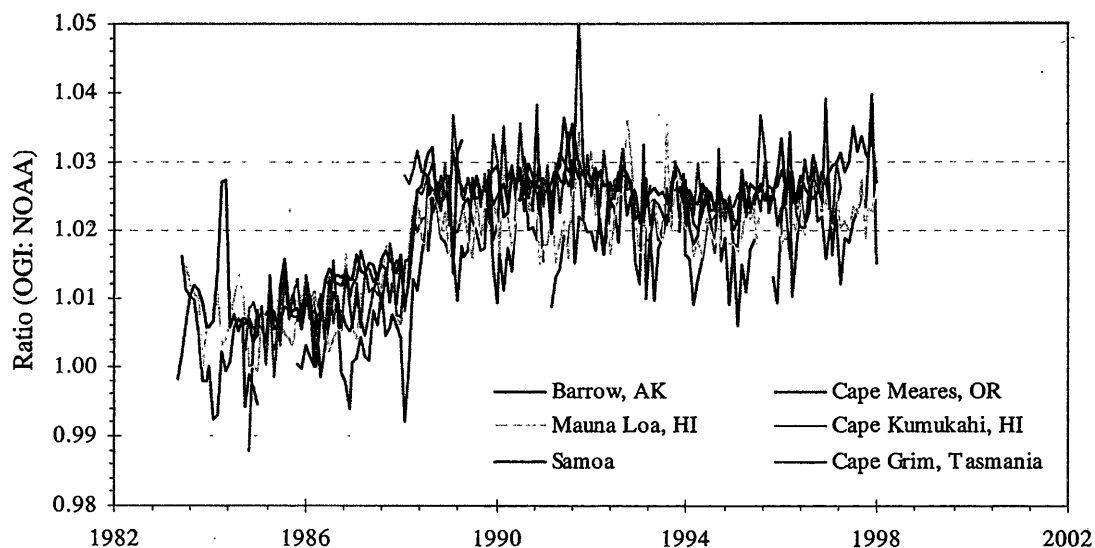
Figure 2.2. Ratio of CH_4 measurements taken by the OGI and NOAA-GMD networks. Ratios are calculated as OGI:NOAA and are shown for sites common to both networks.

Our next goal was to create a composite data set by combining the records from the OGI and NOAA networks. As both networks measured CH_4 from the same sites, this process is straightforward. The only concern was correction for possible calibration differences in the standards used by each network. To determine the calibration ratio

between the two data sets we used measurements from the common sites, Barrow, Cape Meares, Cape Kumukahi, Mauna Loa, Samoa, and Cape Grim. When both sites had data for a particular month we formed the ratio. The time series of ratios is shown in Fig. 2.2.

The ratios were consistent across sites, but there an abrupt transition in the time series occurred February 1998. Before this date the average ratio across all sites was
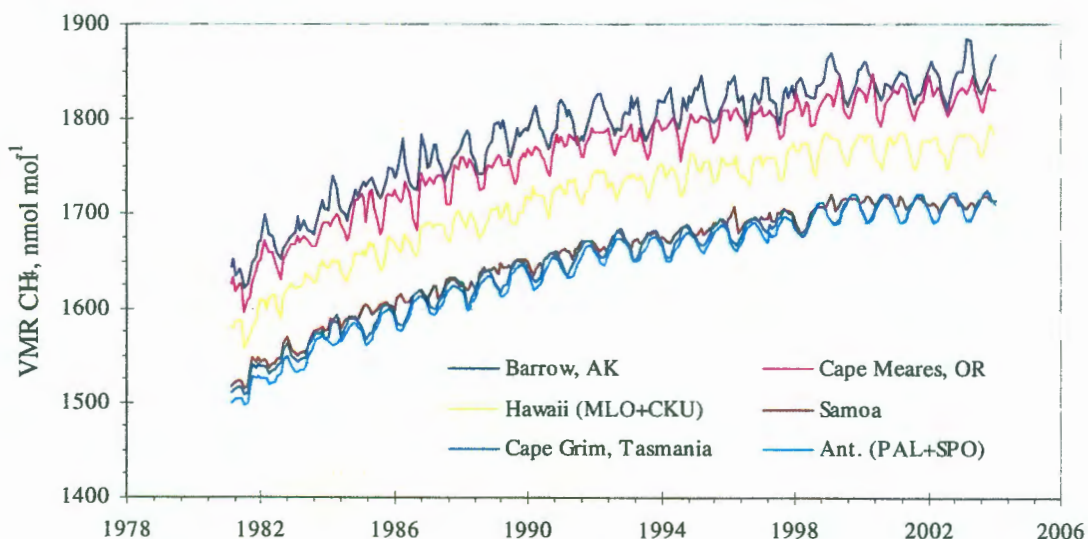
Figure 2.3. The composite record of atmospheric CH_4 constructed by linking the OGI and NOAA data sets.

1.008 ±0.012 and after this date the ratio jumped to 1.024±0.011. We have no explanation as to why the calibration changed at this time. The available NOAA information makes no mention of this. In the past there have been concerns about the stability of the OGI standards (*Aslam Khalil, personal communication*) and so we chose to adjust the OGI data.

In forming the composite time series, we reduced all OGI data before 2/1998 by the factor of 1.008 and by 1.024 after this date. The composite time series was constructed by taking the weighted average of the scaled OGI data and the NOAA data. The weights were $(1/\sigma)^2$, where σ is the standard deviation of the monthly average. The
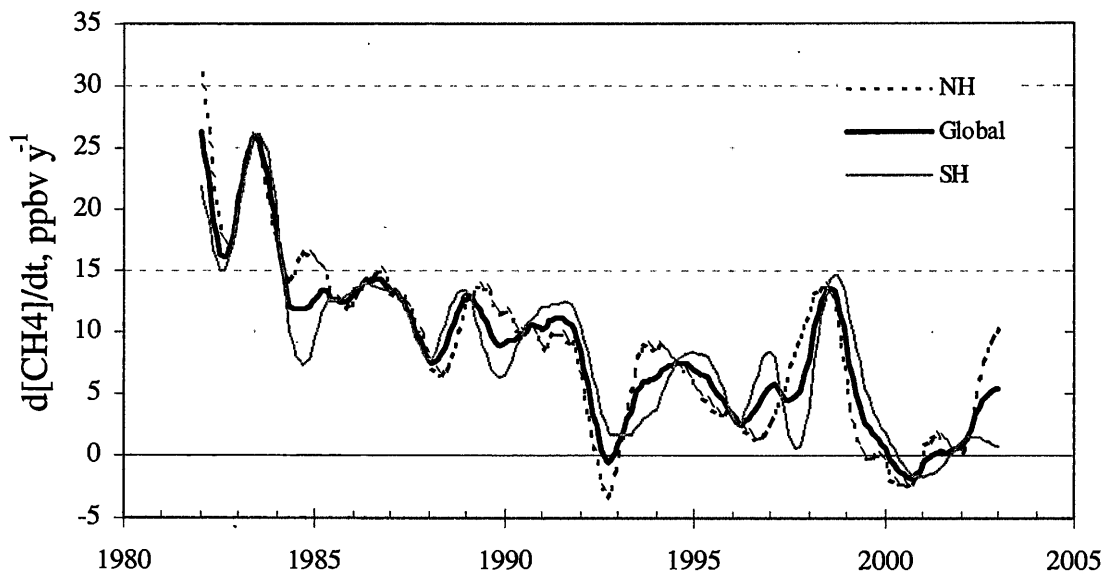
Figure 2.4. The moving trend of the composite CH_4 record. For each 13-month window, the result of the linear regression is plotted. The value is plotted in the middle date of the window. NH=northern hemisphere, SH=southern hemisphere.

composite time series is on the NOAA calibration scale and covers the period Jan 1981 to Dec. 20003. The 23-year time series for each site is shown in Fig. 2.3.

Some notable features stand out. After a rapid increase in the late 1970s and early 1980s, atmospheric CH_4 began to level off around 1990. This has created much

speculation about what the responsible agent may have been and we offer our own thoughts on this below when we invert the measurements. Secondly, there was a strong hemispheric gradient as well as latitudinally varying mixing ratios in the northern hemisphere (NH). As the major sink of CH_4 is OH, and OH levels are observed here to have been broadly symmetric about the equator, the gradient was established by hemispheric differences in sources. Mixing ratios at all three stations in the SH were nearly constant, indicating that the hemispheric air mass was well mixed and that larger sources were absent. Starting from high northern latitudes extending southward to the equator, CH_4 levels fell precipitously. Mixing ratios at Barrow, Alaska were slightly higher than at mid-latitudes. The lifetime of CH_4 is relatively long in the arctic due to the oblique angle of insolation throughout much of the year, which inhibits the production of OH. Only small emissions are required here to maintain this gradient.

A strong seasonal cycle in CH_4 was observed at most stations. This likely was produced mainly by the CH_4+OH oxidation sink, since OH peaks in the summer months of each hemisphere. Wetland emissions in the mid to high northern latitudes also are strongly seasonal and add to the cycle at these locations. There is only weak seasonality at Samoa which is a tropical location where OH levels vary only slightly throughout the year. Emissions from biomass burning, an important source of CH_4 in the tropics, peak during the dry season and also contribute to the seasonal cycle of CH_4 in the tropics. Atmospheric levels of CH_4 are nearly identical at Cape Grim and Antarctica. The large fraction of area here is ocean or ice-covered lands so emissions of CH_4 are minimal. The air mass from latitude 30S southward is well-mixed.

2.3 Trend of the composite record

The rate at which atmospheric CH_4 is changing from year to year provides valuable insight into the behavior of its sources and sinks. We examined how the trend of CH_4 has changed over the 23-year span by calculating a moving linear regression of the time series. Here we used a 13-month moving window over which to calculate the regression (dCH_4/dt) to filter out signals from seasonality and preserve interannual variability. The global and hemispheric trends are shown in Fig. 2.4.

The trend sharply declined from the beginning of the record when methane rose by 25 ppbv per year. From 1993 onwards, the trend was near zero except for some brief positive excursions that may be related to specific events such as volcanic eruptions and wildfires (e.g. *Dlugokencky et al., 1996, Dlugokencky et al., 2001*).

At first glance it appears that emissions must be declining over this period to explain this behavior. If we use the conversion that 1 ppb equals 2.75 Tg of methane *(Feretti et al., 2005)* and assume the total methane sink is constant, the decline implies that CH_4 emissions have dropped by about 70 Tg CH_4 per year, or about 13% of the
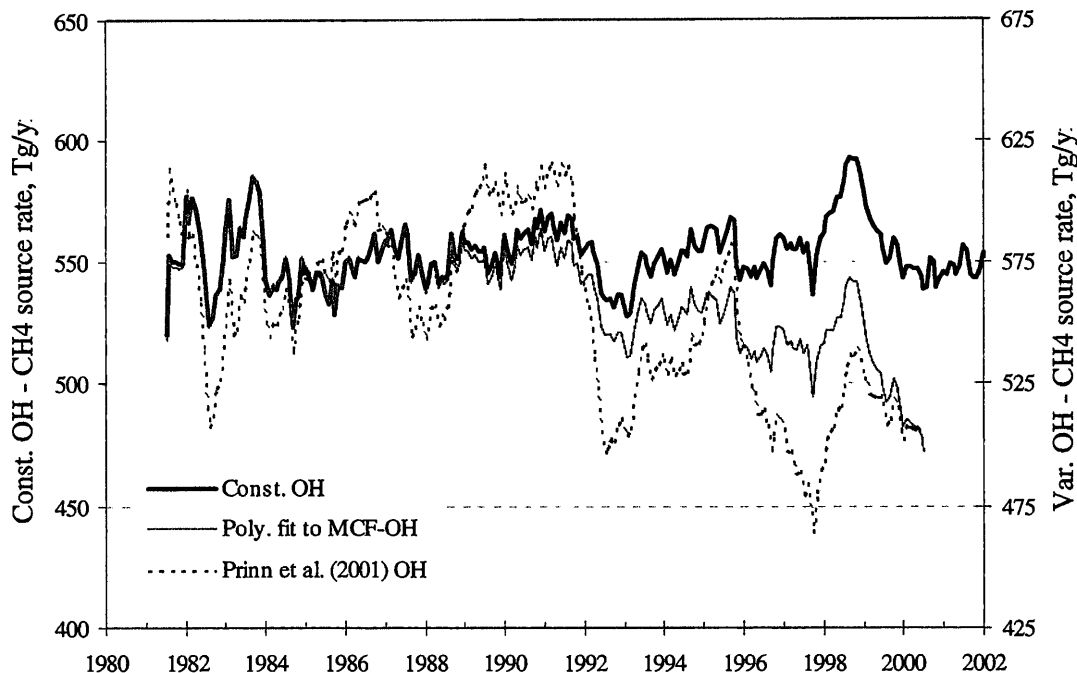
Figure 2.5. The global inverted CH_4 emissions modeled from the composite data record. The solid black line are results assuming that OH is constant throughout. The dashed line gives results based on changing OH time series *from Prinn et al. (2001).* The gray line shows emissions using an OH history derived in Chapter 3.

annual total. Some authors have suggested that CH_4 emissions have declined due to the economic collapse of the former Soviet Union (fSU) *(Olivier and Berdowski, 2001;*

Olivier , 2002). Dlugokencky et al. (2003) found that CH_4 emissions from the natural

gas industry in the fSU decreased by 20 Tg CH_4 y^{-1} from 1991 to 1997.

To investigate this question, we used a two dimensional global chemical-transport

box model to invert our composite CH_4 record. This model is described in detail in

Butenhoff (2002), and we provide additional description in Chapters 3 and 4. For now a
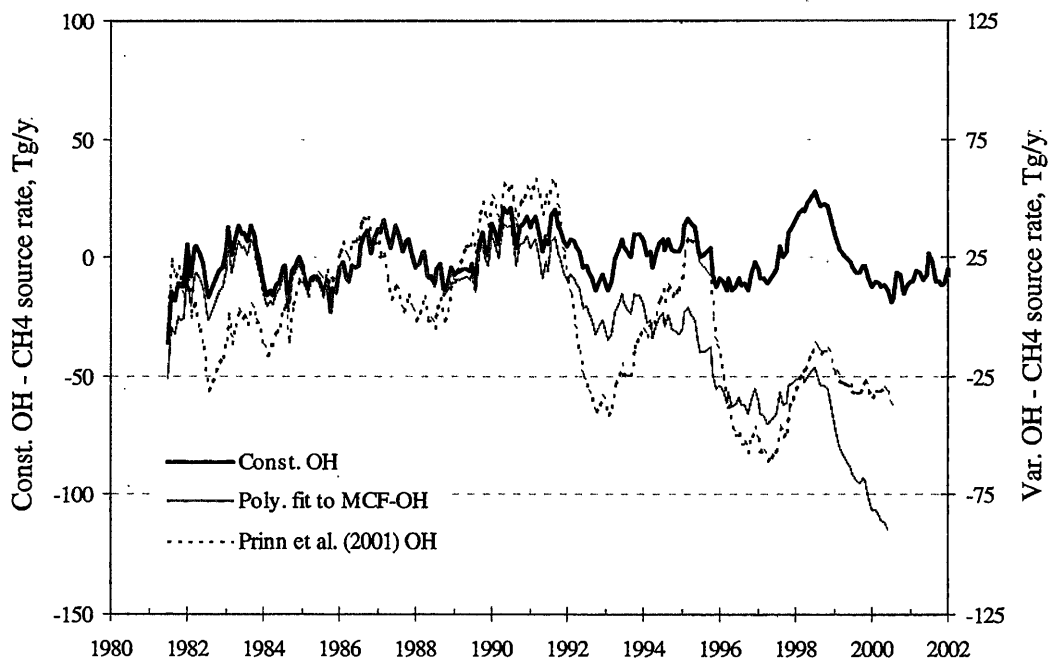
Figure 2.6. Same as in Fig. 2.5 except here emissions are for the northern hemisphere only.

brief overview suffices.

The model was developed to simulate the atmospheric behavior of long-lived

greenhouse gases (lifetimes on the order of months or longer) and consists of four major

environmental compartments, each simulated as a number of two-dimensional well-

mixed boxes: the deep ocean (four boxes), the ocean mixed-layer (six boxes), the

18

troposphere (twelve boxes), and the stratosphere (eleven boxes). The boxes span the latitudes 65-90N, 30-65N, 0-30N, 0-30S, 30-65S, and 65-90S. Gas in the troposphere is transported into the ocean through the thin film model of *Liss and Slater (1974).* Tropical convection brings gas from the troposphere into the stratosphere where it spreads to higher latitudes. Above 100 hPa, the stratosphere is modeled as a series of six 1D layers. Though largely unimportant for CH_4, the model ocean contains a mixed layer and deep ocean components. Transport between atmospheric boxes occurs via both advection and turbulent processes (sub-grid scales). Chemical lifetimes of gases are added as inputs to the model in each box allowing for the chemical destruction of gases. The model can be run either in forward mode, where atmospheric mixing ratios are calculated based on input emissions, or inverse mode, where surface fluxes are derived from atmospheric measurements. We used this mode for the following work.

2.4 Inverted sources

Chemical lifetimes of methane due to the CH_4+OH reaction were calculated for each box in the troposphere using the monthly averaged OH fields of *Spivakovsky et al. (2000).* In the stratosphere, OH profiles from *Bruehl et al (1996)* were used. We derived climatological temperatures from the National Center for Environmental Prediction Reanalysis Project *(Kalnay et al., 1996)* to determine the CH_4+OH rate coefficient according *to Sander et al. (2000).* Results of the inversion are shown in Figs. 2.5, 2.6, and 2.7, for the global, northern hemisphere, and southern hemisphere emissions, respectively. We focus attention first on the source record we derived using a constant OH field.
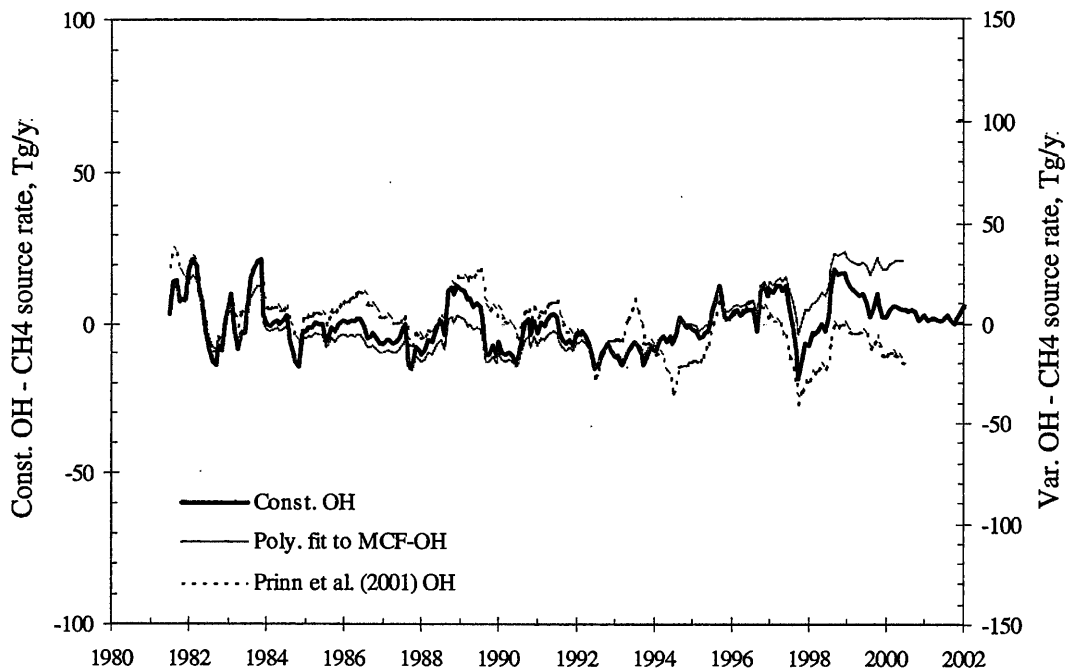
Figure 2.7. Same as in Fig. 2.5 except here the emissions are only for the southern hemisphere.

The inversion produces global emissions of CH_4 that are about 550 Tg y^{-1}. This in good agreement with the CH_4 budgets listed in the latest Intergovernmental Panel on Climate Change (IPCC) working report on climate change (*Denman et al., 2007*). Our estimate is in the middle of the reported budgets. Perhaps more importantly, our inverted emissions remain constant over the entire 23-year period of the simulation. That is, we find that the declining trend of atmosphere methane can be explained by a non-changing source over this time, without a need to find deceasing sources. It implies that atmospheric levels of CH_4 are reaching steady state conditions, meaning that the sinks of CH_4 are coming into balance with the sources. This behavior is seen in both the

northern and southern hemispheres (Figs. 2.6 and 2.7). This is a somewhat surprising and non-intuitive result. We can use a simple one-box model to understand this behavior.

If we model the atmosphere as a single box, the time rate of change of CH_4 in that box is

$$\frac{dC}{dt} = S - \frac{C}{\tau},\qquad(2.1)$$

where C is the mixing ratio of CH_4 in ppbv (nmol mol^{-1}), S is the global emission rate (ppbv y^{-1}), and τ is the lifetime in years. The solution to this equation is

$$C(t) = S\tau + (C_o - S\tau)\cdot\exp(-\tfrac{t}{\tau}),\qquad(2.2)$$

where C_o is the mixing ratio at time zero. If we take the derivative of this we find

$$\frac{dC}{dt} = \frac{(S\tau - C_o)}{\tau}\cdot\exp(-\tfrac{t}{\tau}).\qquad(2.3)$$

With Eqs. 2.2 and 2.3 we can explore what the behavior of CH_4 would be if the lifetime and emissions were constant. In Fig. 2.8 we plot Eq. 2.2 along with the global mean CH_4 mixing ratio and Eq. 2.3 with the time series of CH_4 trend from Fig. 2.4. In both equations we assume constant emissions at 550 Tg y^{-1} as derived from our inversion. We kept the lifetime τ constant at a value that optimized the fits between the one box model and the data records. We found the fit is best when τ=8.9 years. We used this value in both equations.
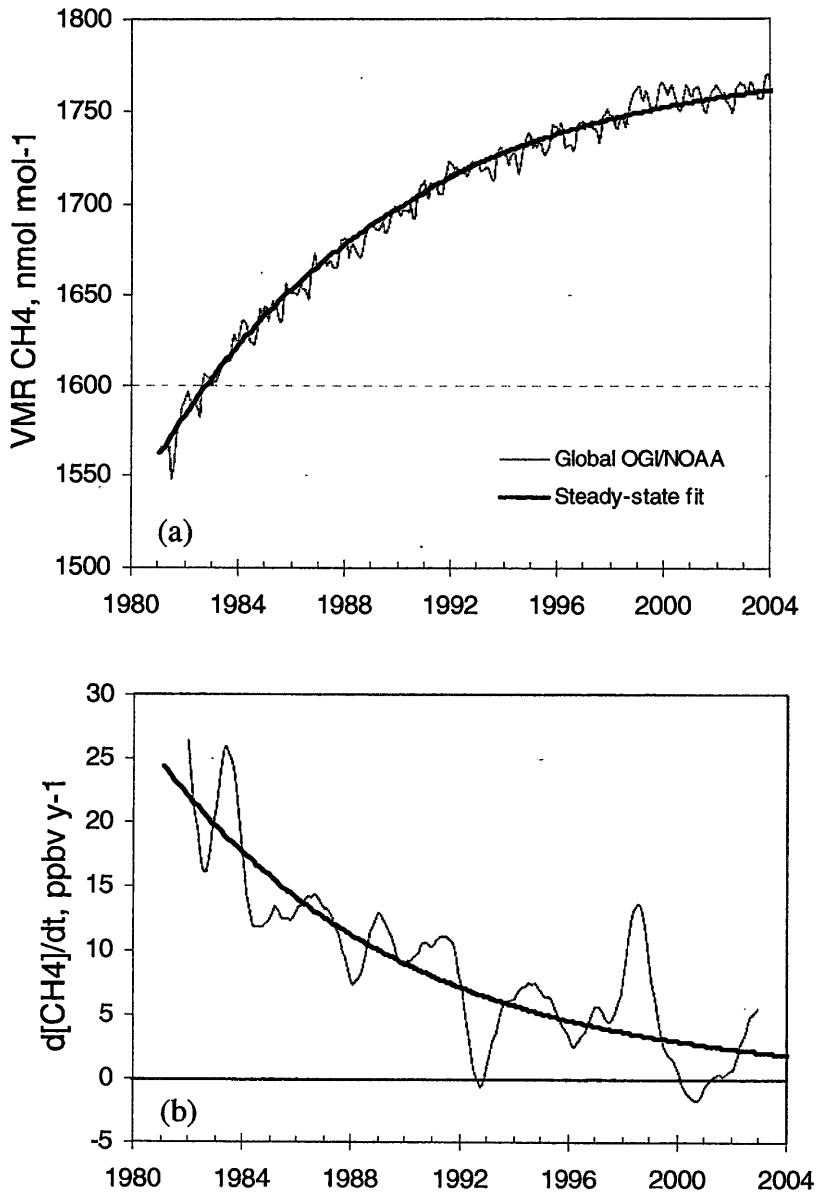
Figure 2.8. Predictions of a one-box model assuming constant emissions of 550 Tg y^{-1} and a lifetime of 8.9 yr. The model predictions are in gray and data from the measurement record are plotted in black.

The match between the fitted steady state model and the actual data is excellent. The decline in the trend follows a smooth exponential with a decay constant equal to the lifetime of CH$_4$. An exponential function also provides a good fit to the increase in

22

mixing ratio observed since the early 1980s. The global burden of CH_4 at steady state is found by setting dC/dt equal to zero in Eq. 2.1 At this point, $C=S\tau$ With $S=550$ Tg y^{-1} (or 200 ppbv y^{-1}) and $\tau=8.9$, C (at steady state) would be 1780 ppbv. In 2004, the global mean mixing ratio was 1760 ppbv.

2.5   Discussion

While the recent behavior of methane can reasonably be explained by an approach to steady state, this explanation requires that the lifetime of CH_4 remains constant throughout this period. For reasons discussed in the next chapter this may not be so. In Figs. 2.8a & 2.8b we also plot results from our inversion study based upon a non-constant OH history. Two different OH histories are used. One is from *Prinn et al. (2001)* where the authors estimated that OH has decreased by 0.64% y^{-1} over this period, and the second one is based on our own evaluation of OH using methyl chloroform measurements. By allowing OH to vary, we are also effectively changing the lifetime of CH_4. Doing so affects the emissions derived from the inversion.

There are two important points to take away from these simulations. Allowing OH to decline, increases the lifetime of CH_4. As the lifetime increases, the emissions required for mass balance also decrease. The model results show that global emissions drop by about 50 Tg y^{-1} if the CH_4 lifetime increases by 10%. Thus there is an alternative scenario to consider when explaining current methane trends. Emissions may not be constant after all, rather they could be declining if the lifetime of CH_4, as governed here by the decreasing OH abundance, is increasing. Thus we can't assume a priori that methane has reached steady state.

The second point is seen by comparing the simulated emissions in the northern hemisphere with those in the southern hemisphere. We see that the non-constant OH does not affect the simulated emissions in the SH. That is, here the emissions remain constant throughout the entire interval. The global drop of 50 Tg y^{-1} occurs in the northern hemisphere. This is an important result in understanding how the sources of methane may be changing. If OH is behaving as modeled, global CH_4 emissions are not constant, but declining, and they are declining only in the northern hemisphere. Thus it is here where we should be looking for decreasing emissions. What we will discover later in this work, is that we have identified one source that is changing in the NH, that is emissions from rice production. We will explore this topic further.

Chapter 3 —— Is The Chemical Oxidation Sink Of Methane Changing?

3.1 Introduction

The most important sink of atmospheric methane is chemical oxidation by the hydroxyl radical OH, which is responsible for about 90% of the total destruction of methane in the troposphere (*Denman et al., 2007*). Smaller sink processes include reaction with OH, chlorine (Cl), and $O(^1D)$ in the stratosphere, as well as a small soil sink (~30 Tg CH_4 y^{-1}, *Denman et al., 2007*) and reaction with chlorine in the marine boundary layer (~20 Tg CH_4 y^{-1}, *Tyler et al., 2000*).

The hydroxyl radical plays a vital role in the chemistry of the troposphere (e.g. *Warneck, 2000; Finlayson-Pitts, Crützen and Lelieveld, 2001*). It is the major oxidant of gas species with bonds to hydrogen, including hydrocarbons (carbon monoxide CO, CH_4, and non-CH_4 hydrocarbons) and the hydrochlorofluorocarbons (HCFCs), which have replaced the banned chlorofluorcarbons. Reactions with OH are responsible for 90%, 80%, 80%, and 25% of the removal of CO, methyl chloride (CH_3Cl), and hydrogen (H_2) from the atmosphere, respectively. If oxidation of hydrocarbons takes place in the presence of nitrogen oxides, photochemical production of ozone ensues. Thus any change in global OH levels will directly affect the abundances of these chemicals and their impacts on the atmospheric environment.

The production of OH is initiated by the photolysis of ozone (O_3) by ultraviolet radiation (< 320 nm) in the troposphere which produces $O(^1D)$, an excited oxygen species. This in turn reacts with water vapor to form OH. Since the production of OH requires short-wave sunlight and water vapor, concentrations of OH are highly seasonal, peaking in the tropics during the summer months of each hemisphere. Its seasonally-averaged global concentration is estimated to be ~1×10^6 molecules cm^{-3} (*WMO, 1999*).

There is concern that OH is decreasing since concentrations of its major sinks, including CH_4 and CO, have increased from pre-industrial levels. There are however competing processes that may offset these changes. Over this same period stratospheric O_3 has decreased, increasing the UV radiation reaching the troposphere. Tropospheric water vapor has likely increased in recent decades due to global warming. Both of these changes would enhance OH production. The net effect of these changes is uncertain as modeling studies produce estimates of the OH trend ranging from –0.06 % y^{-1} (*Wang and Jacob, 1998*) to 0.43 % y^{-1}(*Karlsdottir and Isaksen, 2000*) indicating that OH may be either increasing or decreasing.

In situ measurements of tropospheric OH have been made for many years (*Wang and Davis, 1974; Davis et al., 1976; Campbell et al., 1986; Hard et al., 1992*). Due to its short lifetime (~1-2 s) however, it is not possible to construct a global record of OH since it is highly variable in both space and time, and in situ measurements are representative only of local conditions (*Ehhalt, 1999*).

Despite the lack of direct measurements, global OH levels can be inferred from the atmospheric abundances of proxy gases that are primarily removed by OH. If

emissions of the proxy gas are well defined, OH levels can be determined through mass balance and the atmospheric record.

The most important gas used to date for this purpose is methylchloroform (CH_3CCl_3). Methylchloroform (MCF) is an industrial solvent that has been used by manufacturers and the dry cleaning industry since the 1950s. Despite efforts to recycle and recover it during use, some fraction of it evaporates and reaches the atmosphere, where it is destroyed primarily by OH. The production of MCF is almost entirely anthropogenic and emissions rose rapidly throughout the 1960s and 1970s (*McCulloch and Midgley, 2001*). Due to its long lifetime, MCF reaches the stratosphere and releases chlorine where it is photolyzed. Because of this, MCF production was banned under the Montreal Protocol and its amendments. Since the early 1990s production has nearly stopped and atmospheric levels have dropped precipitously. Industry groups have good records of its production making annual emission estimates possible (e.g. *McCulloch and Midgley, 2001*). This, combined with its relatively long lifetime of 5 to 6 years, makes MCF a good tracer of global OH.

Atmospheric MCF was first measured in 1972 by Lovelock (*Lovelock, 1974*) but systematic measurements only began in the late 1970s and early 1980s by the Oregon Graduate Institute (*Rasmussen et al., 1981; Khalil and Rasmussen, 1981; Rasmussen and Khalil,1986*) and the Atmospheric Lifetime Experiment (*Prinn et al., 1983*). Measurements continue today by the National Oceanic and Atmosphere Association's Global Monitoring Division (*Montzka et al., 2000*) and the Advanced Global

Atmospheric Gas Experiment (*Prinn et al., 2000, 2001*). These programs measure MCF at latitudinally-distributed clean air background sites.

These measurements have been used to estimate the global OH burden (*Lovelock, 1977; Neely and Plonka, 1978; Prinn et al., 1987; Prinn et al., 1992; Prinn et al., 1995; Krol et al., 1998;Montzka et al, 2000; Prinn et al., 2001*). Methylchloroform is also commonly used to test simulations of OH fields from atmospheric chemistry models (*Spivakovsky et al., 2000; Kanakidou et al., 1995*).

A number of studies have used MCF to diagnose the OH trend, but much debate remains about its long-term trend and interannual variability (*Prinn et al., 1995; Krol et al., 1998; Prinn et al., 2001, Prinn and Huang, 2001; Krol and van Leeuwen, 2001; Krol and Lelieveld, 2003; Prinn et al., 2005*). The AGAGE group releases MCF measurements every few years and from these they estimate the OH trend from the beginning of the AGAGE measurements (1978) to the most recent measurements. The calculated long-term trend tends to change with each new release of data.

The first estimate of the OH trend using ALE/GAGE/AGAGE by *Prinn et al. (1992)* suggested that that OH was increasing over the period 1978 to 1990 with a trend of 1 % y^{-1} which was surprising considering the increasing levels of OH sinks. The trend was later revised downwards to 0.0 ± 0.2 % y^{-1} when extended to 1994 (*Prinn et al.,1995*). Over the same time period and using the same measurement data set *Krol et al. (1998)* found that OH trend was still positive, with an estimate of 0.46 ± 0.6 % y^{-1}. The reasons offered for the differences varied. *Prinn and Huang (2001)* attributed the disagreement to different emissions, a different representation of the MCF

measurements, and an incorrect initialization scheme used by *Krol et al. (1998)*.

Though both studies used ALE/GAGE/AGAGE methylchloroform measurements, *Krol et al (1998)* fit these measurements with Legendre polynomials, which *Prinn et al. (2001)* claimed were invalid. According to their modeling, these differences were sufficient to bring the trend estimates in line. *Krol et al. (2001)* concluded that the discrepancy between trends was due to different models and optimization methods used.

Updating their earlier work, *Prinn et al. (2001)* estimated the OH trend from 1978 to 2000 to be -0.64 ± 0.60 % y^{-1}. Thus the trend went from zero to negative. The sign of the estimated trend again changed when *Prinn et al. (2005)* used ALE/GAGE/AGAGE measurements from 1978 to 2003 to calculate a trend of $0.2^{+0.8}_{-0.4}$ % y^{-1}.
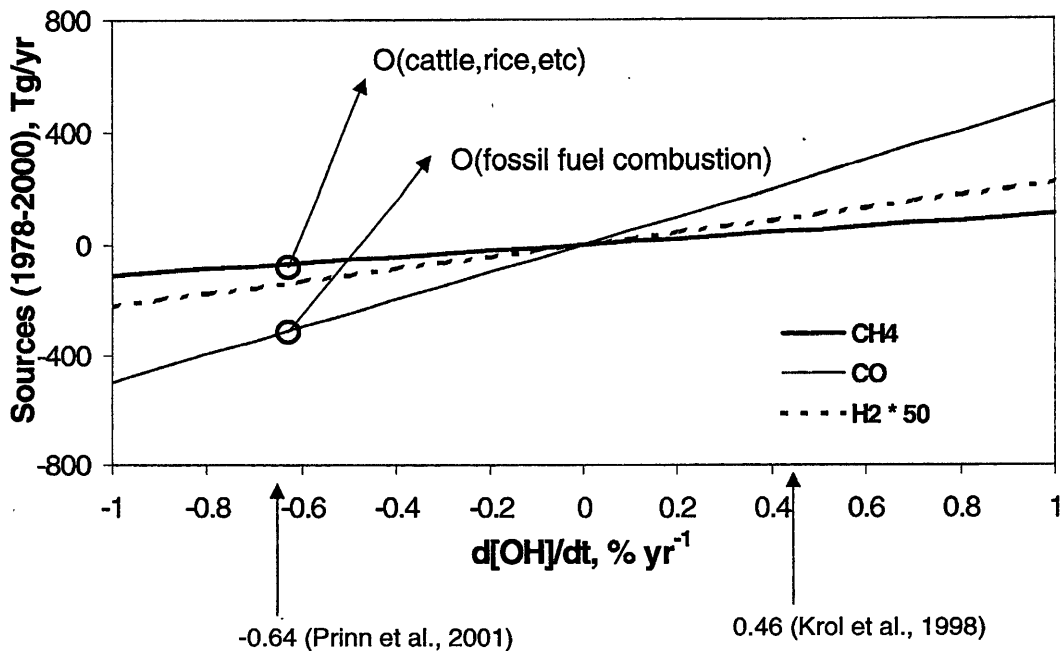
Figure 3.1. The effect of an OH trend over the years 1978 to 2000 on trace gas emissions estimated using inversion techniques. The offsets are relative to emissions calculated for the case with no OH trend. The impact of two trends from the literature are shown. The *Prinn et al (2001)* trend would cause estimates of current CO emissions to be about 400 Tg y^{-1} smaller relative to zero OH trend. The notation O(x) means that emissions are on the order of source x.

Though there is some qualitative agreement in the behavior of OH during the past couple decades, there is still considerable uncertainty to the decadal trends. This uncertainty is propagated to source inversions of trace gases such as methane. In Fig. 3.1 we show the impact that a trend in OH has on inverted emissions of CH$_4$, CO, and H$_2$. For example, an OH trend of -0.61 % y^{-1} over 1978 to 2000 (*Prinn et al., 2001*) would lower top-down estimates of current CO emission by 400 Tg y^{-1} relative to a zero OH trend. Estimates of CH$_4$ emissions would decrease by about 50 Tg y^{-1}. A trend of 0.46 % y^{-1} would increase emissions relative to a zero trend.

30

There's concern that the OH trend has been calculated for the most part with one network of measurements, one atmospheric model, and one inversion scheme. It is unclear how robust the reported OH trend is, and whether it is subject to artifacts from the measurements or modeling.

In this work we investigated the global OH trend using novel modeling and inversion scheme. In addition, we used a set of atmospheric MCF measurements that until now has not been used to infer OH concentrations. In particular, we pose the following questions to investigate:

1. How sensitive is the MCF-derived OH trend to measurements of MCF from different trace gas monitoring networks? There exists three independent time series of atmospheric MCF covering three different periods. We used all three to infer the OH record and assess the robustness of the OH time series across measurement networks, the first time a comparison across data sets has been performed. This helped us identify which features of the OH time series are likely real and not artifacts of the modeling process.

2. How sensitive is the modeled OH trend to emissions of MCF from biomass burning? The release of methylchloroform from biomass burning has been measured from both field and laboratory studies (*Rudolph et al. 1995; Rudolph et al., 2000*). Due to the small number of measurements the global source strength is highly uncertain, but estimates range from 2 to 16 Gg CH_3CCl_3 y^{-1} *(Lobert et al., 1999; Rudolph et al., 2000)*. Until its ban, industrial production of MCF far exceeded the small contribution from biomass burning. However, in recent years as industrial production has declined,

31

the contribution of biomass burning has increased in importance, and now may be the largest source of MCF. Here we assess the sensitivity of the inferred OH trend to the biomass burning source. No study to date has assessed this impact carefully.

3. How does the timing of the MCF emissions affect the calculate OH trend?

We've seen from past efforts that modeled OH rises until 1990 then falls thereafter (*e.g. Prinn et al. 2001, 2005*). Curiously, this is also the temporal pattern of MCF emissions, raising suspicion that changes in the modeled OH are related to artifacts of the emissions record. We investigate whether the major features of the derived OH time series are robust relative to shifts in the industrial emissions of MCF within their estimated uncertainties.

One uncertainty that has not been considered to date is the intra-annual timing of the industrial emissions. The production and emissions of industrial MCF are reported on an annual basis providing no basis to establish the exact monthly timing of the emissions. As input emissions to the mass balance model are specified as rates and not burdens, there is an unrealistic discontinuity in emissions rate between the end of one year and the beginning of the next. One solution is to interpolate rates from one year to the next across months. But this forces us to assign the reported rate to a particular month of the year. With no a priori reason to choose one month over another, there is a range of permitted emission time series. Though this uncertainty seems minor, it can significantly influence the magnitude of the OH concentrations calculated around the time of the emissions peak, which as previously mentioned is the same time that reported OH time series peak.
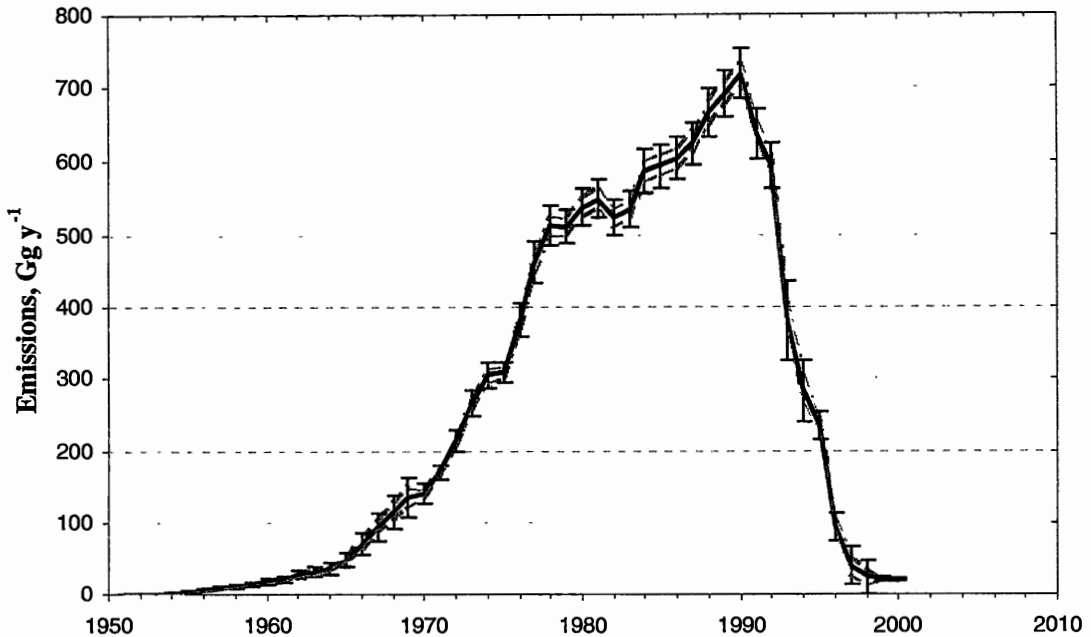
Figure 3.2. Emissions of methylchloroform from industrial production (*McCulloch and Midgley, 2001*). Gray lines show one standard deviation and errors bars are two standard deviations.

3.2 Emissions

Emissions of industrial methyl chloroform are relatively well known from 1951 to 2000. Over the bulk of this period (1970 – 1995), MCF producers in countries belonging to the Organization for Economic Cooperation and Development (OECD) reported and categorized production and sales according to the delay between production and emissions; rapid release (less than one year between production and emission), medium release (between one and two years), and slow release (delay about two years). These data were independently audited and verified for internal consistency. From 1992 onwards parties to the Montreal Protocol were required to report production

figures for compliance providing another source of information over the latter years of production.

Emissions from production and sales were estimated by *McCulloch and Midgley (2001)* using an emissions function based upon the release delay categories. Seventy-five percent of rapid release production is assumed emitted during the year of production and the remainder in the following year. The fractions are reversed for the medium release category, and 25% of slow release production is emitted one year after production and the remainder is emitted two years following production. The resulting time series of emissions rise from about 500 Gg y^{-1} in 1978 to a peak of 700 Gg y^{-1} in 1990 and fall rapidly thereafter (Fig. 3.2). The uncertainty of emissions (1σ) over the period of highest production is about 5 %.

The geographical distribution of MCF sales is known from industry data at the regional level (USA+Canada, Europe, Far East, other north mid-latitudes (30-90 N), northern hemisphere tropics, and the SH). Further refinement was performed by *Midgley and McCulloch (1995)* on the basis of gross domestic product and population which when used in an earlier study, were shown to be good proxies for the distribution of chlorofluorocarbons (*McCulloch et al., 1994*). *Keene et al. (1999)* created a 1×1° gridded inventory based on this distribution for the year 1990. We integrated emissions from this inventory over the boundaries of our atmospheric transport model's regions (0–30°N,S, 30–65°N,S, 65–90°N,S). The percentage of the total source in each region is 0.1%, 91.2%, 5.6%, 1.5%, and 1.5%, for 65 – 90N, 30 – 65N, 0 – 30N, 30S – 0, and 65 – 30S, respectively. We transformed the emissions to a monthly time scale using a
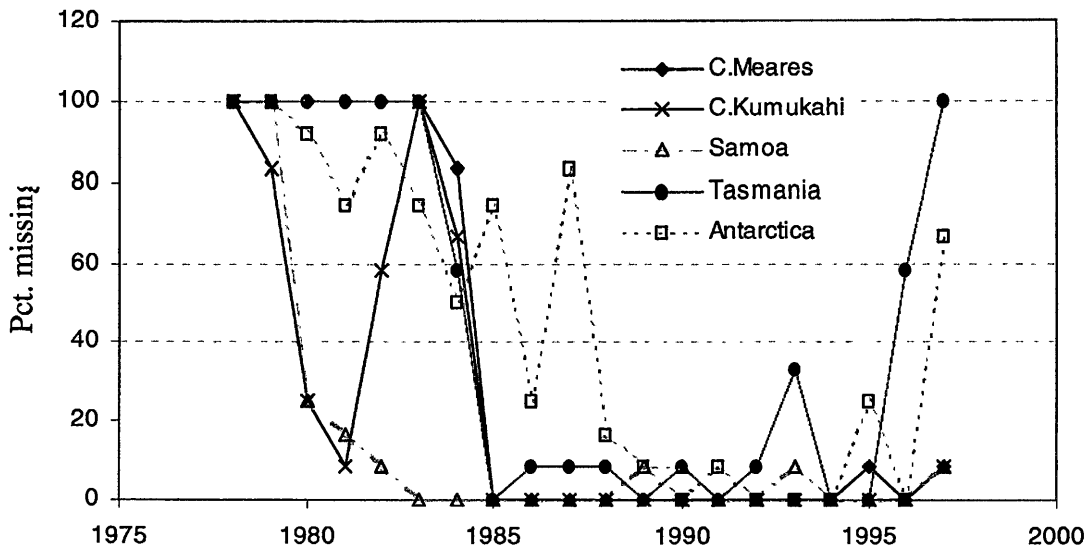
Figure 3.3. Gaps in the measurement record of OGI methylchloroform. The figure shows the percentage of months in a given year when no data are available.

cubic spline interpolation (*Press et al., 1986*). The interpolated emissions were smoother and reduced the variability of the derived OH. We consider this time series the base emissions scenario. We extended these emissions to 2008 below using UNEP-reported production and also consider the contribution of biomass burning.

3.3 Atmospheric methylchloroform measurements

3.3.1 Oregon Graduate Institute

Some of the first measurements of CH_3CCl_3 were made by *Rasmussen et al (1981)* at the South Pole, and Cape Meares, Oregon (45.5N, 124W). These early measurements showed that global MCF was increasing as expected with reported emissions (*Khalil and Rasmussen, 1981*). Sampling continued until 1997 and MCF measurements are available over the time span 1981 – 1996 at the following stations:

35

Barrow, Alaska (71.3 N, 156.7 W), Mauna Loa and Cape Kumukahi, Hawaii (19.3N,

154.5W); American Samoa (14.1S, 179.6E), Cape Grim, Tasmania (42S, 145E), Palmer

Station, Antarctica (-64.5, 64.3W), South Pole (-90). (*Rasmussen et al., 1981; Khalil*

and Rasmussen, 1981), though there are significant gaps in the record for some stations

throughout the period (Fig. 3.3). We filled in small gaps (< 4 months) by linear

interpolation and use neighboring stations to reconstruct longer periods of missing data.

We used Cape Kumukahi as our north tropical site over Mauna Loa since the latter is at

altitude (~3300 m), and Kumukahi is near sea level, compatible with the other sites. We

combined measurements from Palmer Station and South Pole into a single Antarctica

record. The average ratio between Palmer Station and the South Pole is 0.98 ± 0.04.

Over the period of measurements the average gradient between the northern and

southern hemispheres is 1.19 ± 0.07.

3.3.2   ALE/GAGE/AGAGE

Beginning in 1978 atmospheric levels of CH_3CCl_3 have been measured

continuously at four semi-hemispheric sites as part of a series of experiments to

measure atmospheric trace gases, the Atmospheric Lifetime Experiment (ALE), the

Global Atmospheric Gas Experiment (GAGE), and the Advanced Global Atmospheric

Gas Experiment (AGAGE) (*Prinn et al., 1983; Prinn et al., 1987; Prinn et al., 1992;*

Prinn et al., 2000; Prinn et al., 2001). Measurements from the north mid-latitudes (30-

65°N) come from Adrigole, Ireland (52°N, 10°W; 7/1978 – 12/1983); Cape Meares,

OR (45.5°N, 124°W; 1/1980 – 6/1989), Mace Head, Ireland (53°N, 10°W; 1/1987 –

present), and Trinidad Head, CA (41°N, 124°W; 10/1995--present). A single northern

mid-latitude monthly average time series was constructed from these four stations. During those times when only one station was operating, that station's record was used uniquely; during all other times, a weighted mean was calculated based upon each station's latitude and each month's standard deviation. CH_3CCl_3 was measured from a single station throughout the duration of the three experiments from each of the other three semi-hemispherical regions; Ragged Point, Barbados (13°N, 59°W), Point Matatula, American Samoa (14°S, 171°W), and Cape Grim, Tasmania (41°S, 145°E). During times when the ALE, GAGE, and AGAGE experiments overlap, we calculated weighted means based on standard deviations of monthly averages.
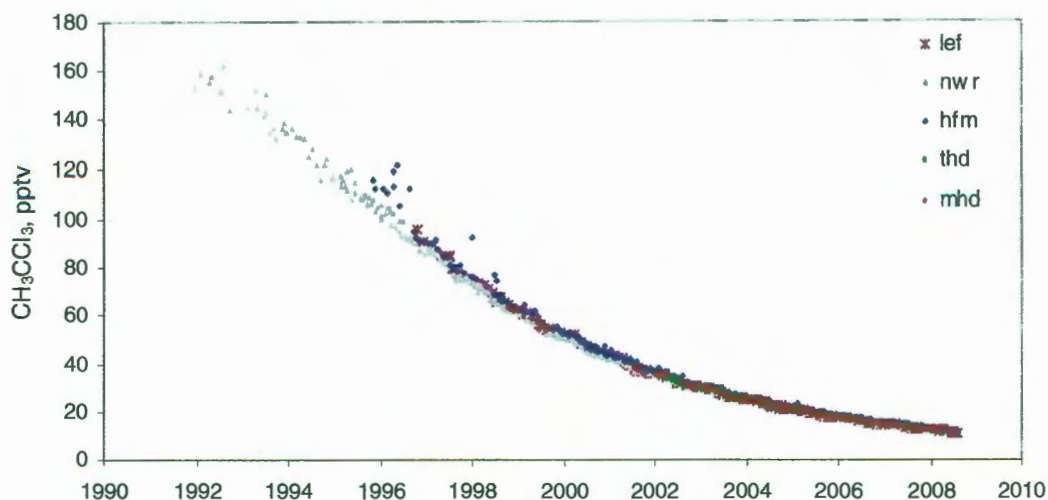
Figure 3.4. ESRL-GMD methylchloroform measurements from northern mid-latitude sites. lef=Wisconsin, USA (45.6N, 90.9W), nwr=Niwot Ridge, CO, USA (40.0N, 105.6W), hfm=Massachusetts, USA (42.5N, 72.2W), thd=Trinidad Head, CA, USA (41N, 124W), mhd=Mace Head, Ireland (53N, 10W).

3.3.3 NOAA ESRL-GMD

The National Oceanic and Atmospheric Administration has monitored CH_3CCl_3 through its Earth Systems Research Laboratory's Global Monitoring Division (ESRL-GMD) since 1991 (*Montzka et al., 2000*). Many of the sites are common with the OGI and ALE/GAGE/AGAGE networks, and in these cases we used CH_3CCl_3 measurements from those sites for this study. ESRL-GMD measures CH_3CCl_3 at a number of northern mid-latitude sites including Niwot Ridge, CO (40.0°N, 105.6°W). We chose this site over the others due to the length of the period over which measurements were taken, extending back to 1991. As a check that we were not biasing our simulations by choosing this site over the others, we compared CH_3CCl_3 from five

mid-latitude stations (Fig. 3.4). By visual inspection we concluded that there were no

meaningful systematic differences in MCF concentrations between sites.
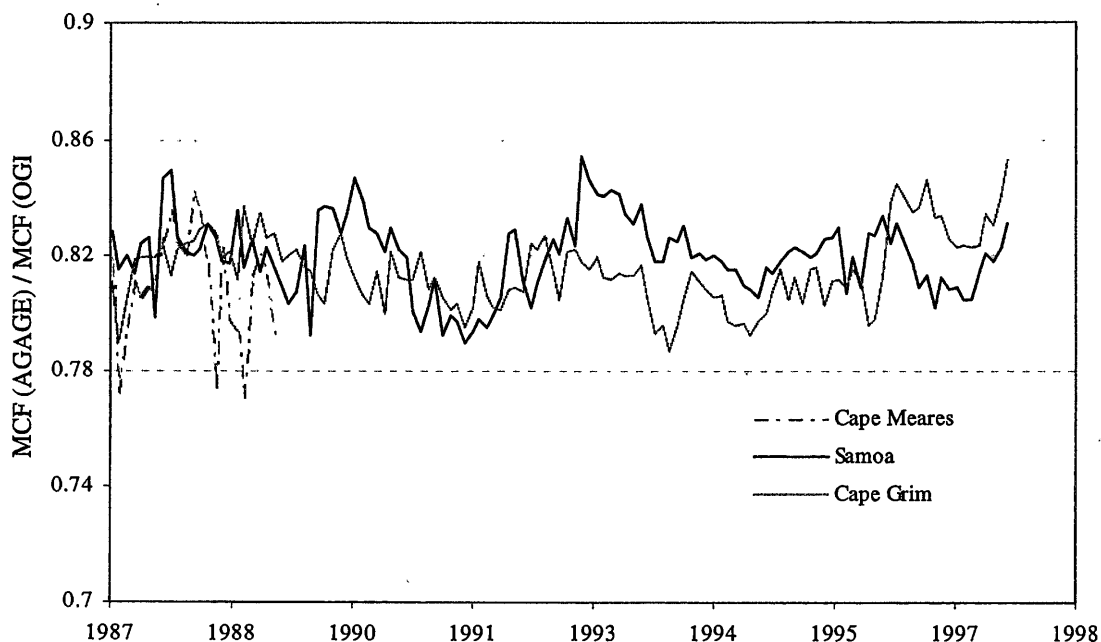
Figure 3.5. Ratio of AGAGE and OGI CH_3CCl_3 mixing ratios measured at common sites.

3.3.4 Comparison of MCF networks

We place the OGI MCF measurements on the ALE/GAGE/AGAGE absolute

calibration scale due to concerns about the absolute scale of OGI measurements (*Aslam*

Khalil, personal communication). This in essence puts the OGI MCF on the Scripps

Institution of Oceanography (SIO)-2005 calibration scale as this is the standard used by

the AGAGE program (*Prinn et al., 2000*). A direct comparison of monthly average

CH_3CCl_3 mixing ratios at common sites of the AGAGE and OGI programs (Fig. 3.5)

revealed a mean scaling factor of 0.82 ± 0.02, i.e. MCF(AGAGE) = $0.82 \times$ MCF(OGI).

Fig. 3.6 shows the scaled OGI, ALE/GAGE/AGAGE, and ESRL-GMD measurements of MCF in the mid-latitudes and tropics. In general, there is good agreement of measured MCF between the networks. The exception is the measurements from the northern tropics. Plotted are the mixing ratios measured at Cape Kumukahi, HI for the OGI and ESRL-GMD networks, and at Ragged Point, Barbados for the ALE/GAGE/AGAGE network. The station at Ragged Point is closer to the equator (13°N) than Cape Kumukahi (19°N) and we expect mixing ratios at Ragged Point to be lower since OH levels are higher there, and the site is farther from major MCF emissions. However this alone can not explain the differences. The OGI Cape Kumukahi MCF begins lower than the Ragged Point series, then crosses and remains above it past 1985. Since it is difficult to envision a realistic scenario that would produce this behavior, the anomaly is likely due to calibration problems. We kept the OGI Cape Kumukahi record as it is, but we used caution interpreting the OH record derived from OGI measurements before 1985.

3.4 Modeling

3.4.1 Description of transport model

We estimated OH from the methyl chloroform measurements and emissions with a two-dimensional transport box model. The model contains twelve boxes in the troposphere and eleven boxes in the stratosphere. The latitudinal resolution of the model is consistent with long term measurements of MCF which are available only at a few locations globally. The troposphere is divided into six latitudinal sections (90-65°N,S; 65-30°N,S; 30-0°N,S) and two atmospheric layers (surface – 500 hPa; 500 hPa –

tropopause, where the tropopause height varies with both latitude and season). The lower stratosphere is divided into six boxes extending latitudinally between the tropopause and 100 hPa. The remainder of the stratosphere (up to 1 hPa) is one-dimensional with increments of 20 hPa. The meridional partitioning of the lower stratosphere allows gas to be transported from the troposphere to the stratosphere in the tropical Hadley cell. Return flow occurs at mid-latitudes.

Transport across box interfaces is described both in terms of advection and turbulence. Additional tropospheric-stratospheric exchange occurs through the changing level of the tropopause. Transport coefficients were derived from empirical meteorological data (*Newell, 1972, Prinn, 1984*) on a seasonal basis. The model transport was calibrated using trichlorofluoromethane (CFC-11) as a tracer and was further validated through the use of trichlorodifluoromethane (CFC-12) (*Butenhoff, 2002*). The latitudinal gradients and stratospheric profiles of these gases were well simulated by the model.

For each model box, a differential equation is written of the form

$$\frac{d\chi_i}{dt} = S_i - \eta_i \chi_i - \sum_{ij} transport_{ij}, \qquad (3.1)$$

where χ_i is the mixing ratio of box i, S_i is the emission into box i in units of mixing ratio per time, $\eta_i = 1/\tau_i$, where τ_i is the lifetime of the gas in box i, and the last term is the summation of the transport between box i and all adjacent boxes j. For the current study, all emissions are confined to the lower tropospheric boxes. A unique feature of

41

the model is the capability of producing an analytical solution of the system of differential equations using matrix techniques (*Khalil and Rasmussen, 1984*). Solving the equations exactly rather than numerically permits us to set the model temporal resolution (one month) to be equal to the transport resolution without encountering errors that would arise using a finite time step in a numerical scheme. The lower resolution requires fewer computational resources with no concurrent loss of information.

The lifetime is determined by the aggregate sinks of the CH_3CCl_3 molecule. The dominant sink for methyl chloroform is the reaction

$$CH_3CCl_3 + OH \rightarrow CH_2CCl_3 + H_2O, \qquad (3.2)$$
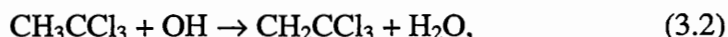
Additional sinks include losses in the stratosphere through photolysis and hydrolysis in the ocean. Since the solubility of CH_3CCl_3 in seawater is low, little gas is transported from the atmosphere to the ocean. *Butler et al. (1991)* estimates that only 5% of MCF is removed by the ocean. In addition, few MCF molecules reach the stratosphere due to slow troposphere-stratosphere exchange and the strength of the tropospheric OH sink. Those that do are removed in the lower layers either through reaction with OH or through photolysis by shortwave radiation ($\lambda < 240$ nm; *DeMore et al., 1997*).

In the troposphere the lifetime is given as τ_{OH} or $1/k[OH]$. In the lower six tropospheric boxes this lifetime is augmented to account for the loss of methyl chloroform to the mixed layer ocean. We used an estimate of 85 yr for the lifetime of

CH$_3$CCl$_3$ with respect to the ocean (*Kurylo and Rodriguez, 1998*). Using other published lifetimes of 89 yr (*Butler et al., 1991*) and 83 yr (*Krol et al., 1998*) had little impact on our results.

We calculated photolysis rates in the stratosphere using the Tropospheric Ultraviolet (TUV) model developed by the National Oceanic and Atmospheric Administration (*Madronich, 1993*). The photolytic coefficients estimated by TUV were integrated and averaged over the dimensions of each of the stratospheric boxes. We calculated a weighted monthly mean OH field in the stratosphere from the data set of *Bruhl (2000)*. Measured OH values were weighted by CH$_3$CCl$_3$ density. Stratospheric OH concentrations are fixed in the model and are not allowed to vary with time. The total lifetime in the stratosphere is

$$\tau_{strat} = \left(\tau_{hv}^{-1} + \tau_{OH}^{-1}\right)^{-1}. \tag{3.3}$$
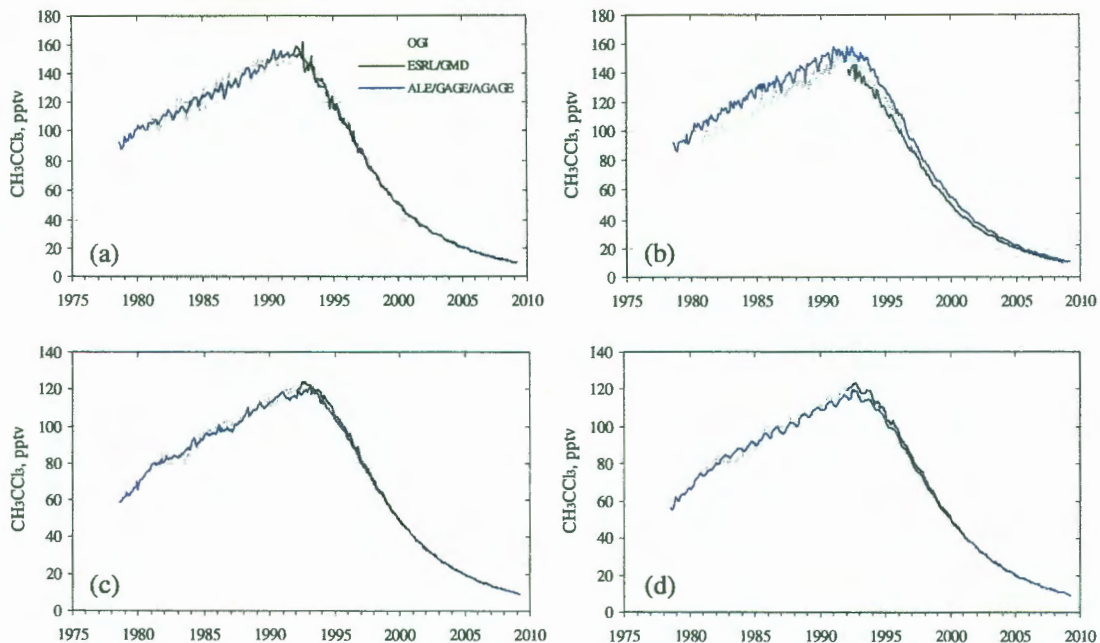
Figure 3.6. Methylchloroform measurements from the OGI, ALE/GAGE/AGAGE, and ESRL-GMD networks. (a) northern mid-latitude, (b) northern tropics (OGI & ESRL - Cape Kumukahi, AGAGE - Ragged Pt., Barbados), (c) southern tropics (Samoa), (d) southern mid-latitudes (Cape Grim, Tasmania).

where $\tau_{h\upsilon}$ is the photolytic lifetime and τ_{OH} is the lifetime due to reaction with OH.

3.4.2   Inversion scheme

Base tropospheric OH levels are initially specified using the global OH fields provided by *Spivakovsky et al. (2000)*. The authors calculated monthly OH concentrations at a spatial resolution of 6°over a global two-dimensional grid using an atmospheric chemistry model. From these we derived our reference OH field. We ran our model over 12 month time increments. For each model run we scaled the OH levels in the northern hemisphere and southern hemispheres independently by the factors β_N

and β_s. The simulated MCF concentrations are compared to the measurements and the fit between the two time series is assessed by a weighted χ^2 parameter given by

$$\chi^2_{global} = \sum_s \chi^2_s \, , \tag{3.4}$$

where χ^2_s is the fit for site s and is calculated as

$$\chi^2_s = \frac{\sum_i w_i \times (C_i^m - C_i^o)/C_i^o}{\sum_i w_i} \, . \tag{3.5}$$

C_i^m and C_i^o are the modeled and observed MCF concentrations, respectively, during month i and the weight w_i is set equal to $1/\sigma_i^2$, where σ_i^2 is the monthly standard deviation of the MCF measurements. Over each simulated time period, the βs are optimized simultaneously and independently, so as to minimize χ^2_{global}. The β parameter space is sampled using a standard gradient search (*Bevington, 1969*). The reference OH values are scaled by the βs that produced the minimized χ^2_{global}. In this manner the optimized OH field is constructed annually and from the resulting time series of global OH averages, the trend is derived.

The measurement record of MCF is influenced by processes and instrumental variability not reproducible by model calculations. Both *Krol et al. (1998)* and *Prinn et*

al. (2001) used functional fits as replacements of the MCF measurements to better reflect the capabilities of their models. Though our model suffers from similar weaknesses as these, we do not smooth the measurements but instead use the raw data directly in our experiments. This preserves the intra-annual variation in the MCF concentrations due to the seasonal cycles of OH and global transport. In practice we find smoothing the measurements had little impact on our results. The difference in the calculated OH average and trend using unprocessed or highly processed (12 month running average) measurements was slight.

3.4.3 Temperature

The rate coefficient for the reaction between CH_3CCl_3 and OH is

$$k = 1.8 \times 10^{-12} \exp(-1500/T) \text{ (Talukdar et al., 1992).} \qquad (3.6)$$

Reference temperatures are calculated for each model box seasonally to determine the appropriate reaction rate coefficient. The coefficient is sensitive to temperature (a 5 % increase in temperature at a typical temperature of 293 K increases the reaction rate by 26 %) and directly influences the derived OH values.

46

Table 3.1. Effective Atmospheric Temperatures (K) For Model Regions

Region[a]	Winter	Spring	Summer	Fall	Annual
NP (L)	241	253	267	256	254
NP (U)	223	227	240	229	235
NM (L)	233	238	249	240	271
NM (U)	233	238	249	240	240
NT (L)	282	284	284	284	284
NT (U)	252	253	255	254	253
ST (L)	283	283	282	282	282
ST (U)	254	253	250	252	252
SM (L)	270	268	264	266	267
SM (U)	242	239	234	237	238
SP (L)	256	247	243	250	249
SP (U)	231	226	222	220	225

[a] NP=north polar, NM=north midlatitude, NT=north tropics, ST=south tropics, SM=south midlatitude, SP=south polar; L=lower troposphere, U=upper troposphere.

We constructed our temperature field from the NCEP/NCAR Reanalysis Project (*Kalnay et al., 1996*) and the 1986 COSPAR International Reference Atmosphere (*Fleming et al., 1988*). The NCEP/NCAR data are compiled from various sources, including the Microwave Sounding Unit (MSU) data (*Christy et al., 2000*), radiosonde networks, and general circulation model meteorological fields. Both data sets provide temperatures on an altitude-latitude grid, and we calculated the reaction rate coefficient at each grid point. Since the MCF loss rate is highest where methyl chloroform and hydroxyl radical concentrations are high, we weighted the reaction rate coefficient by these concentrations. As measurements of MCF at altitude are sparse, we assumed the MCF concentrations falls off with the atmospheric density. We calculated the

appropriate k for each model box through

$$\overline{k_i} = \frac{\int\limits_{r_i,\theta} k(r,\theta)OH(r,\theta)n(r,\theta)dA}{\int\limits_{r_i,\theta} OH(r,\theta)n(r,\theta)dA}. \qquad (3.7)$$

The rate coefficient k is calculated on an altitude (r) – latitude (θ) grid and weighted by

the OH and air density (n). The coefficients are integrated over the boundaries (r,θ) of

the model boxes and the weighted mean is determined. A representative temperature is

derived for each model box i by inverting Eq. 3.6 for T using the rate coefficient

calculated from Eq. 3.7 . We find that the temperatures derived from the NCEP and

COSPAR data sets agree to within 1 %. We averaged the two and used these results as

our reference temperature field (Table 3.1).

3.4.4 Initialization scheme

The computational efficiency of our transport model allowed us to initialize all

concentrations to zero and begin the model calculations in 1951, when MCF emissions

are first reported. During the years when no MCF measurements exist, OH

concentrations were taken to be constant and are optimized with respect to the first

twelve months of the measurement series. For the AGAGE measurements, this means

OH levels are constant during 1951-1979. Hence the OH calculated for 1979 is not

strictly representative of that year, rather it is an OH average over 1951-1979.

An alternative is to initialize the model to conditions immediately preceding the

measurement time series to avoid the necessity of calculation over 1951-1979. For

those model boxes in which measurements stations lie, we simply used the

concentrations from the first month of the measurement time series and started the
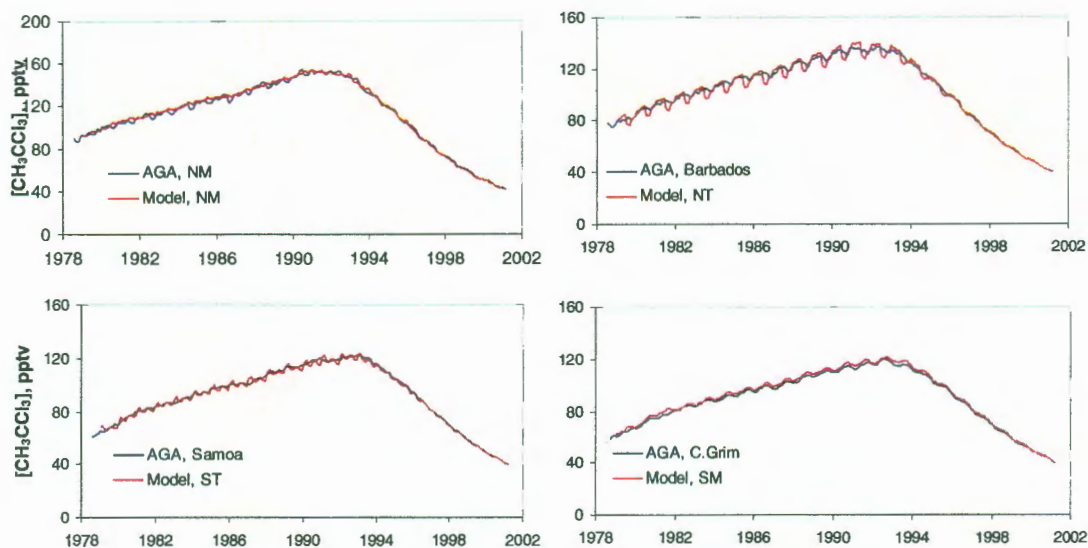
Figure 3.7. Simulated (red line) methylchlorofom is compared with measured data from the ALE/GAGE/AGAGE network. Results are shown for the northern midlatitude (NM), northern tropics (NT), southern tropics (ST), and southern midlatitude (SM).

model run in the following month. For the other model boxes we ran the model in its

original initialization mode (i.e. starting in 1951) and optimized the OH to 1979

measurements. We found the ratios between the non-source and source boxes'

concentrations and applied these to the measurements from the first month to construct

the MCF field used to initialize the model. We refer to this initialization as the "non-

zero scheme" and the previous initialization as the "zero-scheme".

We observed that differences caused by the different initialization schemes

affect only the first three years of calculation, after which the derived OH time series

are identical. We tested the appropriateness and validity of each scheme by conducting

a series of shortened model runs. For the test runs we restricted the

ALE/GAGE/AGAGE times series to the period 1990-2000. We made separate model

runs using each of the two initialization schemes in turn and compared the derived OH

values to those calculated using the full ALE/GAGE/AGAGE time series. Using the full

time series, by the year 1990 the model is fully initialized and the OH values in 1990

and beyond are completely independent of the initialization scheme. We found that

using the non-zero initialization scheme produced derived OH values nearly identical

with the base run, while the OH values derived from the zero scheme varied

significantly over the three year initialization period. On the basis of this experiment,

we utilized the non-zero scheme to initialize the model.

Table 3.2. Inferred OH Trend From Different Measuring Networks

	Sampling network		
	ALE/GAGE/AGAGE	ESRL-GMD	OGI
(1978 – 2008)	−0.43 ± 0.21	...	...
(1986 – 1997)	−0.81 ± 0.85	...	−0.82 ± 1.1
(1992 – 2007)	−0.27 ± 0.53	−0.15 ± 0.61	...
(1979 – 2000)	−0.54 ± 0.36	...	...
(1979 – 2000)	−0.64 ± 0.60[a]	...	...
(1979 – 2000)	−0.27 ± 0.26[b]	...	...
(1979 – 2000)	−0.16 ± 0.29[c]	...	...
(1979 – 2000)	−0.07 ± 0.29[d]	...	...

[a] *Prinn et al. (2001);* [b] derived from an emissions scenario that includes 5 Gg y[-1] from biomass burning; [c] biomass burning emissions of 10 Gg y[-1]; [d] 15 Gg y[-1].

3.5   Results

Simulated CH_3CCl_3 mixing ratios using the optimized OH concentrations are presented in Fig. 3.7 with the ALE/GAGE/AGAGE measurements. Overall the match between the simulations and measurements is quite good and demonstrates the model ably reproduces the time series of MCF at various latitudes. The model tends to overestimate the magnitude of the seasonal CH_3CCl_3 cycle in the northern tropics. The model cycle results from the movement of the Intertropical Convergence Zone (ITCZ) into the northern tropics during the northern hemisphere summer. As it does so, it allows once isolated air in the north to mix rapidly into the southern tropics where levels of CH_3CCl_3 are lower. This lowers the concentration in the north. The AGAGE station in the north tropics, Ragged Point, Barbados, lies above the northernmost extent of the ITCZ and is less sensitive to the annual ITCZ cycle.

Fig 3.8 shows the derived OH time series for each measurement network, and the calculations of OH from *Prinn et al. (2001)* for comparison. The trends of OH over different time periods were estimated using a linear regression method. The results are listed in Table 3.2 along with the formal errors on the trend specified at the 95% confidence level. For a specified data set trends are calculated over a range of time periods to permit direct comparison with the other data sets.

We derived an average trend of -0.43 ± 0.21 % y^{-1} over the time period 1979-2008 using the ALE/GAGE/AGAGE data set and a global mass-weighted OH average of $1.15 \pm 0.08 \times 10^6$ mol cm^{-3}. This corresponds to a decrease in OH of about 14% over this period, though this fall-off is not constant with time, and a single trend does not capture the behavior of OH. As the ALE/GAGE/AGAGE data set is the longest running record of CH_3CCl_3, this is our best estimate of the OH trend over the past three decades using industrial emissions alone, and in later discussions, we refer to this result as the "base run". If we restrict the time interval to 1979 – 2000, the estimated trend is -0.54 ± 0.36 % y^{-1}, which is similar to the *Prinn et al. (2001)* estimate of -0.64 ± 0.60 % y^{-1} over the same interval.
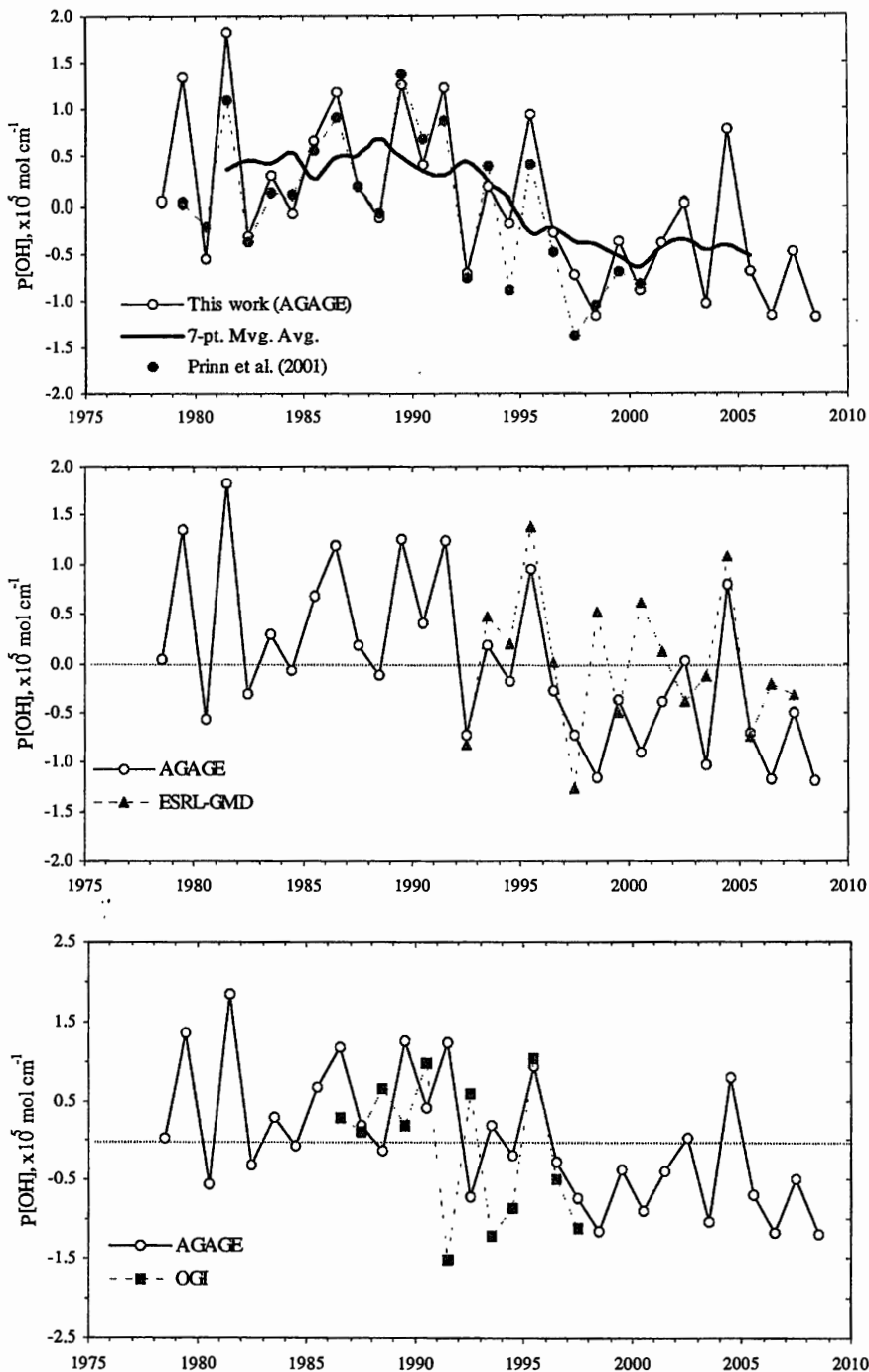
Figure 3.8. Derived OH using (a) ALE/GAGE/AGAGE (upper panel), (b) ESRL-GMD (middle panel), and (c) OGI methylchloroform measurements (lower panel). The OH record *of Prinn et al. (2001)* and the 7-pt. moving average of our AGAGE-derived OH are also displayed in (a).

53

The non-linear nature of the derived OH is apparent when the record is smoothed by applying a 7-point moving average (Fig. 3.8a). There appears to be three distinct periods, pre-1991, 1991 – 2000, and 2000 to present. Pre-1991, OH levels are roughly constant or even increasing slightly from 1982 onwards. The large interannual variability at the beginning of the record confuses the behavior of OH during this period. This large variability in part can be attributed to the relatively low precision of the ALE measurements, which have relative uncertainties four to five times larger than the ensuing years of GAGE measurements. Starting in 1984, the relative uncertainty of the ALE/GAGE/AGAGE measurements improves to about 1-2%. We estimated the trend of OH from 1984 to 1991 is 0.75 ± 1.4 % y^{-1}. From 1991 to 2000, the trend is -1.4 ± 1.2 % y^{-1}, and is -0.53 ± 1.5 % y^{-1} from 2000 onwards. In isolation the only trend that is formally significant is during 1991 – 2000, when OH decreases by about 10% over a ten year period. Thus the overall trend of -0.43 ± 0.21 % y^{-1} from 1978 to 2008 is better understood as a sharp drop in OH in the middle of the time period. We return to this point later in our discussion.

In Figs. 3.8b and 3.8c we plot the OH record derived from the ESRL-GMD and OGI measurements. Each of these records is only roughly half the length of the ALE/GAGE/AGAGE series, but both cover the critical period when the AGAGE-OH rapidly decreases. The ESRL-GMD derived OH agrees well with the AGAGE-OH except during 1998 – 2002, when the interannual variability is anti-correlated. The two records agree remarkably well from 1992 – 1997, which suggests that the dip during

this time is a robust feature of the derived OH record. On average ESRL-OH levels after 1997 are smaller than those before, in agreement with the AGAGE-OH.

After 1997, ESRL-OH is on average 1.5% higher than AGAGE-OH. This is in part due to a relative change in the calibration scale between the ESRL and AGAGE MCF measurements. Fig. 3.9 shows the ratio of ESRL to AGAGE MCF measurements at Samoa and Cape Grim from 1992 to 2007. Over this time ESRL-MCF decreases relative to AGAGE-MCF by about 3%. Mass balance requires the derived OH for ESRL to increase relative to AGAGE-OH by an equal amount. The offset in derived OH is small and doesn't affect our major conclusions, but illustrates the importance of absolute calibration to the modeled OH series.

Except for a three year period (1991 – 1993), the OGI-OH is also in good agreement with the AGAGE-OH. In particular OH anomalies are positive from 1986 to 1990, and the global OH concentration drops rapidly from 1995 to 1997. The global OH concentration from 1991 to 1994 is lower than the AGAGE-OH during this time. This is likely attributable to the disagreement between the MCF measured at Cape Kumukahi and Ragged Pt., Barbados, during this time. The derived OH is sensitive to MCF concentrations in the tropics. For the same emissions, OH levels need to be smaller in order to explain the elevated MCF measured at Cape Kumukahi. We have some reservations about whether these higher MCF measurements are real or reflect a drift in the calibration. If they are real, they may indicate the presence of a local source of MCF, and if so, the concentrations measured here would not represent the larger
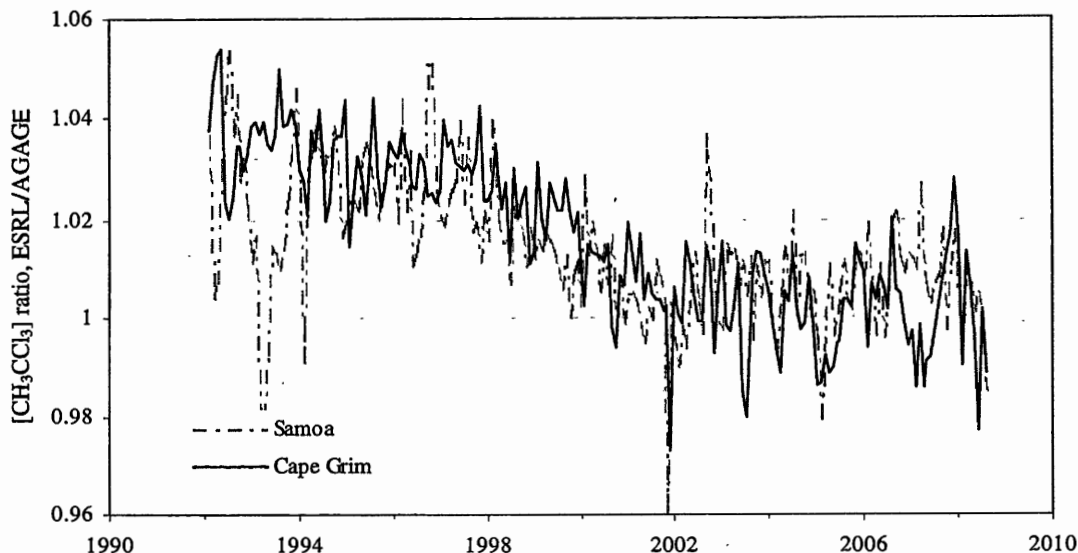
Figure 3.9. The ratio of ESRL and AGAGE MCF at Samoa and Cape Grim, Tasmania. The downward trend in ratio indicates that the ESRL measurements are increasing relative to AGAGE, which in turn elevates the derived ESRL-OH relative to the AGAGE-OH.

northern tropics region. In either case we place lower weight on the OGI-derived OH during this period.

3.5.1 Atmospheric lifetimes

Using the results from the ALE/GAGE/AGAGE analysis we computed lifetimes of MCF with respect to tropospheric OH oxidation τ_{trop} and stratospheric destruction τ_{strat} on a monthly basis. The total atmospheric lifetime is calculated as $(1/\tau_{trop} + 1/\tau_{strat} + 1/\tau_{ocean})^{-1}$, where τ_{ocean} is fixed at 85 yr.

The MCF lifetime is not constant but varies with OH and τ_{strat}. We found that τ_{strat} decreases by 25% over 1979-2000 as MCF is transported to the stratosphere. The average total MCF lifetime over this period is 4.7 ± 0.8 y ($\tau_{trop} = 5.4 \pm 0.8$ y, τ_{strat} 65 ± 6

56
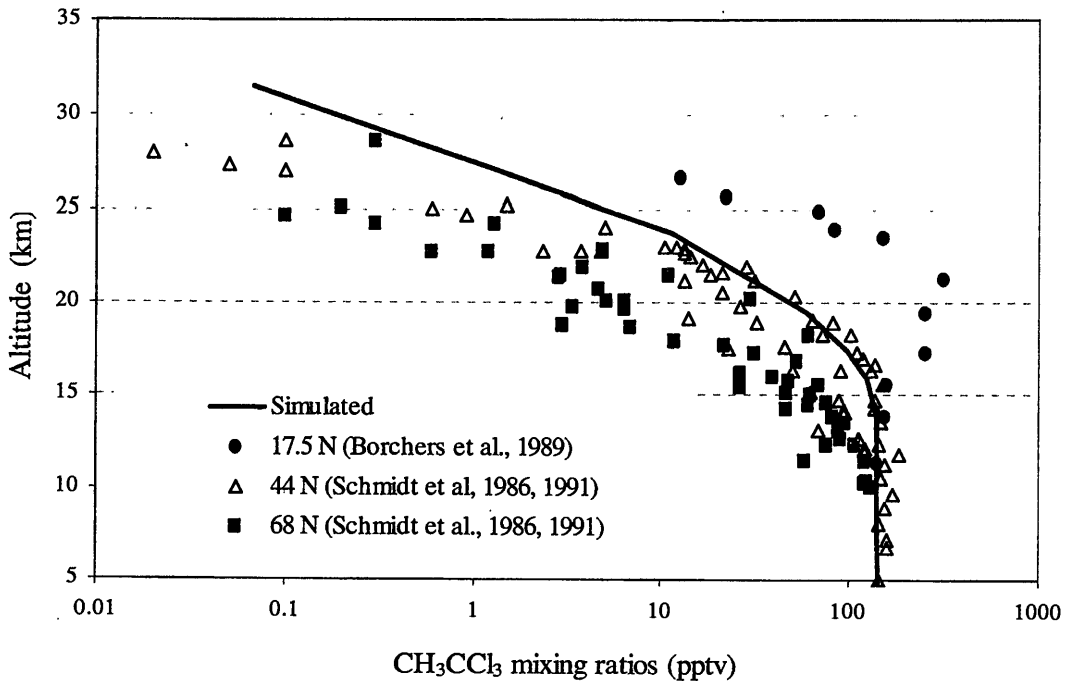
Figure 3.10. Stratospheric profiles of methylchloroform. Modeled concentrations have been averaged across all latitudes and over the time period 1986 to 1991.

y). Our total lifetime is consistent with other estimates by *Prinn et al. (2001)* ($4.90^{+0.62}_{-0.49}$ y), *Montzka et al. (2000)* ($5.2^{+0.2}_{-0.3}$ y), *Kanakidou et al.(1995)* (5.3 y), *Krol et al. (1998)* (4.6 ± 0.1 y), and *Spivakovsky et al. (2000)* (4.6 y). Our calculated τ_{strat} is higher than other estimates: *Prinn et al. (2001)* ($38.9^{+0.34}_{-0.32}$ y); *Krol et al. (1998)* (50 y); *Kanakidou et al. (1995)* (54 y); and *Spivakovsky et al. (2000)* (43 y).

The stratospheric lifetime is determined by the in situ photolytic and oxidation rates and transport both within the stratosphere and across the tropopause. The stratospheric profile of MCF is largely determined by these processes and we compared our simulated profile to observations by *Schmidt et al. (1991)* and *Borchers et al. (1989)*

57

in Fig. 3.10 over the time-averaged period 1985-1990 to verify the validity of our model processes. The modeled concentrations were increased by 20% to adjust for offsets in the calibration scales. By visual inspection we confirmed that the model reproduces the measurements correctly. The simulated data fall between the mid-to-high and low latitude measurements, consistent with the one-dimensionality of the model stratosphere. In addition, the vertical concentration gradients of the balloon and model data are similar.

We next assessed the sensitivity of the stratospheric CH_3CCl_3 profile to τ_{strat}. We scaled the stratospheric transport by appropriate factors to reduce the MCF stratospheric lifetime to 45 yr, consistent with the above estimates. Doing so increased the MCF concentrations at altitude to an extent that the profile was inconsistent with the balloon measurements. Thus we rule out this possibility.

Another method to reduce τ_{strat} is to decrease the photolysis lifetimes. We scaled the lifetimes by 0.60 to reduce τ_{strat} to 45 y to be consistent with the above estimates. Doing so, we found the new stratospheric profile was still consistent with the balloon observations and had similar concentration gradients as the base run. The change in τ_{strat} had only a small effect on the OH trend. Our findings show that the OH trend is insensitive to the stratospheric lifetime, and supports the notion that a range of stratospheric lifetimes are consistent with the observed stratospheric CH_3CCl_3 profile, while largely preserving the tropospheric OH trend.

3.6 Sensitivity of the OH record

A consistent history of OH emerges from the three studies above. OH increases slowly from the early 1980s to a peak around 1995, then falls rapidly and reaches a minimum near 1998. It then rebounds slightly and remains generally constant, though at a lower level than at the beginning part of the time series. The most significant event is the 1996 to 1998 drop. This feature shows up in all three analyses. This is an important result and proves that the feature is robust and not an artifact of the measurement record. This derived history of OH however could be the artifact of other factors, such as the model and inversion method, an atmospheric temperature trend, and most importantly the emissions record. We examined these possibilities in turn, and assessed how sensitive our OH history is to these factors.

3.6.1 Model and inversion method

The best evidence that supports our view that the simulated OH history is not an artifact of our model or inversion method is the direct comparison of our OH with that derived OH from *Prinn et al. (2001)*. The authors used the same ALE/GAGE/AGAGE-MCF measurements and emissions (with minor modification in distribution), but a different chemical-transport model and inversion scheme. In particular, the authors used a recursive weighted-least squares Kalman filter and a twelve-region box model to invert the methylchloroform measurements. Their OH anomalies (difference from mean) are shown in Fig. 3.8a, alongside our AGAGE-OH estimates. The match is remarkably good considering the two independent methods used to deduce the OH. The magnitude and cycle of the interannual variability is nearly the same for both records. The only significant difference between the two OH histories is the mean global OH.

While we calculated a global mean [OH] of $(1.17 \pm 0.08) \times 10^6$ mol cm^{-3}, *Prinn et al. (2001)* estimated the mean [OH] is $(9.4 \pm 1.3) \times 10^5$ mol cm^{-3}. One important reason for this difference is the reference temperatures used to calculate the reaction rates constants. The CH_3CCl_3+OH reaction rate is very sensitive to temperature. A 5% increase in temperature at temperatures appropriate to the lower troposphere produces a 30% increase in the rate coefficient k. For unknown reasons *Prinn et al.*'s reference temperatures are about 4% higher than ours. This would increase k by about 25% and in turn reduce the amount of OH needed for the appropriate CH_3CCl_3 lifetime. This is consistent with the percent difference between our global OH means (24%). We conclude then that the derived OH history is not an artifact of the inverse modeling method.

3.6.2 Temperature trends

As previously discussed, simulated OH values are sensitive to model reference temperatures via the rate coefficient. Temperatures were held constant throughout the experiments we reported above. Here we consider the possibility that by neglecting to include the true atmospheric variations in temperature, we artificially inflict upon the simulated OH a trend that rightly belongs to the temperature record. A positive temperature trend would increase simulated OH with time, since the only recourse of the model is to boost OH in response to the decreasing lifetime of CH_3CCl_3 due to temperature.

We derived tropospheric temperature trends from three different networks; the Microwave Sounding Unit (MSU) satellite data (*Christy et al., 2000*), the Angell

radiosonde balloon network (*Angell, 2000*), and the National Center for Environmental Prediction/National Center for Atmospheric Research (NCEP/NCAR) reanalysis data (*Kalnay et al. 1996*). The MSU products include integrated soundings between the surface and 300 hPa (2LT) and soundings between 300 and 100 hPa (LT). We used these as representative of the lower and upper troposphere in our model respectively, though we recognize that the LT sounding includes the lowermost layer of the stratosphere, which responds differently to forcings than the troposphere. Temperature anomalies were zonally averaged and latitudinally weighted by surface area to form seasonal trends. Annual temperature trends for all three datasets are shown in Fig. 3.11. Trends from the MSU data set were taken over the time period 1979-2001. The 2LT trends range from 0.28 K decade^{-1} in the north polar region (65 – 90°N) to –0.25 K decade^{-1} in the south polar region (65 – 90°S). The model-calculated OH trend are most sensitive to temperature trends in the tropics where OH levels are at their highest. Here the 2LT trends are near zero, –0.025 K decade^{-1} in the northern tropics (0 – 30°N) and –0.013 K decade^{-1} in the southern tropics (30-0°S). The tropical trends are consistent with the 2LT trends calculated by *Christy et al. (2001)* for the region 20°N – 20°S, –0.06 ± 0.16 K decade^{-1}. Trends in the LT layer range from 0.15 K decade^{-1} in the northern mid-latitudes (30 – 65°N) to –0.33 K decade^{-1} in the southern polar region. Trends in the LT tropics are slightly positive at 0.05 K decade^{-1}.
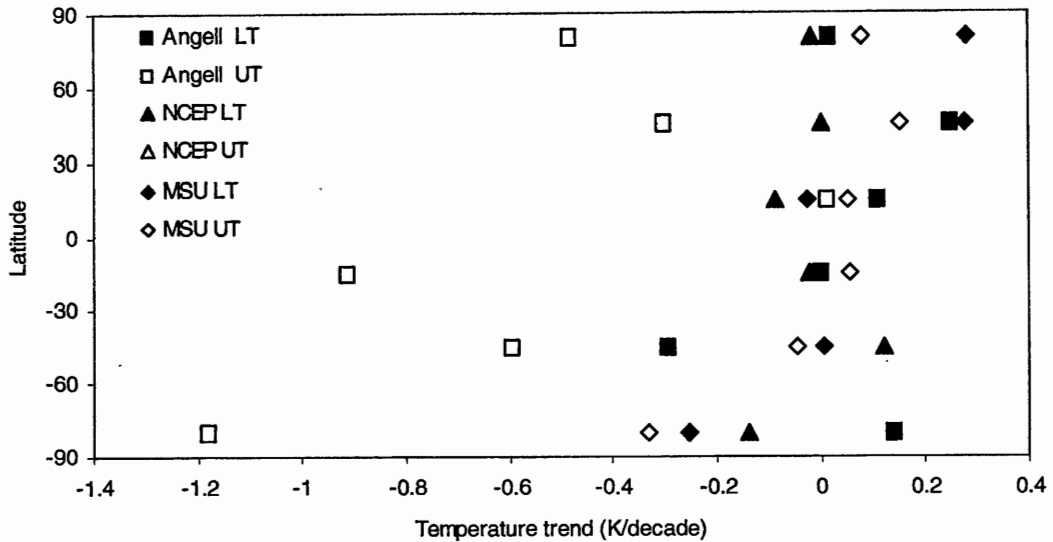
Figure 3.11. Tropospheric temperature trends over 1979-2000 from radiosonde (Angell), satellite (MSU) and reanalysis data (NCEP). UT=upper troposphere which is roughly 300 to 100 hpa. LT=lower troposphere which is 850 to 300 hPa.

Unlike the MSU campaign that has global coverage, the Angell network includes only 63 stations globally. The network measured temperature anomalies since 1951. We calculated trends over the time period 1979–1999. The temperature deviations were averaged over the north and south polar regions (60–90°N,S); north and south mid-latitudes (30–60°N,S); north and south sub-tropics (10–30°N,S); equatorial region (10°S–10°N), and tropics (30°S–30°N). The first two intervals correspond well to our model polar and mid-latitude boxes and we made no changes to these deviations. To calculate appropriate trends for our tropical boxes (0°–30°S,N) we took a weighted average of the sub-tropical and equatorial boxes (e.g. NT = 0.35×tropics + 0.65×equatorial). We used the integrated temperature anomalies over 850–300 hPa and

62

300–100 hPa for our lower and upper tropospheric model boxes respectively. As above, measurements were averaged over the latitudinal boundaries of the model. The weighted temperature trends in the lower troposphere ranged from 0.25 K decade^{-1} in the northern mid-latitudes to −0.29 K decade^{-1} in the southern mid-latitudes. The trends in the tropics were 0.11 K decade^{-1} in the north and 0.00 K decade^{-1} in the south.

In the upper troposphere (300–100 hPa), the trends were lower, as the 100 hPa layer includes the bottom of the stratosphere, where the temperature is decreasing over the past two decades due to the decrease in tropospheric longwave radiation. The trends ranged from 0.012 K decade^{-1} in the northern tropics, to −1.2 K decade^{-1} in the southern polar region. The average trend for the upper troposphere was −0.50 K decade^{-1}, which is larger than the trend of −0.14 K decade^{-1} in the lower troposphere. Again, this difference reflects the inclusion of the lower stratosphere into the upper layer.

Trends computed from the NCEP/NCAR reanalysis were in agreement with those computed from the MSU data as seen in Fig. 3.11. The latitudinal profiles of the NCEP/NCAR trends in the lower troposphere (1000–500 hPa) and the MSU 2LT layer are in good agreement, except for an anomalous NCEP/NCAR trend in the southern polar region. The latitudinal profiles in the upper troposphere are also similar. The NCEP/NCAR trends in the lower tropospheric tropics are small, 0.017 and 0.015 K decade^{-1} in the north and south, respectively. In the upper troposphere the respective trends are −0.087 and −0.021 K decade^{-1}.

We re-ran the MCF inversions separately using the temperature trends from the three networks using AGAGE-MCF. We found that the temperature trends only

63

marginally influenced the derived OH histories. Including the MSU, Angell, and NCEP/NCAR temperature series into the simulations changed the 1979-2000 trend by −3.4%, 6.9%, and 0.0%, respectively. These results point to the fact that global patterns of OH are predominately influenced by conditions in the tropics, and despite temperature trends being large at high latitudes, their impact on the OH budget is small. We conclude that any change in the tropospheric lapse rate due to global warming has little impact on model simulations of the OH record.

3.6.3 Absolute calibration

Calibration standards are difficult to prepare at the required parts per trillion level. As a result CH_3CCl_3 measurements may differ from true values by some scaling factor. For example, when the CH_3CCl_3 standard was improved for the AGAGE phase of the ALE/GAGE/AGAGE experiments, the previous ALE/GAGE measurements had to be lowered by a factor of 0.818 *(Prinn et al., 2005)*. Differences in absolute calibration also exist between the AGAGE and ESRL-GMD measurements before 2002 as we showed above. Errors in calibration, both drifts and constant scaling, can produce false trends in OH derived from inversion techniques like. The effect of a constant calibration error α on the derived OH trend is complicated and depends on the source (dS/dt) and concentration trends (dC/dt) at the time of interest. For example, if dC/dt is constant and negative, OH trends would be overestimated if $\alpha<1$, and underestimated if $\alpha>1$. During a time when concentrations of CH_3CCl_3 are turning over rapidly (i.e. $d^2C/dt^2 \ll 1$) the reverse would be true. Since CH_3CCl_3 concentrations and source
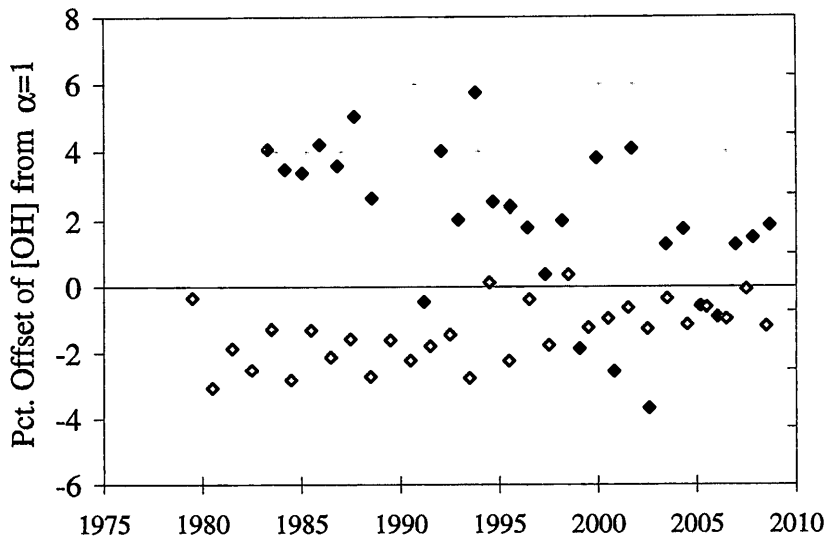
Figure 3.12. Changes in simulated OH due to differences in MCF calibration. The solid symbols are the changes in OH when the ALE/GAGE/AGAGE-MCF was scaled by a factor of 0.97. The open symbols show the case when the scale factor is 1.03.

trends are variable over the time period considered, it is unclear a priori what influence α has on our derived OH.

We used the 3% difference between the ESRL-GMD and AGAGE measurements as a reasonable estimate for the calibration error and simply scaled all AGAGE measurements by 1.03. Doing so reduced the overall trend (1979–2008) to -0.33 ± 0.23 % y^{-1}, a decrease of 23%. When we decreased the measurements by 3%, the trend increased by 44% to -0.62 ± 0.25 % y^{-1}. Fig. 3.12 illustrates the changes in simulated OH due to the application of different calibration factors. We see the OH offsets (relative to OH calculated from the base MCF) are large (~3–4%) early in the record but decay to near zero towards the end. If we solve the one box model version of the mass balance equation ($dC/dt = S - k$ OH C, where C is the MCF concentration, S is MCF emissions, and k is the rate coefficient) for OH, OH is proportional to

$$\frac{S}{\alpha} - \frac{dC}{dt}, \tag{3.3}$$
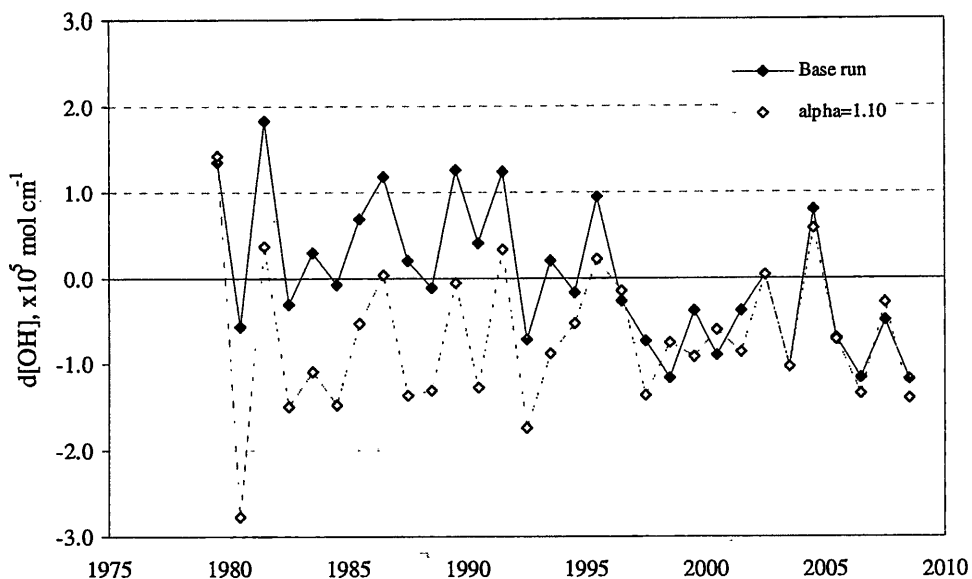
Figure 3.13. Comparison of OH anomalies from the base run and a model run where CH_3CCl_3 measurements were scaled upwards by 1.10.

where α again is the calibration factor. When α is close to unity, it will only affect OH when $S >> dC/dt$. This condition is met early on when MCF emissions are high, but after the ban on emissions, S falls rapidly and OH is no longer affected by α. Thus because emissions are changing over this period a constant calibration factor can influence the derived OH trend. Within the 3% calibration uncertainty band, the OH trend is still statistically significant. If α is increased to 1.10, the trend disappears (0.02 $\pm$ 0.28 % y^{-1}), as seen in Fig. 3.13. Scaling the measurements by this factor pulls down the OH values before 1997 but preserves them thereafter. The net effect is to remove the

66

trend. The implication of this is, if the SIO-2005 standard on which the ALE/GAGE/AGAGE measurements are based is 10% too low, our results suggest the derived OH trend disappears. *Prinn et al. (1995)* estimate that the uncertainty on the SIO-1998 standard, which preceded the current SIO-2005 standard, was ± 5%. Since the SIO-2005/SIO-1998 ratio for CH_3CCl_3 is 0.9957 (*Prinn et al., 2000*) this equally applies to recent calibration as well. If this accurately represents the maximum error on the calibration, we estimate the smallest allowable OH trend is -30 ± 0.25 % y^{-1}, which is still significant. However, intercomparisons of laboratory standards suggest the error may be larger. *Montzka et al. (2000)* reported that intercomparisons of CH_3CCl_3 standards between different laboratories revealed differences of 20 to 35%, suggesting that errors of this magnitude are possible.

In conclusion, the history of OH before the downturn in emissions around 1991 is sensitive to the absolute calibration of CH_3CCl_3 measurements. Even though the derived OH trend persists if measurements are increased to the upper bounds of their reported error range, we note that the drop in OH observed in the derived record, is consistent with an artifact produced by an incorrect calibration.

3.6.4   Emissions

We next determined the optimal MCF emissions consistent with the ALE/GAGE/AGAGE measurements and an OH trend of zero. We then compared these zero-trend emissions with the industrial MCF emissions to see if the two data sets agree within error. To do so, we ran our model in inverse mode and used a constant OH field throughout the simulation period. Though the constant value chosen for OH is not
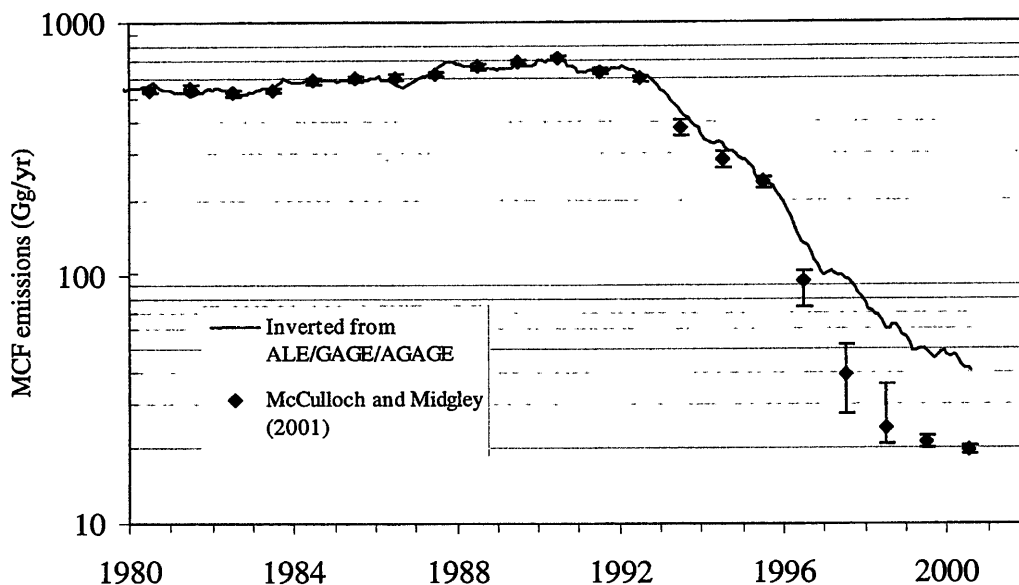
Figure 3.14. Comparison of model-inverted emissions and estimates of MCF industrial emissions The simulated emissions are inverted from ALE/GAGE/AGAGE measurements with the assumption of no trend in the OH fields over the period of study.

important, we used a global mean OH that optimally fit the MCF concentrations over the period 1979-1990. These inverted emissions are plotted against the industrial emissions and their 2σ error bars in Fig. 3.14.

There is very good agreement between the two emissions series up until 1992, when the industrial emissions begin to fall short of the inverted emissions. The divergence is 50 Gg y^{-1} in 1997 and about 20 Gg y^{-1} in 2000. These differences show that the optimal emissions needed for mass balance, assuming a zero trend, are not consistent with known industrial emissions. We are left to conclude that either there is a trend in the OH record, or the current estimates of MCF emissions are in error. Considering the latter, we note that the three largest sources of error in the emissions are

1) non-reported industrial production, 2) delays between sales and emissions, and 3) non-industrial sources of MCF. We first examine sources of possible errors in the industrial emissions, and then consider natural emissions of CH_3CCl_3 from biomass burning. These latter sources are thought to be small but may now be relevant as industrial emissions go to zero.

As mentioned, there are two main sources of error in the industrial CH_3CCl_3 record, uncertainties in the production and uncertainties in the release history following production. *Midgley (1989)* estimated that the average uncertainty for industry-reported net production is ±2.1%. Before manufacturers reported production, the uncertainty is much higher, but this doesn't affect our results since our simulation begins after industries began reporting. The uncertainty in the release history is bounded by practical considerations. First nearly all MCF that is produced is eventually emitted (*McCulloch and Midgley, 2001*) and the only uncertainty is when the MCF is released. According to manufacturers, the quickest release cycle is 75% emission the year of production and 25% the year after. The minimum rate of release is 50% emission the year of production. Overall the 1σ uncertainties to the emissions range from 2-3% when during the 1970s and 1980s when manufacturers reported emissions, to 30% in the 1990s. We used these error estimates to conduct Monte Carlo simulations by varying the emission histories and recalculating the OH histories. For all years of emissions, we created a normal distribution defined by the mean emissions for that year and the 1σ errors. Thus there is a unique distribution for every year of simulation. We constructed new emission histories by randomly sampling each distribution for each year. For each new emission

history we re-ran the simulation and calculated the trend of the simulated OH history. The simulations produced OH trends (1979–2008) that varied over a range of ± 20% (1 σ) of the mean. All trends from the Monte Carlo runs remained negative, which suggests that the reported errors in the industrial emissions are not large enough to negate the trend. We further investigated the possibility of errors in the emissions function used by *McCulloch and Midgley (2001)* to estimate emissions from production. Conceptually the differences between the inverted and industrial emissions can be resolved by increasing the delay between sales and emission. Increasing the delay would lower emissions at the beginning of the time interval and raise them at the end. The resulting time series of emissions could potentially be in agreement then with the inverted emissions, as this change would force the model to lower the constant OH field throughout the simulation, and in so doing the emissions required for mass balance would decrease.

We constructed an alternative emissions time series using production data from *McCulloch and Midgley (2001)* (though production is not explicitly provided, it can be calculated from the emissions and bank data; production equals emissions plus the change in bank from the previous year). We assumed that emissions follow an exponential function with lifetime τ, such that the remaining MCF sold in year y after t years is $MCF(t) = MCF(y) \exp(-t/\tau)$. This model produced emissions nearly identical to estimates of *McCulloch and Midgley (2001)* if $\tau = 0.7$ y. A lifetime τ of 0.7 yr means 76% of the product will be released within the first year of purchase, consistent with the modeling of the short-term release category by *McCulloch and Midgley (2001)* who

assumed that 75% of the product is released the first year. Our goal is to determine if it is possible to optimize τ to produce emissions consistent with the zero-trend inverted emissions. If it is possible, it suggests the reported OH trend could be an artifact of errors in the emissions history.

We found it is not possible to produce emissions that simultaneously match both
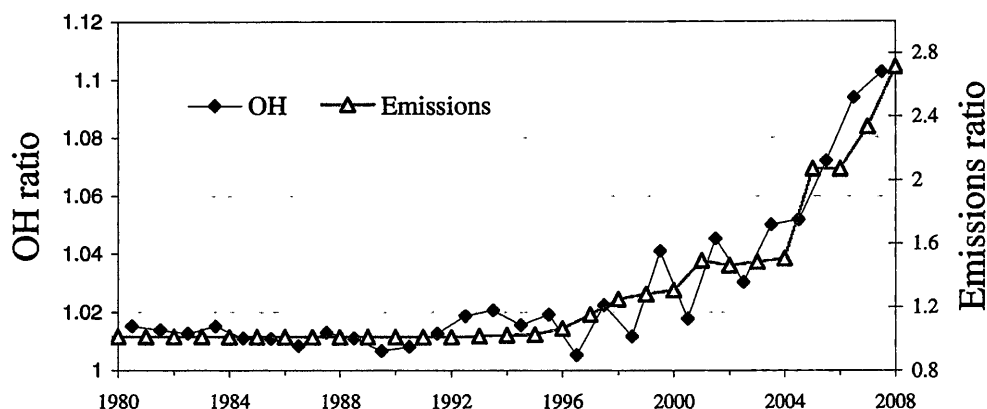
Figure 3.15. Addition of the biomass burning CH_3CCl_3 source to industrial emissions. Plotted are the ratios between total emissions (industrial plus biomass burning) to industrial emissions (open symbols), and the ratio of the OH derived from enhanced emissions to the OH derived from industrial emissions only (closed symbols). The figure indicates the impact of biomass burning emissions is seen only later in the period.

the beginning and end of the inverted emissions time series. Using $\tau=1.9$ y, the industrial emissions are in good agreement with the inverted emissions over 1980-1992, but exceed the inverted emissions by up to 37 Gg y^{-1} from 1992-2000. If we optimize the industrial emissions to the inverted emissions over this latter period, the industrial emissions are too large over the earlier. We conclude that the OH trend is not an artifact

of the release model used to calculate industrial emissions. In this regard and with consideration of the above discussion, we consider the trend robust to uncertainties in the industrial emissions, without recourse to more drastic changes in our understanding of MCF production and emission.

We consider lastly the role of non-industrial CH_3CCl_3 emissions. *Rudolph et al., (1995)* reported emission of methylchloroform from biomass burning on the savannas of West Africa. *Lobert et al. (1999)* extrapolated the fluxes to estimate global emissions at 12 Gg y^{-1}. Follow-up laboratory studies verified emission from tropical wood burning, though the measured flux was considerably lower than that reported from the field studies (*Rudolph et al., 2000*). The authors lowered the global emission rate to 2.5–5.3 Gg y^{-1}. Ice core measurements place an upper limit of ~1.5 ppt on preindustrial levels of CH_3CCl_3 (*Butler et al., 1999*). If we assume a MCF lifetime of 5 yr and steady state concentrations during the preindustrial period, this constrains natural CH_3CCl_3 emissions to be less than ~6 Gg y^{-1}.

We added a constant 6 Gg y^{-1} to our base industrial emissions and reran the ALE/GAGE/AGAGE simulation. Emissions were distributed by geographic region based on the 1×1° gridded inventory of CH_3CCl_3 emissions from biomass burning by *Lobert et al. (1999)*. The authors used biomass burning carbon emissions as a guide to their distribution. The inclusion of biomass burning CH_3CCl_3 makes little difference in the emissions history for most of the study period. At peak industrial emissions, the biomass burning contributes less than 1% of the total budget. However, in recent years, 6 Gg y^{-1} exceeds estimated emissions from industrial production.
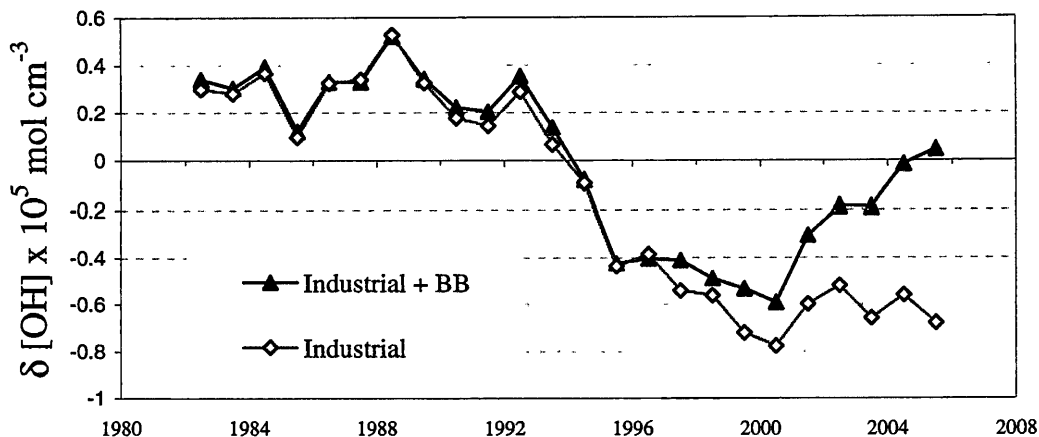
Figure 3.16. Anomalies of the derived OH from industrial emissions only (open symbols) and OH derived from total emissions (industrial plus biomass burning, closed symbols). The addition of biomass burning emissions causes the OH to return to earlier levels.

In Fig. 3.15 we plot the ratio of total to industrial emissions alongside the ratio of simulated OH derived from industrial emissions alone to the OH derived from the inclusion of biomass burning emissions. The additional emissions have little influence on the derived OH record before the year 2000. After this time, the OH derived from adjusted emissions rises rapidly relative to the OH calculated from the base emissions, and is about 10% higher than the base OH by year 2008. The adjusted OH trend from 1979 to 2008 is $-0.27 \pm 0.26 \% \ y^{-1}$.

Fig. 3.16 shows the OH anomalies derived from the base emissions (industrial only) and the enhanced emissions (industrial + biomass burning). Again we see that the OH doesn't respond to the added emissions until after 1996. The effect of the added biomass burning emissions is to force OH upwards to levels approaching those of 1993.

Importantly, however the emissions are not large enough to erase the large dip in OH . This is consistent with our results from the inversion, which showed a deficit in emissions of about 40-50 Gg y^{-1} during this time.

We are now in a period where the potential biomass burning source dominates the record. We see the degree to which this source determines current OH levels based upon the methylchloroform record. As CH_3CCl_3 emissions from biomass burning are highly uncertain, the utility of CH_3CCl_3 as a tracer of atmosphere OH is waning. This work shows that if we want to continue using CH_3CCl_3 as a tracer of future OH, we need more measurements of the biomass burning source over a wide range of burning conditions and ecosystems.

To summarize this section, within the known uncertainties of methylchloroform emissions, both industrial and non-industrial, the OH trend remains. The large drop in OH observed in the simulated record after 1990 requires additional emissions of 40-50 Gg y^{-1} to resolve. It is unlikely the estimates of industrial emissions are in error by this amount, and ice core measurements of CH_3CCl_3 prevent non-industrial emissions from being this large. Biomass burning emissions, if real, now dominate MCF emissions, and will control the future history of atmospheric CH_3CCl_3.

3.7   HCFC-22

We investigated the possibility of using other halocarbons to infer the OH trend. The hydrochlorofluorocarbon $CHClF_2$ (HCFC-22) is a refrigerant in use since the early 1950s. Unlike the chlorofluorocarbons it reacts with OH in the troposphere, and has a lifetime of about 9-10 years (*Miller et al., 1998*). As a result, only a small fraction

reaches the stratosphere. In consideration of this, HCFC-22 was not banned by the Montreal Protocol and its production continues today.

HCFC-22 is purely anthropogenic. Manufacturers report sales and production data to the Alternative Fluorocarbons Environmental Acceptability Study (AFEAS), an industry group that compiles and maintains a production and emissions database (*AFEAS, 2001*). While most western companies report production, manufacturers in China, India, Korea, and Russia do not, creating an information gap in production. To some extent these gaps can be filled using production and consumption data reported by nations to the United Nations Environment Program in compliance with the Montreal Protocol (*UNEP, 2002*). *McCulloch et al. (2003)* synthesized data from AFEAS, UNEP, and various country-based reports production, and estimated emissions of HCFC-22 from 1948 to 2000 using an emissions function that accounts for loss of HCFC-22 from the separate use categories of refrigeration, open and closed-cell foams, and aerosols. Emissions range from 100 Mg y^{-1} in 1948 to a high of 267.6 Gg y^{-1} in 2000. The production of HCFC-22 has fallen in recent years, as use switches to other hydrochlorofluorocarbons such as HCFC-141b (CH_3CCl_2F) and HCFC-142b (CH_3CClF_2). As a result, the percentage of HCFC-22 produced by AFEAS-reporting countries has fallen to less than half of total production (*AFEAS, 2008*). Because of this AFEAS no longer compiles industry data and current emissions are largely uncertain.

We used the emissions history (1942-2000) of *McCulloch et al. (2003)* for our OH simulation and added two additional years to it from an updated AFEAS database. We increased emissions in these additional years by 10% to account for production
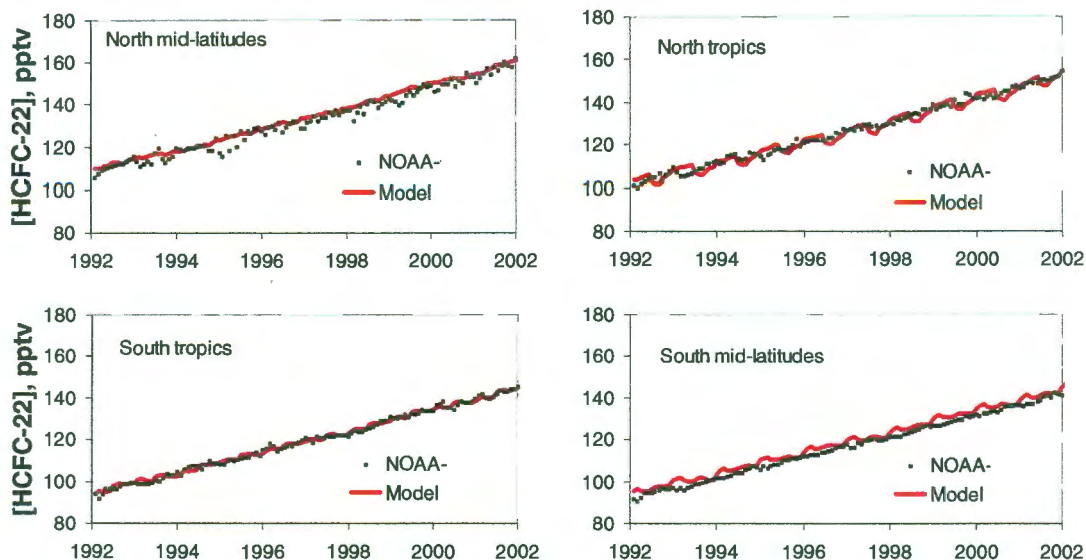
Figure 3.17. Atmospheric concentrations of HCFC-22. Solid circles are NOAA-GMD observations at Niwot Ridge (north mid-latitudes), Mauna Loa (north tropics), Samoa (south tropics), and Cape Grim (south mid-latitudes). Simulated concentrations (solid red line) are from model runs with OH levels optimized for fits.

from non-reporting countries (*Miller et al., 1998*). The geographical distribution of emissions was taken from the 1×1° spatially gridded HFC-22 inventory of *Aucott et al. (1992)*, which is part of the Reactive Chlorine Emissions Inventory. The inventory gives emissions for the year 1990 and we take the distribution to be constant in time. From north to south the fractional distribution of HCFC-22 into the model surface boxes is 0.002, 0.828, 0.116, 0.035, and 0.0 respectively.

Measurements of HCFC-22 concentrations were undertaken by NOAA's Global Monitoring Division starting in 1992 at the same sites that we used for the MCF analysis (*Montzka et al., 1993; Montzka et al., 1996; Montzka et al., 1999*).
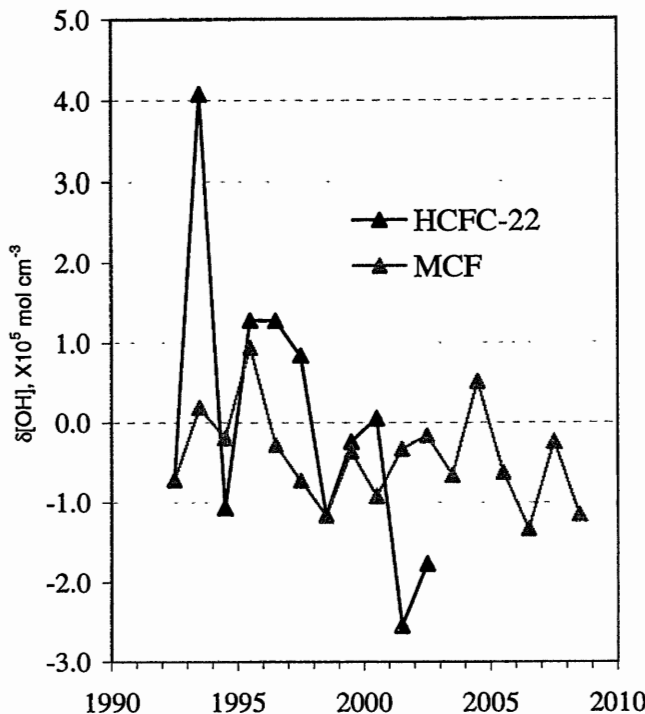
Figure 3.18. Atmospheric OH derived from HCFC-22 and methylchloroform records.

Atmospheric levels of HCFC-22 were about 100 ppt in 1992 and increased to 155 ppt in 2002. This period of time, though short, covers a crucial span of the OH time series where the trend is most negative. Independent verification of the trend during this time through a second proxy gas will strengthen the decreasing OH argument. The ALE/GAGE/AGAGE group also measures HCFC-22, but this record doesn't begin until 1998 and is only available at two sites, so here we restrict our modeling to the NOAA data set.

We again used NCAR's Tropospheric Ultraviolet Radiation model (*Madronich, 1993*) to calculate stratospheric photolytic lifetimes for HCFC-22. The rate coefficient

for the HCFC-22 + OH reaction was taken from *Sander et al. (2000)* (A=1.0×10^{-12}, B=−1600). We ignore loss to the ocean since the lifetime of HCFC-22 with respect to the ocean is 986 yr (*Kanakidou et al, 1995*).

We plot observed atmospheric HCFC-22 concentrations against our simulated results after optimizing OH levels (Fig. 3.17). The agreement is quite good which gives us confidence that our optimized OH values are appropriate. The OH time series is highly variable from year to year and no significant trend can be derived from it (Fig. 3.18.). In general the OH derived from HCFC-22 is about 10% higher than that calculated from MCF. The result that HCFC-22 produces higher OH than MCF is consistent with findings from *Miller et al. (1998)* who used ALE/GAGE measurements of HCFC-22 and MCF. This result could be explained by overestimated HCFC-22 emissions, or alternatively, by absolute calibration standards that are too low for both the NOAA and ALE/GAGE measurements.
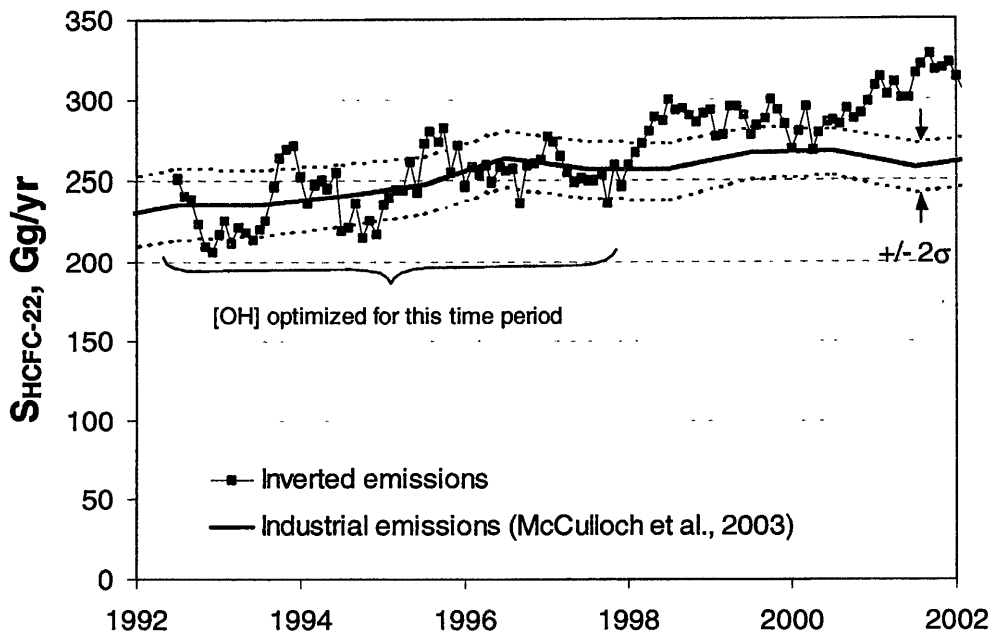
Figure 3.19. Emissions of HCFC-22. The black line shows inverted HCFC-22 emissions assuming a zero trend OH field. The constant OH was optimized so inverted emissions were in agreement with estimated emissions during the first half of the simulation period. Estimated HCFC-22 emissions from industrial production are shown in red along with their 2σ uncertainties.

Though no significant trend can be assigned to the HCFC-22 OH time series, the simulated OH does decrease throughout the 1990s, which is consistent with the MCF work. For a second test, we inverted the atmospheric HCFC-22 record for the HCFC-22 emissions under the assumption of a zero OH trend. In particular we adjusted the constant OH levels such that the inverted emissions would be on average equal to the estimated HCFC-22 industrial emissions (i.e. emissions from *McCulloch et al., 2003*) over the first half of the time period. If OH were constant, we'd expect the inverted emissions over the second half the time period to also match the industry estimates. The results are shown in Fig. 3.19. The plot shows that the inverted emissions are consistent

with the emission estimates up until 1998 then diverge upwards thereafter. On average the inverted emissions are about 30 Gg y^{-1}, or about 11% higher than the estimated emissions during this time. These emissions lie outside the 2σ uncertainty window calculated by *McCulloch et al. (2003)*. The reported uncertainties include contributions from the uncertainty in production, distribution between different end-use categories, timing of emissions from refrigeration, aerosols, and foams.

We conclude that the HCFC-22 record provides some, but not strong, evidence for a negative trend in OH levels over the short period of study that is consistent with OH record deduced from the MCF record. If HCFC-22 emissions are underestimated by about 10%, the suspected trend would disappear. Unlike methylchloroform, HCFC-22 emissions are still high (> 250 Gg y^{-1}), meaning an underreport of 30 Gg y^{-1} would be easier to accommodate than if emissions were near zero.

As a final note, we also tried to use the replacement compounds HCFC-141b, HCFC-142b, and HFC-134a (CH_2FCF_3), as proxies for the OH record. These gases are found at miniscule levels in the atmosphere (< 20 pptv) (*Prinn et al., 2000*). Our experiments revealed that the simulated atmospheric records of these gases are very insensitive to OH levels. As one example, when we scaled the model OH field by factors of 0.5 and 2.5, our modeled HFC-134a varied by only ~5%. As the sink term is proportional to the atmospheric burden, the behaviors of these gases are currently dominated by emissions.

3.8 Discussion

The general pattern of OH deduced from these studies suggests that OH increases by about 10% from the early 1980s to 1991, then falls 15% to a minimum in 1997, before rebounding back in recent years. This behavior is difficult to reconcile with the observational methane record unless methane emissions are correlated with changes in OH, which is unlikely (*Lelieveld et al., 2006*), though there are features of the CO and CH_4 that support this behavior. Large fires occurred both in 1994-95 and 1997-98 (*Novelli et al., 2003; Langenfelds et al., 2002*). We see dips in the OH record near each of these periods. The dip in 1997-1998 coincides with large fires in Indonesia during this time and is consistent with estimates by *Duncan et al. (2003)* that the increased CO and aerosol emissions from fires would decrease OH levels by 6%. Additional emissions of non-methane hydrocarbons from the fires would also add to the decrease of OH (*Prinn et al., 2005*). A decrease in OH would increase the lifetime of CH_4, creating positive anomalies in the CH_4 record. One large anomaly occurs from 1996 to 2000, when the atmospheric CH_4 growth rate increased from 3.9 ppb y^{-1} during 1995-1997 to 12.7 ppb y^{-1} in 1998 (*Dlugokencky et al., 2001; Khalil et al., 2007*). The reverse is also true, large emissions of methane would lower OH levels. These two processes taken together may explain this low period of OH.

Karlsdottir and Isaksen (2000) calculated that OH levels should have increased by 7% from 1980 to 1996 based on increasing emissions of CO, non-methane hydrocarbons, and NO_x (NO and NO_2). This is similar to the rate we observed before the drop in mid 1990s. If this drop is due to fire events, our results are consistent with this modeling, which did not consider enhanced biomass burning emissions. However

81

our modeled OH remains low past this time and only slowly begins to recover in 2004, well past the observed peak in CO concentrations, suggesting that this event alone may not explain this feature. If real, these decadal trends are significant and should show up in the atmospheric record of gases removed by OH.

These trends are supported by other studies Using a three-dimensional chemical-tracer model and ALE/GAGE/AGAGE data, *Krol et al. (2003)* found that OH rose by 12% from 1978 to 1990 and fell by about an equal amount from 1991 to 2000. *Bousquet et al. (2005)* also found positive and negative trends of OH respectively in the 1980s and 1990s respectively as above, but were again smaller. Also using AGAGE methylchloroform, the authors deduced an OH trend of only 0.1 % y^{-1} during the 1980s or a total OH increase of about 1% for the decade. This smaller trend is supported by chemical modeling of OH by *Dentener et al. (2002)* who considered changes in tropospheric water vapor, photolysis rates, and surface emissions of CO and CH_4, and estimated OH increased by 0.28 % y^{-1} from 1979 to 1993. During the 1990s, the decrease in OH inferred by *Bousquet et al. (2005)* is about 30% smaller than that from *Prinn et al (2001)* and *Krol et al. (2003)*.

Recently, measurements of radiocarbon carbon monoxide (^{14}CO) have been used to assess the trend of OH (*Manny et al., 2005*). Though ^{12}CO itself has many sources of unknown strength and variability making it unfit to constrain OH, ^{14}CO is produced primarily in the atmosphere by cosmic radiation at rates that are relatively well quantified, though sensitive to factors such as solar activity. The short lifetime of

carbon monoxide makes this method sensitive to regional and monthly variations of OH.

Manny et al. (2005) measured ^{14}CO in New Zealand and Antarctic over a thirteen-year period from 1989 to 2003. From these measurements, no significant long-term trend of OH was deduced, though recurring variations of 10 % were observed every few months, consistent with the variability found in previous work.

There is good evidence that OH has varied by 10-15% over the past few decades. This conclusion is supported by independent modeling and atmospheric records of methylchloroform and to a lesser degree, HCFC-22. The major impediments to the use of halocarbons in deriving the OH record are uncertainties in their industrial production and the absolute calibration standards used to monitor their atmospheric abundance. We have shown that errors in both, and especially in calibration, can significantly alter the inferred OH trend.

Chapter 4 — Assessment Of Biomass Burning On Decadal Scales Using Atmospheric Measurements of Carbon Monoxide and Hydrogen

4.1 Introduction

One of the major agents of global change today is the burning of the world's living and dead vegetation. Though fires have occurred naturally since the dawn of plants, most fires today are anthropogenic and a strong correlation exists between human settlement and fire frequency throughout history (*Schule, 1990*). Biomass burning is most pronounced in the tropics, where fire is used as a tool in deforestation, removal of crop residues, clearing of grasslands for agriculture, pest control, and energy production, releasing a wide range of trace gases and particulate matter, including methane (CH_4), carbon monoxide (CO), hydrogen (H_2), non-methane hydrocarbons, volatile organic compounds, halides, and nitrogenous species. Roughly 40% of all anthropogenic CO_2, CO, and H_2 comes from biomass burning (*Levine, 1996*). Methane is released in large quantities but estimates vary considerably. In its latest report on climate change, the UN's Intergovernmental Panel on Climate Change include source strengths for biomass burning ranging from 14 to 88 Tg CH_4 y^{-1}, which represent anywhere from 5 to 25% of the total anthropogenic source (*Denman et al., 2007*).

These collective emissions have significant consequences on the local and global environment. The emissions contribute to climate change, stratospheric ozone depletion, acid rain, and perturb the oxidation capacity of the atmosphere. In addition biomass

burning alters the nitrogen and carbon biogeochemical cycles, changes the radiative properties of surfaces, and impacts water run-off and evaporation (*Levine, 1996*).

Since biomass burning is primarily anthropogenic in origin, the extent and frequency of burning vary with socioeconomic, political, and agricultural factors, as well as temperature and precipitation. As population and demand for forest and agricultural products grow, there is increased pressure for greater burning. Though there is speculation that biomass burning has increased over the past couple decades (e.g. *Crutzen and Andreae, 1990; Hao and Liu, 1994*) few studies have investigated whether this is so.

Current assessments of biomass burning and its impacts are typically either for mean conditions or short time periods (*Seiler and Crutzen, 1980; Logan, 1983; Crutzen and Andreae, 1990; Andreae, 1991, Hao and Liu, 1994*). Few studies have produced biomass burning emissions spanning the past couple decades. In this study we used atmospheric records of CO and H_2 over a 20-year period to investigate the trend, interannual variability, and seasonal cycles of biomass burning. In particular the goals of our project were to 1) investigate the use of atmospheric CO and H_2 as tracers of biomass burning, 2) assess the trend and interannual variability of biomass burning in the tropics since the early 1980s, 3) compute the time series of methane emissions from biomass burning over decadal scales.

4.2   Methods of biomass burning assessment

Most biomass burning occurs in developing countries with few resources to compile statistical data on fire frequency and extent. Where data do exist, they are often

inconsistent, inaccurate, or lack the necessary temporal resolution (*Hoelzmann et al., 2004*). The sparseness of available data challenges efforts to quantify trace gas emissions and chart trends and interannual variability of biomass burning. In lieu of direct records indirect means have been used to quantify the impact and variability of this source. These options include biogeochemical modeling of biomass fuel load (e.g. *van der Werf et al., 2003*), satellite remote sensing of burn scar area and fire frequency (e.g. *Levine, 1999; Hoelzmann et al., 2004; Ito and Penner, 2004*), and inversion of atmospheric measurements of trace gases released by biomass burning (e.g. *Bergamaschi et al., 2000a; Bergamaschi et al., 2000b; Petron et al., 2004, Arellano et al., 2006*). Some studies have also pieced together the existing sparse fire activity data and created global estimates but these are prone to larger uncertainties (e.g. *Hao and Liu, 1994; Kasischke et al., 2002; Stocks et al., 2002*).

4.2.1 Bottom-up methods

In general these methods fall within two broad categories, bottom-up and top-down approaches as we introduced above. To calculate emissions from biomass burning using the bottom-up approach requires the use of an equation typically of the form (e.g. *Hao and Liu, 1994*)

$$E_{i,j} = A_j \times B_j \times \beta \times f_{i,j}, \qquad (4.1)$$

where E_{ij} is the emissions of gas species i from vegetation type j, A is the area burned, B_j is the biomass per area for vegetation type j, β is the burning efficiency (i.e. fraction of biomass burned), and f is the emission factor for gas species i and vegetation type j (i.e. mass of gas released for mass of biomass burned).

Burned area is perhaps the most difficult of these factors to estimate. Until recently, global maps of area burned were mainly based on annual country reports that were of questionable quality and available for only some countries (e.g. *the UN's Food and Agriculture Organization* databases). In recent years satellite-borne instruments have been used to detect both active fires and global burnt area (*Simon et al., 2004; Tansey et al., 2004*). *Arrino and Rosaz (1999*) used data from the Along Track Scanning Radiometer 2 (ATSR-2) on the European Remote-Sensing-2 Satellite (ERS-2) to estimate fire counts for the World Fire Atlas. Pixels of surface reflectance maps were considered fire detections if the pixel's nighttime brightness temperature at the wavelength 3.7 μm exceeded 308 K.

Active fire counts however often yield false detections due to the single criterion used to identify them. For example, fire counts may falsely include oil gas flares or city hot spots (*Hoelzemann et al., 2004*). Fire counts may miss daytime fires as the detection algorithm is typically applied only to nighttime imagery to avoid false detections of sun glare. The detection algorithm may also miss low intensity fires like peat fires (*Arino and Plummer, 2001*) or fires below thick canopies. Even when a fire is correctly detected the real spatial extent of the fire is still required to calculate emissions.

An improvement to fire counts is the mapping of burned areas. Burned area can be determined from characteristic properties of burned vegetation such as low surface reflectance and warm temperatures (*Hoelzemann et al., 2004; Simon et al., 2004*). Since fires alter vegetated landscapes and change surface reflectance properties, burned areas

can be identified with algorithms that compare surface reflections for the same region over a period of time (e.g. *Roy et al., 2002; Gregoire et al., 2003; Simon et al., 2004*).

The Global Burnt SCAR (GLOBSCAR) was derived from the daytime ATSR-2 data using an algorithm that searched for pixels with enhanced brightness temperature and low surface reflectance *(Simon et al., 2004)*. A comparison between GLOBSCAR and another burned area product, the Global Burnt Area Initiative (GBA-2000) from the Joint Research Center of the European Commission *(Gregoire et al., 2003)* however reveals considerable uncertainty in this method. These products, which are the two major fire products in use today, currently disagree by nearly 70% in their estimations of global burned areas *(Kasischke and Penner, 2004)*. The disagreement between estimates of global burned forest areas was over 250%.

There are a number of reasons for these differences that highlight the challenges of detecting burned areas. Cloud cover, which is especially prominent in the tropics where most fires occur, obscures fires and burn scars. Surfaces that have naturally low albedos may be falsely detected as burned areas. In both fire count and burned area studies, fire activity may be under detected in the case of sub-pixel fires and fires that are obscured by vegetation canopies. Rapid regrowth of vegetation over burned areas may also cover recent burns. Further, burn scars may persist for many years, producing false detections years after the original fire. And finally some algorithms are unable to detect large areas of woodland or shrub fires *(Simon et al. 2004)*.

In addition, temporal records of biomass burning inferred from satellite records are typically of short duration and cover only a few years. *Schultz (2002) and Generoso*

et al (2003) used ATSR fire counts to estimate seasonal and interannual variability of biomass burning over the five year period 1996 – 2000. *Cooke et al. (1996)* used fire counts from the Advanced Very High Resolution Radiometer (AVHRR) to estimate seasonality of biomass burning from 1984 to 1989. *Herman et al. (1997)* used ozone measurements from the Total Ozone Mapping Spectrometer (TOMS) to infer aerosol loading from biomass burning over the same time period. *Dwyer et al. (2000)* also used AVHRR fire counts to analyze the spatial and temporal distribution of fires during 1992-1993. The study period is typically short due to the time span of the satellite data, and the computational expense of processing and analyzing the spatially and temporally high-resolution data sets.

There are additional challenges to using Eq. 4.1. (i.e. bottom-up methods) to investigate biomass burning impact. Once the area of burn is known, the vegetation type or cover is needed to estimate the available fuel load of the burn. Land cover maps may be determined from regional reports (*Lavoue et al., 2000*), satellite products such as normalized difference vegetation or leaf area index (e.g. *Barbosa et al., 1999*), or biogeochemistry models that compute net primary production and standing biomass, such as the Carnegie-Ames-Stanford-Approach (CASA) model (e.g. *van der Werf et al., 2006*). As a wide range of biomes undergo burning, fuel loads per area can vary by nearly two orders of magnitude (*van der Werf et al., 2003*). The quantification of fuel loads remains one of the chief obstacles to accurate biomass burning emissions (*Kasischke and Penner, 2004*).

In addition, the calculation of trace gas emissions using the bottom-up method of Eq. 4.1 requires knowledge about the burning efficiency β and emission factor f. The burning efficiency, which is the fraction of the fuel load that is consumed, is a function of a number of variables including fuel type, fuel moisture, and fire stage, i.e. smoldering, flaming, etc., which makes it difficult to model across large spatial and temporal extents. It ranges for example from 0.2 for tropical forests and 0.5 for peat (*Levine and Cofer, 1999*). The emission factor also depends on these same variables and is gas specific and is sensitive to fire phase. For example, carbon is primarily converted to CO_2 during the flaming stage of fire, but CO, CH_4 and other hydrocarbons dominate emissions when the fire is smoldering (*Crützen and Andreae, 1990*).

4.2.2 Top-down method

The preceding discussion reviewed the current literature on using bottom-up methods to estimate emissions from biomass burning and delineated some of the challenges faced in using this method. Because of the scarcity of the relevant data, bottom-up methods are typically used to produce either mean climatological biomass burning emissions, or emissions specific to a region or short span of time, for example the Indonesian fires of 1997-98 (*Levine, 1999*). Our goal in this study is to assess the decadal trends of biomass burning, so we looked to other techniques.

Atmospheric CO and H_2 can serve as tracers of biomass burning. As mentioned above, about 40% of the total anthropogenic source of CO and H_2 is from biomass burning, making these gases well suited to this purpose. In fact, both gases share similar sources in general. Both are products of combustion processes and are intermediate

90

steps in the oxidation of methane and other hydrocarbons. Out of an annual global

source strength of about 2600 Tg CO, approximately 1200 Tg CO is emitted due to the

combined activities of anthropogenic combustion and biomass burning, and another

1200 Tg CO is emitted due to the oxidation of methane and non-methane hydrocarbons

(*Khalil and Rasmussen, 1990*). For H_2 the breakdown in the budget is similar.
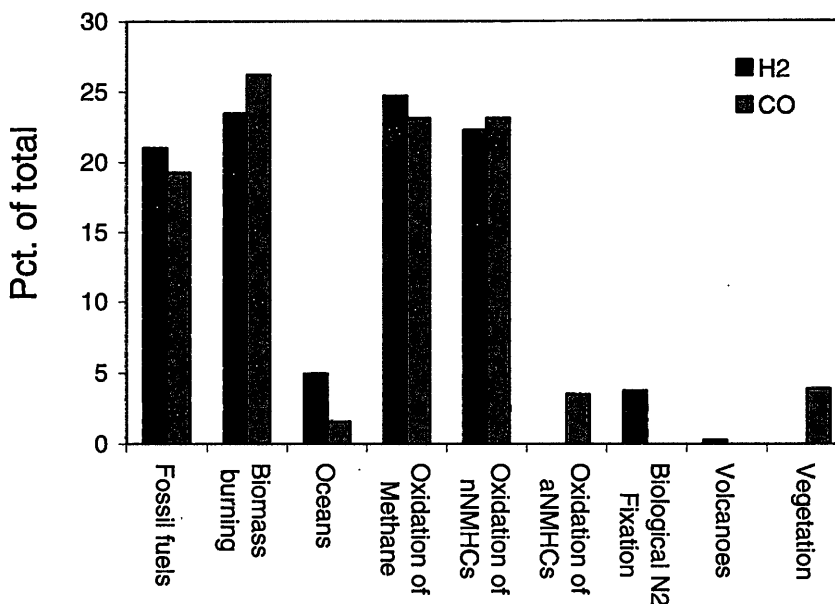
Figure 4.1. Sources of H_2 and CO given as percent of total budget.

Combustion, oxidation processes, and biomass burning are responsible for nearly 90%

of the global source strength of 80 Tg H_2 y^{-1} (*Warneck, 2000*).

Since biomass burning is responsible for much of the temporal variability of

atmospheric CO (*Novelli et al., 2003; van der Werf et al., 2004*), inversion of

atmospheric CO has been effective in constraining emissions from biomass burning

91

using measurements from global surface networks (e.g. NOAA's Global Monitoring Division), regional airborne programs (e.g. Transport and Atmospheric Chemistry Near the Equator - Atlantic, TRACE-A, Southern African Fire-Atmosphere Research Initiative, SAFARI) and space-borne instruments (e.g. Measurements Of Pollution In The Troposphere sensor onboard NASA's Terra satellite) (*Arellano et al., 2004, 2006; Pe'tron et al., 2002; Muller and Stavrakou, 2005; Heald et al., 2004; Palmer et al., 2003; Pfister et al., 2004*). Most of these studies focused on constraining the seasonal cycle or annual source strength of biomass burning emissions. *Bergmaschi et al. (2000a)* estimated the annual source strength of CO from tropical biomass burning to be 653 – 740 Tg CO from three years of surface NOAA-GMD CO measurements. *Petron et al. (2002)* used eight years of NOAA-GMD data to estimate the mean seasonal cycle of biomass burning. *Petron et al. (2004)* and *Arellano et al. (2006)* used CO column retrievals from the MOPITT instrument to constrain the seasonal timing of fire emissions in the Southern Hemisphere. Targeted campaigns such as SAFARI and TRACE-A flew air-borne instruments over regions of interest and measured CO concentration profiles. These are helpful to constrain regional emissions from biomass burning but are limited in both time and space (e.g. *McMillan et al., 2003*).

Carbon monoxide and hydrogen compose a unique pair of gases, for while they share similar sources (Fig. 4.1) their means of destruction differ. Carbon monoxide is removed primarily by oxidation with the hydroxyl radical OH (90% of its total sink; *Khalil et al., 1999*), while H_2 is oxidized in the soil by extra-cellular enzymes (~90% of its total sink; *Warneck, 2000*). This means that if emissions of these gases can be

inverted from their atmospheric records, we have confidence that any coincident

patterns will reflect changes in their sources and not their sinks, since it is unlikely their

disparate sink processes

Table 4.1. Sites and dates of CO measurements

Latitudinal Region	OGI	NOAA-GMD	CSIRO
North Polar	8/1980 – 12/1997 (Barrow)	12/1989 – 6/2002 (Barrow)	2/1992 – 12/2001 (Alert)
North Mid-latitudes	10/1984 – 12/1997 (Cape Meares)		
North Tropics	11/1979 – 12/1997 (Cape Kumukahi)	12/1989 – 6/2002 (Cape Kumukahi)	1/1992 – 12/2001 (Mauna Loa)
South Tropics	12/1979 – 12/1997 (Samoa)	2/1989 – 6/2002 (Samoa)	2/1992 – 12/2001 (Cape Fergusen)
South Mid-latitudes	8/1984 – 5/1996 (Cape Grim)	11/1992 – 6/2002 (Cape Grim)	3/1985 – 12/2001 (Cape Grim)
South Polar	8/1984 – 5/1996 (South Pole*)	9/1993 – 6/2002 (South Pole)	1/1992 – 12/2001 (South Pole)

should behave similarly. Biomass burning is the largest source of CO in the tropics

(*Crutzen and Carmichael, 1993*), where contamination from other anthropogenic

sources such as combustion is minimal. Overall, CO is more sensitive to the variation of

biomass burning emissions in the southern hemisphere than in the northern hemisphere

as CO emission from fossil fuels and biofuels is relatively low in the SH (*Bien et al.,*

2007).

To summarize, inverse or top-down techniques are valuable methods to

constrain emissions and lend insight into biomass burning. To date, most studies have

focused on quantifying annual budgets and investigating the seasonal cycle of emissions

over short time spans. In this study we use long-term measurements of both CO and H_2

in tandem to investigate the temporal variability of biomass burning in the tropics where

most fire activity occurs. From these measurements, we constructed unique records of

atmospheric CO and H_2 using global surface measurements that have not previously been used for this purpose. Using a low resolution chemical-transport model we inverted the time series and constructed a history of CO and H_2 emissions. We used this paired emissions history to investigate the patterns of biomass burning activity on decadal scales.

Table 4.2. Sites and dates of H_2 measurements

Latitudinal Region	OGI	NOAA-GMD	CSIRO
North Polar	10/1985 – 3/1997 (Barrow)	1/1989–12/2003 (Barrow)	2/1992 – 12/2001 (Alert)
North Mid-latitudes	4/1985 – 3/1997 (Cape Meares)	1/1992–12/2003 Cape Meares et al.	
North Tropics	10/1985 – 3/1997 (Cape Kumukahi)	7/1989–12/2003 (Cape Kumukahi)	1/1992 – 12/2001 (Mauna Loa)
South Tropics	4/1985 – 3/1997 (Samoa)	6/1989–12/2003 (Samoa)	2/1992 – 12/2001 (Cape Fergusen)
South Mid-latitudes	3/1985 – 3/1997 (Cape Grim)	6/1991–12/2003 (Cape Grim)	2/1992 – 12/2001 (Cape Grim)
South Polar	2/1985 – 3/1997 (South Pole)	4.1993–12/2003 (South Pole)	1/1992 – 12/2001 (South Pole)

4.3 Time series of atmospheric CO and H_2

The foundation of this work is the long-term time series of atmospheric measurements of CO and H_2 concentrations. We used measurement data from three sources, the Oregon Graduate Institute (OGI) (*Khalil and Rasmussen, 1984, Khalil and Rasmussen, 1988, Khalil and Rasmussen, 1994*), the National Oceanic and Atmospheric Administration Global Monitoring Division (NOAA-GMD) (*Novelli and Masarie, 2009*), and the Global Atmospheric Sampling Laboratory of Australia's Commonwealth Science and Industrial Research Organization (CSIRO-GASLAB) (*Steele et al., 2007*). Specific sites and dates of measurements used for this are shown in Table 4.1. Though

some measurements began in the late 1970s no single continuous record exists over this period, and part of our effort here was to construct such a record by conjoining measurements from the networks. The sites chosen were those that predominately experience well-mixed background marine air. This is important to ensure that the CO and H_2 mixing ratios are representative of large air masses and free from local sources.

4.3.1   OGI

Carbon monoxide and hydrogen were monitored at clean air sites between the early 1980s and 1998 as part of the Oregon Graduate Institute trace gas sampling program. Triplicate air samples were collected at each site in 0.8 l flasks and analyzed at OGI by gas chromatography (GC) with flame ionization (FID) and mercury oxide (HgO) detectors. Absolute calibration was maintained with National Institute of Standards and Technology SRM 1677B standards (*Khalil and Rasmussen, 1994*). Specific start dates of available data varied with location and are provided in Table 4.1. Sites were strategically selected worldwide to monitor the major semi-hemispherical air masses. Long term measurements were made at Pt. Barrow, Alaska (71.3°N, 156.6°W), Cape Meares, Oregon (45.5°N, 124°W), Mauna Loa, Hawaii (19.5°N, 155°W), Cape Kumukahi, Hawaii (19.5°N, 155°W), Tutuila, American Samoa (14.2°S, 170.8°W), Cape Grim, Tasmania (40.7°S, 144.7°E), and the South Pole (90°S). These stations were chosen to reflect concentrations of trace gases in air masses representing north polar latitudes, north mid-latitudes, north tropics, south tropics, south mid-latitudes, and south polar latitudes, respectively. Short term records exist at other sites but these were not used in this work. At most locations samples were taken several times per month
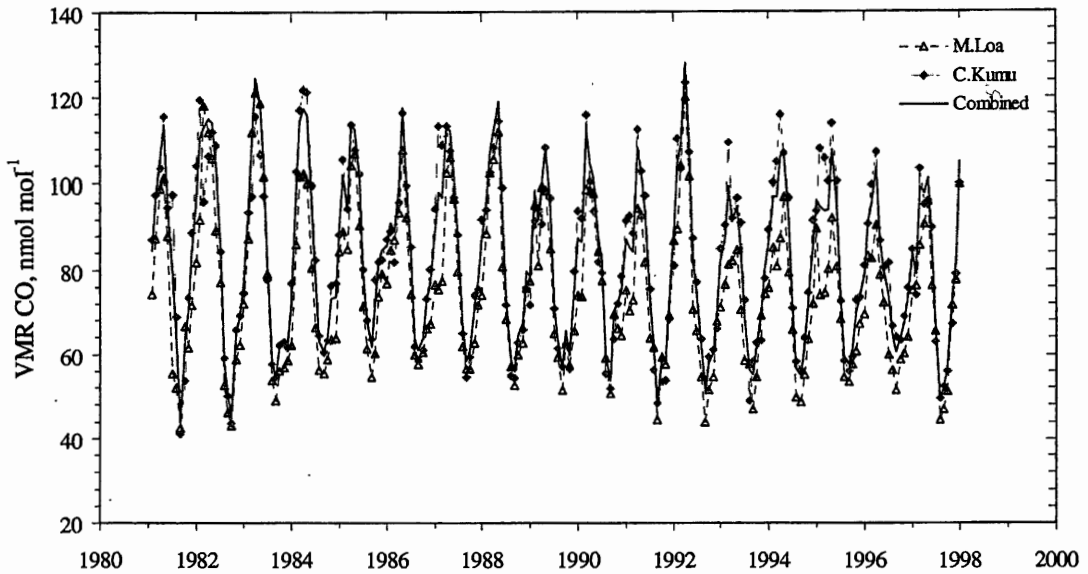
Figure 4.2. CO volume mixing ratios for Mauna Loa and Cape Kumukahi. Data from the OGI network.

and monthly averages were constructed from these. We filled in gaps in the data record

by linear interpolation if only one month of data was missing, or by an interpolation

method based on seasonal gradients between sites.

All sites are located at or near sea level with the exception of the Mauna Loa

Observatory (elevation 3397 m). To cover gaps in the measurement record, we created a

single data record at Hawaii by combining the Mauna Loa measurements with those at

Cape Kumukahi, which is a sea level site receiving air from the marine boundary layer.

Mauna Loa nominally samples air from the free troposphere, though on occasion

upslope wind conditions may transport air from the marine boundary layer *(Karl et al.,*

2002). Typically away from landmasses and sources, vertical gradients of CO are small

(Bergamaschi et al., 2000).

96

The CO records at both sites are shown in Fig. 4.2 along with their seasonal

cycles in Fig. 4.3. The seasonal cycles are well matched with maxima and minima

occurring on the same month throughout the time series. Carbon monoxide levels at

Cape Kumukahi are about 10% higher on average than at Mauna Loa. The higher CO at

Cape Kumukahi may be due to local sources, though this is unlikely, since the station

receives predominately marine air brought in by consistent northeasterly trade winds.

The offset between the sites tends to increase during the fall and early winter, and

reaches a peak during the early spring, which follows the cycle of biomass burning
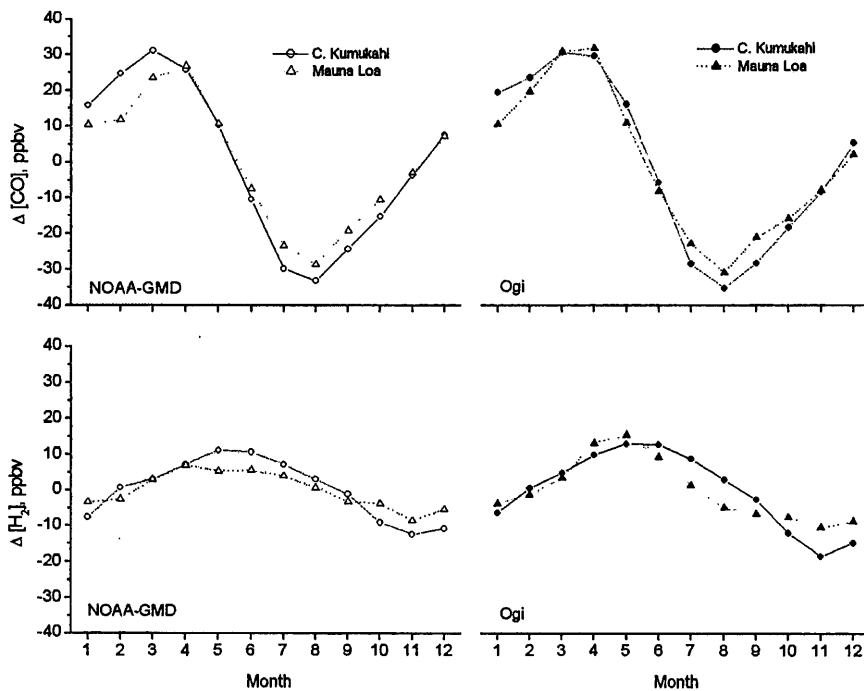
Figure 4.3. Seasonal cycles of CO (upper) and H_2 (lower) mixing ratios at Cape Kumukahi and Mauna Loa. Measurements from both the OGI (right) and NOAA-GMD (left) are shown.

emissions in the northern tropics (*Hao and Liu, 1994*). The measurements are better matched at the CO minima during the late summer months when the sink term dominates the CO trend. Long range mixing and some chemical destruction likely leads to the small vertical gradient between the sites. For consistency with the other surface sites, we scaled the Mauna Loa data by a single factor (1.10) and found the average of the modified time series with the Cape Kumukahi data to create a single time series for the northern tropics (Fig. 4.2).

For H_2, the direction of the difference is reversed, with higher mixing ratios observed at Mauna Loa than at Cape Kumukahi (Fig. 4.4). The lower surface levels are maintained by microbial consumption in the soils, which is the largest sink for hydrogen. Seasonal cycles observed at the two sites are again similar (Fig. 4.3). There is a small seasonal cycle observed in the ratio of mixing ratios, varying from 1.02 to 1.04 (MLO/CKU). We again scaled the Mauna Loa data and averaged the two sites to create a single H_2 time series at Hawaii. We note that the H_2 data from the NOAA-GMD network showed similar behavior at Mauna Loa and Cape Kumukahi and have nearly the identical vertical gradient.

4.3.2   NOAA-GMD
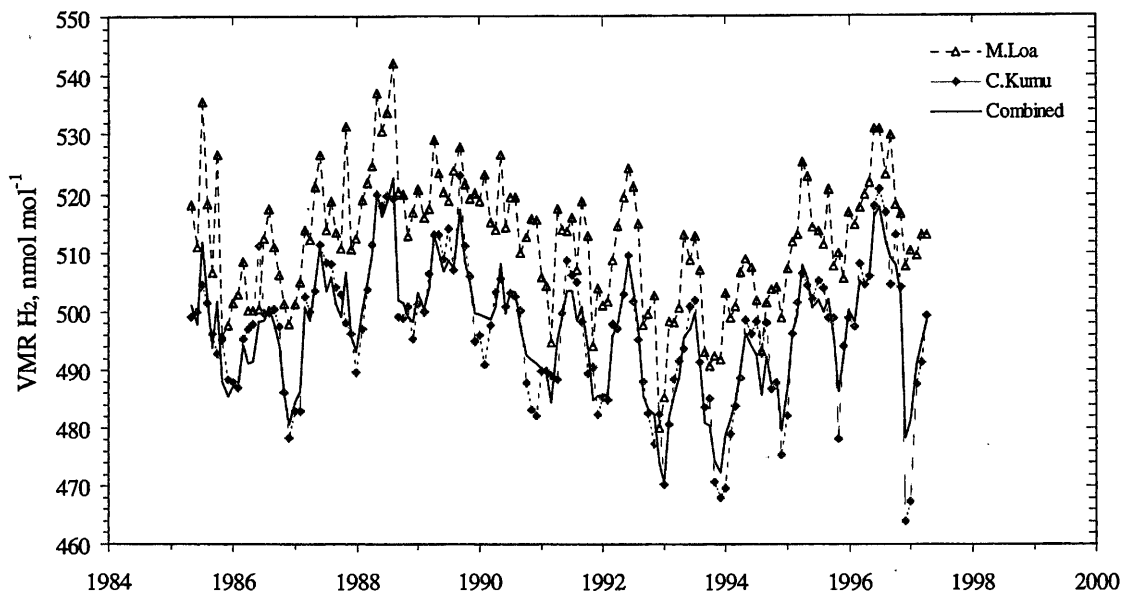
Figure 4.4. Volume mixing ratios of H_2 measured at Mauna Loa (dashed line) and Cape Kumukahi (solid gray). Data come from the OGI flask network. Also plotted (solid black) is the combined record for Hawaii, which is the simple mean of the Cape Kumukahi data and scaled Mauna Loa.

Measurements from NOAA-GMD begin in the early 1990s and continue today (Table 4.1). NOAA-GMD samples air at the same six sites as the OGI network and we principally use measurements from these six sites throughout this work. However sampling was discontinued at Cape Meares in 1998 and an alternate site was necessary to continue the record. NOAA-GMD measures H_2 and CO at numerous north mid-latitude sites (30–65°N) as part of its Cooperative Air Sampling Network. We narrowed the list of candidates to include only marine sites receiving predominantly clean background air, which are located at or near sea level. These sites would measure air masses most similar to those sampled at Cape Meares. We also excluded any sites that had considerable spans of data missing for any reason. This left us with five possible
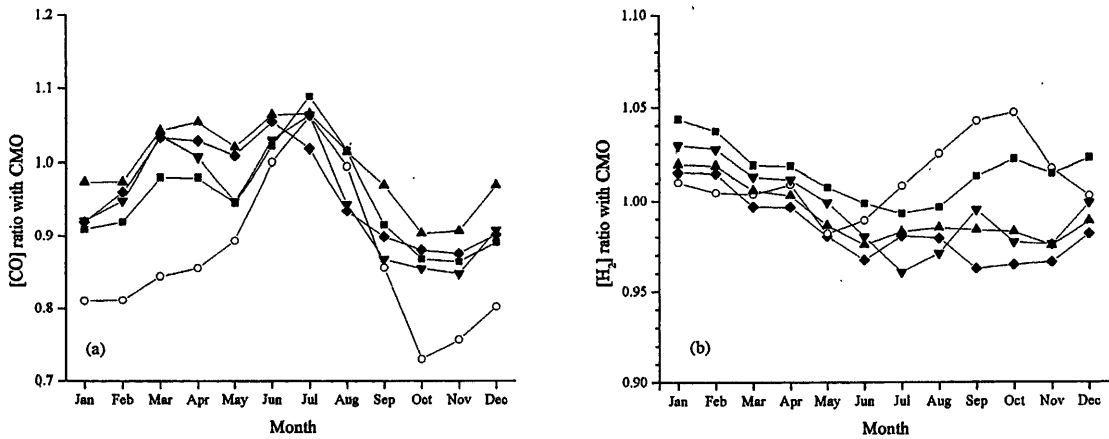
Figure 4.5. Comparison of (a) CO and (b) H$_2$ seasonal cycles at several NOAA-GMD northern midlatitude sites. The data are the ratios between CO mixing ratios at Cape Meares, OR to Shemaya Is., AK (upward triangle), Cold Bay, AK (diamond), Iceland (downward triangle), Mace Head, Ireland (square), and Azores, Portugal (open circle).

replacement sites, Terceira Island, Azores (38.8°N, 27.4°W), Cold Bay, Alaska (55.2°N, 162.7°W), Storhofdi, Iceland (63.3°N, 20.3°W), Mace Head, Ireland (53.3°N, 10.0°W), and Shemya Island, Alaska (52.7°N, 174°E).

The degree of similarity between each of these sites and Cape Meares was investigated by taking ratios between the seasonal CO cycle of each site and Cape Meares (Fig. 4.5). There is a clear grouping of four of the sites (all but Azores) with seasonalities that are most similar to Cape Meares, though there is a departure during October and November when CO levels at Cape Meares are noticeably higher than at these sites. The seasonality at Azores shows departures from Cape Meares and the other four sites in all months except June-August. This is due to overall lower CO levels at

Azores (by about 10%) and also due to its smaller seasonal cycle amplitudes. We computed the latitudinally-weighted average of these four sites and added the record to the Cape Meares data to complete the NOAA-GMD northern mid-latitude CO record. We used a similar scheme to construct the NOAA-GMD northern mid-latitude H_2 record, but in this case the Azores data were not obvious outliers (Fig. 4.5), and we included measurements from this station in the composite record.

4.3.3   CSIRO

Australia's CSIRO began measurements of CO and H_2 in the early 1980s at the Cape Grim Baseline Station (Cape Grim, Tasmania) as part of the World Meteorological Organization's Global Atmospheric Watch program (*Cooper et al., 1999*). The program grew into the Global Atmospheric Sampling Laboratory (CSIRO-GASLAB) and trace gas sampling was expanded globally to nine other stations in 1992 (*Francey et al., 1996*). Both CO and H_2 were analyzed by GC/HgO instruments. Calibration was based on the NOAA-GMD (then Climate Monitoring and Diagnostics Laboratory) standard.

The extended network has three sites in common with the OGI program (Mauna Loa, Cape Grim, and the South Pole) and four with the NOAA-GMD network – the above sites plus Alert, Nunavut, Canada (82.5°N, 62.5°W). In addition, CSIRO measured CO and H_2 at Shetland Islands, Scotland (60.2°N, 1.2°W), Estevan Point, B.C., Canada (49.4°N, 126.5°W), and Cape Ferguson, Australia (19.3°S, 147.1°E). The first two sites represent northern mid-latitude air masses and the latter samples the southern mid-latitude air mass.

We analyzed the data sets at Shetland Islands and Estevan Point to determine if the air sampled at these locations is drawn from similar air masses. To do so, we deconstructed each time series and compared the various components. The
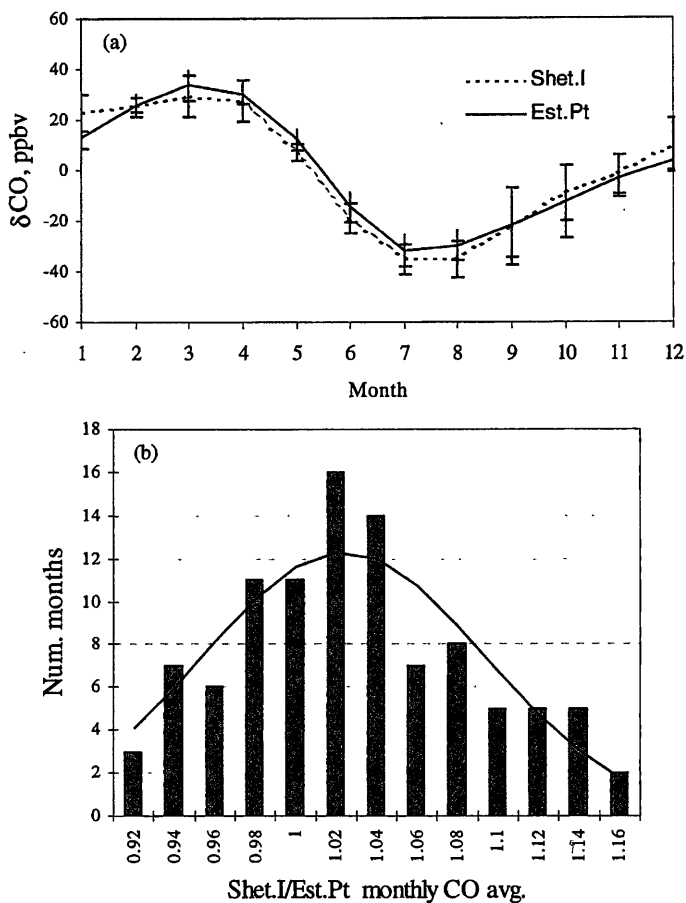
Figure 4.6. CSIRO-CO measurements at northern mid-latitudes. (a) Seasonal cycle at Estevan Pt., B.C., and Shetland Is., Scotland. Errorbars show one standard deviation of the mean. 1=Jan, ..., 12=Dec. (b) Ratios of the monthly averages measured at each site (columns). The solid line is a Gaussian fit to the data.

measurement time series at any site can be written as

$$C(t) = \overline{C}(t) + \Delta_s(m(t)) + \varepsilon(t) , \qquad (4.2)$$

where $\overline{C}(t)$ is the slowly varying baseline component, Δ_s represents the seasonal anomaly from the baseline which is specified monthly, $m(t)$ is the current month, and ε is a random fluctuation. The baseline component can be approximated by taking a running average of the time series of length $2\Delta t$,

$$\overline{C}(t) = \frac{\int_{t-\Delta t}^{t+\Delta t} C(t) dt}{\int_{t-\Delta t}^{t+\Delta t} dt} . \qquad (4.3)$$

Typically Δt is 6 mo.

The CO seasonal cycles at Shetland Is. and Estevan Pt. are in close agreement (Fig. 4.6a). The maximum and minimum occur at the same month for both records and the peak-to-peak amplitude is nearly identical for both. We also took the running ratio of the baseline CO (e.g. Eq. 4.2) at Shetland I. to Estevan Pt. (Fig. 4.6b). The distribution is roughly normal indicating that the trends at both sites are similar, and that there is no systematic difference in the behavior of CO at each site. The mean ratio of the CO baselines is 1.02 ± 0.01 (95% CI) in the sense that CO levels at Shetland Is. are about 2% higher than at Estevan Point. This is a small difference and we conclude that each site is measuring the similar northern mid-latitude air masses. We chose the Estevan Pt. series to represent CO and H_2 concentrations in the mid-latitudes since it is closer to the middle of the region (i.e. 49.4°N).

We plot the deseasonalized H_2 and CO in Figs. 4.7 and 4.8 respectively, along with the moving averages of each series. In the notation of Eq. 4.2 the deseasonalized

103

data are found according to $C(t) - \Delta_s(m(t))$, and the moving averages are $\overline{C}(t)$ with Δt = 12 mo.

The general features of the CO measurements include a pronounced latitudinal gradient. CO levels at north mid-latitudes are about three times higher than at equivalent latitudes in the southern hemisphere. The gradient is maintained by large northern hemisphere CO emission as we discuss further below. Polar CO is nearly equivalent to
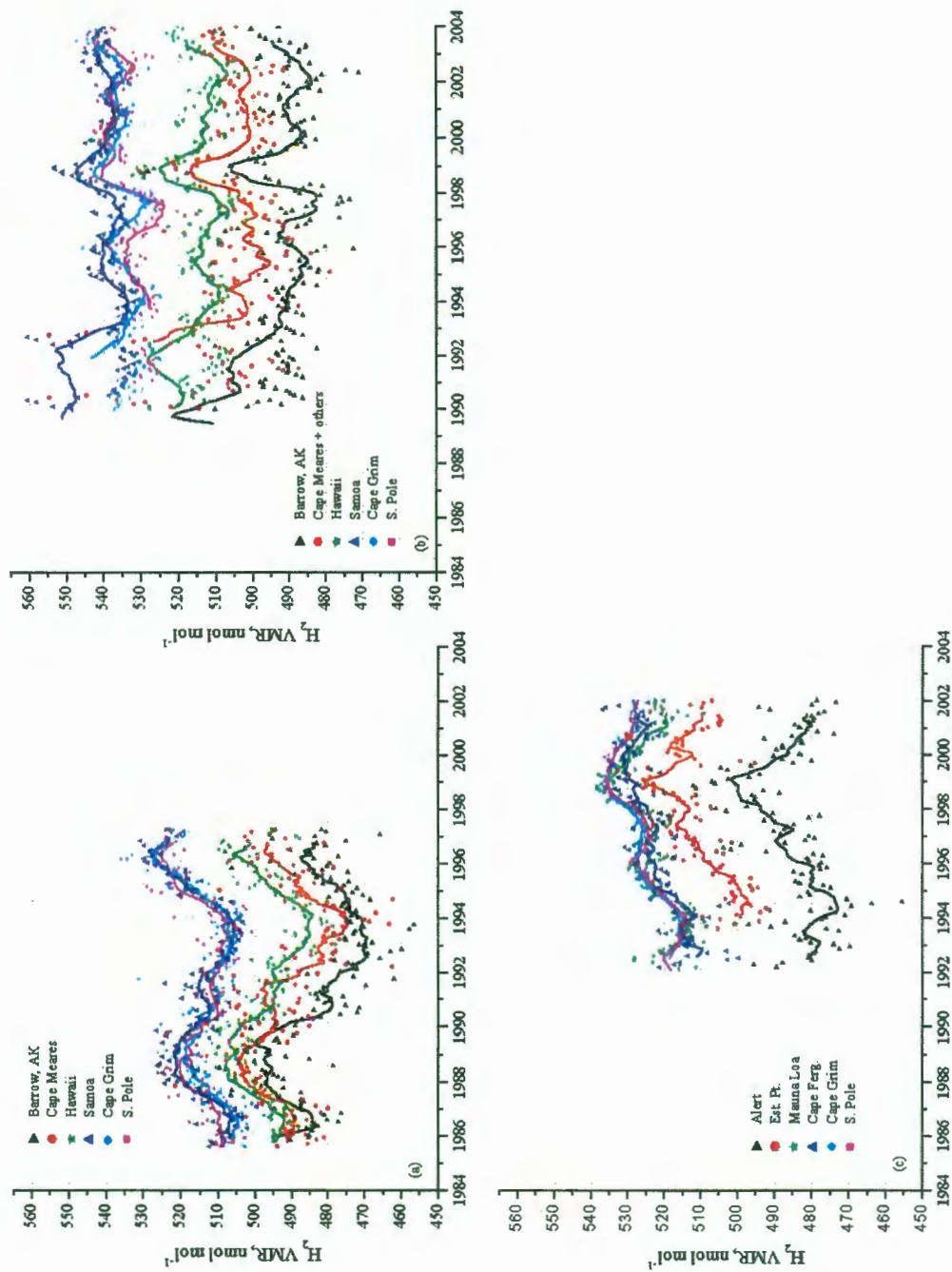
Figure 4.7. Atmospheric H$_2$ mixing ratios from three different trace gas monitoring networks, (a) OGI, (b) NOAA-GMD, and (c) CSIRO-GASLAB. The symbols are deseasonalized monthly averages, while the solid lines show the 12-month moving averages.

mid-latitude CO in both hemispheres indicating that CO emissions at high latitudes are negligible. A strong OH "trap" exists in the tropics, which destroys CO as it moves across the ITCZ. This produces a ratio of nearly two to one between CO levels at the northern tropical site (Hawaii) and its partner station in the south at Samoa and also at Cape Ferguson.

Also evident in Fig. 4.8 are strong positive CO anomalies during 1997-99. Though we discuss these features in more detail below when we deconvolute the measurement record, here we note that in the north the anomaly appears first at the tropical site and occurs at mid- and polar latitudes a few months later. Likewise in the southern hemisphere. Also the signal appears in the southern hemisphere before it shows up in the north. This suggests a signal that starts in the tropics and spreads to higher latitudes. These features are thought to be the result of wildfires brought on by El Nino drought conditions. The emissions required to produce these features are estimated below using inverse modeling.
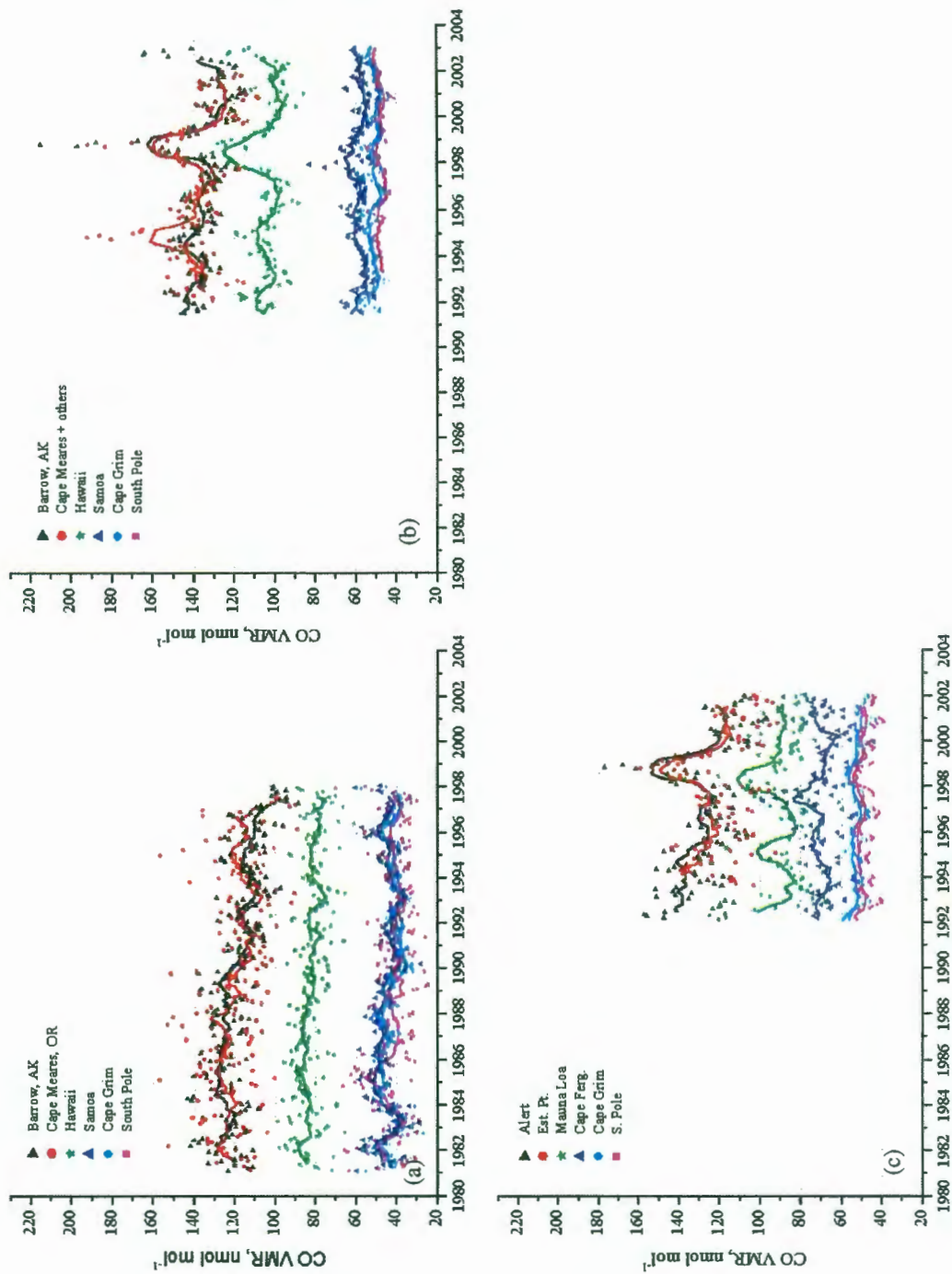
Figure 4.8. Atmospheric CO measurements from three different trace gas monitoring networks, (a) OGI, (b) NOAA-GMD, and (c) CSIRO-GASLAB. The symbols are deseasonalized monthly averages, while the solid lines show the 12-month moving averages.

There is also a secular downward trend in CO levels at northern hemisphere sites observed in all three networks. The trend is largest at polar and mid-latitudes where CO levels drop about 15% over 1981 to 1998 in the OGI data. This trend continues in later years as observed in the NOAA and CSIRO time series. Despite these long term changes in the north, there is little evidence for a similar trend in the south. CO levels overall are quite steady over the past few decades. The existence of the tropical OH trap largely isolates the CO in each hemisphere, so the hemispheric behavior of OH need not be the same in the north and south, as observed here.
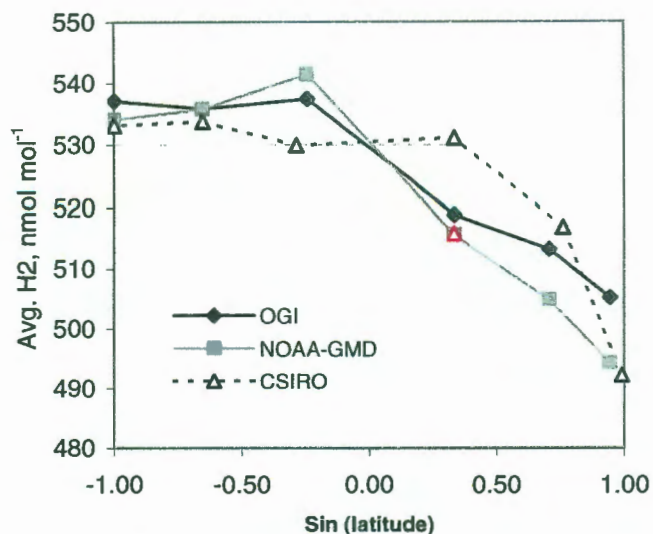
Figure 4.9. Latitudinal gradient of H_2 measured by three different networks. The plotted data are averages over the respective measurement periods. The red open triangle is the CSIRO average at Mauna Loa scaled to be consistent with the surface site at Cape Kumukahi. With this adjustment, the gradients are in good agreement.

In contrast to CO, H_2 levels are highest in the southern hemisphere (Fig. 4.7). As sources of CO and H_2 are similar, this gradient must be maintained by processes that remove atmospheric H_2. As mentioned above, the largest sink of H_2 is uptake by soils, which is larger in the northern hemisphere owing to the presence of the major continental land masses. The lifetime of H_2 is longer in the southern hemisphere and leads to higher H_2 levels. H_2 levels are also nearly constant at all sites in the southern hemisphere, in contrast to the north where large latitudinal gradients exist (Fig. 4.9). This suggests that sources and sinks in the southern hemisphere are small compared to those in the north, and transport times in the south are short enough to homogenize the H_2 here.

Though there is large interannual variability observed in all records, in part due to this variability, there are no significant trends. OGI is the only network with pre-1990 measurements, and here we see a large peak in H_2 levels, at all sites, centered about 1988-1999. Another peak occurs around 1998-99 and this is observed in all networks. The peaks are modest in magnitude, though exaggerated in the figure due to scale. The 1988-89 peak is about 2-3% higher than the average during this period and the 1998-99 peak is similar. We investigate below the emission anomalies required to produce these peaks.

4.3.4   Comparison of data sets

4.3.4.1   Carbon monoxide

Significant differences in the absolute calibration of the H_2 and CO measurements are evident in Figs. 4.7 and 4.8. Differences in the absolute calibration scale of the three networks were determined through direct monthly comparison of the gas concentrations at the common sites (Fig. 4.10). We excluded the OGI South Pole data from the analysis due to problems with the site's absolute calibration. The calibration scale of this site was set with respect to Cape Grim based upon the Cape Grim:South Pole ratio calculated from the NOAA-GMD data.
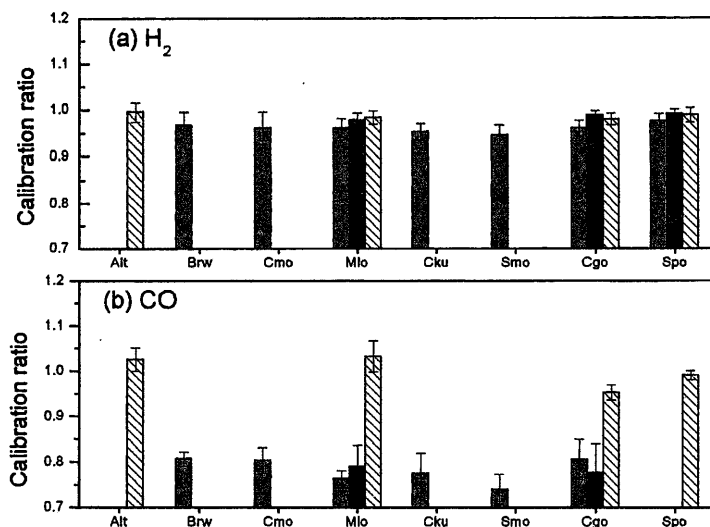
Figure 4.10. Ratios of (a) H_2 and (b) CO mixing ratios measured by different networks. The diagonally striped column gives the ratio of CSIRO to NOAA-GMD, gray columns are ratios of OGI to NOAA-GMD, and black columns are ratios of OGI to CSIRO. Error bars show one standard deviation of the mean. Station abbreviations are Alt=Alert, Brw=Barrow, Cmo=Cape Meares, Mlo=Mauna Loa, Cku=Cape Kumukahi, Smo=Samoa, Cgo=Cape Grim, and Spo=South Pole.

Based on the other common sites the average ratio between the CO calibration scales is 0.80±0.01 (OGI/NOAA-GMD) with a range of 0.74 (Samoa) to 0.81 (Barrow). Performing a similar analysis on the OGI and CSIRO data sets, the average ratio is 0.79±0.04 (OGI/CSIRO) with a range of 0.78 (Cape Grim) to 0.79 (Mauna Loa). Finally, using common sites of the NOAA-GMD and CSIRO networks we calculate the average ratio to be 0.96±0.01 (NOAA/CSIRO) with a range of 0.94 (South Pole) to 1.03 (Mauna Loa).

The close agreement between the NOAA and CSIRO networks is not surprising as CSIRO uses a NOAA standard for their measurements. As the OGI calibration is considerably lower, we scaled all OGI measurements by 1.25 to put them on the NOAA-GMD scale. We also applied a modest correction of 0.96 to the CSIRO data.
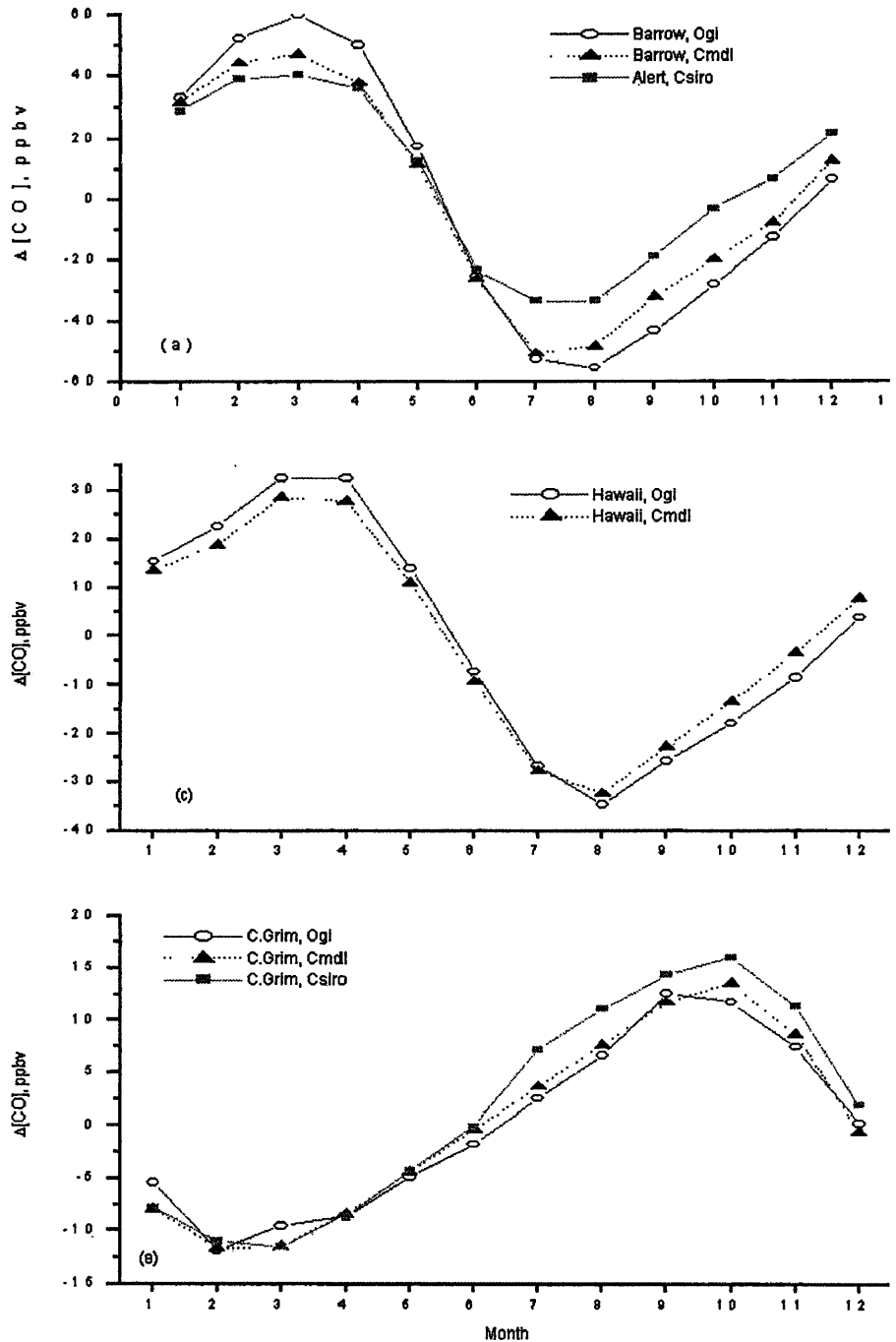
Figure 4.11. Seasonal cycles of CO at different sites and measured by different networks. "Cmdl" labeled data refer to the NOAA network.

After making the calibration adjustments, we constructed the seasonal cycles

(these are the $\Delta_s(m(t))$ from Eq. 4.2) for all sites and networks (Fig. 4.11) as well as the

12-month moving averages ($\overline{C}(t)$), which are plotted in Fig. 4.12. With the exception of

the South Pole, there is good agreement between the OGI and NOAA-GMD cycles at

all sites. The May peak in CO observed in the OGI South Pole data is not a permanent

feature of the seasonal cycle, rather it can be attributed to high concentrations during

this month in 1986 and 1991. These years have a disproportionate weight to the

seasonal average as there are significant gaps in the OGI South Pole record, and the

interpolated data covering these periods are not used to derive the seasonal cycle.

The seasonal cycle measured at Alert, Canada, by the CSIRO network has a

smaller amplitude than observed at Barrow from the other networks. As Alert

(lat=82.5°N) is considerably more north than Barrow (71.3°N), the summertime trough

is shallower since OH levels decline with higher latitudes and reduce the oxidation sink

of CO at Alert. At the other two common sites, Cape Grim and the South Pole, we see

good correspondence in the phase of the CSIRO cycles, though the peak-to-peak

amplitude is larger. This occurs because the global scaling factor used to calibrate the

CSIRO data underestimates the true difference here, producing a residual calibration

difference of about 2% (in the direction that CSIRO-CO is higher than NOAA). As this

is a polar site, the small discrepancies here will not significantly impact our findings in

the tropics.
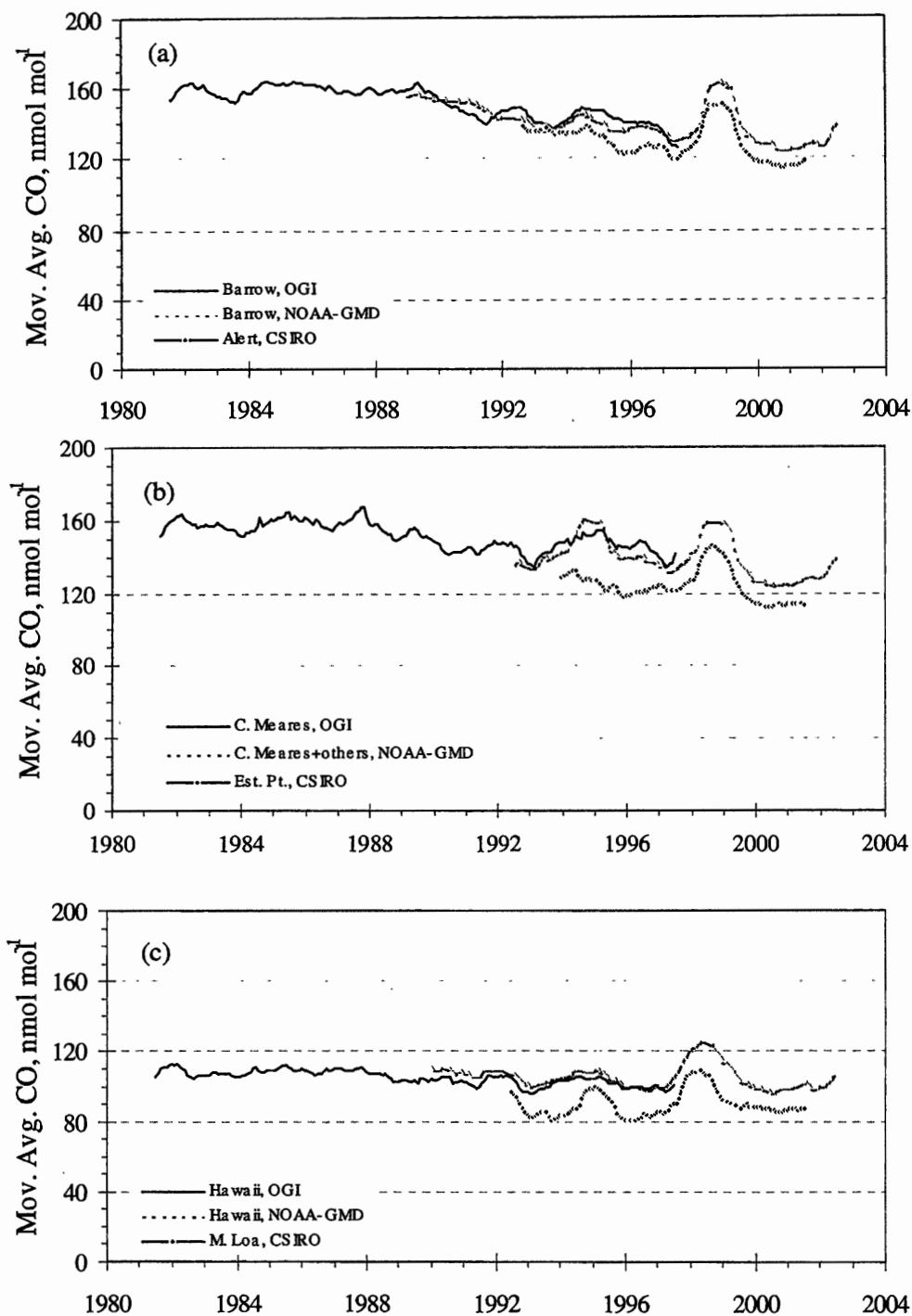
Figure 4.12. Adjusted CO records at different sites and by different sampling networks. The data plotted are 12-month moving averages that have been scaled by the appropriated calibration factor to place measurements on the NOAA-GMD standard. (a) north polar, (b) north mid-latitudes, (c) north tropics.

115
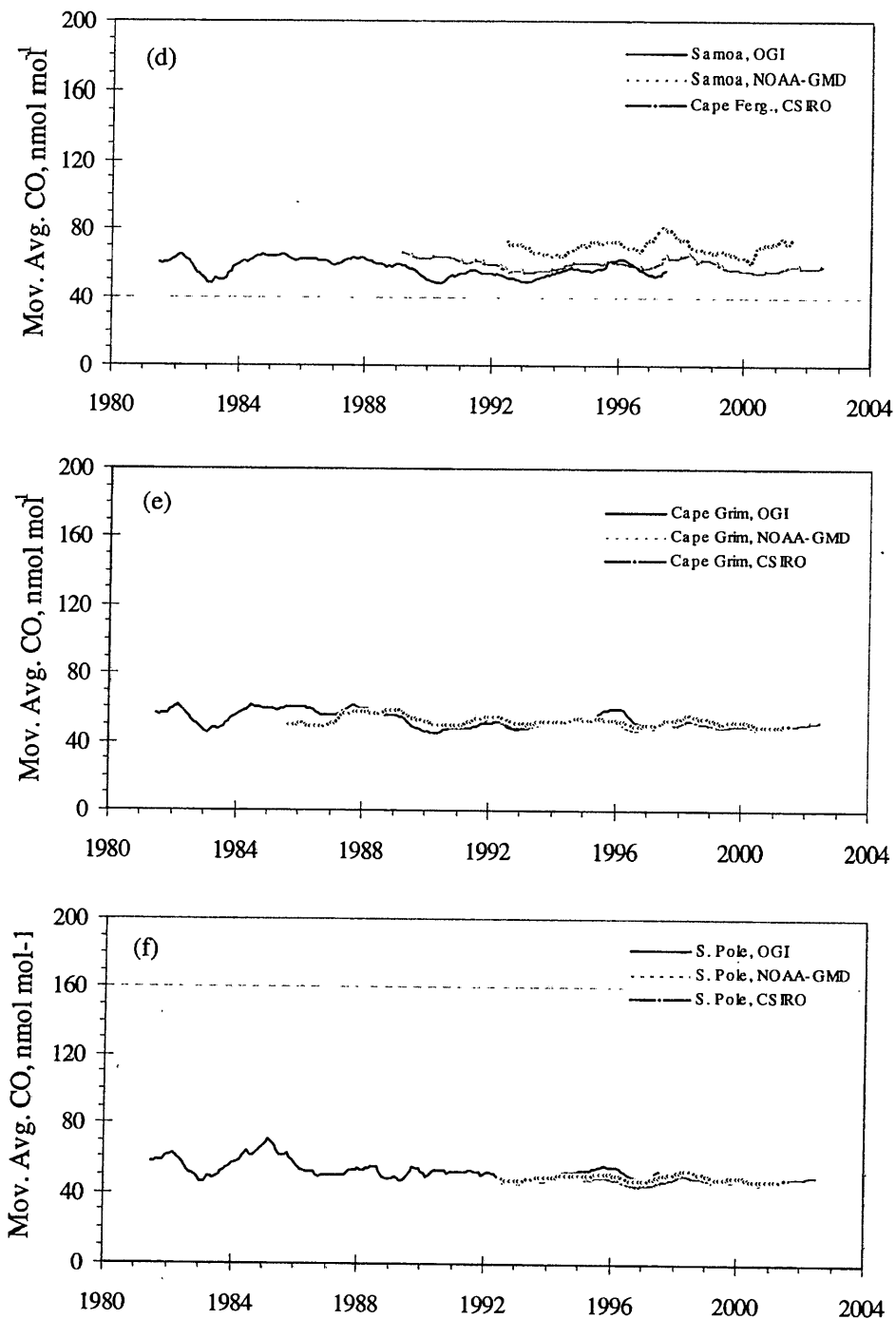
Figure 4.12 (cont). (d) south tropics, (e) south mid-latitudes, and (f) south polar region.

116

We next compared the calibrated moving averages at each site from all networks (Fig. 4.12) to assess whether it is feasible to composite records from different networks into a single long term time series. It is evident from this figure that the latitudinal gradient measured by the OGI network is in excellent agreement with NOAA-GMD measurements. Though overall the moving average records for all sites show few features, the "hump" observed from 1993-1997 in the northern mid-latitudes is seen in both records. In addition, the slight interannual variability over the same time period at Hawaii is also evident in both records. There is also good correlation between the small features in the South Pole records. We conclude that the OGI and NOAA records are in close enough agreement to create a composite CO time series that spans from 1981 to 2004. To our knowledge this is the longest CO time series that has been constructed. We inverted this composite time series below to estimate the CO emissions over this time period.

4.3.4.2 Hydrogen

As we mentioned above, the hydrogen record shows some interesting behavior over the time span of measurement (Fig. 4.7). Broadly, this behavior is seen across all networks. During the period of measurement overlap between the OGI and CSIRO data sets, H_2 levels rise from a minimum in 1994. This rise is captured in both data sets. The OGI data set finishes just after H_2 peaks in 1996-97. The CSIRO measurements, which extend past this time, reveal that this peak sits on the shoulder of a broader feature that peaks a couple years later in 1998-99. After this CSIRO-H_2 levels fall rapidly by 4-5 ppbv y^{-1} until the record ends in 2002.

117
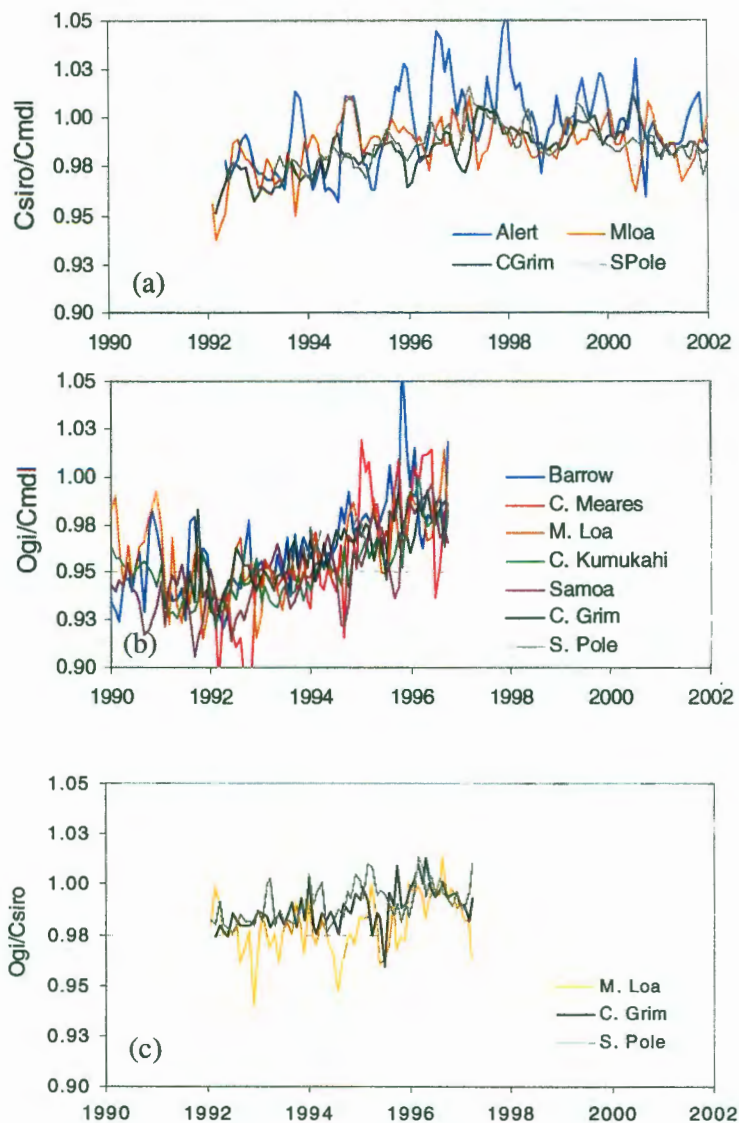
Figure 4.13. Evidence of a calibration drift is seen in the time series of calibration ratios. Plotted are the ratios of (a) CSIRO H_2 to NOAA-GMD (Cmdl), (b) OGI to NOAA-GMD, and (c) OGI to CSIRO. Ratios are derived using measurements from common sites (labeled). ratio of H2 data between different networks.

Consistent with the OGI record, NOAA H_2 also falls from the start of the record in 1989 to a minimum in 1993-94 and then rises again to another peak in 1996.

However unlike the OGI record, H_2 levels do not rebound back to 1989 levels after the 1993-94 minimum. The OGI record indicates that H_2 levels are comparable in 1988-89 and 1996-97. Even past this 1996-97 peak, NOAA H_2 never returns to the levels at the beginning of the time series in 1989. Because of this, there is an overall downward trend in the NOAA H_2, which is not present in the records from the other two networks.

In part this is due to a drift in the calibration seen in the NOAA-GMD and CSIRO H_2. This drift can be seen in the inter-network comparisons of H_2 shown in Fig. 4.13. Here we plot the time series of CSIRO/NOAA, OGI/NOAA, and OGI/CSIRO ratios of H_2 for all sites in common between networks. The largest drift in calibration exists from 1992 to 1997 between the OGI and NOAA measurements. Over this interval, the calibration ratio increases from 0.94 to 0.99 for a trend of 1.23% y^{-1}. A trend also exists, though smaller, in the ratios from the other two network intercomparisons. We calculated a trend of 0.67% y^{-1} and 0.60% y^{-1} for the OGI/CSIRO and CSIRO/NOAA ratios. Since all intercomparisons reveal a trend in the calibration, there must be a drift in the calibration for at least two networks. Since the CSIRO scale is based on NOAA standards, it seems reasonable that the calibration standard for both networks is drifting. If so, and if the OGI standard was stable, then from 1992 to 1997 the NOAA calibration drifted downwards at a rate of -1.23 % y^{-1}, and the calibration for the CSIRO data declined by -0.6% y^{-1}.

After 1997 the calibration stabilizes and the CSIRO/NOAA ratio is close to unity during this time. We adjusted the OGI measurements to the NOAA scale correcting for this drift. We use caution when interpreting the emissions inverted from
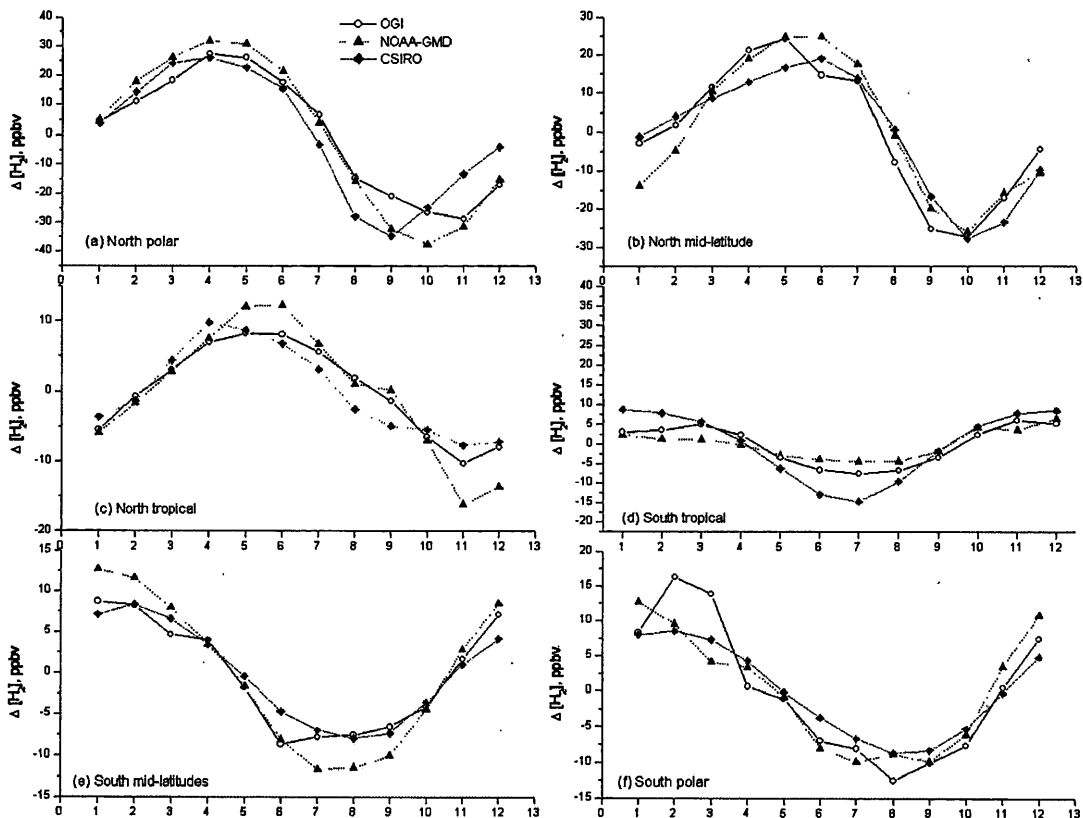
Figure 4.14. Seasonal cycles of H_2 at different sites and measured by different networks. The sites for each region are (a) Barrow (OGI, NOAA), Alert (CSIRO); (b) Cape Meares (OGI, NOAA), Est. Pt. (CSIRO); (c) Mauna Loa for all three, plus Cape Kumukahi (OGI, NOAA, avg. with M.Loa); (d) Samoa (OGI, NOAA), Cape Ferguson (CSIRO); (e) Cape Grim (all); and (f) South Pole (all).

the measurement record from 1992 to 1997 from the NOAA and CSIRO networks. We note that the OGI measurements span this period of concern, and we generally base our conclusions on the OGI record during this time.

Despite absolute calibration differences, there is good agreement of the seasonal cycles of H_2 measured at each station (Fig. 4.14). The timing of the peaks and the troughs is consistent between networks at all sites except at the north polar sites where

120

the minimum of the seasonal cycle for each network occurs at a different month. The minimum at Alert occurs a month earlier than at the NOAA Barrow station, which in turn occurs a month earlier than at the OGI Barrow location. Since the minimum is largely determined by the soil sink, it is reasonable that the shorter growing season at Alert would produce an earlier minimum than Barrow is southward. It is unclear why the timing is different for the other two networks as both are sampling air from the same station. The cycles indicate the H_2 maximum is reached during April and May throughout the northern hemisphere, and during December and January in the southern. The minimum in the northern hemisphere occurs at later dates in the year for southern sites showing the dominance of the destruction term. We also observe that the amplitude of the seasonal cycle is largest at the higher latitudes in the northern hemisphere, again consistent with the strong seasonality of the climate there and large land mass area, both which determine the strength of soil uptake. In general the amplitude of the cycle is largest for the NOAA-GMD measurements. This is consistent with our finding that the NOAA-GMD absolute calibration is higher than the others during the period of overlap.

4.3.5 Composite record

We show the composite record of CO in Fig. 4.15. This was created by joining together the scaled OGI and unscaled NOAA-GMD measurements. During the period of overlap, monthly averages from each site were weighted by their respective standard deviations and the weighted average was determined. The monthly data are decomposed
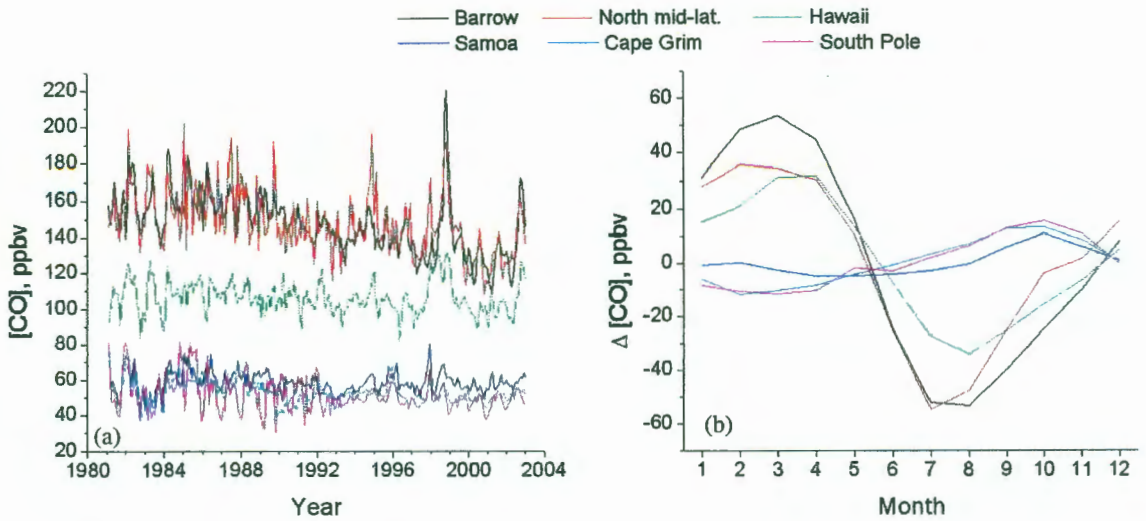
Figure 4.15. Composite time series of CO using measurements from the OGI and NOAA-GMD networks. (a) Deseasonalized time series at the major latitudinal sites. (b) Average seasonality of the composite record at each site.

into two components: the deseasonalized data, $C(t) - \Delta_s(m(t))$, and the seasonal cycles $\Delta_s(m(t))$.

The deseasonalized CO composite series stretches from Jan 1981 to Dec. 2003, a twenty-three year time span. Besides the variability and departures from the average seasonality seen in the time series, the most notable feature is the trend, and the change in trend with latitude. The trend for each site was computed over the entire time span (Table 4.3). We find two different behaviors of the CO concentrations at the different sites; large decreases and negative trends for Barrow and Cape Meares, (-1.01 ± 0.14 % y^{-1}, and -0.86 ± 0.17 % y^{-1}, respectively, where the uncertainties relate to 90% confidence intervals), while the more southerly sites show little to no decrease (the trend ranges from -0.07 % y^{-1} to -0.31 % y^{-1}). The trends at the sites reflect

122

predominately changes in local sources and sinks owing to the relatively short lifetime of CO (~ 2 months).

Trends can be produced in the atmospheric record by changing sources and/or sinks, or perhaps a mixture of the two. More information about the nature of the trend can be obtained by looking at the pattern of the seasonal cycle strength over these years. We calculated the cycle strength in the following manner. For each site we selected a three-month window centered on the cycle maximum and a window centered on the cycle minimum. For each year we found the maximum and minimum concentrations that fall within the windows. We defined the cycle strength to be the difference between these two values.
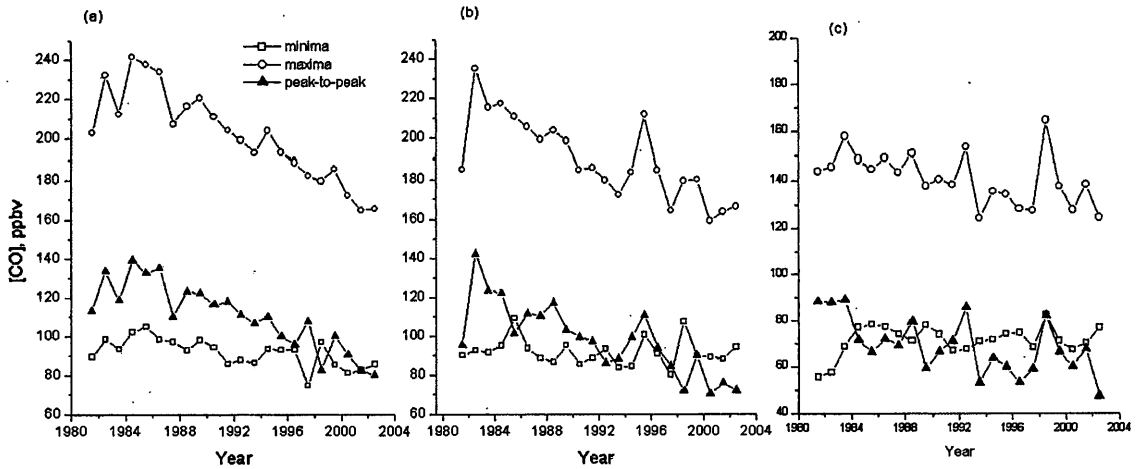
Figure 4.16. Analysis of CO seasonal cycles in the northern hemisphere. As described in the text, minimum and maximum values of the seasonal CO cycle were determined from the composite record. Peak-to-peak values is the difference between the two. (a) Barrow, (b) Cape Meares, (c) Hawaii.

Fig. 4.16 shows the trend of the cycle strengths for the sites in the northern hemisphere. At these sites the cycle strength decreases faster than the decrease in concentration (-2.1, –2.3, and -1.7 % y^{-1} vs. –1.0, -0.86, and –0.14 % y^{-1}, respectively from north to south). Furthermore we see that it is the fall in the cycle maxima that causes

Table 4.3. Trends of the CO composite time series

Location	Deseasonalized % yr^{-1}	Cycle Strength % yr^{-1}	Cycle maxima % yr^{-1}	Cycle minima % yr^{-1}	D trend (maxima – minima) % yr^{-1}
Barrow	-1.01 (0.14)[a]	-2.08	-1.50 (0.32)	-0.79 (0.36)	-0.70 (0.49)
Cape Meares et al.	-0.86 (0.17)	-2.34	-1.29 (0.39)	-0.15 (0.45)	-1.14 (0.60)
Hawaii	-0.14 (0.10)	-1.66	-0.62 (0.39)	-0.38 (0.50)	-1.01 (0.64)
Samoa	-0.07 (0.07)	0.99	0.00 (0.53)	-0.68 (0.75)	0.38 (0.73)
Cape Grim	-0.22 (0.06)	-0.45	-0.59 (0.48)	-0.68 (0.75)	0.10 (0.89)
South Pole	-0.31 (0.15)	-1.68 ()	-0.98 (0.70)	-0.30 (1.14)	-0.68 (1.34)

[a] Values in parenthesis are 90% confidence limits

the strength to decrease with time as the cycle minima remain constant or nearly so. For these three sites the trends in the maxima are negative and are significantly different than the respective trends in the minima at the 90% confidence level (Table 4.3). This is not the case for the three southern hemisphere sites. From this fact we conclude that the reason for the drop in CO concentrations is due to a fall in its sources rather than an increase in its sinks. An increase in CO's sink, i.e. in the concentration of the hydroxyl radical, would not only decrease the cycle's maxima but also its minima. Though a decrease in CO source would decrease the cycle's minima, it would have a greater impact on the cycle's maxima, since the maxima represents an integrated sum of CO emissions over the months when the lifetime of CO is long, namely the winter season, whereas in the summer the concentration of CO is more a reflection of acute emissions due to the short lifetime of CO during these months. Thus the observed decrease in CO

cycle strength must be in response to diminishing CO emissions in the northern

hemisphere.

Table 4.4. Trends of the H_2 composite time series

Location	Deseasonalized % yr^{-1}	Cycle Strength % yr^{-1}	Cycle Maxima % yr^{-1}	Cycle Minima % yr^{-1}	Δ Trend (maxima – minima) % yr^{-1}
Barrow	-0.94 (0.14)	-1.2 (1.4)	-0.34 (0.10)	-0.21 (0.21)	-0.12 (0.24)
Cape Meares et al.	-0.45 (0.12)	-1.4 (1.9)	-0.27 (0.10)	-0.15 (0.19)	-0.11 (0.21)
Hawaii	-0.20 (0.10)	1.3 (2.8)	-0.08 (0.10)	-0.15 (0.13)	0.07 (0.17)
Samoa	0.28 (0.08)	-0.02 (2.9)	0.01 (0.10)	0.01 (0.09)	0.00 (0.14)
Cape Grim	0.37 (0.08)	-0.15 (2.8)	-0.01 (0.10)	0.01 (0.09)	-0.01 (0.14)
South Pole	0.24 (0.08)	-1.5 (1.8)	-0.03 (0.10)	0.04 (0.08)	-0.07 (0.13)

There is somewhat different behavior in the hydrogen composite time series

than observed in the CO data. There are again significant negative trends in the

deseasonalized data in the northern hemisphere, but in the southern hemisphere where

CO was also decreasing, we observe hydrogen to be increasing slightly but statistically

significant (Table 4.4). Whereas the average CO trend in the NH is –0.51 ± 0.07 and –

0.18 ± 0.04 % y^{-1} in the SH, for hydrogen we find the average NH trend is –0.44 ± 0.07

and the average SH trend is 0.30 ± 0.05 % y^{-1}.

In addition, we find different behaviors in the cycles. There is no significant

decrease in hydrogen cycle strength, nor is there any significant difference between the

trends in the minima and maxima in either hemisphere (Table 4.4). Rather we find the

average minima and maxima trends in the NH are both negative and are both positive in

126

the SH, thereby producing a nearly constant cycle strength throughout this period in both hemispheres. Also the average NH maxima trend is significantly different than the SH maxima trend and likewise for the minima trends.

We found above that the observed behavior of CO can be explained by a decrease in its sources. Since the sources of CO and H_2 are similar, it follows that H_2 sources are also decreasing. Though the behavior of H_2 is different than CO, decreasing emissions are consistent with the observed trends considering the lifetime of H_2 is more than ten times greater than the lifetime of CO.

4.4   Modeling

Inverse modeling exploits the mass balance equation to estimate emissions based on the atmospheric record of a gas. For a one-box model, the mass balance equation can be written

$$(\alpha \cdot n)\frac{d\chi}{dt} = S - (\alpha \cdot n)\frac{\chi}{\tau} , \qquad (4.4)$$

where χ is the globally-averaged volume mixing ratio of the gas (e.g nmol mol^{-1}), S is
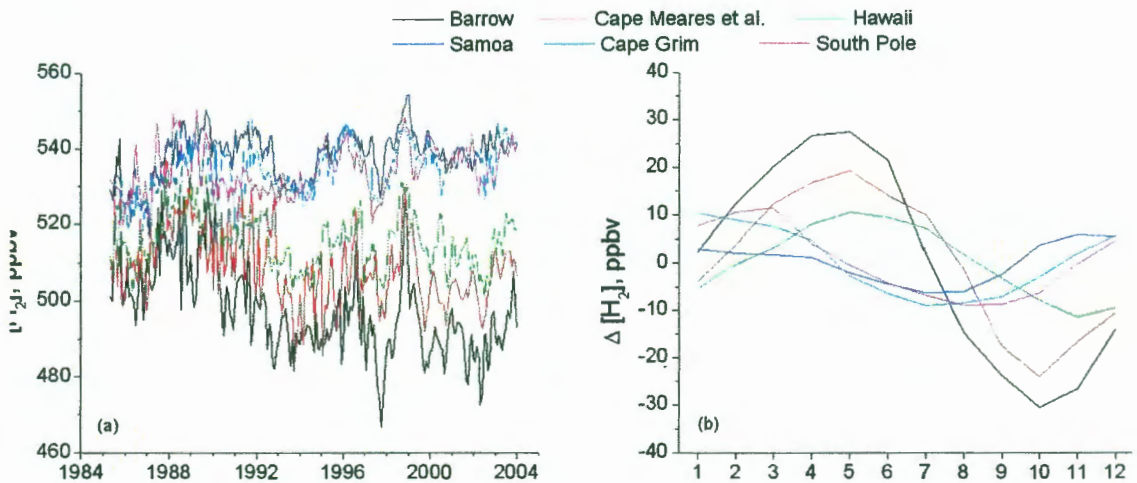
Figure 4.17. Composite time series of H$_2$ using measurements from the OGI and CSIRO networks. (a) Deseasonalized time series at the major latitudinal sites. (b) Average seasonality of the composite record at each site.

the emissions per time interval (e.g mol y^{-1}), τ is the lifetime of the gas, and n is the size of the atmosphere in moles (mol), and α is a conversion factor that translates, in this example, nmol to mol. If the temporal record of χ is known, the equation can be "inverted" for the global emissions S

$$S = (\alpha \cdot n)\left[\frac{d\chi}{dt} + \chi\!\Big/\!\tau\right]. \qquad (4.5)$$

In practice τ will be a function of time since removal processes are rarely spatially or temporally homogeneous. Nonetheless the above equation gives a good first order approximation of global emissions. Here we wish to estimate emissions over specific geographical regions where biomass burning is most prevalent so the one box model approach is not appropriate.

In principle we can apply the above equations to any homogeneous volume of atmosphere, within which the mixing ratio and lifetime are spatially constant. This volume element or "box" is considered well-mixed, which requires that transport times are short enough to overcome small spatial differences in sources and sinks. The major complication that arises when adding spatial resolution to the one-box model of Eq. 4.4 is the transport of the gas into and out of the volume element. This transport can be roughly categorized as either turbulence or advection. Adding transport processes, the one box model above becomes

$$\frac{\partial \chi}{\partial t} = T - \vec{\nabla} \cdot \left(\langle \chi \rangle \langle v \rangle + K \cdot \frac{\partial \chi}{\partial \vec{x}} \right). \qquad (4.6)$$

Here T represents both the sources and sinks of the gas and the second term on the right hand side is the transport processes. Advection is characterized by the mean flow v, thus the first term in the brackets is the flux of the gas across the boundary of the volume element. The second term in the brackets specifies turbulent flow characterized by the eddy diffusivity coefficient K. Since our model has two spatial dimensions K is a two-dimensional matrix. Turbulent transport is then the product of K with the mixing ratio

129

gradient $\partial \chi / \partial \vec{x}$. Mean winds and eddy coefficients were derived from meteorological data (*Butenhoff, 2002*).

By integrating Eq. 4.6 over well-mixed volume elements and using matrix methods Eq. 4.6 can be written as

$$\frac{d\chi}{dt} = \mathbf{S} + \mathbf{\Omega}\chi. \qquad (4.7)$$

Here the bold style denotes a one or two-dimensional matrix and $\mathbf{\Omega}$ is a two-dimensional matrix that contains all the transport and lifetime terms. The solution to Eq. 4.7 is

$$\chi(t) = \chi_o \exp(\mathbf{\Omega}t) + \mathbf{\Omega}^{-1}\mathbf{S}[\exp(\mathbf{\Omega}t) - \mathbf{I}], \qquad (4.8)$$

where I is the identity matrix. The equation can be inverted to find the emissions S,

$$\mathbf{S} = (\exp \mathbf{\Omega}t - \mathbf{I})^{-1}\mathbf{\Omega}\chi^1 - (\exp \mathbf{\Omega}t - I)^{-1}\mathbf{\Omega}(\exp \mathbf{\Omega}t)\chi^0. \qquad (4.9)$$

Here χ^1 and χ^0 are the current and initial mixing ratios, respectively. As written, $\mathbf{S}$ includes sources from all model boxes. For our purposes we are only interested in emissions into the surface model boxes since this is where biomass burning occurs. Both H_2 and CO have non-surface sources due to oxidation processes. Emissions from these sources will not be part of the model inversion, rather we include them into the simulation. To accommodate this, we split Eq. 4.8 into two equations, one equation for surface emissions, and the other for non-surface emissions. To simplify notation we define

$$G = (\exp \Omega t - \mathbf{I})^{-1},$$
$$X = \exp \Omega t,$$
$$S = \text{surface boxes},$$
$$N = \text{non - surface boxes},$$
$$\text{and } T = \text{all boxes}.$$
(4.10)

In the following equations, the subscripts refer to the dimensions of the matrix. We also

drop the bold style for convenience as the subscripts clearly denote matrices. With this

notation the emissions from the surface boxes are found by

$$S_S = G_{ST} \Omega_{TT} \chi_T^1 - G_{ST} \Omega_{TT} X_{TT} \chi_T^0, \tag{4.11}$$

and the emissions from the non-surface boxes are

$$S_N = G_{NT} \Omega_{TS} \chi_S^1 + G_{NT} \Omega_{TN} \chi_N^1 - G_{NT} \Omega_{TT} X_{TT} \chi_T^0. \tag{4.12}$$

Since we do not know χ_N^1 (the current mixing ratios in the non-surface boxes) *a priori*,

but do know the emissions here, we rearrange Eq. 4.12 to solve for χ_N^1:

$$\chi_N^1 = G_{NT} \Omega_{TN}^{-1} (S_N - G_{NT} \Omega_{TS} \chi_S^1 + G_{NT} \Omega_{TT} X_{TT} \chi_T^0). \tag{4.13}$$

All terms on the right hand side are known. S_N is the emissions from oxidation of

methane and other hydrocarbons in the upper troposphere, and χ_S^1 is the surface mixing

ratios of CO and H_2 known from measurements. By calculating χ_N^1 and supplementing

with χ_S^1, we can construct χ_T^1, which then allows us to calculate the surface sources S_S

in Eq. 4.11. Note that the inverted surface emissions will still include the oxidation

products in the lower troposphere. These we remove *a posteriori*. In the next two

sections we discuss the modeling of the removal process of both gases, and emissions of

H_2 and CO from oxidation of hydrocarbons.

4.4.1 Sink processes

Reaction with OH is about 90% of the total CO sink but is responsible for only about 5% of hydrogen's total removal. To model the OH sink, monthly OH fields were taken from *Spivakovsky et al. (2000)* and averaged over the mass balance model latitudinal and altitudinal boundaries The reaction rate coefficient between OH and CO is pressure-dependent and specified as $k_{CO+OH} = 1.5 \times 10^{-13}(1+0.6p[atm])$, *(DeMore et al., 1997)*. We also include the loss of CO and H_2 by stratospheric oxidation using the stratospheric OH fields of *Bruhl et al. (1990)*.

Soil uptake by biological processes is the dominant removal mechanism for hydrogen, representing some 90-95% of its total sink *(Warneck, 2000)*. Soil uptake is less important for carbon monoxide, but still accounts for about 5-17% of its total sink *(Conrad and Seiler, 1985)*. The removal of atmospheric CO and H_2 by soils is due to the oxidation of these gases by soil bacteria (CO) and extra-cellular enzymes (H_2) *(Yonemura et al., 2000)*. Field studies indicate that deposition rates vary little with temperature (R^2=0.171, 0.150, 0.05, from a field study in Japan; *Yonemura et al, 2000*), but fluctuate strongly with soil moisture, being lower in moist soil conditions *(Yonemura et al., 1999, Yonemura et al., 2000; Conrad and Seiler, 1985)*. *Yonemura et al. (2000)* reported R^2 values of 0.861 (CO) and 0.676 (H_2) between deposition velocities and soil moisture over a limited range of soil moisture levels (soil moisture content, ratio in volume, =0.2 to 0.4). This observation is likely a result of a reduction in the exchange of air between the atmosphere and soil when soil pores are clogged with water *(Conrad and Seiler, 1985)*. Soil moisture levels may also affect rates of microbial

activity (*Shuler and Conrad, 1991*). *Conrad and Seiler (1985)* estimated global deposition values of 7×10^{-4} m s^{-1} for H_2 and 3×10^{-4} m s^{-1} for CO.

There is little information about the seasonal or regional patterns of either H_2 or CO deposition. Previous studies have used net primary production (NPP) as a proxy to allocate deposition velocities spatially (*Hauglustaine and Ehhalt, 2002; Müller and Brasseur, 1995*). Though primary production is influenced by soil moisture, it also depends on sunlight, nutrient level, and temperature, variables that are not expected to influence deposition.

Instead of NPP, we used soil moisture to model the variability of deposition. We used 0.5×0.5° maps of soil moisture from the University of Delaware Climate Resource Center (data downloaded from http://gcmd.nasa.gov/records/GCMD_UDEL_CSD.html) Soil moisture is quantified as an index between −1 (dry) and 1 (saturated) on a monthly cycle from 1950 to 1999. For simulation years outside this range, we used a mean seasonal climatology.

We transformed the soil moisture indices (SMI) to deposition velocities (*V*) using a logistics equation of the form

$$V = \frac{AV_o}{BV + (A - BV_o \exp(-A \cdot SMI)}, \qquad (4.14)$$

where A and B are constants and related by $B=A/V_{max}$, and V_{max} and V_o are the maximum and minimum deposition velocities, respectively. The use of the logistics equation ensures that the deposition velocity stays within a specified range which was determined from the literature, and that the relationship between soil moisture and

deposition is nearly linear over much of the range of soil moisture which is consistent with the field studies of *Yonemura et al. (2000)*. $V_{max}^{.} = 0.14$ and 0.07 cm s^{-1} respectively for H_2 and CO, and $V_o = 0.01$ and 0.05 cm s^{-1} respectively for CO (*Conrad and Seiler, 1985; Yonemura et al., 2000*). The constant A was adjusted until the global median was equal to 0.07 cm s^{-1} for H_2, which was reported by *Conrad and Seiler (1985)*. The same value of A (2.2) was used to compute the CO deposition velocities. The mean seasonal cycle of H_2 deposition velocities based on soil moisture only are plotted in Fig. 4.18 for each model region. Deposition velocities are highest during the summer months of the northern polar and mid-latitudes.
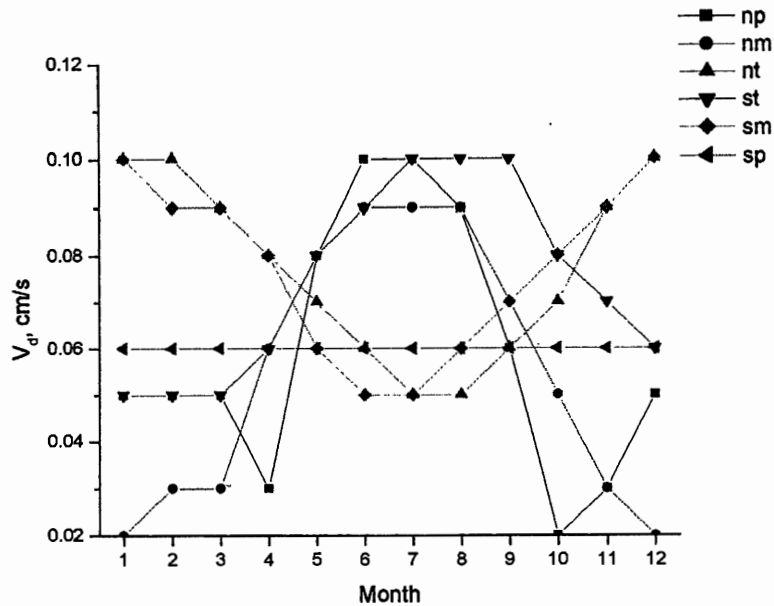
Figure 4.18. Average seasonality of H_2 soil deposition velocities for the six latitudinal regions of our simulation. n=north, s=south, p=polar, m=mid-latitudes, t=tropics. Month 1=Jan, 12=Dec.

Past work has found that deposition velocities go to zero when soils freeze (*Bergamaschi et al., 2000*) and when the temperature exceeds 40°C, which is too high to support relevant microbial activity (*Liebl and Seiler, 1976*). Globally gridded 1×1° maps of monthly average surface temperatures were used to filter out dates and pixels meeting these conditions. Non-soil land types such as permanent wetlands, snow and ice, and water bodies were removed from area estimates using the 1×1° MODIS Land Cover Product which includes 17 different land cover categories (*Strahler et al., 1999*). We also excluded deserts and barren lands as soil moisture needs to be at least 5-10% for deposition to occur (*Conrad and Seiler, 1985*). From the filtered data set, a time series of frost-free land areas was derived for use in calculating soil uptake over the

model regions. We assumed the areas of the land cover types were not seasonally dependent.

4.4.2 Oxidation of methane

Methane and non-methane hydrocarbons (NMHCs) react with atmospheric OH and produce a number of oxidation products, including both CO and H_2. Oxidation occurs throughout the atmosphere meaning some CO and H_2 will be produced in both the lower and upper tropospheric layers of our model atmosphere. Before inverting the CO and H_2 records, we need to include these emissions of CO and H_2 from oxidation into the model, otherwise simulated surface fluxes would be forced in error to account for this atmospheric production. According to the above notation, emissions of CO and H_2 in non-surface boxes are labeled S_N.

The first stable product from the CH_4+OH reaction is formaldehyde (CH_2O). The photodissociation of CH_2O has two branches, one that produces both CO and H_2 directly,

$$CH_2O + hv \rightarrow H_2 + CO, \qquad (R1a)$$

and a second branch that produces HCO by

$$CH_2O + hv \rightarrow HCO + H, \qquad (R1b)$$
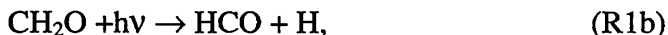
which is then oxidized to CO:

$$HCO + O_2 \, OH \rightarrow HO_2 + CO. \qquad (R2)$$

The oxidation of formaldehyde by OH also leads to CO through the intermediary product of HCO

$$CH_2O + OH \rightarrow HCO + H_2O. \qquad (R3)$$

136
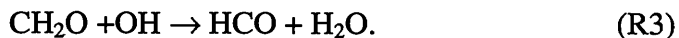
The fraction of CH_2O that is oxidized decreases with altitude due to decreasing OH levels. *Warneck (2000)* estimated that about 40% of the CH_2O produced from CH_4+OH reaction is oxidized. Of the fraction that is photolyzed, branch 1a occurs about 68% of the time.
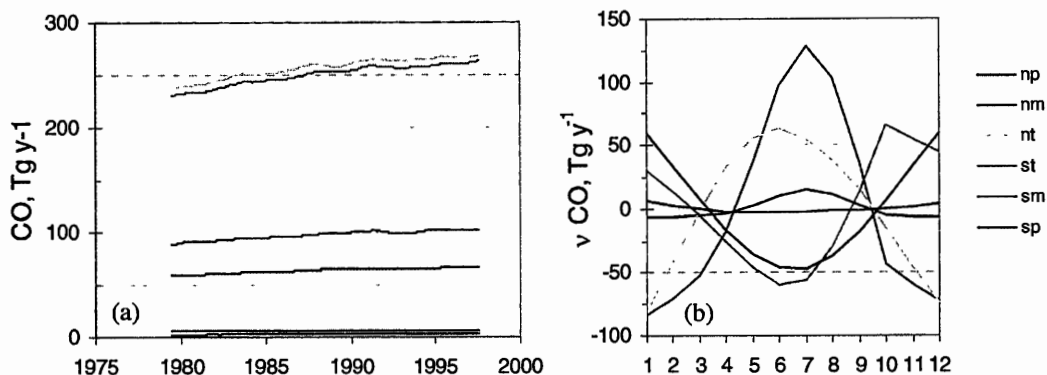
Figure 4.19. CO production from CH_4 oxidation. (a) 12-mo moving avg. of CO production from CH_4 oxidation. (b) Seasonal cycle of CO production averaged over time series. n=north, s=south, p=polar, m=mid-latitude, t=tropics.

Formaldehyde is water soluble and can be scavenged by rain before conversion to CO. From inverse modeling studies, *Bergamaschi et al. (2000)* estimated an average CO yield of 86% from methane oxidation, and we adopted that figure here. We calculated a time series of CO production from the CH_4+OH reaction using the composite OGI-NOAA methane record and the monthly OH fields from *Spivakovsky et al. (2000)* For the upper troposphere where no systematic measurements exist, we scaled surface concentrations by 0.9 to account for the slight vertical gradient. Over the

137

entire time interval (1981 – 2004), the average loss rate of CH_4 due to OH oxidation was 473 Tg y^{-1}.

This compares well with the range of global loss rate cited in the 2007 IPCC report (425-511 Tg y^{-1}) (*Denman et al. 2007*). We computed CO production by scaling these emissions by the 0.86 factor above and multiplying by the ratio of molecular weights (28.01 g mol^{-1}/16.0 g mol^{-1}). We found on average annual CO production from CH_4+OH oxidation was 826 Tg y^{-1}. This is quite close to the value of 830 Tg y^{-1} estimated by *Bergamaschi et al. (2000)*. The CO production for all surface model regions is plotted in Fig. 4.19 along with the average seasonal cycle. Consistent with the atmospheric methane trend, the CO produced from the CH_4 oxidation has been nearly constant in past years. We estimated that 75% of the total CO production occurs in the tropics, and only 1% in the polar regions.

The H_2 production was found by

$$S_{H_2}(t) = 0.68 \cdot 0.60 \cdot \gamma S_{CH4}(t) \cdot (M_{H_2} / M_{CH_4}), \tag{4.15}$$

where γ is the fraction of CH_2O not removed by scavenging, 0.6 is the fraction of CH_2O photolyzed, 0.68 is the quantum yield of branch a, and $S_{CH4}(t)$ is the time series of CH_4 oxidized as calculated above. From this we calculated an average production of 25.4 Tg y^{-1}. This is comparable to the estimate of *Warneck (2000)* of 20 Tg y^{-1}.

4.4.3 Inversion

Due to latitudinal gradients, H_2 and CO levels are not constant through the volume elements represented by boxes in our model. To account for the small mixing

ratio gradients we integrated the latitudinal profile $\chi(\theta)$ over the latitudes (θ) of each

model box i,

$$\overline{\chi}_i = \frac{\int_{\theta_1}^{\theta_2} \chi(\theta) d\theta}{\int_{\theta_1}^{\theta_2} d\theta}. \qquad (4.15)$$

In practice we do not know the mixing ratios at the boundaries of each model box (i.e.

θ_1 and θ_2). Instead we interpolate values using the mixing ratios at neighboring sites. In

this manner the modified mixing ratio $\overline{\chi}_i$ reflects the true abundance of the gas in each

model box. This adjustment has the greatest impact in the tropics boxes where the

interhemispherical gradient lowers the effective mixing ratio in the north and increases

it in the south. In the vertical direction, observations indicate that the mixing ratios of

CO and H_2 remain nearly constant in clean air where there are few surface sources

(*Emmons et al., 2004*; GTE aircraft,). The vertical profile is maintained by production

of both gases at altitude by oxidation processes.

The mathematics of our mass-balance transport model allowed us to invert the

time series of atmospheric concentrations directly without recourse to an optimization

scheme. To do so, we needed to describe the state of the atmosphere with regards to the

CO and H_2 mixing ratios at the date of initialization. We did this using an a priori set of

emissions that are optimized so that model-simulated mixing ratios are consistent with

the observed mixing ratios at the beginning of our time interval in the surface boxes. If

we run this simulation for a number of years, mixing ratios in the upper troposphere and

stratosphere come into steady state with the mixing ratios in the lower box. This steady-

state field of mixing ratios was then used to initialize consequent model runs.

The output of the model inversions was monthly surface emissions of CO and H_2 distributed by latitude. Our focus here was primarily on the tropical boxes spanning the region from 30S to 30N. The reason for this was twofold. About 90% of global biomass burning occurs in the tropics dominated by savanna, grassland, and biofuel burning. And secondly, biomass burning is the dominant surface source of CO and H_2 in the tropics. Thus the record of CO and H_2 emissions that we inverted from the atmospheric record should largely reflect the variability and trend of biomass burning.

4.5   Source deconvolution

The deconvoluted CO and H_2 emissions are presented in Fig. 4.20. A comparison of CO and H_2 emissions is shown in Fig. 4.21 for the ST region. They include all emissions in the lower tropospheric boxes. This includes not only surface fluxes but in
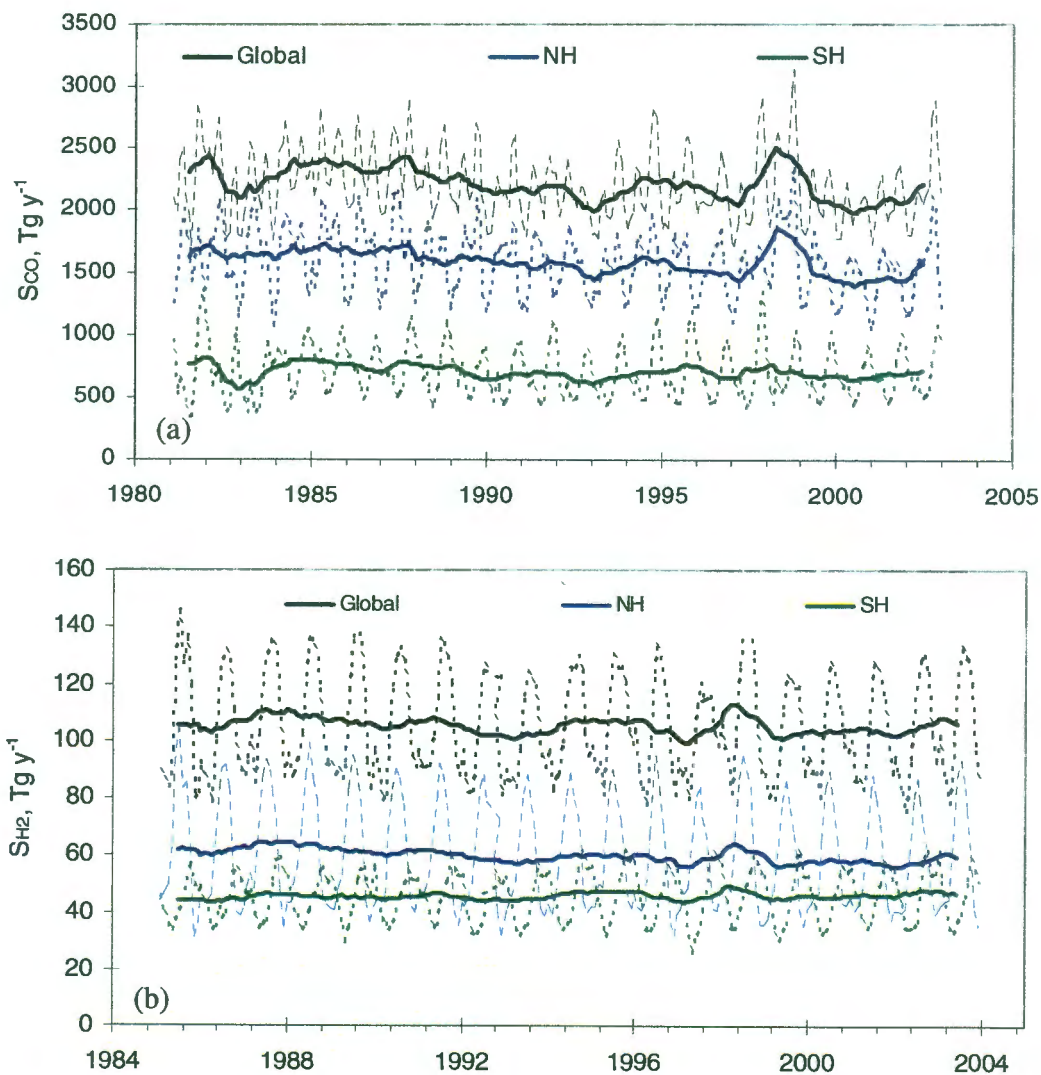
Figure 4.20. Simulated (a) CO and (b) H_2 emissions based on our inversion. The solid lines are 12-month moving averages of the average monthly source strengths (dashed lines). Emissions are shown for global (black), northern hemisphere (blue), and southern hemisphere (black) totals. Data shown include all sources of emissions except for production in the upper troposphere from CH_4 oxidation.
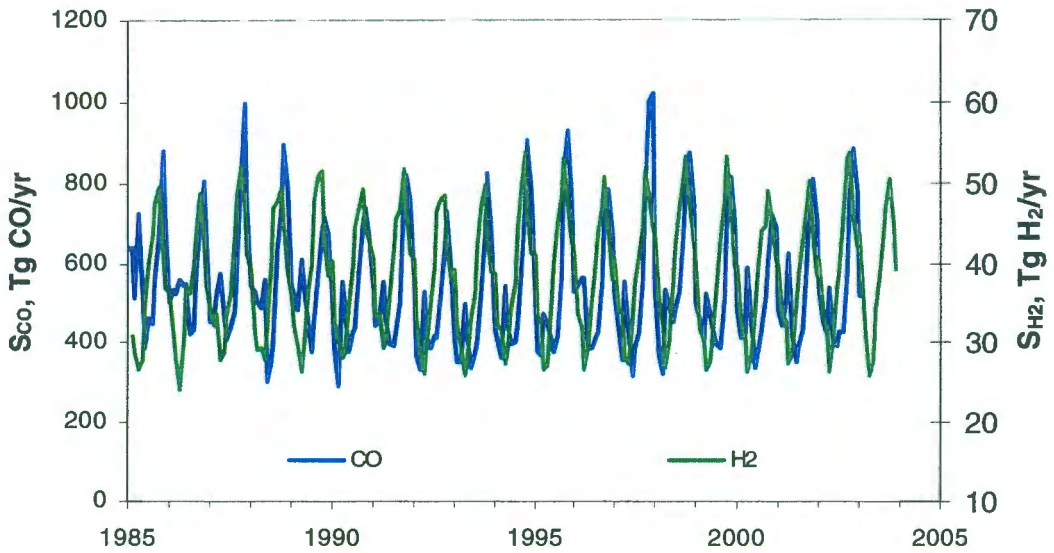
Figure 4.21. Simulated emissions from inversion for the south tropical (ST) region.

situ production of CO and H_2 from the oxidation of both CH_4 and NMHCs in the lower troposphere. Production in the upper troposphere is not part of the total.

We estimated the total CO source strength is 2210 Tg y^{-1}. If we included the CO from the CH_4+OH reaction in the upper troposphere, this increased to 2340 Tg y^{-1}. This is within the range of recent estimates if not on the low end (*Khalil and Rasmussen, 1990; Pacyna and Graedel, 1995; Hauglustaine et al. 1998; Bergamaschi et al., 2000*). The inverted records also indicate the predominance of northern hemisphere (NH) emissions to the global total. We estimate that CO production in the NH is 2.3 times higher than in the southern hemisphere. This is primarily due to the burning of fossils fuels in the transportation and industrial sectors.

There is an evident downward trend to the global CO source strength that begins in 1988 and continues to the end of record. Though there is a small trend in the SH emissions from 1988 to 1993, the emissions past this point remain nearly constant. The global trend is for the most part caused by the behavior of CO in the NH. If we remove the positive anomaly in the NH CO around 1997, the CO trend from 1998 to 2003 is $-0.7 \% \text{ y}^{-1}$. Over the course of this period, this is a decline of 11% or about 270 Tg CO y^{-1}. The most probable reason for this is the reduction of CO emissions from vehicles. The U.S. Environmental Protection Agency estimates that CO emissions from on-road vehicles (i.e. cars, light and heavy trucks, etc.) have declined by 40% since 1970 (*EPA, 2010*).

The coincidence of the seasonality of CO and H_2 emissions is evident in Fig. 4.21. This is further evidence that CO and H_2 share similar sources. In the ST region, the cyclical nature of emissions is driven primarily by biomass burning and oxidation of hydrocarbons. We expect the contribution from the oxidation cycle to be modest in the tropics, since the production of OH is not as seasonally variable as it is at higher latitudes. We see clear interannual variability of the cycle amplitudes over this twenty year period. Both the H_2 and CO emissions show similar variability. This is evidence that the cycles are being driven by changes in sources and not sinks due to the diverse nature of the major sink processes for the two gases.

We expect emissions from biomass burning to be located primarily in the tropics. Before we analyzed the emissions from the northern and southern tropical regions, we removed other non-biomass burning emissions based on known information. We review

these other sources next, and discuss the methods we used to estimate their contribution to these regions. After we remove this contribution, the emissions left behind should be dominated by the biomass burning source. This is the record we will analyze to assess the interannual variability of biomass burning. Our discussion here will focus primarily on the south tropical region, but the methods applied here are similar to those we used to remove the non-biomass burning emissions from the northern tropical region.

4.5.1   Sources of CO and H_2 in the tropics

4.5.1.1   Direct natural sources

Oceans and land-based vegetation are the only natural sources that directly emit CO. Natural wildfires would also be included, but here we treat natural and anthropogenic fire emissions as a single group as it is impossible to distinguish them in our treatment. The total emissions from these two sources fall within the range 40-100 Tg y^{-1} and 75-130 Tg y^{-1} (*Logan et al., 1981; Seiler and Conrad, 1987; Khalil and Rasmussen, 1990; Pacyna and Graedel, 1995*) respectively with likely values near 50 Tg y^{-1} and 75 Tg y^{-1}. The oceans are supersaturated in CO with respect to the atmosphere with production thought to be from photoactive organic compounds in the seawater (*Warneck 2000*). As the supersaturation is reported to be independent of latitude (*Lamontagne, 1974; Seiler 1974; Seiler and Schmidt, 1974; Conrad et al., 1982*), we apportioned the global ocean emissions into model boxes based on ocean area fractions. This put ocean emissions of CO from 0-30°S at 14 Tg y^{-1}.

The mechanisms for CO production and emission in land-based vegetation are unclear but have been observed for numerous plant species (*Seiler et al., 1978; Bauer et*
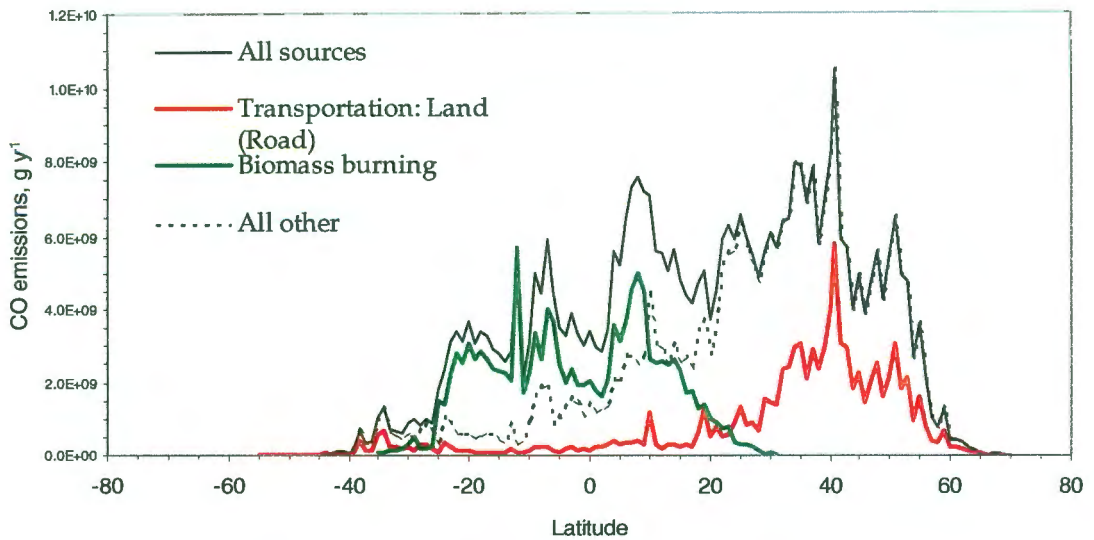
Figure 4.22. CO emissions from anthropogenic sources. Data are from the GEIA inventory *(Olivier et al., 1999)*.

al., 1979, Guenther et al., 2000). Proposed mechanisms include degradation of chlorophyll *(Troxler and Dokos, 1973)* and photooxidation of plant cellular material *(Bauer et al., 1979)*. Without specific information on plant type or regions we spatially apportioned the emissions based on vegetation land cover. Doing so, we estimated the vegetation CO source in the ST box to be 21 Tg y^{-1}.

Direct natural sources of H_2 are limited to the oceans and biological nitrogen fixation *(Seiler and Conrad, 1987; Novelli et al., 1999; Warneck, 2000)*. There likely is some small negligible emission from volcanoes as well *(Warneck, 2000)*. H_2 emission from oceans and nitrogen fixation is each about 3-5 Tg y^{-1}. Like CO, the oceans are supersaturated in H_2. Lacking any specific latitudinal distribution of oceanic H_2 emissions, we calculated ocean emissions in the southern tropical (ST) region based on

145

ocean area. This produced 1.1 Tg y^{-1} in the ST region. H_2 emission from biological fixation is assumed to follow vegetation distributions. We used vegetation land cover map to distribute this small source.

None of these direct natural sources contributes significantly to the total source and most likely can be safely ignored. Since the precise mechanisms for these natural sources are not well known, it is difficult to comment on trends in these sources over the past twenty years. The deforestation and desertification of the ST region may produce a negative trend in the vegetation source.

4.5.1.2 Direct anthropogenic sources

CO and H_2 are directly emitted from biomass burning, industry, and the transportation sector, among others. A GEIA (Global Emissions Inventory Activity) inventory of gridded CO emissions provides the latitudinal distribution of these sources *(Olivier et al., 1999)* which allowed us to assess the importance of these sources in the ST region (Fig. 4.22). Overwhelmingly biomass burning is the largest direct anthropogenic source of CO (and H_2) in this region, contributing 67 out 94 Tg CO y^{-1} or 72% of the total anthropogenic emissions. We distributed the remainder of the emissions over the year, as there is no evidence for any seasonality, and subtract these emissions from the inverted ST emission record, assuming there is no trend to emissions. Since these emissions are small relative to biomass burning, any real trend would likely have little influence on the total emissions in this region.

About 30-45% of all H_2 emissions are emitted directly from anthropogenic sources *(Seiler and Conrad, 1987; Novelli et al., 1999)*. Studies indicate that the H_2/CO volume

ratio resulting from anthropogenic emissions is close to unity. This permits us to use the GEIA gridded inventory of anthropogenic CO sources as a proxy for hydrogen emissions as no such inventory exists for hydrogen. Of the total direct CO anthropogenic emissions (not including biomass burning), about 9% are emitted in the ST region. *Warneck (2000)* reports 20 Tg y^{-1} of total hydrogen emissions from non-biomass burning anthropogenic sources. Assuming a similar distribution of hydrogen as CO, about 2 Tg of H_2 are emitted per year in the ST,

4.5.1.3 Oxidation of natural NMHCs

We discussed the production of CO and H_2 from CH_4 oxidation above. Here we focus on the production of these gases from non-methane hydrocarbons (NMHCs). Natural NMHCs come primarily from biogenic processes in vegetation foliage. Isoprene and terpenes are the main hydrocarbons emitted from vegetation. The former is emitted primarily by deciduous vegetation, while the major source for the latter is conifers. Field studies reveal that isoprene emissions are related to photosynthesis (*Warneck, 2000*) and net primary production has been used as a proxy for isoprene emissions. Estimates of global isoprene emissions range widely, from 175 to 500 Tg y^{-1} (*Muller et al., 1992; Guenther et al., 1995*). *Guenther et al. (1995)* modeled natural volatile organic compound emissions from vegetation based on such ecological factors as plant foliage biomass, light intensities, and temperature. Emissions of isoprene and monoterpenes were gridded on a 1×1° map on a monthly basis. Global isoprene and terpene emissions were estimated to be 502 and 127 Tg C y^{-1}, but emission estimates

may be in error by a factor of 3 (*Guenther et al., 1995*). These source strengths are about twice those estimated by *Mueller et al. (1992).*

Terpenes and isoprenes are rapidly oxidized within a few hours of production (*Bergamaschi et al, 2000*) by OH and ozone which initiates an oxidation pathway that converts a fraction of the original gas to H_2 and CO. The yield of CO from isoprene has been estimated at 0.2 to 0.8 (*Crutzen et al., 1985; Jacob and Wofsy, 1990; Kanakidou and Crtuzen, 1999*). *Myoshi et al. (1994)* found that CO yields under NO_x–rich conditions was 74%, but only 35% when NO_x levels were low. Since NO_x levels are higher over land masses where isoprenes are emitted, we used a yield of 0.74 for our calculations. Using the isoprene distribution of *Guenther et al. (1995)* we estimated global CO production from isoprene oxidation at 865 Tg C y^{-1}. Of this, about 427 Tg y^{-1} is produced in the south tropics and 324 Tg y^{-1} in the north tropics. The yield factor from terpenes is thought to be smaller since some fraction of terpenes is converted to aerosols after oxidation. Based on experiments by *Hanst et al. (1980), Warneck (2000)* estimates that 20% of carbon in terpenes is converted to CO and we adopt that figure here. From this, we calculated that 59 Tg y^{-1} of CO is produced from terpenes, and 78% of this is emitted in the tropics. Together we estimated CO emissions from the oxidation of natural NMHCs to be 924 Tg y^{-1}.

Like CO, not all oxidation processes lead to the production of H_2. Formaldehyde is a necessary intermediary compound for the production H_2. The oxidation of terpenes produces little formaldehyde . *Novelli et al. (1999)* estimate total H_2 production from terpenes at 0.2-5 Tg/yr. This is a negligible amount and we can safely ignore it. For
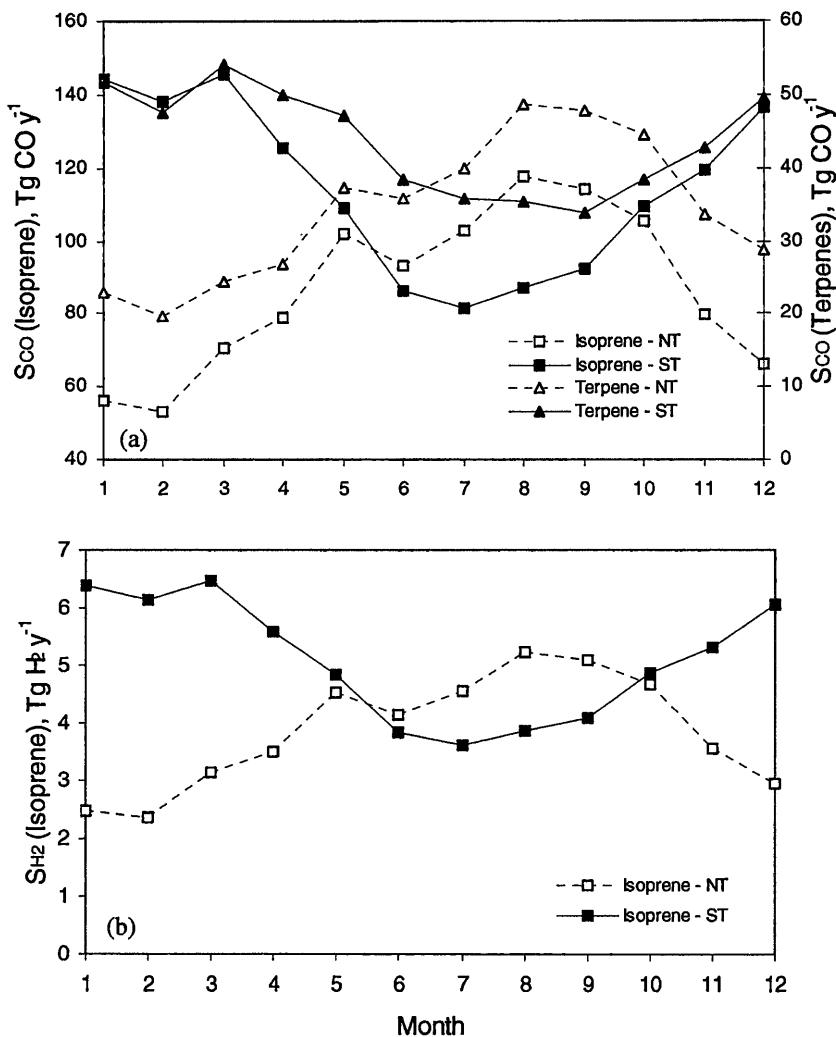
Figure 4.23. Emissions of (a) CO and (b) H_2 from the oxidation of terpenes and isoprene. The seasonal cycles are based on the inventory of *Guenther et al. (1995).*

every carbon molecule in isoprene, between one and three formaldehyde molecules are produced. The exact number depends on NO_x concentrations. *Novelli et al. (1999)* estimate total H_2 production from isoprene to be 2-7 Tg y^{-1}. This is significantly different from the 18 Tg y^{-1} estimated by *Warneck (2000)*. We took the former estimate as more reliable as it accounts for the sensitivity of formaldehyde to NO_x. As isoprene emissions are highest in the ST region, we took 5 Tg y^{-1} to be a reasonable estimate for H_2 production here. *Novelli et al. (1999)* estimated H_2 production from the other biogenic NMHCs at 0.4-12 Tg y^{-1}. With no further information about its distribution, we partitioned this amount based on vegetation distribution and arrived at 2 Tg y^{-1} in the ST region. The total of all these sources is then about 7 Tg y^{-1} from oxidation of natural NHMCs. Seasonal cycles of CO and H_2 emissions in the tropics are plotted in Fig. 4.23. In the north tropics emissions from both isoprene and terpenes peak in NH late summer/early fall, which is about 6 months out of phase with emissions in the SH. This pattern reflects the seasonality of the wet season in each hemisphere. Importantly as we discuss below, these emissions are out of phase with emissions from biomass burning peak during the dry season. This means that uncertainties in our estimates of isoprene and terpene emissions will not fully propagate into our estimates of biomass burning emissions.

4.5.1.4 Oxidation of anthropogenic NMHCs
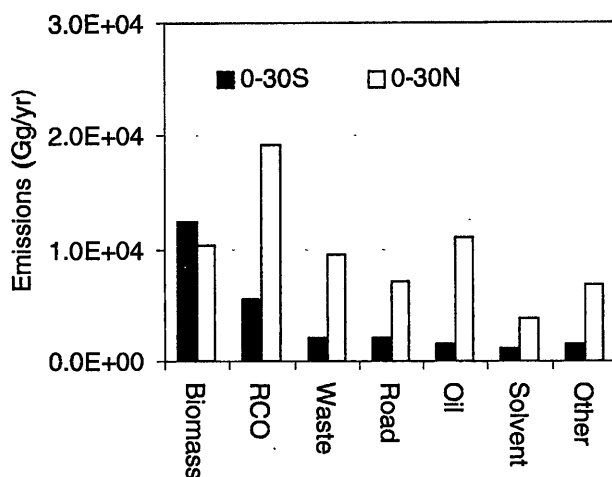
Figure 4.24. Emissions of hydrocarbons from anthropogenic sources. Data come from the EDGAR inventory (*Olivier et al., 1996*).

The indirect anthropogenic sources of CO and H_2 are largely the same as the direct sources, namely technological sources and biomass burning. The former includes hydrocarbon emissions from such sources as automobiles, the dry cleaning industry, and organic solvents, but it is a smaller percentage of the total (48%) than what is estimated for the direct CO sources. Unlike the natural NMHCs, there are no single hydrocarbons that dominate this group (alkenes, alkanes, aromatics, and aldehydes), thus it is difficult to assign a single yield factor. Heterogeneous processes will remove many of the reactive oxidative intermediates (*Novelli et al., 1999*). *Bergamaschi et al. (2000)* assumed that 30% of the carbon in this group is converted into CO. From this, they estimated that 80 Tg CO y^{-1} are emitted. *Novelli et al. (1999)* estimated the H_2 source from this category at less than 2 Tg H_2 y^{-1}. Since the main source of

151
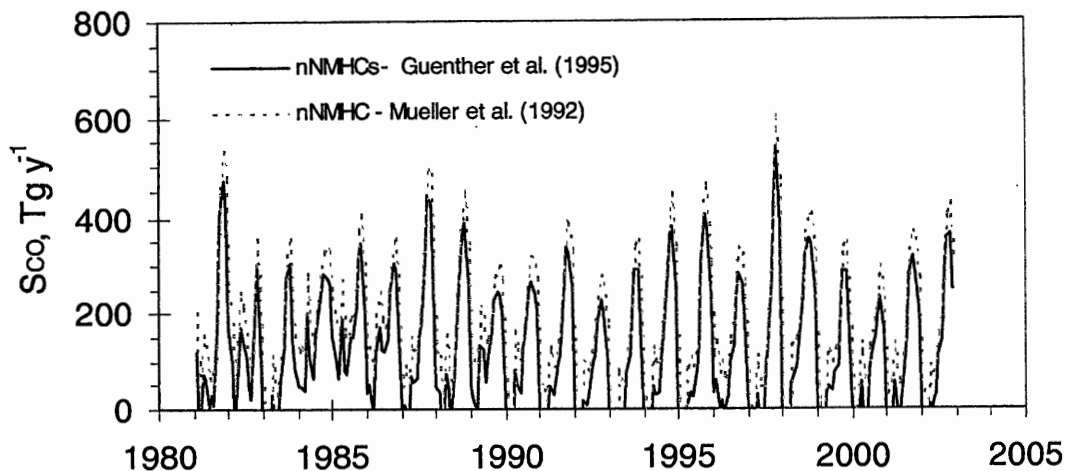
Figure 4.25. Inverted emissions with contributions from the oxidation of natural NMHCs removed. Shown are the adjusted emissions using two different global inventories of isoprene and terpene emissions.

anthropogenic NMHCs in the tropics is biomass burning (*Olivier et al., 1996*) (Fig. 4.24), we argue that emissions from technological hydrocarbons are unimportant; one, because emission is small, and two, there is likely no seasonality to these sources. Any trend would not contribute significantly to the overall CO trend.

4.5.2   Emissions from biomass burning

After correcting for the above sources, the inverted emissions decrease significantly. We show the corrected CO emissions from the ST region in Fig. 4.25. We see that during the first two or three months of each year, the emissions are nearly zero. This is reasonable if we have successfully removed all sources except those from biomass burning and some small technological sources. As we show below, biomass burning happens in the second half of the year in the southern tropics, and so we would

152

expect a peak here, and near-zero emissions before. We also plot emissions based on the *Mueller et al. (1992)* isoprene and terpene inventory. Since the Mueller emissions are lower than those estimated by *Guenther et al. (1995),* the corrected CO emissions are higher. It makes a small difference to the overall record, but importantly it does not affect the amplitudes of the seasonal cycle. The seasonal cycle is what we use below to estimate biomass burning emissions.
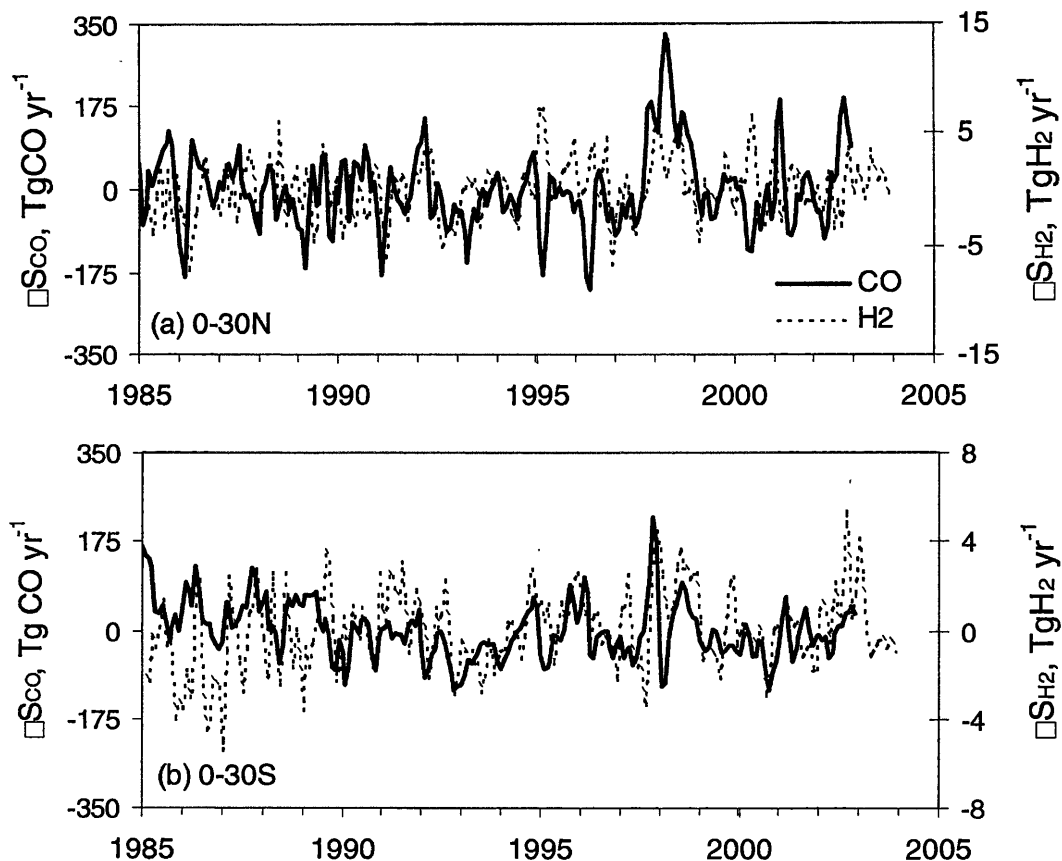
Figure 4.26. Deseasonalized inverted emissions of CO and H_2 in the (a) northern tropics (NT) model region, and the (b) southern tropics (ST) regions. The mean of each deseasonalized record was subtractedand the residuals of this calculation are plotted.

We analyzed the time series of emissions by decomposing the inverted emissions for both gases into a deseasonalized component and the seasonal cycle. Fig. 4.26 shows the deseasonalized records for both gases in the NT and ST regions. The deseasonalized record is derived as follows. From the original emissions data we calculated the 12-month moving average record. We subtracted the moving averages from the original emissions to construct the detrended emissions record. We then averaged the monthly record over the entire time series of the detrended data. This we call the seasonality of

154

the sources. The seasonal cycle is then removed from the original record. In addition, we removed the mean of the deseasonalized record for both gases for ease of comparison. The axis scales are also adjusted to aid comparison. The residuals produced tell us how the amplitude seasonal cycle in any given year compares with the temporal average. For years of strong biomass burning, we would expect to see positive anomalies.

If our inverted tropical emissions are predominately driven by biomass burning, we expect there to be a correlation between the CO and H_2 records In general the pattern of emissions seen in both gases is well matched throughout much of this record. For example, in the ST region from 1990 to 2004, the ups and downs of the deseasonalized data correspond closely between the gases. Both gases have large peaks during the 1997-99 period and fall to a dip in 2001. They then rise again to the end of the record. The pattern of peaks and valleys during the early 1990s is also consistent between H_2 and CO. However before this period, the agreement is less good. From 1985 to 1990, H_2 lies below the CO record. The absolute offset is not a concern since the records could simply be shifted to match during this time. However the trends of H_2 and CO are different during this time, with CO on a downward track while H_2 slightly rise. It is unclear what could physically cause this divergence in behavior and this could be evidence of a calibration problem during this time.
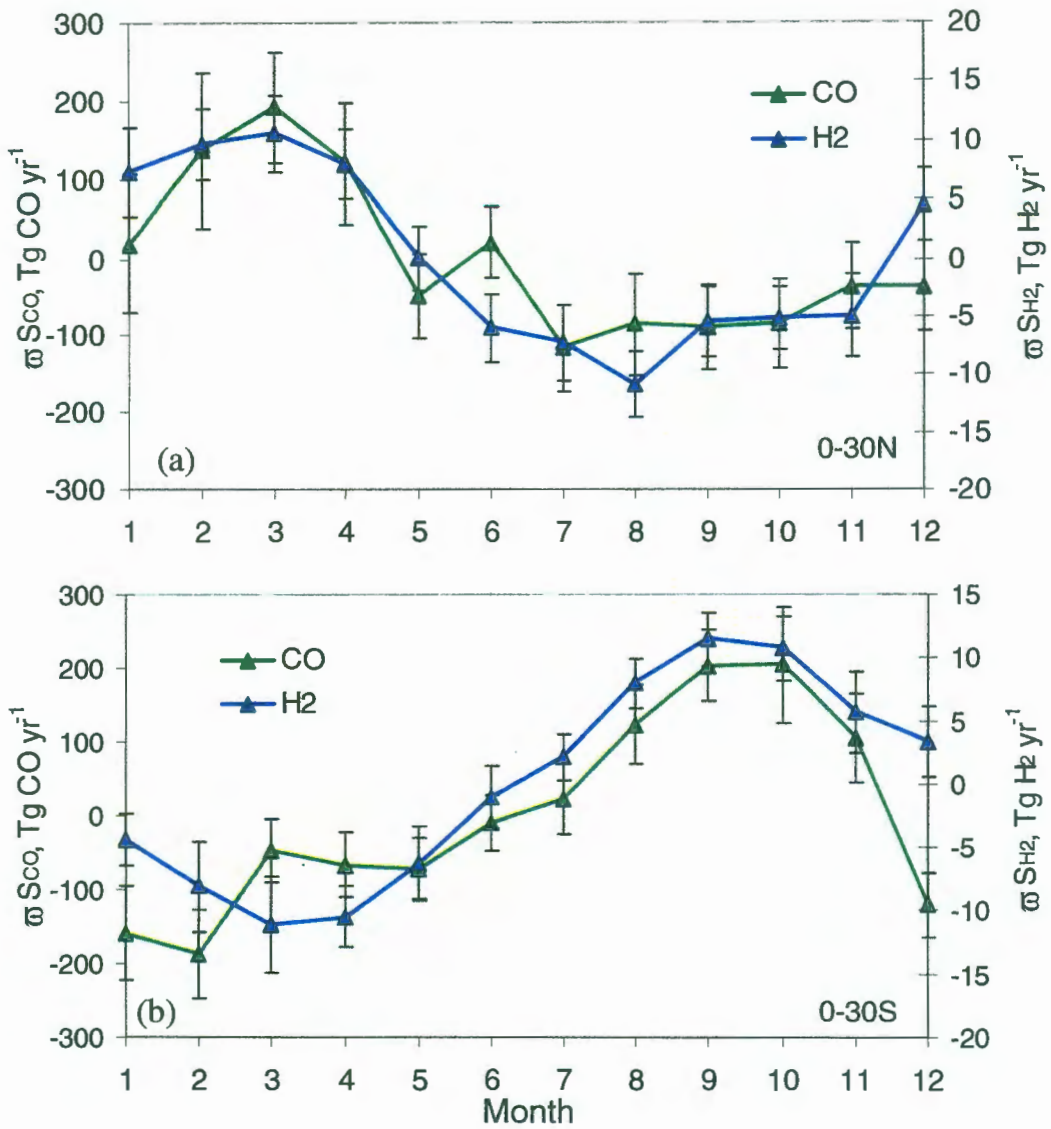
Figure 4.27. Seasonal cycles of inverted CO and H_2 emissions. Cycles are shown for the (a) north and (b) south tropical model regions. Month 1=Jan, 12=Dec.

The large 1997-99 positive anomaly is also present in the NT records of both

gases. As there is little transport across the ITCZ, the occurrence of this feature in both

hemispheres indicates that local burning events were responding to the same pressure.

During this period an unusually strong El Nino event occurred and produced severe droughts across much of the western Pacific, including the countries of Indonesia, Malaysia, Singapore, and Papua New Guinea. Normal biomass burning events to clear fields and crop residues spread rapidly due to dry conditions and set off uncontrolled wildfires in forests, peatlands, and bush areas. An estimated land area of 45,600 km^2 burned (*Levine, 1999*). The peak of the fires is thought to be late 1997/early 1998 which is when we see the positive anomalies. The anomaly is greater in the NH. During NH winter, the ITCZ is located below these island nations so emissions would be largely contained to the NH. We see from this comparison, that emissions of CO and H$_2$ are well correlated. Again, we expect this behavior due to what we know about the nature of their sources. We next use the seasonal pattern of biomass burning to help us understand how the strength of this source has varied during the past two decades.
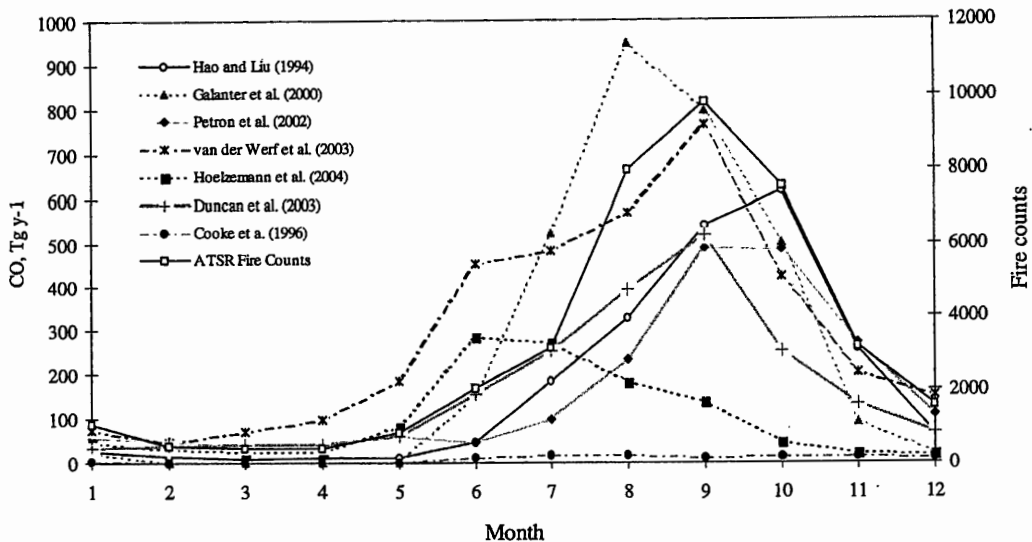
Figure 4.28. The seasonality of CO emissions from biomass burning from various studies. Emissions by *Hoelzemann et al., Duncan et al.*, and the ATSR fire counts are derived from satellite imagery. Month 1=Jan., 12=Dec.

We plot the seasonal cycles of tropical CO and H_2 emission in Fig. 4.27. In the SH emissions of both gases begin to rise in July and reach a peak during September to October. The minima occur during March/April. The NH cycle is anti-correlated with the cycle in the SH. In the NH the peak occurs during early NH spring, around March and April, with a broad minimum extending from August to November. This behavior is seen for both gases. If CO and H_2 are good indicators of biomass burning, the seasonal cycle of emissions should peak at the end of the dry season in each hemisphere when most fires occur, roughly February-March in the northern hemisphere, and September-October in the southern hemisphere. This is consistent with our results.

158

In Fig. 4.28 we show estimates of the seasonal cycle of CO emissions from biomass burning, along with satellite-derived fire counts. A number of methods have been used to estimate the seasonality of biomass burning emissions. Noting that surface ozone (O_3) concentrations peaked during the dry season in the Congo, Angola, and Brazil, which would coincide with the burning season, *Hao and Liu (1994)* used O_3 to distribute annual biomass burning emissions. *Galanter et al. (2000)* used regional cultural information, local climate, and satellite information to derive the timing of CO, NO_x, and O_3 emissions from a range of burning types. *Petron et al. (2002)* optimized the distribution of biomass burning CO emissions to NOAA-GMD CO surface measurements. *van der Werf et al. (2003)* modeled emissions using the Carnegie-Ames-Standford Approach biogeochemical model. In other cases, satellite-derived burn scars (*Hoelzemann et al., 2004*) and fire counts (*Duncan et al., 2003*) were used for this purpose. The peak of emissions from most of these studies occurs in September $\pm$ 1 month. This is in good agreement with our derived cycle and supports our view that our residual inverted source record is largely dominated by biomass burning emissions.

There is less information about biomass burning emissions in the northern tropics. Fig. 4.29 shows seasonality of emissions derived by *Galanter et al. (2000)*. Here, CO emissions peak during Februrary/March then flatten from June through September. This is the same pattern of emissions we saw in the simulated cycle from the model NT region. Again this supports our view that our simulated emissions provide information about biomass burning in the tropics.

159

The only other large source of CO in this region is fossil fuel-use, which shouldn't exhibit strong seasonality (e.g. the EDGAR inventory, *Olivier et al., 1996*). Also, although there is considerable uncertainty to the source strength of CO and H_2 from the oxidation of methane and non-methane hydrocarbons, this source peaks seasonally out of phase with biomass burning, occurring at the end of the wet season (e.g. *Petron et al., 2004*). Thus any errors in our estimate of the oxidation source strength should not affect our conclusions about the variability of biomass burning.

4.5.3 Fire counts

To further validate that our inverted emissions track biomass burning emissions, we compared our emission record with seasonal and interannual variations of fire count data derived from satellite imagery. Fire counts provide a useful proxy for the seasonal variation of biomass burning as they have global coverage and high temporal frequency. Fire counts used here were measured from the Along Track Scanning Radiometer
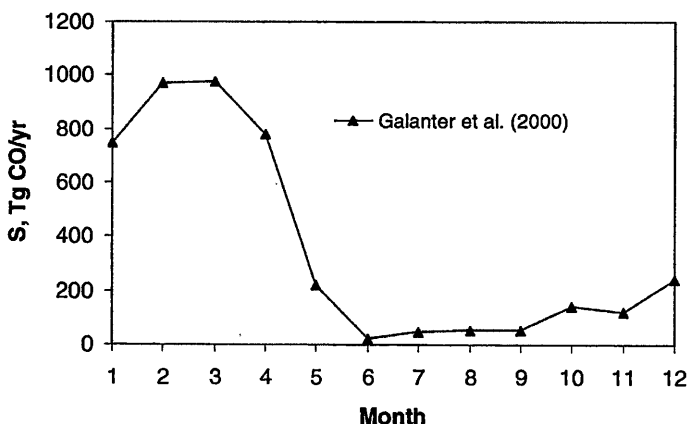
Figure 4.29. Seasonality of CO emissions from biomass burning in the northern tropics (0-30 N). Month 1=Jan, 12=Dec. The cycles shown here are similar to the cycles of our inverted emissions in the NT model region.
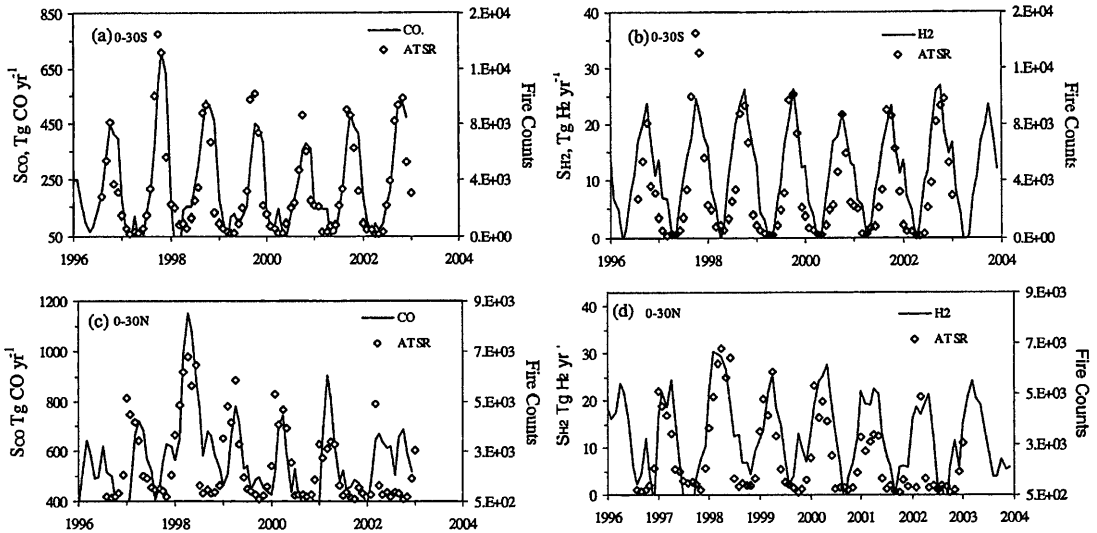
Figure 4.30. Comparison of satellite-derived fire count data with our inverted emissions. CO emissions are shown in (a) and (c), and H_2 is plotted in (b) and (d). The fire count data are derived from the European Space Agency's Along Track Scanning Radiometer aboard the ERS-2 satellite.

(ATSR) aboard the European Remote Sensing-2 satellite (*Arino and Rosaz, 1999*). As we discussed earlier, fire counts were determined from nighttime satellite images using the 3.7 μm channel on the radiometer. A pixel was counted as containing a fire event if the brightness temperature of the pixel exceeded 308 K. Data are available from 1996 to 2004 on a 1×1° grid. We integrated the grid over the latitudes of our tropical model boxes and created a monthly time series of fire counts.

We compare the time series of fire counts against our CO and H_2 emissions in Fig. 4.30 for both the NT and ST model regions. There is excellent agreement in timing in all four plots, with the fire count data peaking on the same month as our emissions for nearly all cycles. There is considerable interannual variability in the peak height of the fire count data during this interval. The CO data track this variability well;

161
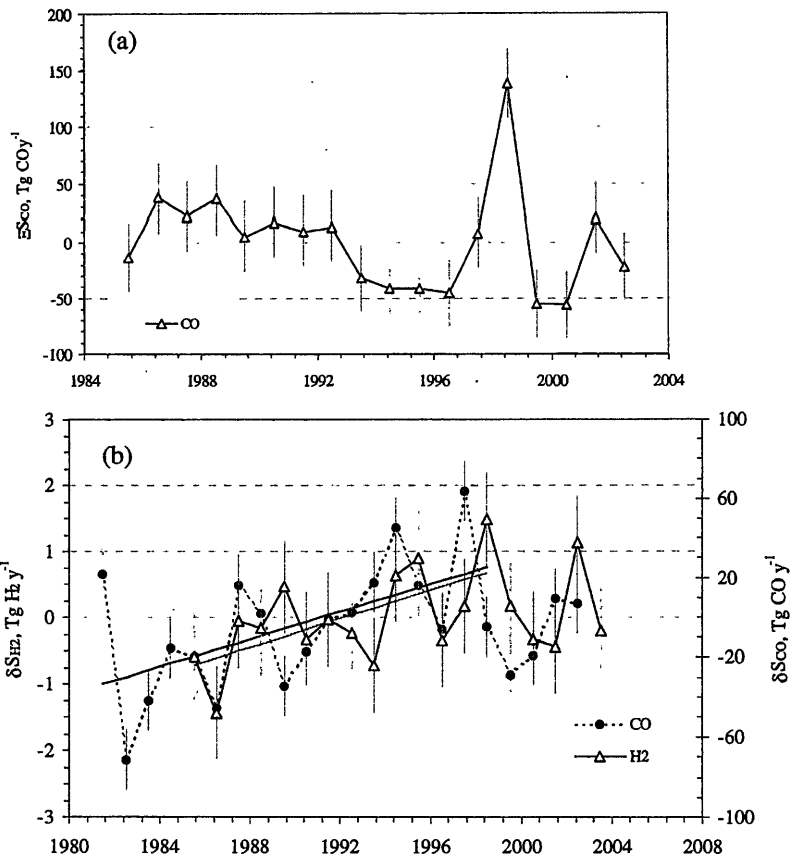
Figure 4.31. Integrated emission peaks of CO in the (a) NT region, and emission peaks of CO and H_2 in the (b) ST region. The solid straight lines in (b) are linear fits to the emissions up to 1998.

especially in the southern tropics where we think our emissions record best reflects biomass burning. We also note that we do not expect one-to-one agreement between fire and emissions peaks. Since fire counts do not provide information regarding fire size or type (e.g. smoldering or flaming), emissions from the same fire count may vary considerably.

Overall there is small variability to the H_2 peaks in the ST region, and a bit more in the NT. The H_2 data do not track the fire count data as well as the CO data. H_2

162

emissions are considerably smaller than CO emissions from biomass burning, as we expect the sensitivity of H_2 to be smaller for fire events. The lack of variability in the H_2 record may also indicate that our H_2 sink, soil deposition, dominates the inversion. This may indicate that our source sink here is too strong. This possibility is supported by the larger global H_2 emissions estimated by the inversion compared to hydrogen budgets form other sources. In the ST, where the soil sink is smaller, we see greater sensitivity of H_2 to fire events, which again is consistent with our interpretation. This comparison increases our confidence that our seasonal peak in emissions captures biomass burning. We conclude that CO serves as an excellent tracer of biomass burning, while the utility of H_2 is limited to the ST region.

4.5.4   Integration of source peaks

The above discussion shows that the fall/spring peaks in the CO and H_2 source record reflects biomass burning. The source strength of a biomass burning season will be the integrated emission over the season. To integrate the cycle we summed emissions above a baseline over the months when the cycle is positive, June to December for the SH, December to June for the NH and for each year. We took this to be an estimate of the biomass burning strength for that year. The time series of integrated peaks is shown in Fig. 4.31. In the ST, biomass burning emissions for both CO and H_2 rise from the beginning of the record to a peak in 1997/98. We estimated that the CO emissions increase by 2.7 % y^{-1}, and the H_2 emissions rise by 1.2% y^{-1}. This suggests that biomass burning emissions have increased by about 20% over this period.

The integrated CO emissions for the NT region are plotted in Fig. 4.31a. A much different behavior is seen here. The exceptional feature is the large peak in 1997/98. These emissions come from the El Nino-related fires mentioned earlier. We estimate that emissions during this event were elevated by 20 Tg CO relative to normal biomass burning seasons. *Levine (1999)* estimated CO emissions from the 1997 Indonesian fires to be between 16 and 49 Tg CO.

We conclude that there is evidence from the H_2 and CO measurement records that biomass burning emissions have increased in the southern tropics, though likely not in the northern tropics. Our conclusion is supported by the unique nature of H_2 and CO, a pair of gases that share sources, but whose primary sink processes are different. This gives us confidence that the errors in our removal processes are not responsible for the simulated positive trend, since it is unlikely errors would be of similar magnitude and in the same direction. Also the fact that CO emissions do not increase in the NT, shows that the positive trend is not due to a systematic problem with our CO modeling, since if it were, we would expect this modeling artifact to produce similar behavior in the NT.

Chapter 5 — Variability Of Methane Flux From Rice Paddies

5.1 Introduction

Rice is grown in paddy fields under a wide variety of climates, soil conditions, and agricultural practices, perhaps more so than any other crop *(Neue and Roger, 2000)*. The aggregate of all paddy variables, both human and natural, is called the paddy treatment. Not only does the paddy treatment vary from field to field, it may also vary from season to season within a given paddy field, as factors such as water and crop residue inputs may change from one rotation to the next. How the paddy field is managed before planting commences also influences yield and greenhouse gas emissions, and therefore also contributes to the paddy treatment. This is often the case in tropical fields where triple-cropping is commonly practiced.

It is well known that methane fluxes vary widely by paddy treatment responding to differences in factors such as inundation, soil organic carbon content, rice cultivar, and temperature *(Khalil and Shearer, 1991; Khalil et al., 1998; Neue and Roger, 2000; Shearer and Khalil, 2000, Wassmann et al., 2000; Yan et al., 2005)*. One recent survey of published field studies reported fluxes that ranged from 0.1 to 56 mg CH_4 m^{-2} hr^{-1} over a number of paddy systems in monsoon Asia *(Yan et al., 2005)*. To account for this variability, researchers typically organize rice-growing regions into treatments and apply canonical fluxes to the harvested areas over which the treatment is practiced

(Matthews et al., 1991; EDGAR, 2008). Alternatively, emissions are estimated using process-level models, which include both physical and biogeochemical processes important to methane production and release, and which compute fluxes directly from factors that characterize a paddy system *(Matthews et al., 2000; van Bodegom et al., 2001; Zhang et al., 2002; Yao et al., 2006)* Though the heterogeneity and complexity of rice agriculture across systems hinders attempts to estimate emissions at large scales, much effort has been spent in understanding it.

Not so for the type of variability we introduce here. Unlike the above variability that is characterized by differences in methane fluxes between paddy systems, little work has been performed trying to characterize and quantify the variability of methane fluxes within a paddy system, that is the intra-system variability.

Intra-system variability results from heterogeneous conditions within a field such as microclimates, uneven distribution of fertilizers, and pooling of water. Fluxes from paddy fields are typically measured using static chambers, which are placed over small areas typically no larger than one square meter *(Wassmann et al., 2000a)*. This area is smaller than the scale of variability so measured fluxes can vary from plot to plot, sometimes substantially. A common practice to sample this spatial variability is to measure methane fluxes from three replicates or plots within a field *(Khalil et al., 2008)*; though in some campaigns six *(Khalil et al., 1998)* or more plots *(Wassmann et al., 2000a)* have been used. The time series of fluxes from all plots are then pooled to estimate the seasonally averaged flux for the paddy treatment under investigation. In many cases the seasonally averaged flux (SAF) is used to estimate national and global

166

emissions inventories; hence, uncertainties in SAFs propagate into our understanding of larger issues such as budgets and emissions mitigation policy.

Though standard statistical tools can be used to evaluate the accuracy of seasonally averaged fluxes retrospectively, to date no statistical modeling of paddy variability exists that could be used to plan field sampling strategies that would ensure the seasonally averaged flux reaches desired levels of accuracy. The statistical modeling developed here can also be used to retrospectively evaluate past studies to discern if the accuracy of the estimated SAF is captured by the reported sample standard deviation, which is the most commonly reported statistic of variability. As we show below, three plots in many cases are not enough to capture the full spatial variability of the field, and consequently the accuracy of the reported SAF will be overestimated.

This study is motivated by over fifteen years measuring methane flux measurements from rice paddies in China (*Khalil and Rasmussen, 1991; Khalil et al., 1998a; Khalil et al., 1998b, Khalil et al., 1998c, Khalil et al., 2008a; Khalil et al, 2008b*). During this time 8853 fluxes were sampled from fields under various conditions. From this data set we have come to realize that intra-field variability can lead to large uncertainties when plot-sized fluxes are extrapolated to larger scales. Having such a large data set of fluxes gives us a unique ability to study this variability and assess its importance on larger scales. To our knowledge this is the only study of its kind to investigate this variability. In particular the questions we explore in this study are:

(1) For a sampling strategy that uses P number of plots and D sampling days, how close will the measured flux be to the true field flux? This perhaps is the main question to be addressed. If a field study includes P plots and D sampling days, how close can the researcher expect the measured seasonally averaged flux be to the true field flux?

(2) Given a standard sampling schedule (e.g. weekly, bi-weekly, and once every two weeks) what is the minimum number of plots required for the measured flux to be within a specified percentage of the true field flux?
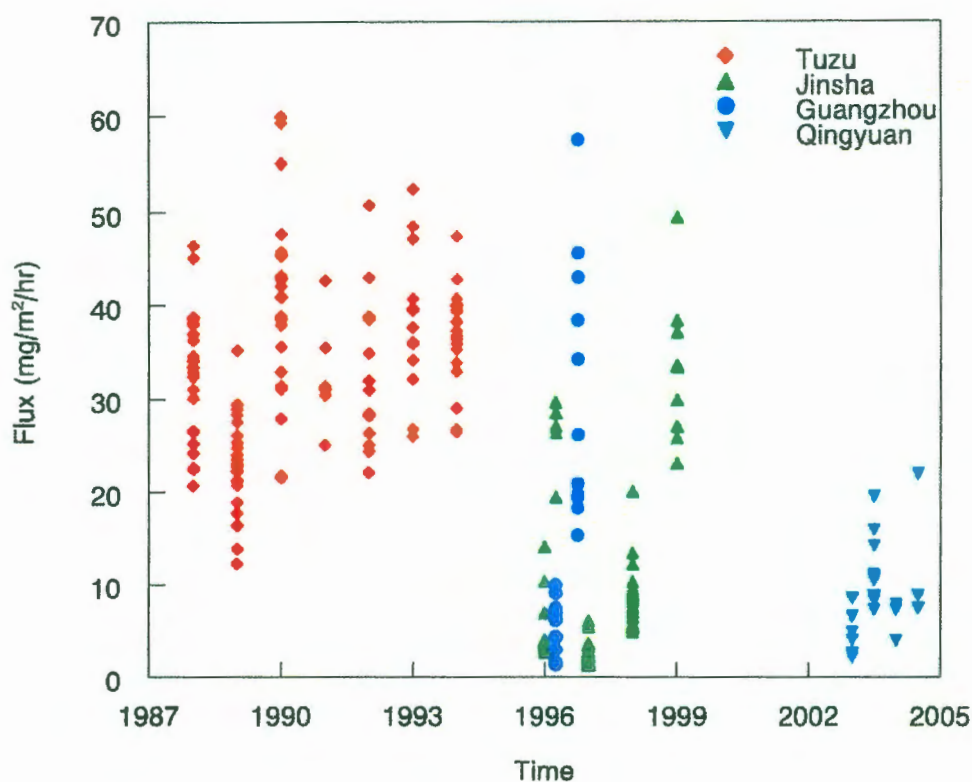
Figure 5.1. Seasonally averaged fluxes from eighteen years of measurements in China. Each grouping is a paddy system that is sampled by anywhere from 3 to 24 plots. The data reveal the spatial variability inherent to paddy systems. From *Khalil and Butenhoff (2008)*

.

(3) What is the minimum number of samples $(P*D)$ required for the measured flux to be within a specified percentage of the true flux ? Here we examine the total number of flux measurements that are required throughout the growing season if we wish to be within a specified percentage of the true field flux.
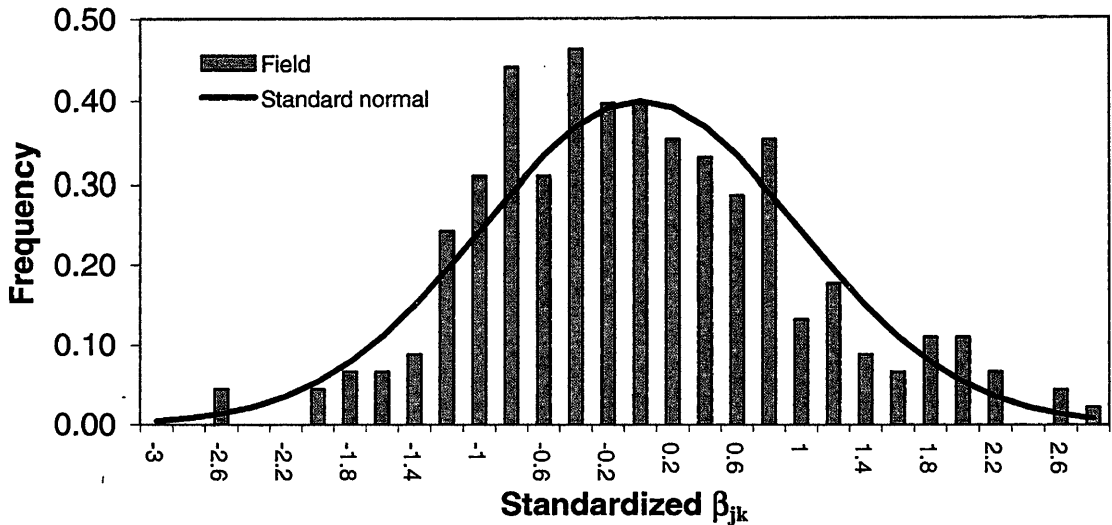
Figure 5.2 The histogram shows the differences between seasonally averaged fluxes from single plots and the mean flux from all plots in the same system. The differences for a given system were normalized according to the mean and standard deviation of plot fluxes within the same system. The figure shows that the distribution of spatial anomalies within paddy systems is near normal.

(4). What are the diminishing returns if the intensity of the sampling strategy is increased? At some point increasing the number of plots or the sampling frequency will no longer significantly increase the accuracy of the experimentally measured SAF. Knowing where this threshold occurs will prevent wasting resources by oversampling the field.

(5). What is the probability that the measured flux will be within 10% of the true field flux if the most practically intensive sampling strategy is adopted? There is a practical limit to the intensity of sampling, perhaps twenty plots sampled every other day. Given this threshold, how likely is it that the measured flux will be within 10% of

the true flux? This is an interesting question as it addresses how well we can realistically know the true flux from a paddy field. This has greater implications when extrapolating to regional and global scales.

Together, the answers to these questions will aid in retroactively evaluating past field studies to better understand the uncertainties of the extrapolations, and the answers will help future researchers design field studies efficiently.

5.2 Empirical functions of spatial and temporal variability

Methane fluxes from rice paddies were measured from 1988 to 2004 at several sites in Sichuan Province and Guangdong Province, China (*Khalil et al., 1998b, Khalil et al., 1998c, Khalil et al., 2008a; Khalil et al, 2008b*). Over this time fluxes from 230 plots in 63 fields were measured for the total of 8853 values The number of plots sampled per field ranged from three to twenty-four, which provides a rich data set to discern the relationship between sampling strategy and variability. In total, fluxes were measured from seventeen unique paddy systems over this period (Fig 5.1).

In addition to the spatial variability discussed above due to the heterogeneity of field factors such as inundation levels and fertilizer concentrations, the measured flux from a single plot also varies in time. This temporal variability has both high and low frequency components. Flux varies slowly through the season due to factors such as changes in solar insolation, plant growth, and onset of senescence. These changes are regular and can be modeled with a smooth function. The high frequency variability has a timescale of hours or days, and presumably is random. The exact cause of the

variability is unknown but is likely driven by factors such as ebullition (bubbling), wind and pressure disturbances, or acute changes in microbial populations and rates.

With this understanding, we can consider the daily flux $F_{jk}(t)$ measured from plot j in paddy system k to be the sum of three distinct components (*Khalil and Butenhoff, 2008*),

$$F_{jk}^{'}(t) = F_k(t) + \beta_{jk}(t) + \Delta_{jk}(t).$$ (5.1)

The first component $F_k(t)$ is the smoothly varying function for paddy system k, i.e. the function which describes how the space-averaged flux from system k would vary throughout the season in the absence of temporal variability. From our data set we find that nearly all growing seasons can be adequately described by one of three canonical functions (*Khalil and Butenhoff, 2008*). The functions describe the rise and fall of flux throughout the season. For a single season, a normal function is used to describe the single hump of the flux time-series (function type I). For a double rice crop, two offset Gaussians are added to create a double-humped function, with the dip corresponding to the beginning fo the second rice crop (function type II). The third canonical function is positively skewed and single humped, which describes the case where flux initially rapidly increases, then gradually declines (function type III).

The second component in Eq. 5.1 captures the plot to plot spatial variability of system k. The smoothly varying function describing the flux from any plot j within system k, $F_{jk}(t)$, is the system function $F_k(t)$ plus a time varying offset $\beta_{jk}(t)$. From the

observational data set described above, it was found that the $\beta_{jk}(t)$'s are normally distributed (see Fig 5.2) with a mean of zero and a standard deviation given by *(Khalil and Butenhoff, 2008):*

$$. \; \sigma = \left(\overline{F_k(t)}\right)^{0.55},$$

(5.2)

,

where the overbar on $F_k(t)$ indicates the seasonal average. This relation, derived from the seasonally averaged fluxes from the 63 plots, indicates that spatial variability increases with flux. Any plot *j* will have an offset from the system SAF drawn from this distribution. Figure 5.3 shows simulated spatial variability in four fields using this relation.

The final component, $\Delta_{jk}(t)$, in Eq. 5.1 represents the high frequency temporal variability of day to day measurements. It is a random offset added to function $F_{jk}(t)$. The distribution of the $\Delta_{jk}(t)$s is determined by the field data above and can be described by the Laplace function with a flux-dependent standard deviation given by *(Khalil and Butenhoff, 2008)*
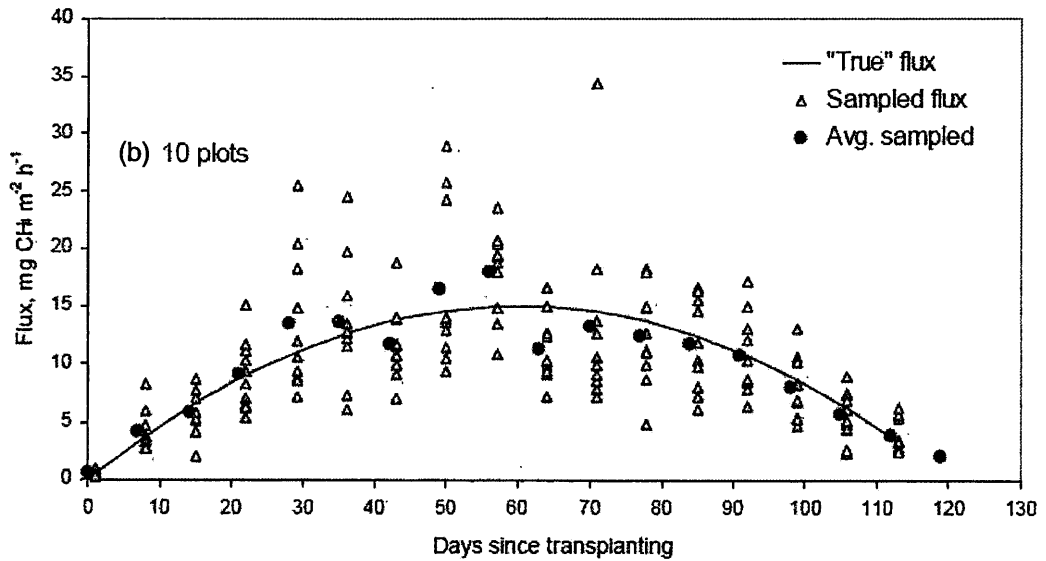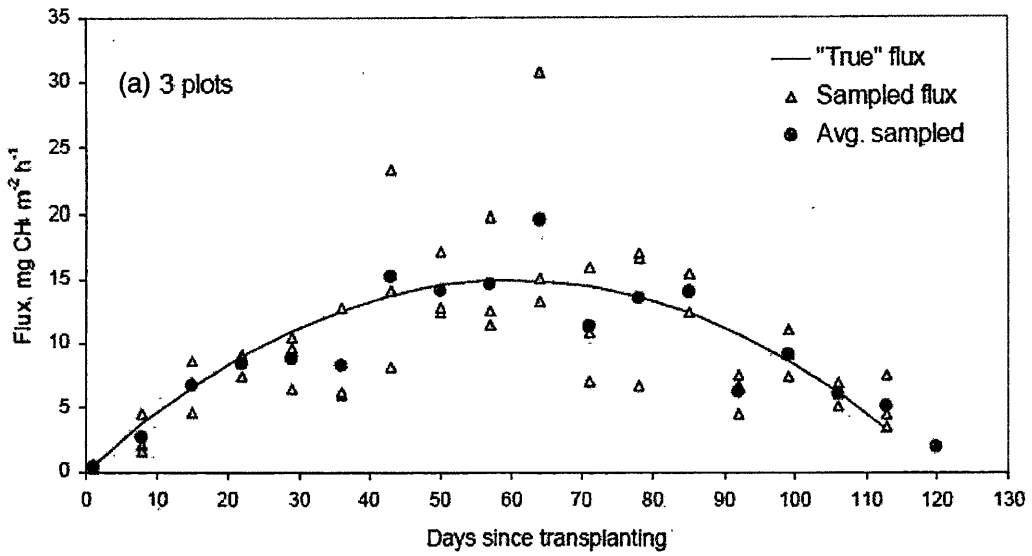
Figure 5.3. Simulated temporal variability for a "type I" canonical function for a paddy system with (a) 3 plots and (b) 10 plots. The solid line shows the underlying function, the triangles show the day to day flux, and the red dots are the daily means. The seasonal averaged is calculated from the mean of the daily fluxes.

$$\sigma = \left(\sqrt{2b(F;t)} \right), \qquad (5.3)$$

174

where

$$b(F;t) = 0.53 \big(F_{jk}(t)\big)^{0.77} . \qquad (5.4)$$

Here the flux is not the seasonally-averaged flux as in Eq. 5.2, rather it is the value of the smoothly varying function for plot j and system k at time t. Since this is a function of time (e.g. number of days from beginning of season), the distribution from which the $\Delta_{jk}(t)$s are drawn changes from day to day, and must be calculated every simulation day for the flux modeling we describe below. We show simulated temporal variability in Fig. 5.3. The figure shows that variability of the simulated flux increases with increasing daily flux, as borne out by the observations.

With this description of the flux, we simulated flux from a single plot, with spatial and temporal variability representative of field conditions. To summarize, the underlying base function captures the slowly varying component of the flux due to changes in temperature, plant maturity, etc. The spatial variability captures the heterogeneity in field conditions. The flux from each plot in the field $F_{jk}(t)$, has the same base function $F_k(t)$, as other plots, but there is some offset $\beta_{jk}(t)$ due to spatial heterogeneity. Finally, the temporal variability $\Delta_{jk}(t)$ captures the random day to day variability due to short term changes in temperature, inundation, soil conditions, and measurement uncertainty.
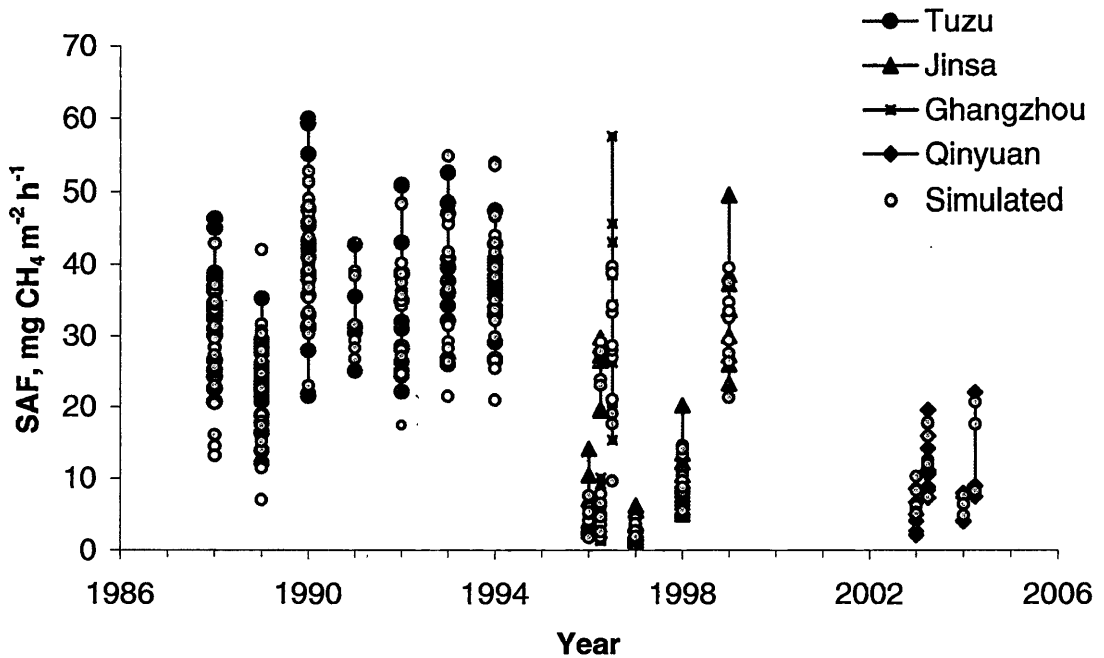
Figure 5.4. Simulated seasonally averaged fluxes (yellow circles) with their measured counterparts (blue symbols) for four sites in China. For the most part the spread of the simulated data matches the observed range quite well. At high fluxes, there is a tendency for the statistical model to underestimate the variability.

To test how well our statistical model captured the observed variability, we simulated all 230 seasonally averaged fluxes shown in Fig. 5.1. The model was run for all seventeen paddy systems over the eighteen year period of measurements. The number of plots used for each system and the number of days that fluxes were sampled in each case were treated as inputs to the model. Simulated SAFs are overlaid on top of the measured fluxes in Fig. 5.4 and the distributions of both simulated and measured fluxes are shown in Fig. 5.5. From these plots we see that our statistical model captures the variability observed in the real data set of fluxes. In particular it reproduces reasonably well the bimodal distribution of field fluxes seen in Fig. 5.5. In Fig. 5.6 we

176

plot the simulated and measured fluxes against one another. The linear fit of the plot is described by *Simulated* SAF $= -0.7$ $(\pm 5.8) + 1.025$ $(\pm 0.3) \times$ *Measured* SAF, with a correlation coefficient of 0.92. Within the uncertainty, the slope is one, again showing that the statistical model is performing well. It does tend to underestimate variability at higher flux (Fig. 5.4). Thus the model does a reasonable job reproducing field variability and can be used to answer the proposed questions above.

5.3 Modeling Approach

To answer the questions posed above with this statistical flux model, requires *a priori* knowledge of the canonical base function appropriate for the paddy system under investigation, and the system seasonally averaged flux. The base function is dictated primarily by the crop cycle, i.e. single-rice, double-rice, so is known to the experimenter beforehand. The seasonally averaged flux is not known in advance, rather is one of the primary statistics to be determined by the study. However, reported fluxes from similar systems can be used to provide a reasonable estimate. For this work, we simulated paddy systems with seasonally averaged fluxes that span 10 to 70 mg CH_4 m^{-2} h^{-1}, at intervals of 10 mg CH_4 m^{-2} h^{-1}. This range covered most reported fluxes (*Yan et al., 2005*).
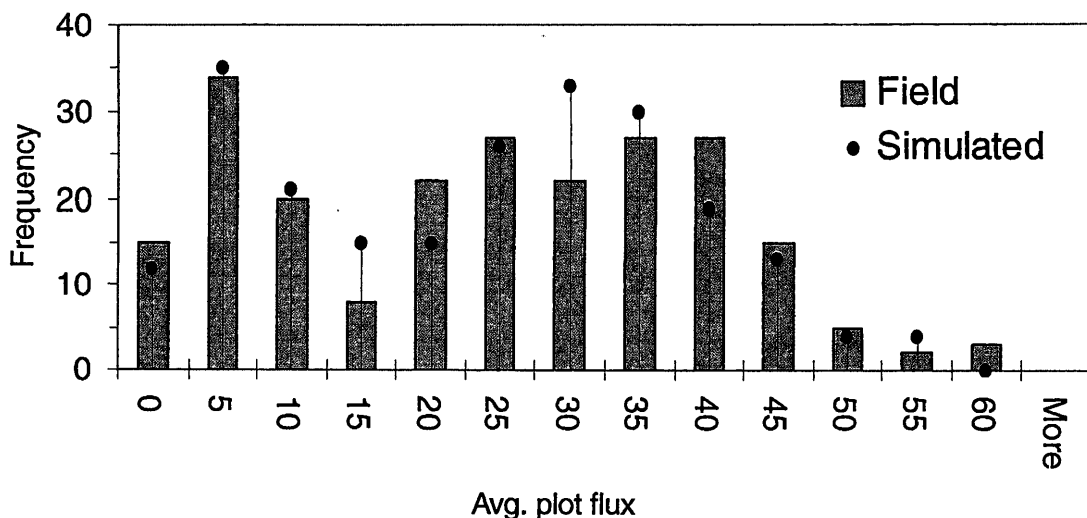
Figure 5.5. Distribution of simulated (filled black circles) and measured (filled bars) SAFs from the eighteen-year record of rice paddy studies. Fluxes have units of mg CH_4 m^{-2} h^{-1}. Both data sets are bimodally distributed with a tail extending to high fluxes. The lower mode peaks around 5 mg CH_4 m^{-2} h^{-1}, while the upper mode is centered about 30 mg CH_4 m^{-2} h^{-1}. The comparison shows the distribution of measured fluxes is well simulated by the model.

We started with the three canonical functions for the underlying function that describes the shape of the methane flux function during the rice-growing season. We added the random variations in flux from day-to-day (temporal variability) and across fields from plot-to-plot (spatial variability). These forms of variability add "noise" to our measurements and reduce the accuracy of our estimate of the seasonally averaged field flux $\overline{F_{jk}(t)}$, which for simplicity of notation we henceforth call F_k'. Again the k denotes the paddy system and the prime here signifies that this is an estimate of the true seasonally averaged flux F_k. To quantify the impact of the variability on F_k' we designed a series of computational experiments that simulated the measurement of methane fluxes during the growing season. The experiments simulated paddy systems

178

where the flux is described by one of the three canonical functions with F_k's from 10 to 70 mg CH_4 m^{-2} h^{-1}. We can sample these simulated fields using any number of plots we choose at any sampling rate. For this work we set the maximum number of plots per field at forty and allow the sampling rate to be as high as daily. It is unlikely any real sampling strategy would be more intense than this.
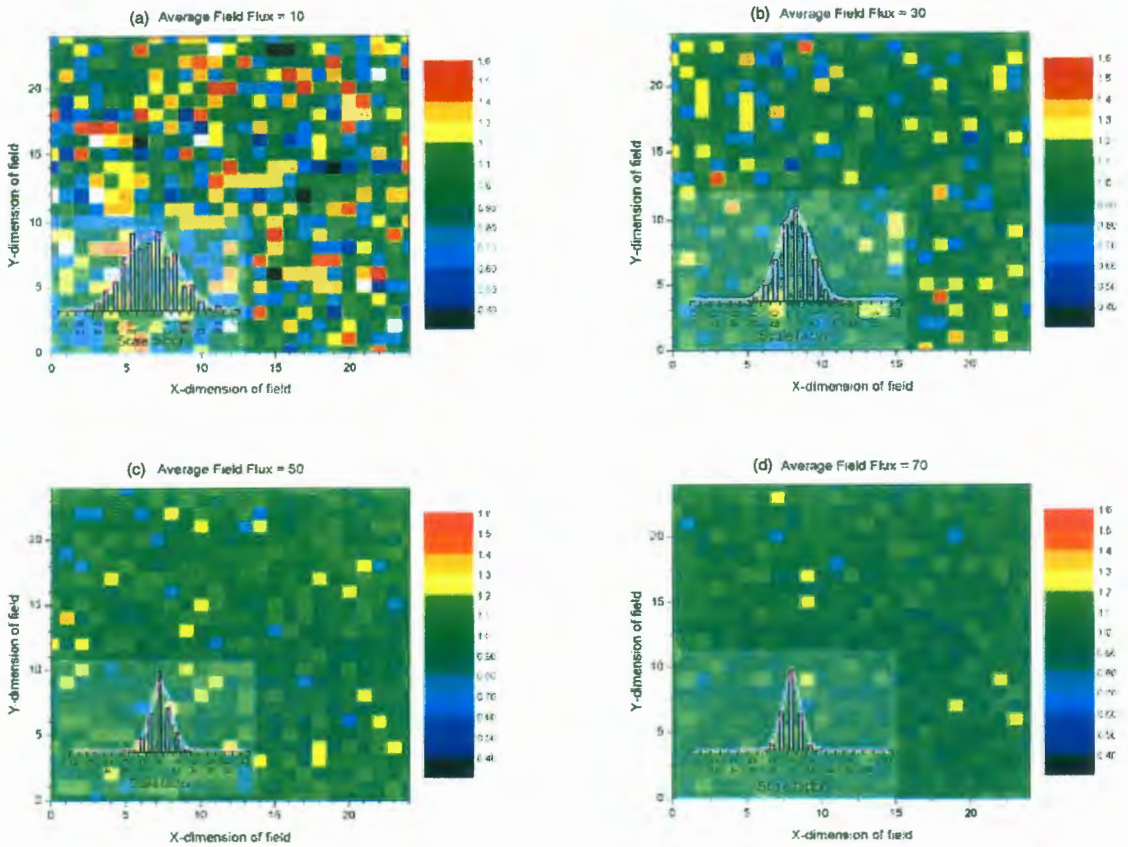
Figure 5.6. Simulated variability of the seasonally averaged flux over a spatial scale of 1 m². This resolution corresponds roughly to the size of a standard flux chamber. The panels represent four fields with average source strengths of (a) 10, (b) 30, (c) 50, and (d) 70 mg CH_4 m^{-2} h^{-1}. The values displayed are the ratios between the flux of the grid cell and the average flux of the entire field. For example, a cell in panel (a) with a value of 1.2 has a flux of 12 mg CH_4 m^{-2} h^{-1}. The inset histograms show the distribution of ratios in each simulated field. The simulated data reproduce the pattern of declining relative variability with flux strength observed in real paddy systems.

Our experiment simulated twenty-one different paddy systems corresponding to the three flux functions at seven different field averages, F_k = 10, 20, 30, 40, 50, 60, and 70 mg CH_4 m^{-2} h^{-1}. To each of these field conditions we added spatial and temporal

variability as specified by the power law relations derived from the field measurements. We "measured" flux from these simulated fields using different sampling strategies. We defined a sampling strategy by the number of plots we sampled per field (P, range is 1 to 40) and the sampling rate (D, 1 to 100% of the total number of days in the growing season, evenly distributed in time). The number of samples that are measured per season (P∗D) then ranged from one (one plot sampled once per season) to 4000 (40 plots sampled every day) for a 100-day growing season. We thus performed a total of 84,000 different experiments using all permutations of field conditions (21) and sampling strategies (4000).

Due to the random nature of the prescribed spatial and temporal variability, a Monte Carlo style analysis was performed and each experiment was conducted 500 times to gather the required statistics to assess the mean and standard deviation of the underlying distribution which is nearly normal. The number of simulations is a compromise between computational efficiency and the robustness of the statistical parameters.

In Figure 5.6 we show the simulated spatial variability (scale factors of the average field flux) in 50 m × 50 m fields on spatial scales of 1 m × 1 m. The latter dimensions are typical of the field area sampled by standard flux chambers. Though these graphs are for visualization only, we chose field and chamber dimensions to be representative of typical conditions. Simulated fields with average seasonal fluxes of 10, 30, 50, and 70 mg CH_4 m^{-2} h^{-1} are shown.

These plots reflect the relationship observed in the real field measurements described above, namely fields with lower emissions have higher relative spatial variability. Due to their higher spatial variability, low emission fields require more intensive sampling to reduce uncertainties in the seasonally averaged flux, though it is important to remember that the absolute uncertainties are still lower than in the high emission fields. It is the spatial not the temporal variability that primarily determines the relationship between sampling strategy and the true field flux.

We also simulated the eighteen-year record of field experiments using the same number of plots and sampling frequency as used in the original experiments. Each simulation was run once per field campaign. At the end of the simulated season, the seasonally-averaged flux was computed. We then compared the simulated fluxes with the real fluxes in Fig. 5.7. Within the uncertainty of the slope, there is a one to one correspondence between the simulated and measured results. This shows the model captures the range and variability of the actual field experiments.

5.4 Results

Results from our experiments are shown in Figs. 5.8-5.11. Each figure is a response to a question posed while evaluating or designing an effective sampling strategy to measure methane flux in the field. The figures quantify the relationship between the number of measured flux samples and the accuracy of the estimated field flux. They are meant to help the researcher achieve the accuracy required in their research plan with the minimal number of samples, or alternatively to evaluate measurements already completed.
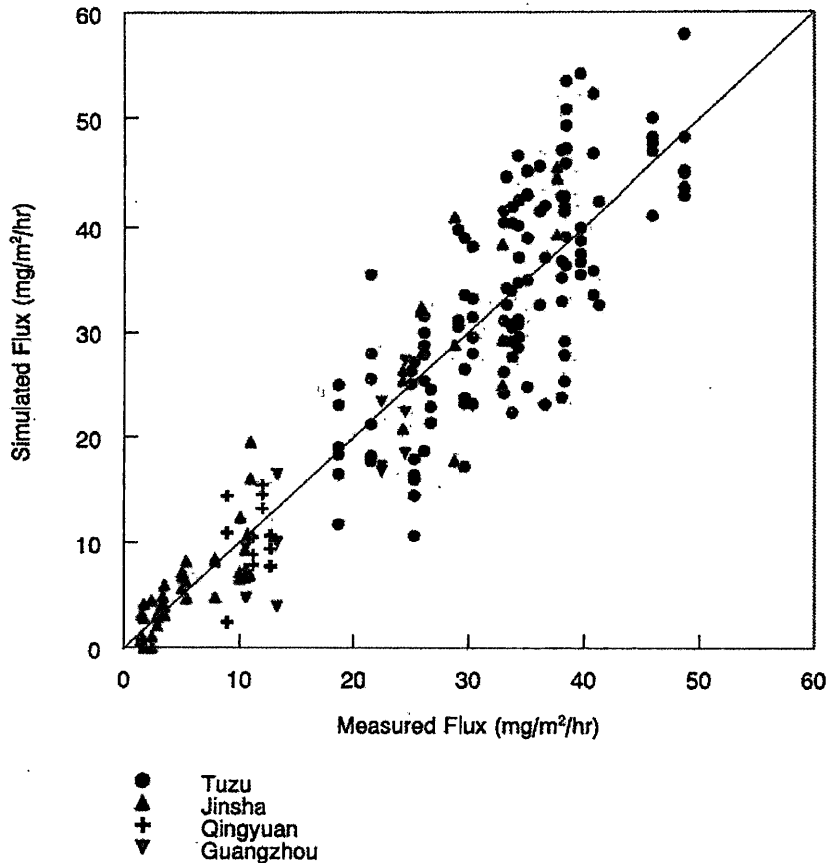
Figure 5.7. The plot shows the results of a test of our statistical model to simulate our eighteen-year flux data set. Different symbols are used to represent data for different field sites. The equation for the linear regression is y=-0.7 (±5.8) + 1.03 (±0.3)x, with a correlation coefficient of 0.92.

For concision, we only show results for a single canonical function or averages over all three functions. There are only small differences in the results using different underlying functions, so the data displayed here are representative of all three functions. This also gives us confidence that our conclusions are valid for other functions not considered in this work. We also remind the reader that our results are probability-based. For each experiment involving field condition and sampling strategy, we

183

determined the normal distribution of the simulated flux. The flux for any one run, that is, a single growing season of field measurements, will vary over a range of values defined by the distribution. We do not know how close the flux from any one run will be to the true flux, but can only state the probability that it will be within some percentage of the true flux. For the remainder of the chapter we adopt the criterion of 90% probability. Thus question 1 is more accurately stated as: given P plots and D sampling days, there is a 90% chance that the measured flux will be within a specified percentage of the true flux. To aid readability we omit the reference to the 90% criterion in the remainder of this chapter.
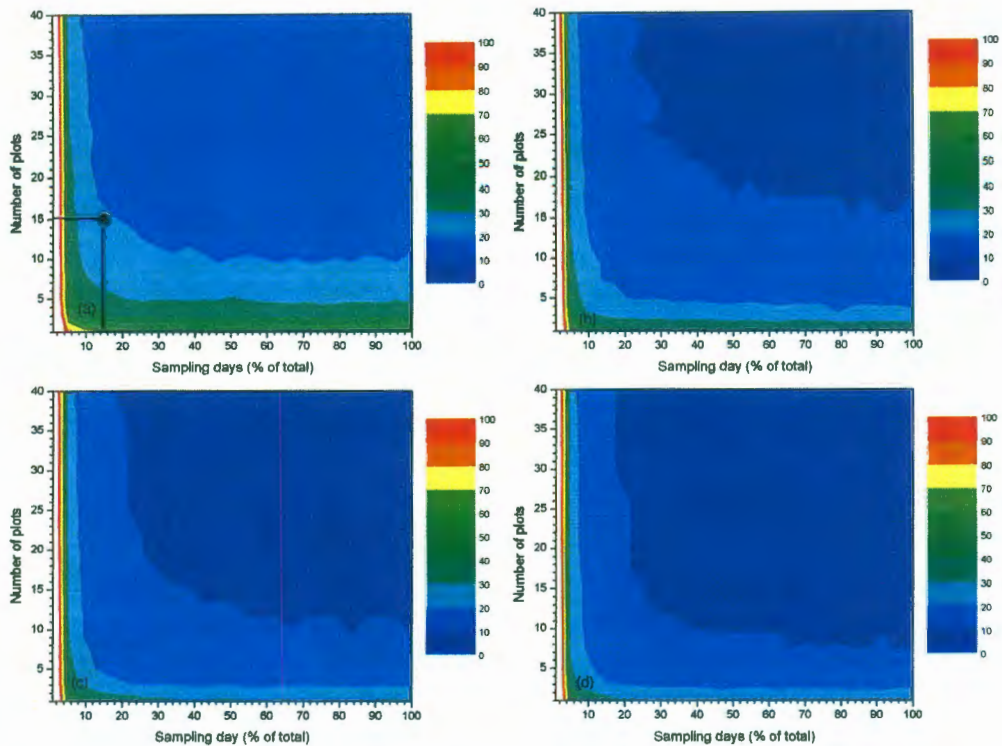
Figure 5.8. Maximum percent offset (90% confidence interval) between the simulated seasonally averaged flux and the true flux for a range of sampling strategies and average field fluxes (F_k). Areas of white along left margins of each panel indicate offsets greater than 100%. This figure is used to determine how close we expect measured field fluxes to be to the true field fluxes for different sampling strategies. Results are shown for F_k = (a) 10, (b) 30, (c) 50, and (d) 70 mg CH_4 m^{-2} h^{-1}. For example, if we use 15 plots at a sampling frequency of 15% for a field of low average flux (e.g. panel a), there is a 90% chance that the measured flux will be within 30% of the true flux. We expect the relative accuracy of the measured field flux to improve with source strength. The data shown here are for the "type I" canonical function, but results are similar for other function types.

5.4.1 Question (1)

Figure 5.8 shows results from all 4000 simulated experiments for four field conditions. The flux function for all four plots is type I, and the season averages are 10, 30, 50, and 70 mg CH_4 m^{-2} h^{-1}. For each experiment, we sample fluxes from the

simulated field over the entire growing season using the specified sampling strategy. After the run, we calculated the average flux over the season and compared it to the true flux. We repeated the experiment 500 times to build the distribution of fluxes. From the distribution we then calculated how close the flux is to the true flux. We call this the offset percentage. The figure illustrates how the accuracy of the measured flux is expected to change with sampling strategy. For the low emission conditions (10 mg CH_4 m^{-2} h^{-1}), if we want our measurements to lie within 30% of the true flux F_k, we need to sample 15 plots at a rate of 15% of the growing season. As expected, the accuracy improves as we increase the number of plots and sampling rate. We see also that relative accuracy improves as field emissions increase. This is due to the nature of the spatial variability as discussed previously.
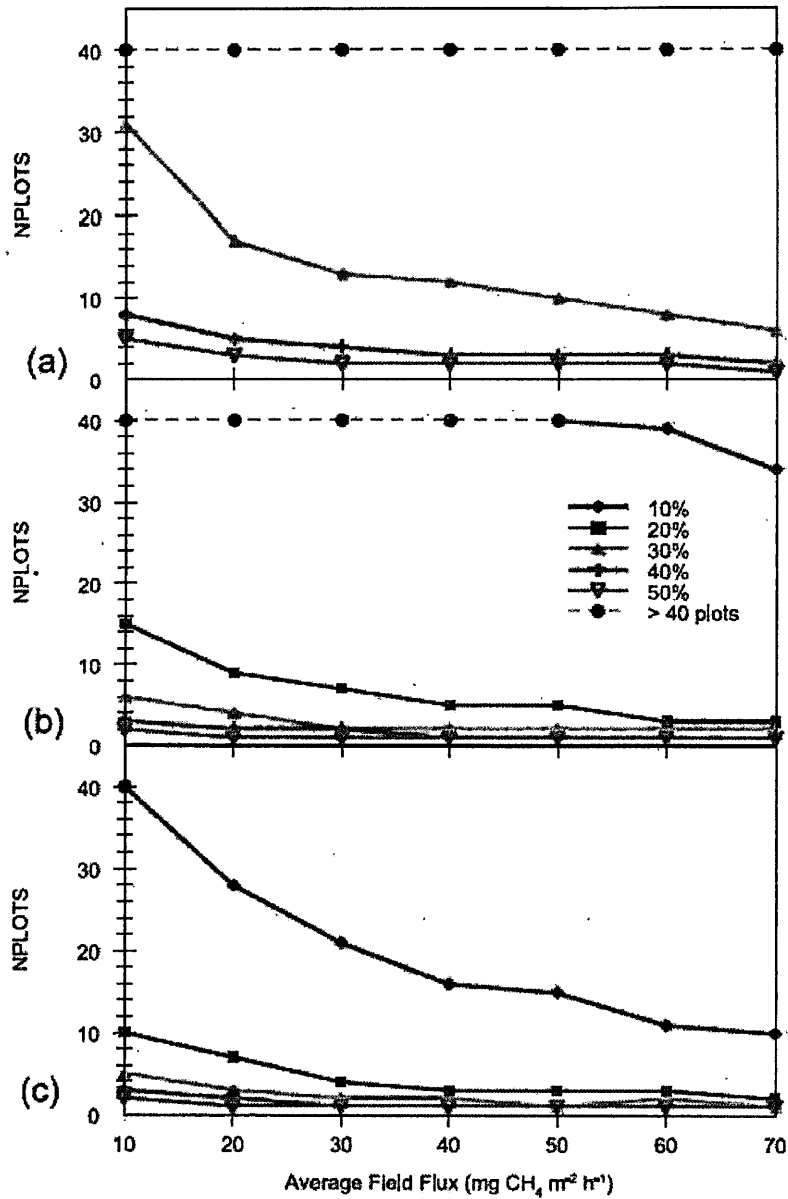
Figure 5.9. The minimum number of plots required to ensure the measured field flux is within 10% (diamonds), 20% (squares), 30% (solid triangles), 40% (plusses), and 50% (open triangles) of the true flux for three typical sampling rates, (a) 5%, (b) 15%, and (c) 30%. The rates were chosen to represent biweekly , weekly, and semiweekly sampling for a 120-day season. A dotted line indicates that the minimum number of plots required exceeds our simulated maximum of 40. Data are for the "type I" canonical function but are similar for the other function types. In the top panel, neither the 10% nor the 20% threshold is achievable with 40 plots or less.

187

5.4.2 Question (2)

Question 2 is addressed in Fig. 5.9 where we give the minimum number of plots required to ensure that the measured flux is within 10, 20, 30, 40, and 50% of the true flux for three typical sampling rates (5, 15, 30%). These rates roughly correspond to sampling intervals of biweekly, weekly, and semiweekly, respectively, for a 120-day growing season. The dotted line indicates levels that are not achievable within our 90% probability criterion.
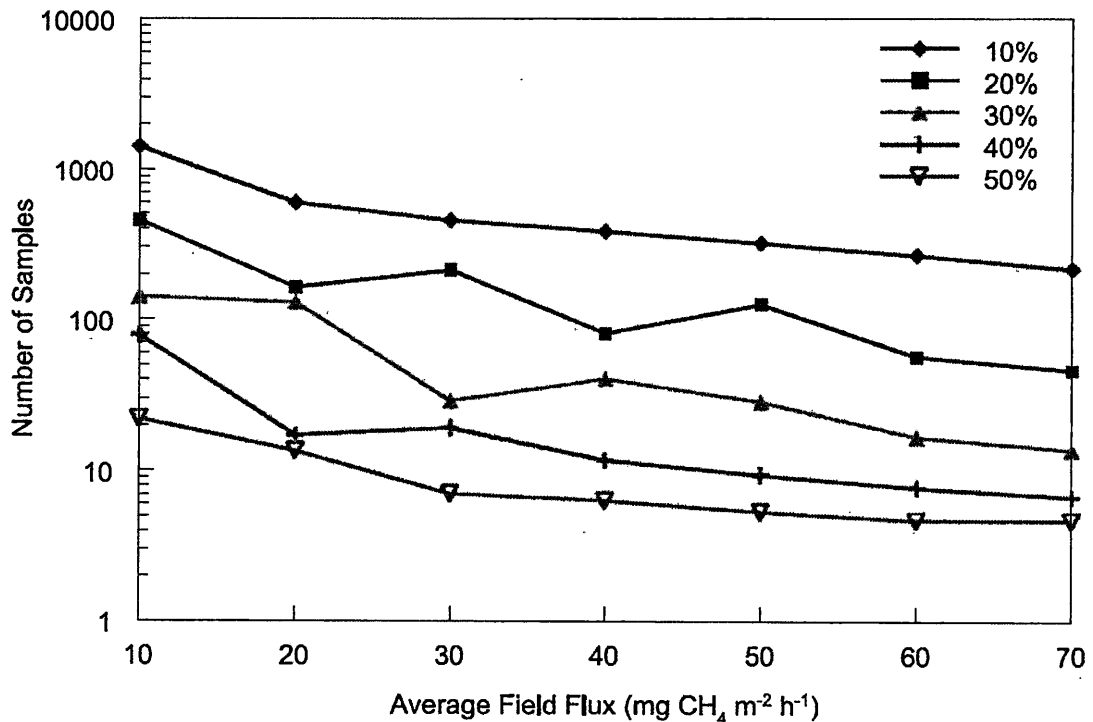
Figure 5.10. Minimum number of samples required to attain the specified accuracy limits. The sample size is the number of plots times the sampling rate assuming a 100-day field season. For other season lengths the number of samples needs to be scaled by the ratio (new season length: 100).

These experiments show the difficulty in reaching the highest accuracy levels at these modest sampling rates. In fact, the highest accuracy expected using a small

188

number of plots (P≤3) is typically 30-40%. Only for those fields with large methane emissions do we expect the measured flux to be within 20% of the true flux if three or fewer plots are used.

5.4.3 Question (3)

To answer question 3, we considered the total number of measurements required over the course of the growing season to meet our accuracy standards (Fig. 5.10). The numbers given in the figure are based on a 100-day field season but are easily modified to accommodate any season length.

The number of samples required range from 1400 per season to ensure the measured flux is within 10% of the true flux for the lowest emission fields to only five samples to meet the 50% mark in the highest emission fields. In general we never need more than about 20 samples per season to reach the 50% mark for any field flux. However if we wish to reach the 10% standard, we have to sample more than 200 times.

5.4.4 Question (4)

From our results in Fig. 5.11 we see that improvements in the accuracy of the measured flux decreases rapidly with increasing plot number and sampling rate and in fact become negligible past a certain sampling intensity. Clearly there is no need to increase the level of sampling past this point. We quantify the diminishing returns of increasing the sampling intensity by defining an offset gradient relative to both the number of plots and sampling rate. The offset gradient (dC/dD) is simply the change in the offset percentage (C) divided by the change in sampling rate (D) or number of plots (P), in which case the offset gradient is dC/dP. It tells us how fast the offset is changing

189

as we increase our sampling. We chose D and P to be three and calculated the gradients over all grid points for the data in Fig. 5.8. We divided the gradients by two so that the resultant is the change in the offset percentage per unit increase (either plot number or sampling rate). These are plotted in Fig. 5.11.
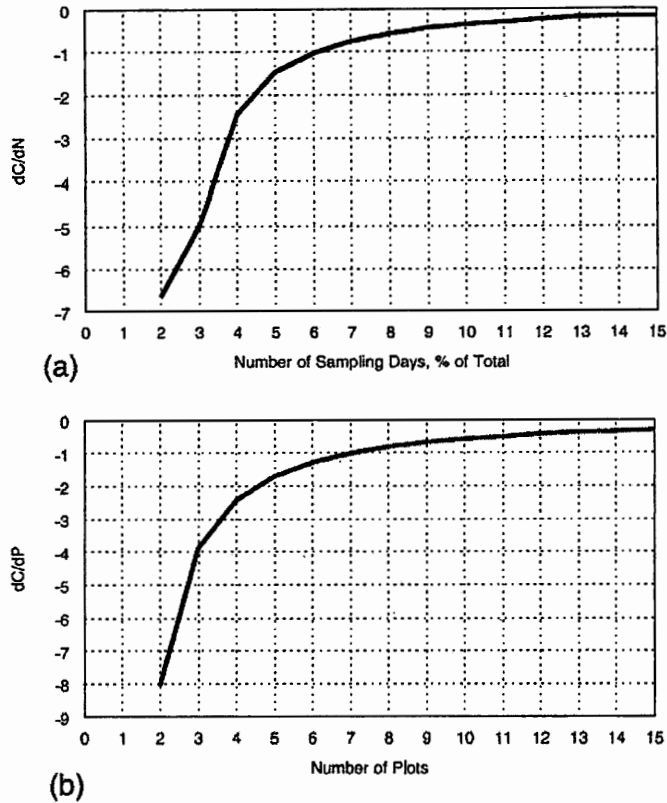
Figure 5.11. The figures quantify the impact of increase the intensity of the sampling strategy by one unit (i.e. either by one plot or by one sampling rate percentage point) on the accuracy of the measured field flux. In effect the figures help us determine the point of diminishing returns when increases in the accuracy of our field flux estimate become negligible. *dC/dN* is the rate at which the percent offset fro the true flux changes with an increase of one rate percentage point (i.e., one sampling day for a 100-day field season). *dC/dP* is similar but with an increase of one plot. In the upper panel (a) we show how *dC/dN* changes with the sampling rate, and in the lower panel (b), we show how *dC/dP* changes with the number of plots. For example, if we increase the number of plots from three to four, we expect the accuracy (expressed as percent offset from the true flux) to increase by 4%.

We see that rapid improvements in accuracy diminish past about ten units in each plot. Further gains in accuracy past this point can only be achieved by significantly intensifying the sampling strategy. Unfortunately this may be required. If we locate the (N=10, D=10) sampling strategy in the offset percentage graphs in Fig. 5.8, we see that

this strategy only takes us to within 30-40% of the true flux. In many cases we would like to achieve a higher standard than this, which will require more flux measurements.

5.4.5   Question (5)

Finally for question 5, there is a practical limit to the intensity of sampling. A reasonable limit may be set at twenty plots sampled every other day. This would require 1200 flux measurements over a 120-day growing season. Doing so we find we can get to within 7 to 14% of the true flux depending on the average field flux.

5.5   Discussion and Conclusions

We have examined the observed variability of methane emissions from rice fields and delineated its components. The nature of this variability affects the accuracy of regional and global extrapolations and the reliability of field experiments. The prevailing sampling practices tend to have fairly frequent measurements of about once a week and more. Because of that, the temporal variability is not likely to be a major source of uncertainty in the calculated seasonally averaged flux. The spatial variability however is large, and is not as well handled in the usual sampling strategy by triplicate plots. A minimum of three plots is convenient and permits statistical comparisons, but according to our results, it leads to large uncertainty in the calculated flux of 40%–60%. When the flux is low, our calculations show that it takes an unrealistically large number of replicates to overcome the effects of spatial variability. This is partly because we have defined accuracy as a relative measure. Therefore if the true flux is $1 \text{ mg m}^{-2}\text{h}^{-1}$, to be within 20% we must have a sensitivity of measurement that can distinguish 1 mg $CH_4 \text{ m}^{-2}\text{h}^{-1}$ from 1.2 mg $CH_4 \text{ m}^{-2}\text{h}^{-1}$, which is nearly impossible. But for a large flux,

192

say 20 mg CH_4 $m^{-2}h^{-1}$, to be within 20% requires us to distinguish between 20 and 24 mg CH_4 $m^{-2}h^{-1}$, which is possible. On the other hand, a great deal of accuracy for low emitting fields is not needed since such fields do not make a large contribution to the regional or global emissions. While these statements are true for rice fields, for other sources such as wetlands, the problem is not so easily dismissed. There are cases where the flux is low over most of an extensive area. Then the low fluxes are the major contributors to the regional and global emissions. In such cases chamber methods looking at small areas are unreliable.

Chapter 6 — Application of an Empirical Rice Flux Model to National and Global Spatial Scales

6.1 Introduction

Rice agriculture is an important source of atmospheric methane but its global source strength remains uncertain (*Denman et al., 2007*). In large part this is due to the many different ways that rice is grown. *Neue and Roger (2000)* claim that rice is "cultivated under a wider variety of climatic, soil, and hydrological conditions than any other crop", and as a result, methane fluxes range broadly (*Wassman et al., 200b; Yan et al., 2005*). Far from being static, these conditions will respond to pressures brought about by increasing human population, climate change, water shortages, and changing agricultural practices. Evaluating how emissions respond to these changes is necessary to predict future forcings of climate and consequent changes.

Emissions from paddy fields are influenced by both natural and anthropogenic factors, such as climate and the agricultural practices used by the farmer to manage the field. The practice of intermittently draining paddy fields for example is known to reduce methane emissions, as is the use of synthetic fertilizers over organic fertilizers. Considering this, and the fact that methane is twenty times more potent than carbon dioxide on a per molecule basis, rice agriculture is an attractive source to target for emissions reduction. This increases the importance of evaluating its source strength both at the national and global levels. Currently, all countries that are signatories to the

194

United Nations Framework Convention on Climate Change (UNFCCC) are required to periodically report national inventories of greenhouse gas emissions from all sources, including rice agriculture. The Intergovernmental Panel on Climate Change has developed "good practice" guidelines (*IPCC, 1997, 2000*) for countries to estimate emissions from these sources based on default seasonal CH_4 emission factors and scaling factors. These IPCC methods will likely be the methods used by countries to assess reductions in emissions.

Generally, emissions are estimated over large scales either by upscaling field measurements or using process-based modeling. As we discussed in the previous chapter, methane flux from rice agriculture is typically measured using static chambers, both in the field and in greenhouse studies. Early estimates of global methane emissions were often based on flux measurements from a single site and tended to be large. For example, *Holzapfel-Pschorn and Seiler (1986)* used flux measurements from Italy to derive global emissions of 120 Tg y^{-1}. Using fluxes from multiple sites *Khalil and Shearer (1993)* revised this down to 66 Tg y^{-1}. Other studies used a number of proxies to scale emissions including crop biomass, grain yields, and net primary production. (*Taylor et al., 1990; Neue et al., 1990; Anastasi et al., 1992; Kern et al., 1997*).

More recently mechanistic or process-based models have been used to simulate the dynamics of methane production, oxidation, and emission. Because details of these processes are largely unknown, in many cases the dynamics of these processes are linked to other more easily measured variables. For example, *Cao et al. (1998)* related methane production to soil Eh, and *Huang et al. (1998)* linked the rate of root exudation

195

to the daily aboveground biomass. Others calculated these mechanisms directly. The Decomposition-Denitrification (DNDC) biogeochemical model captures soil redox dynamics by simulating soil Eh and the activity of microbial reducers (*Li et al., 2002*). *Matthews et al. (2000)* presented a model (MERES) that simulates soil organic matter decomposition and predicts the amount of carbon substrate available for methanogenesis. It simulates nitrogen transformations in the soil and calculates the uptake of water and nitrogen by the rice crop.

These mechanistic models are useful in simulating the dynamics and variability of daily emissions over the duration of the rice growing season for a single site, but both the data needs and computational expense to apply the models at multiple sites become prohibitive when applied to global scales. For example, the DNDC model requires information on soil texture, pH, bulk density, and organic carbon content, besides crop management properties. Though available at local scales, these details are not known over wide areas.

Recognizing this difficulty some process models keep the number of input variables low at the expense of increasing the number of fixed model parameters. A model described by *van Bodegom et al. (2001)* requires only eight input variables but includes about twenty fixed parameters such as root decomposition rate, oxidation rate, and rice growth rates. Though they are kept constant, there is little knowledge about how these parameters vary from site to site or during the growing season.

Also some variables that control paddy emissions can change on yearly timescales, such as fertilization and water management. To investigate the changes

these factors make on global emissions requires a model that is deft enough to permit multi-year simulations. The flux model we used and describe below, allowed us to do just this and study how known decadal changes to paddy management in China and elsewhere would translate into changes in the global source strength of methane. We used this flux model to develop a new global inventory and to investigate possible changes to the paddy methane budget.

Besides assessments, spatially gridded inventories are useful in other applications. Spatially resolved inventories provide insight to high emission source areas at sub-national scales. These regions may be targeted for future study or mitigation and help focus research efforts. Spatially distributed emissions are necessary as inputs to regional and global climate models as well as chemical-tracer models. Patterns of atmospheric concentrations produced by these latter models can themselves be inputs to various regional climate and chemistry models. This work is becoming increasingly important as the need for planning mitigation and adaptation strategies around regional climate and impacts increases. Furthermore the patterns of concentrations predicted by chemical-tracer models can be compared with surface and remotely-sensed measurements of concentrations to both verify and improve inventories based on bottom-up techniques. In addition, this forward modeling of surface emissions helps us to identify the best sites to place instruments in order to monitor emissions and constrain estimates. Finally, and perhaps most importantly, spatially resolved emission estimates help us predict the future trend of gas emissions. For example, since paddy emissions are sensitive to soil inundation which is often achieved through irrigation, we

197

can predict that methane emissions from rice-growing regions of the world that face future water scarcity, will decrease.

At present few gridded inventories of paddy emissions exist at either national or global scales. Process models have been applied primarily to country-level emissions, for example China (*Huang et al. 2006; Li et al. 2004*) and India (*Pathak et al., 2005*), and the few global inventories that exist are based on proxy or statistical methods. *Matthews et al. (1991)* produced a global 1×1° inventory of methane from rice production, but lacking information on how flux varied from site to site, chose instead a constant flux, such that global emissions were 100 Tg y^{-1}. *Bachelet and Neue (1994)* updated this work by scaling methane fluxes to soil type and estimated methane emissions from Asia are 63 Tg y^{-1}. The most used global inventory is part of the Emission Database for Global Atmospheric Research (EDGAR) project. For this *Olivares et al. (2005)* used rice ecosystem-based fluxes from *Neue (1997)* and scaled them by national harvested rice areas from *FAO (2000)*. Though an improvement over single flux methods, only four different flux values were used with no consideration of the influence of climate or fertilizer among other factors that control methane flux. Perhaps the most detailed inventory to date is by *Yan et al. (2009)*. Here the authors used the United Nations Framework on Climate Change Convention (UNFCCC) Tier 2 method to estimate fluxes. The Tier 2 method specifies a base methane flux appropriate for continuously-flooded fields with no fertilizer inputs. The base flux is then scaled by designated factors for fields under different management. This inventory estimated global emissions at 25.6 Tg y^{-1}.

Emissions from these inventories have not yet converged at either national or global levels, indicating a need for continued study and refinement. Our effort sought to move us closer to this goal by using novel methods and data sets, including the following innovations.

First, the new inventory is based on a model that is empirically derived from controlled experiments in a greenhouse and confirmed by measurements in the field. Though the model is simple in structure, it is complete in the sense it includes the major variables that control methane from the paddy environment, namely organic carbon and nitrogen inputs, water management of the paddy, and climate factors. Though more detailed models exist that adequately predict paddy fluxes they require input that is difficult to gather at the appropriate spatial and temporal scales. The current model determines flux based on variables that can reasonably be acquired.

Secondly, we used orbital remote-sensing of vegetation to estimate application rates of crop biomass to paddy fields, a major source of organic-carbon material and driver of methane flux. This method provides global coverage of this factor at high spatial resolution.

Finally, our model includes the impact of nitrogen fertilizer on methane emissions. Our experimental results indicate that increased rates of nitrogen application increased methane emissions in paddies continuously flooded but decreased methane emissions otherwise. To our knowledge, the sensitivity of methane to N-fertilization has not been included in any other methane inventory.

6.2 PSU-Rice Emissions Model

Our model is based on a three-year study of methane flux from rice paddies in Nanjing, China, and experimental pots in the PSU greenhouse during the years 2005 – 2007 (*Khalil et al., unpublished*). At both sites, the major factors that determine flux were controlled at various levels and the response of the methane flux measured. The factors investigated included soil type (sandy loam and silt loam), water management (continuously flooded, intermittently flooded, and drainage interval), organic carbon application rate (crop residues), nitrogen fertilizer application rate (urea), and soil temperature. In China, rice was grown in adjacent plots that measured 4 m × 4 m, while in the PSU greenhouse, rice was grown in microcosms that had footprints of 45 cm × 63 cm. At both sites, methane and nitrous oxide fluxes were measured by the rate of accumulation in static chambers placed over the rice plants. A summary of results from both the greenhouse and field site is shown in Fig. 6.1 for seventeen experimental conditions.

The figure shows that there is good agreement between the fluxes measured from the greenhouse and the Nanjing plots, which gives us confidence that the relations between flux and factor developed from all these data are robust and may be applied to other sites. All relations are based on evaluation of the seasonally averaged flux. We summarize these relations as follows.
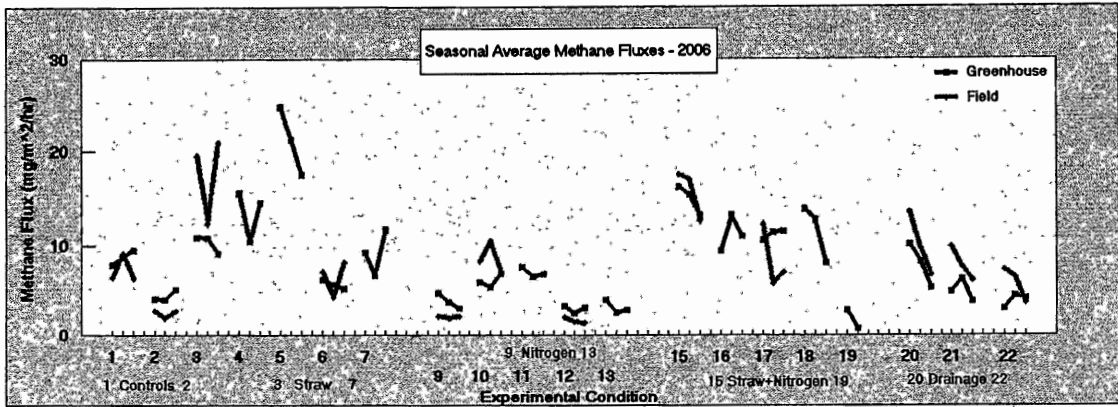
Figure 6.1. Methane fluxes from greenhouse (red) and field (green) studies. Fluxes are plotted against different factors and levels of factors. Key to numbers: The experiments are classified by water management (W), organic carbon inputs (S=straw), and nitrogen fertilization (N). W0=continuous flooding, W2=intermittent flooding, Sx = Straw added, where x=0,1,2,3 and depends on application rate (0, 3, 6, and 9 Gt dry matter ha^{-1}, respectively). Nx= nitrogen fertilizer where x=0,1,2,3 depending on level (0, 100, 220, and 300 kg N ha^{-1}, respectively). The last three experiments are for midseason drainage conditions Dx, where x=1,2,3 showing increasing drainage (5, 10, and 15 days, respectively). 1=W0S0N0, 2=W2S0N0, 3=W0S1N0, 4=W0S2N0, 5=W0S3N0, 6=W2S1N0, 7=W2S3N0, 9=W2S0N1, 10=W0S0N1, 11=W0S0N3, 12=W2S0N2, 13=W2S0N3, 15=W0S2N1, 16=W2S2N1, 17=W0S1N2S1, 18=W0S1N2S0, 19=W0S1N2 (no plant), 20=W2S1N2D1, 21=W2S1N2D2, 22=W2S1N2D3. From *Khalil et al. (unpublished)*.

Methane flux increased when increasing supplies of organic carbon was added to the soil (experiments 3-5 in Fig. 6.1). At both sites, the organic carbon was supplied by the addition of rice straw. Methane flux decreased when sites were managed under an intermittent flooding regime, i.e. fields were drained at least once during the season (experiments 6-7). The addition of synthetic urea decreased the methane flux (experiments 15-19), while methane flux also decreased as the drainage period increased (experiments 20-22). From these measurements the following relation was developed (*Khalil et al., unpublished*)

$$F = F_o e^{\alpha(T) \cdot C} e^{\beta \cdot N} . \tag{6.1}$$

Here F is the methane flux in units of mg CH_4 m^{-2} h^{-1}, F_o is the base flux with no

organic carbon or nitrogen fertilizer application, C and N are the amounts of added

organic carbon and nitrogen fertilizer with units of g (dry biomass) m^{-2} and g N m^{-2},

respectively, α is the sensitivity of the flux to the added organic carbon, and β is the

sensitivity to nitrogen fertilizers. $F_o = 7.3 \pm 2.7$ and 2.4 ± 0.8 mg CH_4 h^{-1} m^{-2}, and β

$=0.016$ and -0.036, for continuously and intermittently flooded fields respectively. The

experiments showed that α is temperature dependent according to

$$\alpha = \alpha_0 + \rho_1 T + \rho_2 T , \tag{6.2}$$

where $\alpha_0 = 0.021$, $\rho_1 = -0.0021$, $\rho_2 = 0.0000551$, and T is the average soil temperature

(at 10 cm depth) in degrees Celsius over the first 60 days of the season (described

below).

The rates of nitrogen fertilizer and organic carbon application varied by a factor

of three in the study, while temperatures spanned the range over which most rice is

grown, ensuring the model will have wide. The next step was to apply the model to

national and global rice agriculture and create a spatially gridded inventory of methane

emissions.

6.3 Model inputs

Regional and global extrapolation of the empirical flux model developed from the field and greenhouse studies required spatially resolved climate and agriculture data. While some of these data are readily available, others such as organic carbon and synthetic fertilizer application rates are available only over limited areas and spatial resolutions. Data such as water management and crop residues, which are often incorporated back into the paddy, do not exist in any official form. Properly representing the field conditions and paddy management over national and global scales remains one of the primary sources of uncertainty in estimates.
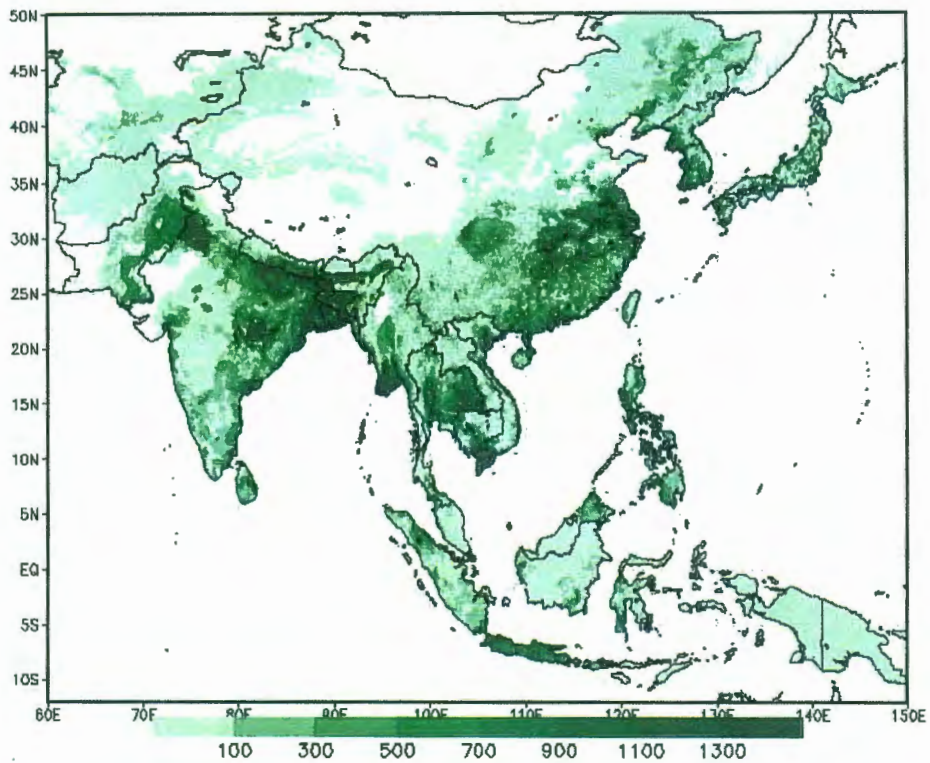
Figure 6.2. Harvested area of rice agriculture in units of hectares per cell. Harvested area is the area of rice harvested per year. For multiple croppings of rice, the harvested area will exceed the physical area. Harvested data are from *Monfreda et al. (2008)*. Resolution of map is 5 arcmin.

We constructed underlying data layers as model input for the following factors: rice location and area, crop calendar (i.e. planting and harvesting dates), soil temperature, organic carbon and nitrogen inputs, and water management (inundation). A brief description of each follows.

6.3.1 Location and extent of rice growing areas

Rice growing locations and areas are taken from *Monfreda et al. (2008)* and shown for monsoon Asian countries in Fig. 6.2. The authors distributed statistical national and subnational rice cropping areas on a 5 arcmin × 5 arcmin (~10 km × 10 km at the equator) grid based on a global cropland base map (*Ramankutty et al., 2008*). The base cropland product provided fraction of pixel area that is determined by two sources of satellite land cover data. The data provided are harvested areas, which may be larger than actual land area if more than a single crop is harvested seasonally on a single parcel of land. The total area of harvested rice from this product is 152 million ha.

6.3.2 Crop phenology

The timing and duration of rice seasons is needed not just to calculate annual emissions from a flux, but as we describe below this information is also used to estimate appropriate soil temperatures and straw inputs to the paddy field. Crop phenology is complicated by the practice of multiple cropping seasons in a single year. Though some rice growing regions may only have a single rice crop due to climate limitations or economic preferences for alternate non-rice crops, other areas practice double or triple rice crops in a single year. A typical rice season in the tropics may be 100 days but 130 days in temperate regions.

We used rice crop calendars developed by *Matthews et al. (1991)* for this study. *Matthews et al. (1991)* compiled rice crop calendars from the United Nation's Food and Agriculture Organization (*FAO, 1978*), the International Rice Research Institute's World Rice Statistics (*IRRI, 1985*), and other national and subnational agricultural statistical handbooks and atlases (see Appendix of *Matthews et al., 1991* for complete

205

list) and distributed them across a 1×1° global grid. A total of 36 different crop cycles were included in the data base including single, double, and triple cropped rice. The number of months per year rice is grown ranged from 4 to 12. Crop calendars were available at the national level for most countries, but for China and India, calendars were provided at the provincial and state levels. Since the resolution of our inventory (5 arcmin) is higher than the crop calendar grid (1 deg.), we took the calendar to be constant throughout the one deg. grid cell. Also, in those rice-growing regions where no cropping information was provided by the *Matthews et al.* map, we use a nearest neighbor algorithm to assign appropriate cropping data.

As rice-cropping management is based on climatic, ecological, and cultural factors, as well as individual decisions made by the farmer, large differences in planting and harvest dates, crop duration, and number of crops per year, exist. In addition, multiple cropping may occur on a regional scale but not necessarily at the individual field level. While there may be early, intermediate, and late season rice crops within a region, a single field may only be planted for one of these seasons, while others in the same region may be planted for two or all of the seasons. The agricultural statistical data needed to delineate these differences in rice cropping were unavailable at this level and we recognize this as a source of uncertainty in the final inventories.

6.3.3 Soil temperature

From our flux measurements we determined the sensitivity of both methane and nitrous oxide flux to soil temperatures. The data indicate that temperature is an important driver of methane flux, but less so for nitrous oxide. In our empirical flux
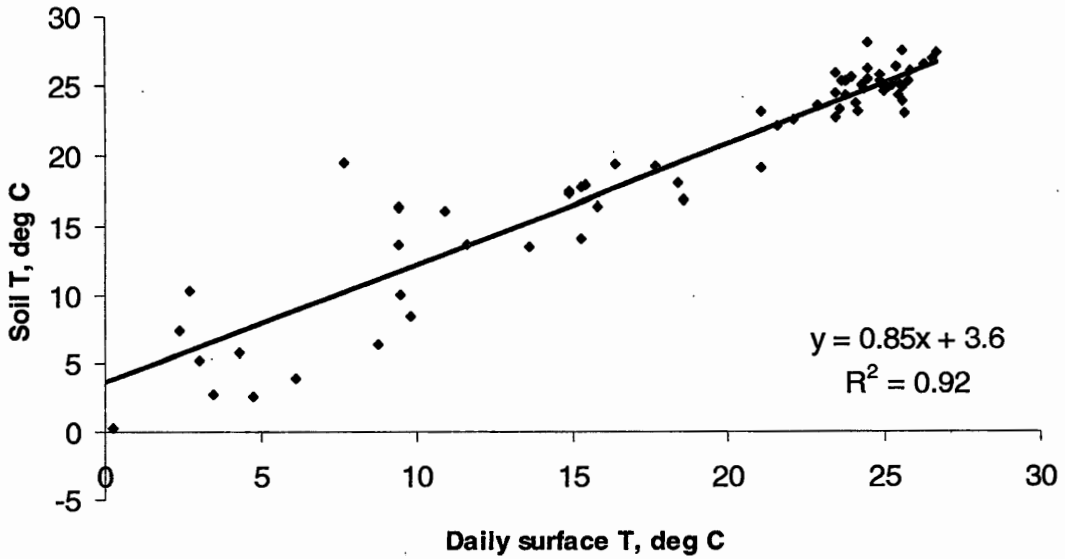
Figure 6.3. Surface and soil temperature at Tuzu, Sichuan Province, China (2005-2006). Soil temperatures were measured at a depth of 5 cm.

model, the parameters α and β are the sensitivity factors that relate both CH_4 and N_2O fluxes to organic carbon and nitrogen inputs respectively. Our experiments revealed that α is a strong function of soil temperature, while β shows no significant dependence on soil temperature.

Soil temperatures were derived from reanalysis surface air temperature from the National Weather Service's National Center for Environmental Prediction. Surface air temperature data are distributed globally on a 2.5×2.5° grid at a daily time scale. Daily temperatures from the years 1948 to 2006 were averaged to produce a climatological record for use in deriving the soil temperature data.

From the greenhouse and field measurements of methane flux, the functional relationship between α and T was statistically stronger using the average soil

temperature over the 60-day period following rice planting rather than over the entire rice season. To this end, the beginning of the rice season was determined separately for each grid cell based upon the crop calendars described above. Daily air temperatures were averaged over the 60-day period following this date. After the daily averaging was performed, surface air temperatures were converted to soil temperatures (at approximate depth of 10 cm) using a linear relationship derived from two years of soil/air temperature data from field measurements in Tuzu, China (Fig. 6.3). The map of soil temperatures is shown in Fig. 6.4.
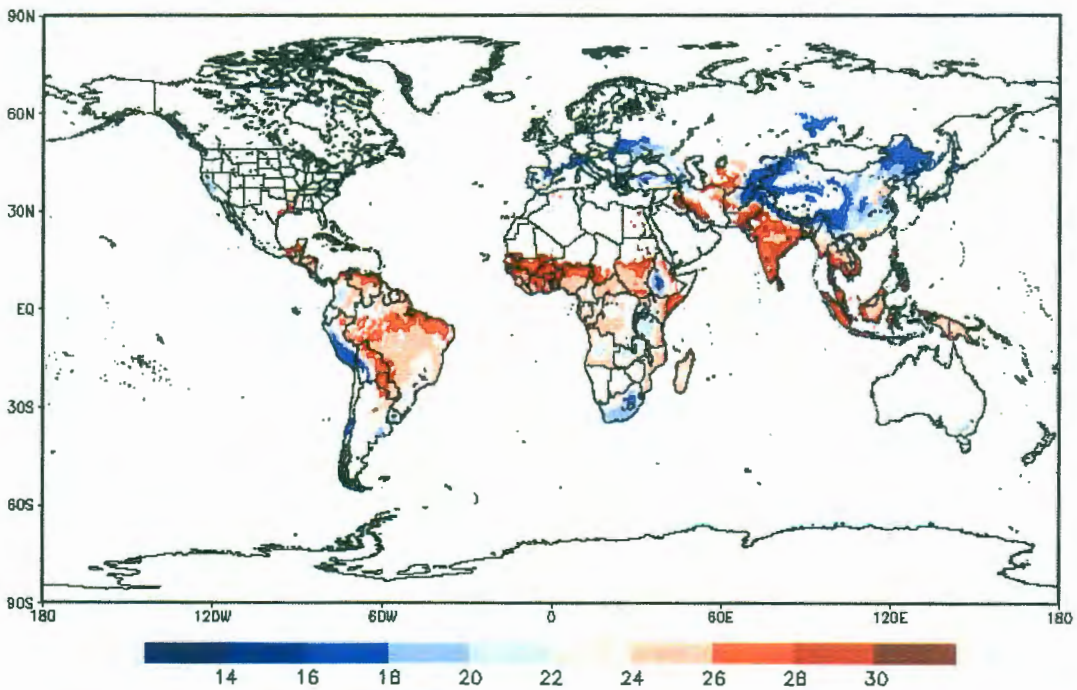
Figure 6.4. Soil temperatures at 10 cm depth averaged over the first 60 days of the growing season. Temperatures are notably higher in the Indian sub-continent producing larger fluxes in paddy fields.

6.3.4   Organic carbon inputs

Both greenhouse and field experiments clearly show the strong dependence of CH_4 fluxes on organic carbon inputs. In these experiments organic carbon was added to paddy soils in the form of straw. In practice, organic carbon can be added in myriad ways.

To simulate the addition of organic carbon to paddy fields in our model we considered the largest sources of organic carbon, including straw, crop roots, stubble, and farm manure. It is common practice to add rice straw and other residues back to the field after harvest (*Neue et al., 1996; Wassman et al., 1996*). These organic amendments are an important source of fermentable carbon for soil methanogens (*Wassman et al., 1996*) and increase methane emissions. Methanogens utilize the labile carbon preferentially leaving the cellulosic materials behind (*Yagi and Minami, 1990, Cao et al., 1995, van Bodegom et al., 2001*). As this labile carbon has a short residence time in the soil, perhaps one to two months under the right soil and environmental conditions (*van Bodegom et al., 2001*), only the organic matter received by the paddy soils within a couple months of rice planting will stimulate methane emissions.

The application rate of crop residues depends on the crop standing biomass and the fraction of residue returned. In some cases the residue is burned, used for energy, or used in straw products (*Wassman et al., 2000*). The crop biomass production is variable and depends on factors such as rice cultivar, length of growing season, water stress, and CO_2 levels (*Summers et al., 2003; Cheng et al., 2008*). This variability adds uncertainty to estimates of methane emissions across large areas. Though some survey data exist from Chinese farmers quantifying this input (*Huang et al., 2006*) in general there is very

209

little information about the amount of straw and residues added to paddy fields. To our knowledge none exists on a gridded basis.

Remote sensing data can help fill in these gaps. Surface reflectance measurements from space have been used over the past decades to construct land use and land cover maps, and to estimate biophysical parameters from vegetation (*cf. Mather, 1993; Alexander and Millington, 2001; Liang, 2004*). Of particular interest for this study is the use of satellite products to infer biophysical parameters from crop agriculture *(Tan et al., 2005, Zhang et al., 2005; Zhang et al., 2006)*. Remote sensing has been shown to provide accurate assessments of crop growth, production, and area, and yield (Tucker et al., 1980, *Sharman et al., 1992; Moulin et al., 1998*). For example, crop monitoring by space provided better estimates of U.S. Corn Belt crop yields during the 2005 droughts than standard methods *(Zhang et al., 2006).*
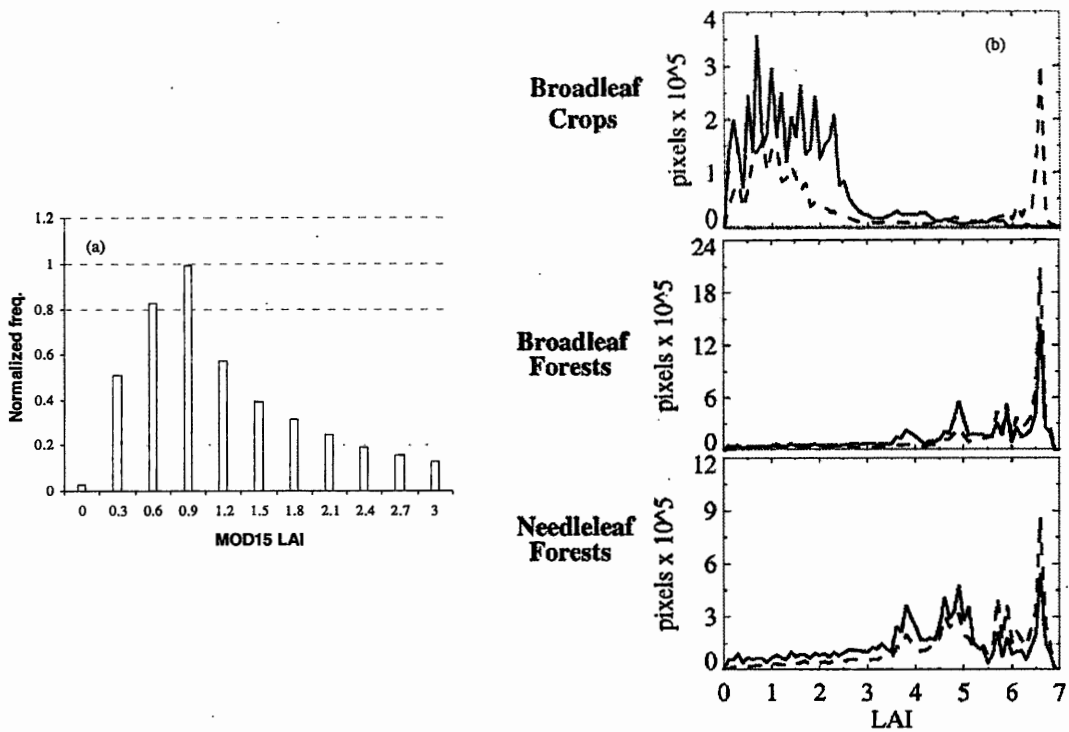
Figure 6.5. Distribution of leaf area index (LAI) for (a) modeled rice agriculture lands, and (b) other vegetation types. Solid line in (b) is from the MODIS Collection 4 product, while dotted line is from Collection 3. LAIs in plot (a) range up to about 3 with a median value of 0.92. This is similar to the general distribution of LAI observed for all broadleaf crops seen in (b) confirming that MOD15 LAI is correctly picking out croplands. Figure (b) from *Shabonov et al. (2004)*.

We used crop leaf area index to estimate standing biomass in rice growing regions. The leaf area index (LAI) is the ratio of the total one-sided leaf area to the area of the footprint the plant projects. It can be as high as seven for dense forest canopies (e.g. *Shabonov et al., 2005*), but is typically 1 to 1.5 for croplands and rarely exceeds three *(Shabonov et al., 2005; Tan et al., 2005)* (Fig. 6.5). Leaf area index products are calculated from satellite observations by optimizing the match between measured and modeled surface reflectances. Simulated reflectances are calculated using a radiative

211

transfer model that considers variables such as soil reflectance, leaf reflectance, and canopy transmittance for a number of vegetation categories (*Myneni et al., 1997; Liang 2004*). The vegetation categories are supplied by a land cover map.

We used the Collection 5 MOD15 LAI products at 1 km resolution (*Myneni et al., 1997, Myneni et al., 2002*) for the year 2001. This product has been validated against ground measurements and compared against other satellite derived LAI retrievals (*Garrigues et al., 2008*). In general it reproduces the seasonal variability of cropland vegetation well, and among the four LAI products tested in *Garrigues et al. (2008)*, it most accurately reproduced the ground measurements. However, the MOD15 LAI tends to underestimate cropland LAI (*Garrigues et al., 2008*) and we scale all MOD15 LAI by a factor of 1.4 to correct for this.

Though the MOD15 product is available every eight days, we used monthly averages since our crop phenology is specified at monthly timescales. For each grid cell with harvested paddy area, we determined the beginning month of each rice season based on the crop calendar described above. For the two months preceding this date we determined maximum LAI for the grid cell using the MOD15 product. Again our assumption is that residues from the crop preceding rice planting will be added to the paddy field the following season. We used a time frame of two months to account for a possible transition month between crops. We used the maximum LAI over this period, rather than the mean since LAI may go to zero after harvest and perturb the mean.
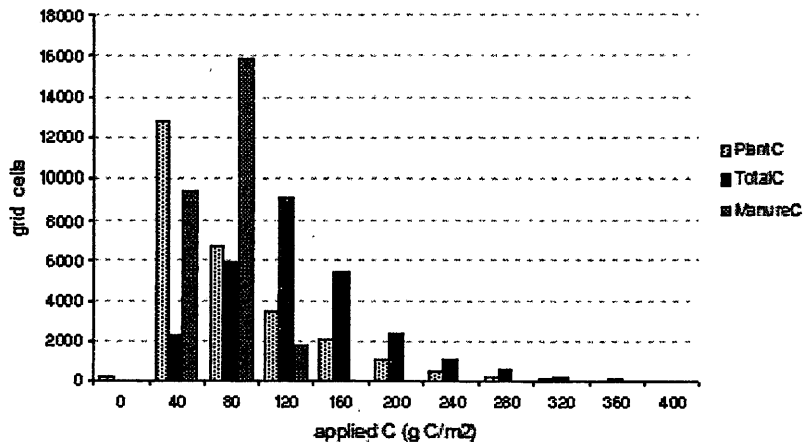
Figure 6.6. Simulated organic amendement application rates from all model grid cells with harvested rice areas. Contributions from crop residues (PlantC) and farm manure (ManureC) is shown along with the combined rate (TotalC). Values are in the range, but on the low end, of rates reported from actual farm practice.

Though there is variability between vegetation types, overall there is a good relation between LAI and aboveground biomass (e.g. *Baccini et al., 2008; Xioasong et al, 2008)*. For rice and related crops at maximum height, the ratio between aboveground mass and LAI is about 310 ± 20 *(Xiaosong et* al., 2008) and we scaled all LAIs by this ratio to determine biomass production.

After grain harvest, the aboveground biomass is the sum of straw and stubble. The mass of crop stubble is about 13% the mass of the straw *(Huang et al., 2006)*, so the aboveground biomass is 1.13×straw. The mass of crop roots is about 10% the mass of the aboveground biomass *(Huang et al., 2006)*. If the roots and stubble are incorporated back into the field as standard practice shows *(Huang et al., 2006)* and

213
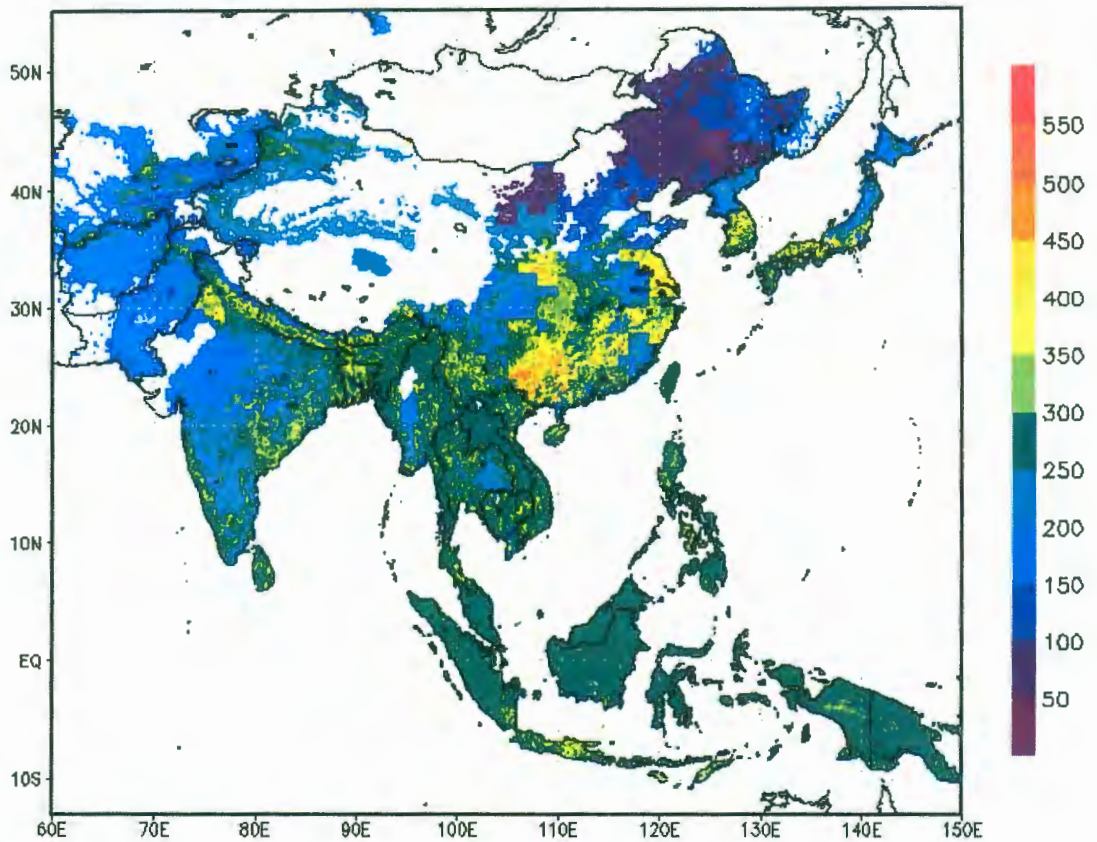
Figure 6.7. Simulated organic amendment application rates for rice producing regions of monsoon Asia. Units are g (dry matter) m^{-2}. Values include contributions from both crop residues and organic manure. The rates range from 15 to 1020 g (dry matter) m^{-2}, with a median of 253 g (dry matter) m^{-2}.

some fraction f of the straw is added to the field, then the organic matter amendment from the previous crop is given by:

$$\text{crop residue application} = \text{AGB} \times \left(0.1 + \frac{f + 0.13}{1.13} \right) \tag{6.3}$$

214

where AGB is the aboveground biomass ($g\ m^{-2}$). For China, the fraction of straw added to the paddy field varies between 5 and 30% by province according to farmer (*Huang et al., 2006*). Outside China the average fraction is 15%.

Animal manure is sometimes added to rice paddies and increases carbon substrates in rice paddies. Farm animal manure remains the primary fertilizer in some rice producing countries, but is being replaced by mineral N fertilizers elsewhere. The amount of manure applied to paddy fields is uncertain globally, but good estimates exist for China from agricultural surveys. Reported inputs are available by province and range from 6 to 100 $g\ C\ m^{-2}$. Elsewhere we estimate application rates based on farm animal populations (*FAO, 2005*) and country-based manure production per head of animal (*Mosier et al., 1998*). Dry manure values were converted to carbon using carbon fractions from *Bustamante et al. (2008)*.

Our estimated total organic matter application rates are shown in Fig. 6.7. Rates ranged from 15 to 1020 g (dry matter) m^{-2}, with a median of 253 g (dry matter) m^{-2}. Our simulated rates peak around 120 $g\ C\ m^{-2}$. If we assume a carbon fraction 0.4 for dry biomass, this rate translates into an application rate of 3 t ha^{-1}. This value is consistent with actual farm practices, though on the low end of reported values (*Neue et al., 1996; Khalil et al., 1998*).

6.3.5 Nitrogen inputs

Nitrogen fertilizer inputs affect not only nitrous oxide emissions but methane emissions as well, though the relation is more complex for methane. Our measurements indicated that under continuously flooded conditions, methane paddy flux increased

with increasing nitrogen additions; however, under intermittently flooded conditions the relation is reversed as the methane flux decreased with increasing nitrogen inputs.

Nitrogen application rates are determined from two sources. The FertiStat database of FAO includes rates of N fertilizer applied to rice paddies (kg N ha^{-1}) for all countries over the years 1995 – 2003 (http://faostat.fao.org). In addition, the FAO FertiStat data includes the percentage of rice paddy area fertilized in each country. Only for this fraction of paddy area do we apply the specified fertilizer rate. For the remaining area set the application rate to zero.

For China, we used total N fertilizer application rates (for all crops) at the county level (*EOS_Webster, http://eos-webster.sr.unh.edu/home.jsp*). We scaled these totals by the fraction of total cropland that is rice paddy area at the county level and grid appropriately.

6.3.6   Inundation

Our flux model differentiates paddy fields that are managed under continuously flooded regimes versus those that are intermittently flooded throughout the rice season since fluxes are significantly different between the two. For example, CH_4 flux was approximately three times higher in the continuously flooded control plots (no organic carbon or N-fertilizer additions) than in the intermittently flooded plots (7.3±2.7 vs. 2.4±0.8 mg CH_4 m^{-2} h^{-1}).

Yan et al. (2009) used statistical databases from the FAO (http://faostat.fao.org) and the International Rice Research Institute (http://www.irri.org/science/ricestat/pdfs/Table%2030.pdf) and rice maps from *Huke*

and Huke (1997) to compile proportions of paddy areas in each country that were managed under continuously flooded, intermittently flooded with single drainage, and intermittently flooded with multiple drainages. Outside of Vietnam where nearly all paddies are continuously flooded, the typical proportion of paddies that are continuously flooded is 20-30%. In China, roughly 80% of paddy fields are intermittently flooded with multiple drainages. A greater proportion of paddy area in India is continuously flooded (30% vs. 20%), and the remainder area is roughly evenly split between single and multiple drainages. These country proportions are implemented in our gridded inventories by calculating averages of fluxes for each water regime weighted by the country-specific area proportions.
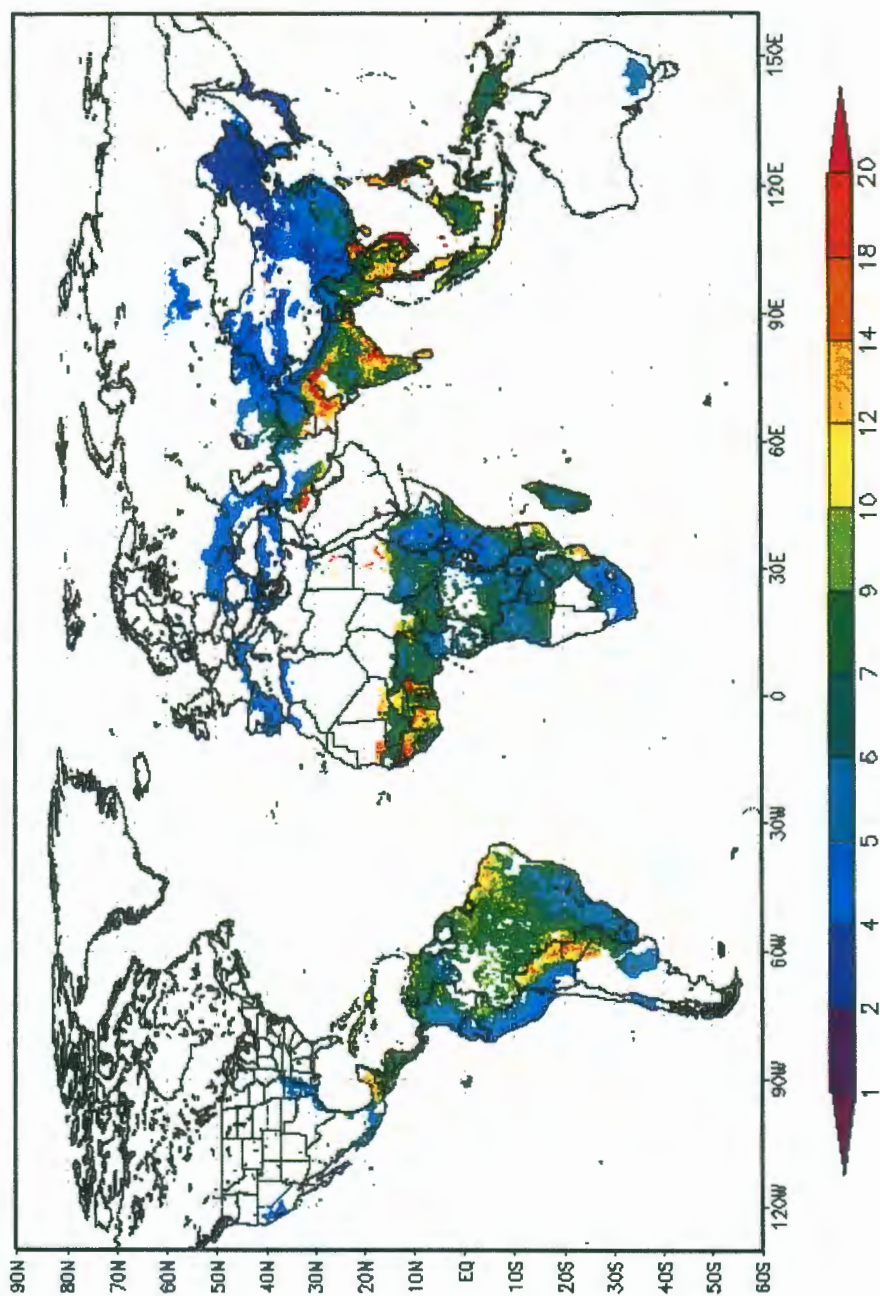
Figure 6.8. Simulated seasonally averaged methane fluxes across all rice-producing areas. Units are mg CH_4 m^{-2} h^{-1}. Grid cells are 5×5 arcmin. For grid cells that contain fields that are multiply cropped, fluxes displayed are averages across seasons.

218

6.4 Methane fluxes and emissions

We created gridded maps at 5 min × 5 min resolution for each of the above input variables. Using the functional relations in our model that were derived from the field and greenhouse work, we calculated the seasonally averaged flux for each grid cell and crop season (Fig. 6.8). As some fields have three crops per year, the fluxes shown are averages over all seasons if the crop calendar for the grid cell indicated that fields within the cell were multiply cropped. Over the course of the simulated year, over 719,000 fluxes are calculated for all grid cells and seasons. Simulated fluxes ranged from 3.1 to 170 mg CH_4 m^{-2} h^{-1}, though as Fig. 6.8 shows, most fluxes are within the lower part of this range. This is consistent with the range of 3000 fluxes from measured from paddy fields in China (1 – 180 mg CH_4 m^{-2} h^{-1}) reported by *Khalil and Rasmussen (1991)*. *van Bodegom et al. (2000)* also estimated that seasonally averaged fluxes across China, the Philippines, and Indonesia vary by two orders of magnitude using a process-based model for rice paddy emissions.

Our area-weighted mean flux over all countries and seasons is 6.6 ± 2.3 mg CH_4 m^{-2} h^{-1}. This compares well with the base emission factor of 5.4 mg CH_4 m^{-2} h^{-1} recommended in the 2006 IPCC Guidelines for National Greenhouse Gas Inventories (*Yan et al., 2005; IPCC, 2007*). The baseline factor is for continuously flooded fields with no organic amendments. Our average flux includes contributions from fields that are both intermittently flooded and those that receive organic amendments. Since these two factors drive fluxes in opposite directions, we can expect our average flux to be close to the baseline emission factor. Our mean flux is also typical of values measured from European and American rice fields. Published fluxes from Spanish, Italian, and

219

Californian rice fields range from 4–16 mg CH_4 m^{-2} h^{-1} (*Cicerone and Shetter, 1981; Seiler et al., 1984, Holzapfel-Pschorn and Seiler, 1986; Schutz et al., 1989*). This suggests that our model is simulating fluxes reasonably well worldwide.

The spatial distribution of fluxes in Fig. 6.8 shows some new and interesting results. Fluxes in China are generally lower than in other monsoon Asian countries. In particular we see "hot spots" of flux along the India/Pakistan border, near the coastal regions of southeastern India, and in Vietnam. Fluxes are lower in China mainly for two reasons. First, average soil temperatures here are lower than in lower latitude countries, but secondly, much of the paddy fields in China are drained at least once throughout the season. It is estimated that only 20% of paddy fields in China are continuously flooded (*Li et al., 2002*). The fraction of fields that are continuously flooded is higher in most other Asian countries. In Vietnam, nearly all paddies are continuously flooded and this leads to an average flux in Vietnam of 19 mg CH_4 m^{-2} h^{-1}, which is about 3.5 times higher than China's average flux.
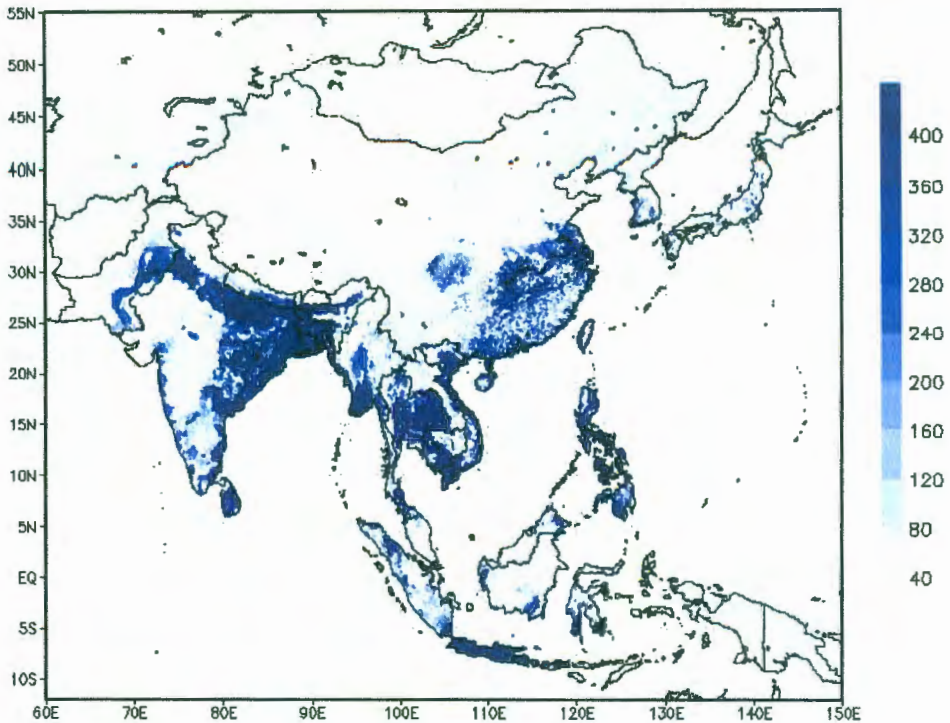
Figure 6.9. Methane emissions from south and southeast Asia paddy fields. Units are metric tons CH_4 y^{-1}.

Emissions were calculated by integrating fluxes over growing seasons and harvested areas of each grid cell. Emissions from multiply cropped fields were summed for annual totals. Gridded emissions are displayed in Fig. 6.9 for monsoon Asia and national sums for select countries are given in Fig. 6.10.

We estimated that the annual emission from rice paddies globally is 49 ± 18 Tg CH_4 y^{-1}. This lies towards the low end of the historical range of estimates, but is roughly in the middle of more recent estimates (Fig. 6.11). Over time, estimates of global emissions have generally decreased. In part, this is due to the limited number of fluxes

from which early estimates were calculated. Fluxes were seldom measured over an entire growing season, or if they were, they were measured only from a single field under one set of conditions. For example, the first published global estimate of 190 Tg y^{-1} *(Koyama, 1963)* was based on laboratory incubation of paddy soils. *Schutz et al. (1989)* extrapolated the flux from a single Italian rice field to estimate global emissions of 100 Tg y^{-1}. Early studies also used a rice-growing season length of 140 – 150 days, based upon growing seasons in California where many of the early measurements were made (*Cicerone and Shetter, 1981; Seiler et al., 1983*). Growing season length is quite variable worldwide, and in the tropics may be only 77 days (*Matthews et al., 1991*).
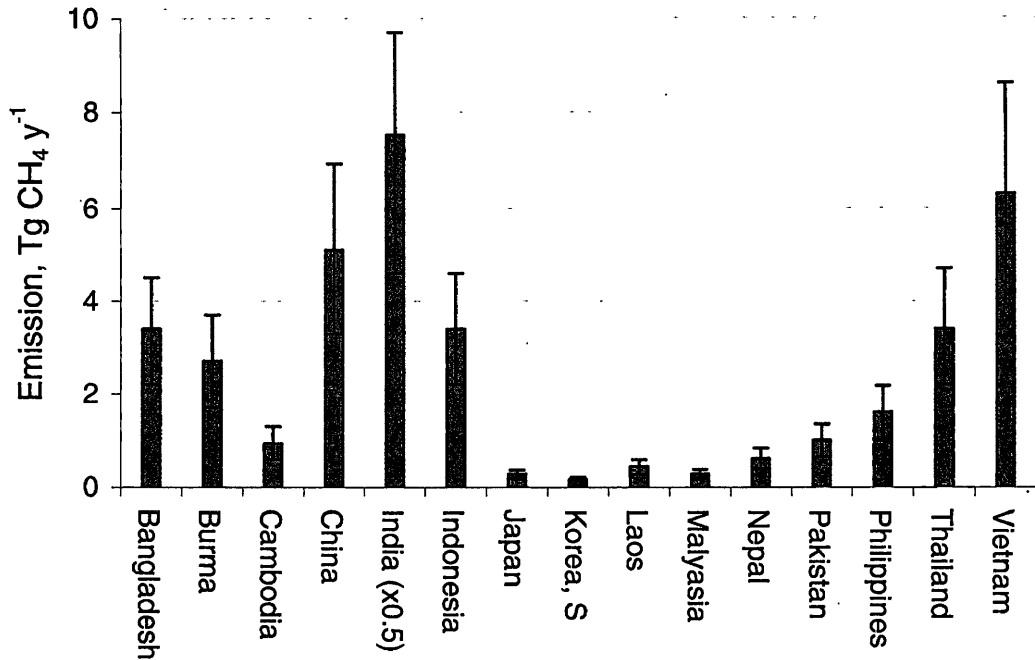
Figure 6.10. Annual emissions from rice agriculture for select countries of monsoon Asia.

With more studies, it became apparent that CH_4 fluxes varied widely over fields where rice was grown under different ecosystems and conditions. This led to a revision downward of estimates. Recognizing this, *Neue et al. (1990)* reduced the estimated range of emissions to $25 - 60$ Tg y^{-1}. More recently *Yan et al. (2009)* estimated global emissions to be 26 Tg CH_4 y^{-1} using the 2006 IPCC Guidelines (*IPCC, 2007*). This is somewhat lower than our estimate. Though it is difficult to determine the exact cause for the difference, it likely has to do with temperature effects. There are no temperature scaling factors in the IPCC Guidelines, meaning there is no variation of flux with temperature throughout the rice-growing regions, despite an abundance of observational and experimental evidence that shows temperature is important (e.g. *Seiler et al., 1984;*

Holzapfel-Pschorn and Seiler, 1986, Khalil and Rasmussen, 1991; Khalil et al., 1998). Fluxes in our model are sensitive to temperature ($Q_{10} = 3.7$) and are significantly higher than the IPCC baseline emission in regions where the seasonally averaged temperature is higher than about 25°C. This causes the integrated emissions over these regions to be much higher than the estimates of *Yan et al. (2009).* We discuss the temperature effect further below.

Though rice is grown globally as seen in Fig. 6.8, most emissions are from south and southeast Asia where rice is a staple crop and provides a large percentage of the daily calories. We estimate that this region is responsible for about 90% of the world's emissions, with major contributions from India, China, Vietnam, and Bangladesh along major rivers and deltas (Fig. 6.10).
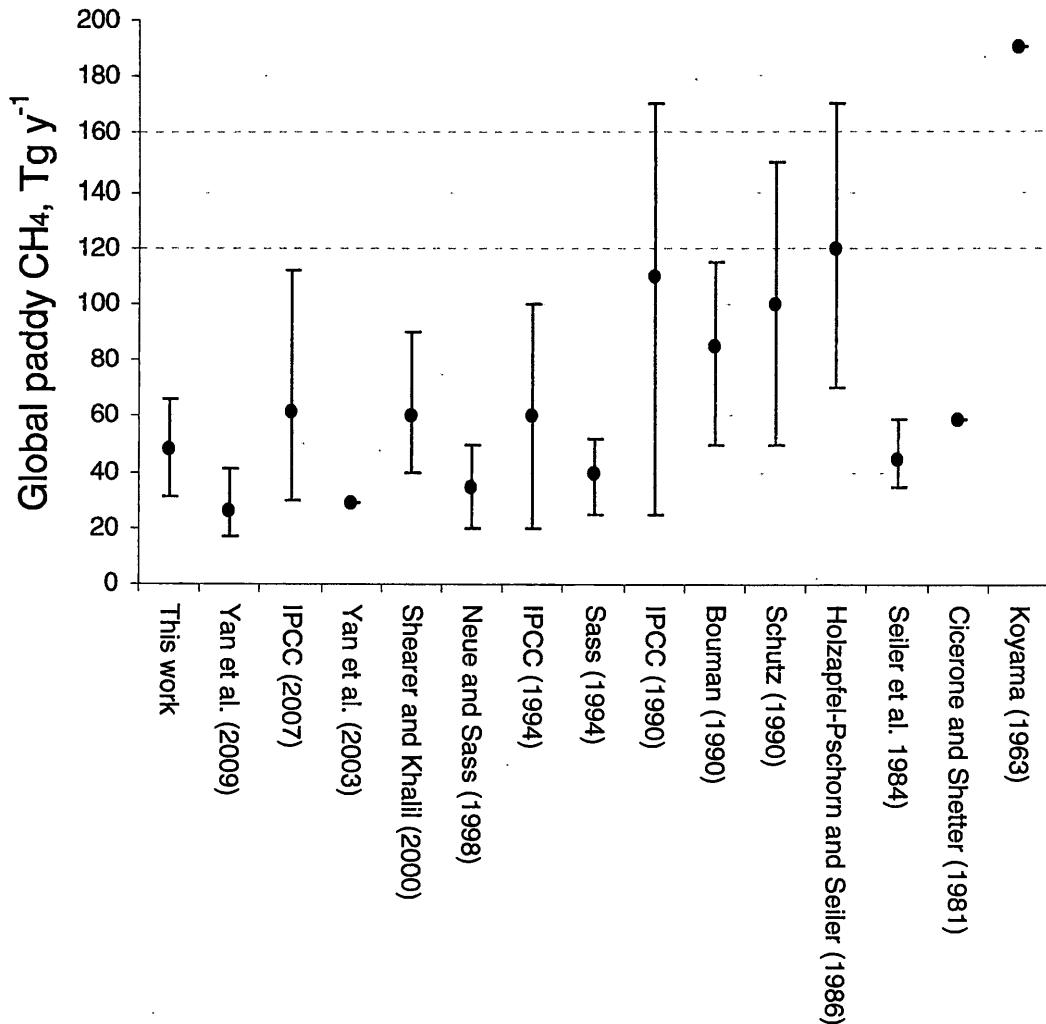
Figure 6.11. Published estimates of global CH$_4$ emissions from rice agriculture.

Noteworthy is the distribution of emissions between countries within this region. We estimate emissions from China to be 5.1 ± 1.8 Tg y^{-1}. This is considerably smaller than an early estimate of 30 Tg y^{-1} (*Khalil and Rasmussen, 1991*), but is consistent with more recent work. *Yan et al. (2009)* and *Huang et al. (2006)* estimated emissions from China to be 7.4 Tg y^{-1} and 6.0 Tg y^{-1}, respectively. National emissions reported by the

225

Chinese government to the UN Framework Convention on Climate Change were 6.1 Tg y^{-1} in 1994 (UNFCCC, 2000). Chinese paddy emissions in the popular EDGAR3.0FT2000 data set (Emission Database for Global Atmospheric Research, *Olivier et al., 2005*) are over twice as large (13.7 Tg y^{-1}). The EDGAR inventory uses an emission factor of 340 kg CH_4 ha^{-1} for China based upon a report by *Neue (1997)*. If we assume a season length of 120 days, this translates into a flux of about 12 mg CH_4 m^{-2} h^{-1}, which is about double our value. The discrepancy arises because the reported emission factor in *Neue (1997)* is for irrigated fields only, which in general have higher fluxes that rainfed or deepwater rice (*Neue, 1997; Wassman et al., 2000*). With full accounting of all rice ecosystems, national emissions of 5 –7 Tg y^{-1} are more reasonable.

While China is commonly considered the world's largest source of paddy CH_4, we estimate that India has significantly higher emissions than China (Fig. 6.10). In part, the misconception stems from a report by *Mitra (1992)*, wherein the author reported that total paddy emissions in India totaled only 3 Tg y^{-1}. This surprisingly low total was due to a nearly zero emission rate measured from India's irrigated rice fields, which make up about 45% of India's total harvested area. It was later revealed that the low fluxes were measured from fields that had high percolation rates, and were flooded for perhaps only 1-2 days per week (*Neue, 1997*).

Our estimate of emission for India is 15 ± 5 Tg y^{-1}. This is higher than the estimate of 6 Tg y^{-1} and 9 Tg y^{-1} by *Yan et al. (2009)* and *Olivier et al. (2005)*, respectively. National emission of 4.1 Tg y^{-1} was reported by India to the UNFCCC in

1994 (*UNFCCC, 2000*). These however were based on measurements by *Mitra (1992)* and are presumably underestimated for reasons given above. *Olivier et al. (2005)* used a global default emission factor for India's irrigated rice fields, due to confusion with the *Mitra (1992)* data set. The default value is lower than all other national emission factors in monsoon Asian countries, except the Philippines. For reasons related to temperature described below, this is unlikely. Therefore the EDGAR value is likely underestimated.

Our findings are consistent with known changes to rice management that have occurred in China over the past couple decades In the early 1980s Chinese farmers realized that intermittent draining of their rice fields midway through the rice season increased grain yields (*Neue, 1997*; *Li et al., 2002*). As a result, only about 20% of paddy fields are now left flooded throughout the season (*Yan et al., 2009*), which dramatically lowers methane fluxes. *Li et al. (2002)* estimated that CH_4 emissions from Chinese paddies decreased by about 5 Tg y^{-1}. since the early 1980s. Our results support this reduction in emissions as we discuss in the next chapter.

Besides these differences, Chinese emissions are also smaller due to lower seasonally averaged temperatures. Our experimental results showed that methane emissions respond strongly to temperature, and this is reflected in the flux model. The area-weighted seasonally-averaged soil temperature is 21.3°C, and 24.5°C for India. The baseline emission factor used by *Yan et al. (2009)* does not account for temperature, and produces low emissions. China also has a larger fraction (~30%) of its total harvested rice area planted in the early spring when temperatures are cooler than India (<5 %) (*Matthews et al. 1991*).

One final consideration is the use of mineral N-fertilizer. Our experimental work showed that the addition of N-fertilizer enhanced CH_4 flux in continuously flooded fields but reduced the flux in intermittently flooded paddies. Globally, N-fertilization has little impact on emissions; however, at the country level it does. In China, N-fertilization decreased emissions by 0.6 Tg CH_4 y^{-1}, while in Vietnam it increased emissions by 1 Tg CH_4 y^{-1}. The difference is due to the larger fraction of continuously flooded paddy area in Vietnam.

One final noteworthy result is the relatively large emissions from Vietnam (6.3 Tg y^{-1}), which puts it on par with China, despite China having over four times more harvested area than Vietnam. Again this result is due to water management. It is believed that all of Vietnam's paddies are managed as continuously flooded, making it unique among Asian countries (*Yan et al., 2009*). If we set the water management of Vietnam equal to that of China, Vietnam's emissions would be halved. We again see the importance of water management on rice paddies, and quantifying this factor accurately across all rice growing countries would be a major contribution to the methane budget. We are investigating the use of backscattering data from space-borne instruments to map inundation at high resolution spatial scales.

If methane emissions are about 50 Tg y^{-1} as we suggest, rice agriculture is one of the most important anthropogenic sources of methane. The large range of emissions reported for other sources makes it impossible to rank rice agriculture unequivocally. The only anthropogenic source that consistently has emissions ranked higher than 50 Tg y^{-1} is ruminants (80 – 100 Tg y^{-1}). This means that rice agriculture makes a significant

contribution to atmospheric levels of methane. It is believed that the increase in rice cultivation 5000 years ago led to the reversal of a natural decline in atmospheric CH_4 (*Ruddiman et al., 2008*). Growth in rice production during the twentieth century added to the increasing methane burden. Future scenarios of methane emissions must take into account rice agriculture and how emissions from it may respond to changing drivers. We take up this challenge in the next chapter.

Chapter 7—Trends of Methane Emissions From Rice Fields and Mitigation Potential

7.1   Introduction

Rice agriculture is one of the largest sources of anthropogenic methane and may be an important source to target for mitigation (*Neue et al., 1997; Ding et al., 1999*). Its production has nearly tripled over the past fifty years with a nearly constant 3% annual growth rate (*IRRI, 2010*). In parts of the world where rice is grown, changing paddy management practices have likely led to reduced methane emissions. Quantifying these changes is difficult however, as the production and release of methane from paddy fields depends on a large number of spatially and temporally heterogeneous variables which are poorly quantified over large areas.

In this study we used a novel empirical model derived from multiple years of greenhouse and field studies to assess the trends in rice agriculture emissions. We considered mainly the impact of changes in the use of organic carbon and nitrogen fertilizers, water management, and temperature to paddy emissions. Our time frame of interest was from 1980 to the present when management practices changed dramatically. Our results indicated significant decreases in methane emissions over this time. We also considered the future trend of emissions based on expected scenarios, and assess how much further decrease in methane emissions we could expect under mitigation strategies.
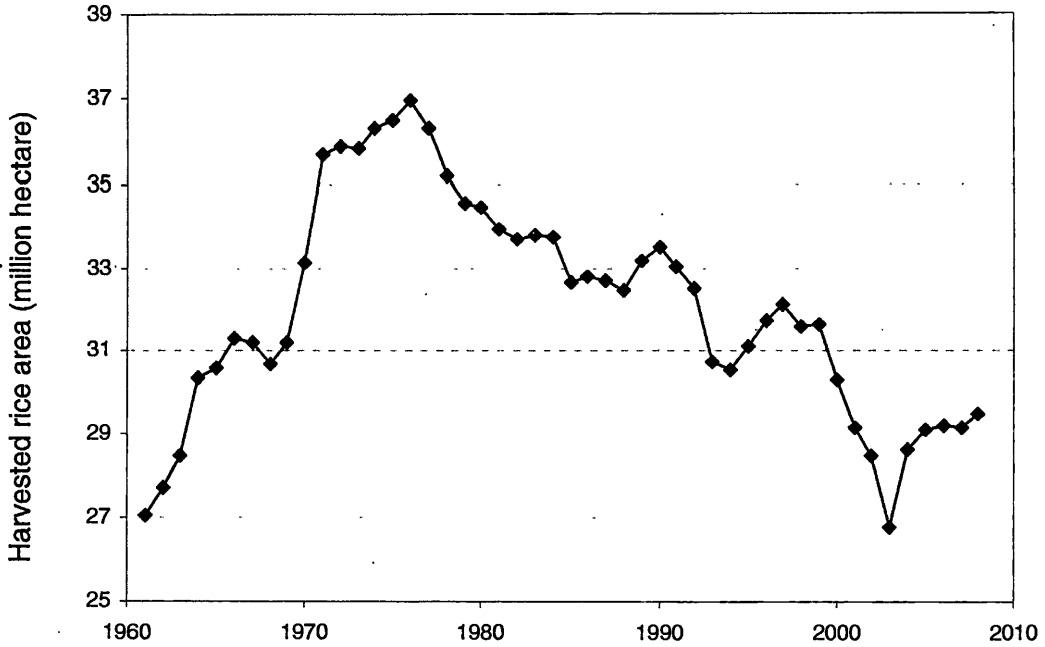
Figure 7.1. Harvested hectares of rice in China. Data from the Food and Agriculture Organization (*FAO, 2009*).

We limited our analysis to China, for which we have reasonable information regarding changes in water management and fertilizer usage. We explored global mitigation possibilities by developing scenarios of drivers.

7.2   Changes in drivers

We can generically express emissions $E(t)$ (g y^{-1}) from any source by

$$E(t) = \mathrm{EF}(t) \times A(t),$$
(7.1)

231

where EF*(t)* is the effective emission factor (g ha^{-1} y^{-1}) across all regions of emissions, and *A(t)* represents the activity data. Here, the activity is the harvested area of rice (ha). Since the emission factor varies with paddy system, we can think of the effective emission factor as an area-weighted average of all emission factors for all paddy systems. In general all three quantities in the equation are functions of time. The effective emission factor can change for many reasons; for example, changes in fertilizer type, application rates water management practices, temperature, or ecosystem types. Changes in rice harvested area will directly affect emissions.

We consider below changes in both emission factor and area. There is limited information available about how the underlying drivers have changed over the past decades. Fortunately we have reasonable data on how the major drivers have changed, namely water management, fertilizer, temperature, and harvested area. We describe briefly the information available for each and then force our flux model with these changes. We also consider what impact predicted temperature changes have on emissions from China and globally. Finally we discuss the potential of mitigating emissions from rice agriculture.

7.2.1 Harvested area

There is good data on the rice harvested area in China through the years as these data are collected, compiled, and released by the Food and Agriculture Organization of the United Nations (*FAO, 2010*). Fig. 7.1 shows that the harvested area of rice production in China increased at a near constant rate of about 2% y^{-1} from 1960 – 1975, but has been decreasing by 1% y^{-1} ever since. There has been a slight increase in recent

years. The post-World War II growth followed the Great Famine of 1959-1961, which was brought about by the social and economic policies of the Great Leap Forward *(Tyler, 1995)*. After this period, Chinese leaders heavily promoted the use of chemical fertilizers to farmers through increased production and price subsidies. Rice agriculture followed population growth which increased by 3% annually from 1961–1975 *(FAO, 2010)*.

The multi-decadal decline starting in 1975 was caused by a number of reasons. First population growth began decreasing during this largely due to China's one-child policy. Cultural reforms by the Chinese government in 1978 abolished the commune system and led to partial privatization of farmlands. This encouraged farmers to pursue more profitable crops such as fruit and vegetables after grain quotas were met *(Hamburger, 2002; Khalil and Shearer, 2006)*. Higher yielding rice cultivars allowed grain quotas to be satisfied with fewer hectares of harvested area *(Peng, 2007)*. Migration of labor out of agricultural lands to urban centers may have contributed as well, along with lost land due to heat and water stresses *(Peng, 2007)*.

7.2.2   Water management

Since the early 1980s there has been an increased adoption of midseason drainage of paddy fields in China *(Neue, 1997; Shen et al., 1998; Loeve et al., 2004; Khalil and Shearer, 2006; Peng, 2007)*. There are at least three reasons for this. For one, water shortages limit the amount water available for irrigation. This trend is likely to continue in the future as demand for rice increases by 70% over the next thirty years *(IRRI, 2002)*. The second reason is due to the deterioration of China's irrigation

infrastructure. Much of this was built in the 1970s and maintenance and improvement since then has been limited (*Peng, 2007*). Third, midseason drainages improve crop yields.

The transition from continuously flooded fields to midseason drainage started around 1980 in northern China in order to reduce water use, but later the practice spread to the Yangtze River valley and to the southern provinces in 1990s (*Shen et al., 1998; Li et al., 2006*). By 2000, 80% of rice paddies were drained at least once throughout the season (*Li et al., 2006*). The timeline of this transition as quantified by the percentage of paddy fields drained was reconstructed *by Li et al. (2006)*. They estimate the percentage to be 1%, 5%, 33%, 60%, and 80%, in 1980, 1985, 1990, 1995, and 2000, respectively. We adopted these values for our trend analysis and interpolated fractions in between the given years.
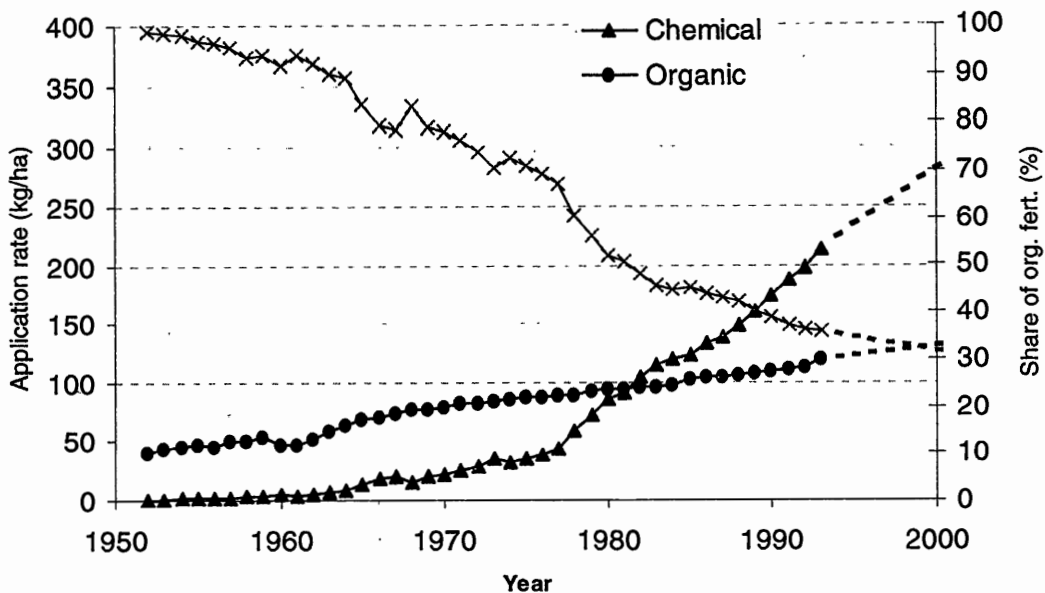
Figure 7.2. Fertilizer usage in China from 1961 to 2000. The blue line with cross symbols is the share of organic fertilizer usage as a percentage of total fertilizer use. Data for 1994-200 are projections based on linear trends in the preceding periods. Data are from *Wang et al. (1996)*. The rates of organic fertilizer use are expressed in chemical fertilizer equivalent nutrient weight.

7.2.3 Fertilization

Chinese farmers have traditionally used organic fertilizers from a variety of

sources including animal and human manures, crop cover green manures, and oil cakes,

which are made from the residues remaining when grains and other solids are pressed to

extract oils and liquids. Chemical fertilizer use in China has rapidly increased over the

past fifty years (Fig. 7.2) and China is now the world's largest consumer of chemical

fertilizers (*FAO, 2010*). Over a twenty year period, China's application of chemical

fertilizers increased from 63 kg ha^{-1} in 1973 to 331 kg ha^{-1} in 1993, a fivefold increase.

Globally, application rates only doubled over the same period. The use of chemical

235

fertilizers in China has largely replaced the traditional use of organic fertilizers such as farm and human manure and green manure. The switch from organic to synthetic fertilizers began in earnest in the 1960s with changes in technological and land reform policies brought about the recognition by Chinese leaders that crop yields needed to grow to feed the increasing population, and paddy fields were depleted in nutrients due to thousands of years of use (*Wang et al., 1996*). Increasing demand of chemical fertilizers by farmers has also driven these trends, as farmers attempt to maximize crop yields to take advantage of the liberalization of land policy brought about the "household responsibility contract system", which allows farmers to decide how much and what kind of crop to grow.

Fertilization has increased so much there are now concerns of overfertilization (*Wang et al., 1996; Peng, 2007*). Chinese fertilization rates were about 75% higher than the global average. Excessive use of N-fertilizers may actually reduce crop yields and make plants susceptible to pests and disease (*Peng, 2007*). Nutrient run-off from fields has contaminated water supplies and caused other environmental problems.

These trends in fertilizer usage will impact methane emissions from rice agriculture. As discussed in the previous chapter, application of organic manure to paddy fields strongly increased methane fluxes. The effect of chemical N-fertilizers on the methane flux is more complicated. Methane fluxes increased in fields under continuous flooding management, but decreased when fields were drained. As fertilizer data are only available to 1993, we projected these trends forward to 2000 using a

simple linear trend calculated over 1977-1993 for the chemical fertilizer rate, and 1965-1993 for organic fertilizer.

The fertilizer data of *Wang et al. (1996)* and similar data from *Kueh (1984)* indicate that the use of organic fertilizer has not declined in China as chemical fertilizer has increased, rather organic fertilizer application rates continue to increase through this period, though not nearly as rapidly as chemical fertilizer. According to these data, which are based on information from the State Statistical Bureau of China (*SSB, 1994*), organic fertilizer use has increased by 50% since 1980 and doubled since 1960. Thus organic fertilizer is still a major source of nutrients for crops.

This conclusion is corroborated by a survey conducted by *Huang et al. (2006)*, in which the authors asked more than 300 rice farmers across all provinces of China about the type and amount of fertilizer they applied to their fields. The application rates of farm manure ranged from 60 to 1000 kg C ha^{-1}, with a mean rate of 520 kg C ha^{-1}. This translates roughly into 1.3 t (dry weight organic material) ha^{-1}.

Is this value consistent with the rates estimated by *Wang et al. (1996)*? In *Wang et al. (1996)* organic fertilizer rates are reported in units of equivalent chemical fertilizer weight, i.e. the weight of chemical fertilizer required to achieve the same level of nutrient usage as the organic fertilizer. The details of this conversion, which include data on nutrient absorbtivity for different types of manures and nutrients, are not included in the paper, but we can make a reasonable estimate. We assume the following: moisture content of manure is 80%, the manure weighted-average total nutrient coefficient ($N + P_2O_5 + K_2O$) for is 1.3% (*Kueh, 1984*), the nutrient and

manure-weighted ratio of the plant absorption rate for natural fertilizer to chemical fertilizer is 0.5 (*Wang et al., 2006*), and farm manure is 86% of the total organic fertilizer weight (*Wang et al., 1996*). With these assumptions the organic fertilizer rate estimated by *Wang et al. (1996)* for the year 1993 is 3.2 t (dry farm manure) ha^{-1}. This compares reasonably well with the average rate from farm surveys, but is two and a half times larger.

Some insight into these differences perhaps comes from a paper by *Khalil and Shearer (2006)*. Here, the authors state that organic fertilizers were applied at their highest rate in China during the late 1970s and then declined as chemical fertilizers became popular and affordable. This conclusion comes from work by the International Rice Research Institute in the Philippines (*Wen, 1984; Yuan, 1984*). Based on interviews with farmers by *Khalil and Shearer (2006)*, organic fertilizers would not be used on rice paddies if chemical fertilizers were available.

There is no doubt that animal populations have increased continuously in China (*FAO, 2009*) and therewith, animal manure. The large amount of manure produced per animal requires frequent removal to avoid accumulation, which generally means dispersal over agricultural fields. It is possible that the use of organic fertilizer has increased for some crops but not others. Unlike upland crops, laborers in flooded paddy fields are in constant contact with the slurry of manure and paddy water, and likely the use of manure in paddy fields would be avoided if possible due to sanitation. Also the rate of degradation of organic matter is much higher in upland aerobic conditions, versus the flooded anaerobic conditions frequently found in paddies. Therefore the

application rate of organic fertilizer could be higher on upland fields than in rice

paddies. It is now common in China to grow one or two upland crops such as wheat,

rape, or vegetables, in rotation with rice. It is possible manure would preferentially be

used on these fields. If so, organic fertilizer usage overall could be increasing, while

usage in rice fields is on the decline. Even if this were true, there is still the possibility

that the application of manure during non-rice seasons could increase soil organic

carbon during the rice season.

Because of these competing storylines we considered two different scenarios for

organic fertilizer usage. Scenario one followed the trend shown in Fig. 7.3 as described

above, but scenario two is consistent with the experiences related by *Khalil and Shearer*

(2006). In the second scenario we separated farm manure from other types of organic

fertilizers such as crop residues. We allowed farm manure application rates to increase

until 1975 as in *Wang et al. (1996)*, where according to their data the farm manure

application rate was 2.3 t (dry matter) ha $^{-1}$, but then we decreased rates linearly to 1.2 t

(dry matter) ha^{-1} by 2000, which is the current rate determined by the farmers'

interviews above. This linear decrease is consistent with the increase of chemical

fertilizer use during the same period. In all years, we assumed the crop residue

application rate is constant.

In both scenarios, the organic fertilizer rate in 2000 is set to the rate calculated

previously using crop residues and manure rates set by survey data. For scenario one,

the total rate increased from 1961 to its current value. Thus for all dates, the usage of

organic fertilizer is lower than it is currently. For scenario two, we kept the crop residue
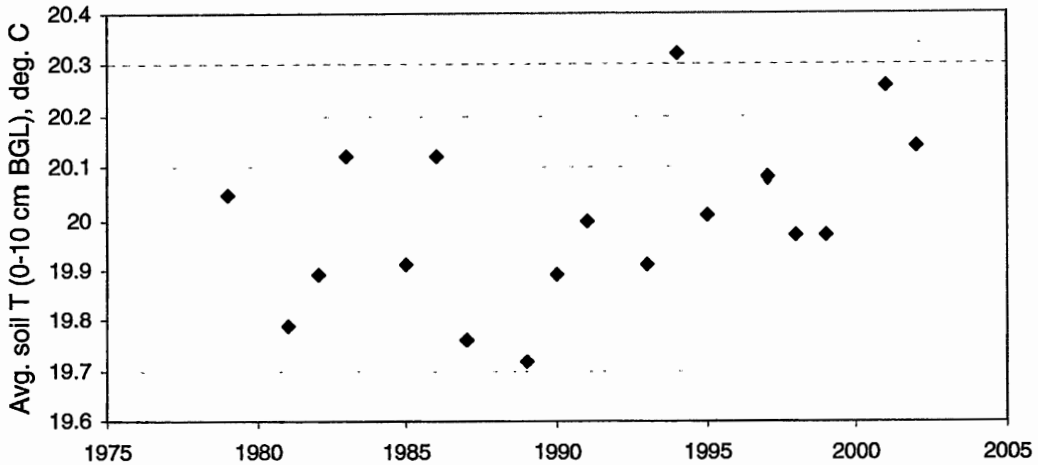
Figure 7.3. Average seasonally-averaged soil temperatures for paddy fields in China. Temperature corresponds to 0-10 cm below ground level.

rate constant, but allowed the farm manure rate to vary. In this scenario, we assumed that the farm manure rate has been higher in the past, so the usage of total organic fertilizer was higher in the past.

7.3   Temperature

Laboratory and field studies show that methane fluxes respond to temperature. The overall effect is a combination of temperature-dependent processes connected to the production, oxidation, and transport of methane within the rice ecosystem. Temperatures are likely to affect microbial processes, decomposition of organic materials, diffusion and transport of methane through the soils and into the rice plants, as well as other possible effects. The temperature dependency of flux is typically quantified through a Q_{10} value defined by

240
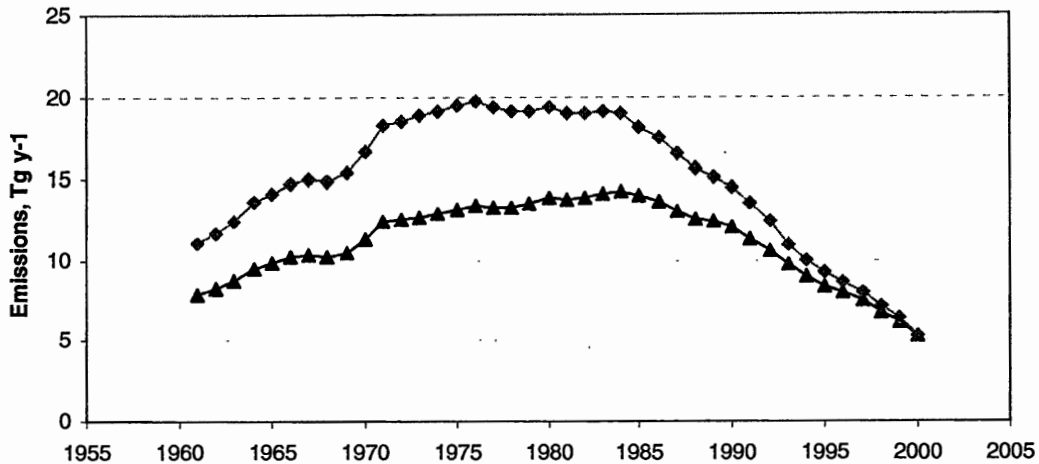
Figure 7.4. Estimated methane emissions from rice agriculture in China. The black line with triangles shows emissions calculated using the first organic fertilizer application rate scenario, which assumes the rate has increased since 1961. The gray line with diamonds shows emissions calculated using the second scenario where the use of farm manure decreases after 1975.

$$Q_{10} \equiv \frac{F(T_o + 10)}{F(T_o)}. \qquad (7.2)$$

Here $F(T)$ is the methane flux at temperature T, and T_o is a reference temperature. Thus Q_{10} tells us how much we can expect the flux to change for an increase of temperature of 10°C. From our field and greenhouse studies, we find Q_{10} to be 3.7 for temperatures typical of regions where rice is grown.

Daily average temperatures are available for China at 2.5-degree spatial resolution from the National Center for Environmental Prediction and Dept. of Energy Reanalysis project (http://www.esrl.noaa.gov/psd/data/gridded/data.ncep.reanalysis.html) (NCEP-DOE Reanalysis 2) over the years 1979 – 2002. These were used to calculate average

soil temperatures over the growing season of each rice crop. Area-weighted annual averages of these temperatures over all seasons and crops are shown in Fig. 7.3.

Though the trend is not statistically significant, there is a slight increase of 0.2°C in the average soil temperature. We extrapolated this trend backwards, in 1961 the average soil temperature would be about 2% lower than in 2002, or about 0.4°C. We included this trend in our simulation.
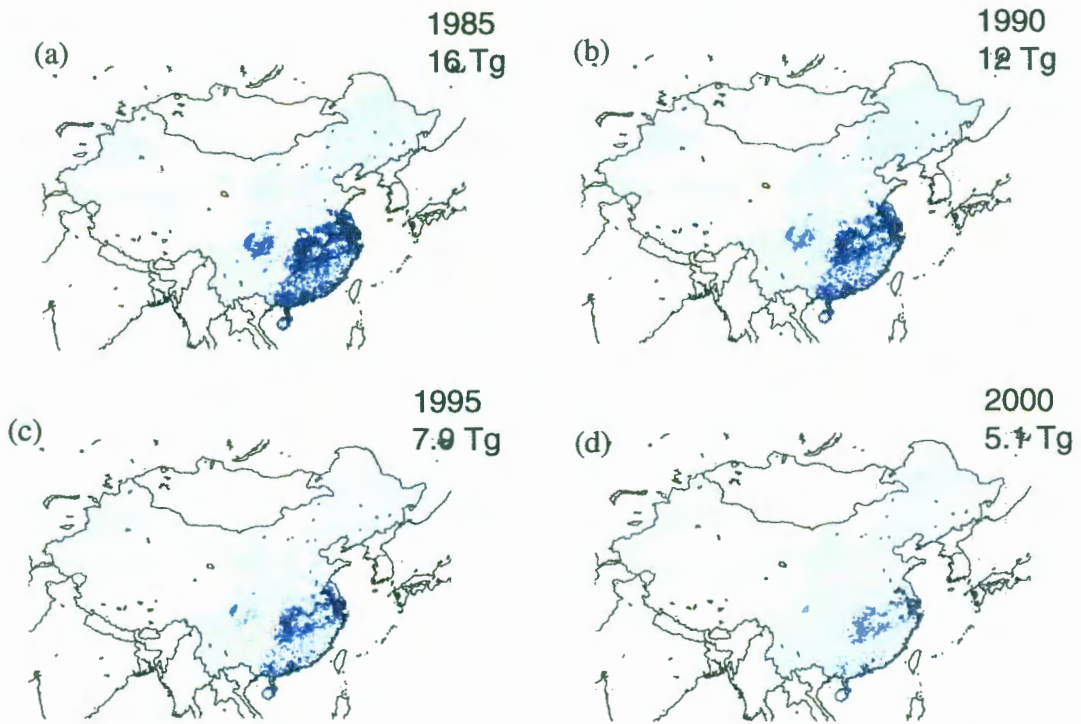
Figure 7.5. Methane emissions from rice agriculture in China. The modeled trend in emissions is due to changing water management practices over this time. While in 1985 95% of all paddy fields were kept under continuously flooded conditions throughout the growing season (a), this percentage dropped to 67% in 1990 (b), 40% in 1995, and 20% in 2000 (d) as midseason drainage became popular.

7.4 Emission trends (1961-2000)

We calculated emissions over the period 1961 to 2000 based upon the trends in drivers described above using our rice flux model described in the previous chapter. The trend of emissions over this time reflects the interplay of the underlying trends of the drivers. In isolation, changes in paddy area increased emissions up to 1975 and led to a sharp decline thereafter. The rapid increase in chemical fertilizer usage caused methane emissions to decline from 1961 onwards. The switch in practice from continuously flooding fields to midseason drainage reduced emissions starting in the early 1980s.

Increasing use of organic fertilizer throughout the model period as described by scenario one would tend to increase emissions continuously, while the decreasing use of farm manure since 1975 would cause emissions to decrease from that time onwards.

The results are shown in Fig. 7.4. Emissions in both scenarios increased from 1961, peaked some time later, then decreased rapidly in the late 1980s and 1990s. For scenario two, emissions peaked around 1975 when the use of farm manure was highest, while the emissions peaked about ten years later for scenario one, since manure rates continued to increase. Over a twenty year period emissions fell by 10-15 $Tg\ y^{-1}$. Emissions in China may have been three to four times higher in the past than they are today.

According to our model results, the most important driver of this decrease is the transition to midseason drainage. If we fix all drivers except the water management of paddy fields, the model emissions fall by 10 $Tg\ y^{-1}$ over the twenty-year period from 1980- to 2000 (Fig. 7.5). The impact of temperature is minor. The 0.4°C over this interval increased emissions by 0.2 $Tg\ y^{-1}$. Temperature is expected to have a larger impact in the future and we discuss this possibility below.

The increase in chemical N-fertilizer decreased emissions by 0.4 $Tg\ y^{-1}$. Though not discussed in detail here, emissions of nitrous oxide increase with N-fertilizer use. We have also developed functional relations between drivers and N_2O fluxes based upon our field and greenhouse work. These functions are not as robust as those for CH_4 due to highly transient nature of N_2O release from rice paddies. When we applied these functions to worldwide rice production, we estimated that the global N_2O emission is

244

0.05 Tg y^{-1}. Unlike methane, we found China is the largest emitter of paddy N_2O. We estimated the increase in the use of chemical N-fertilizer has increased N_2O emissions by a factor five. Considering N_2O is ~15 times more potent than CH_4 as a greenhouse gas (using $GWP_{CH4} = 20$, $GWP_{N2O} = 310$), the increasing use of N-fertilizer in rice agriculture could be an important contributor to global warming.

As discussed above, total rice harvested area increased from 1961 to 1975. We estimated this increased CH_4 emissions by 4.8 Tg y^{-1} over this period, which is about half the total estimated increase in emissions during this time. The increase in harvested area happened by the spreading of rice agriculture into new lands, and a transition into double or triple cropped rice systems on existing lands. Both were in response to demands by Chinese leaders to increase crop yields. Following 1975, the total harvested area decreased for reasons given above. This caused emissions to drop by about 4 Tg y^{-1} from 1975 to 2000.

7.5   Future trends and mitigation possibilities

Future emission of CH_4 from rice agriculture will be the product of a complex array of factors and driving forces such as population, socio-economic development, technology, and natural variables. For example, rising prices or environmental consequences of chemical fertilizers may reduce N-fertilizer application rates in some countries, while application rates in other countries increase due to economic growth. The water available for paddy irrigation will likely decrease in many countries due to competing demands of population and hydroelectric production. There is little information available about how emission drivers will change in the future. In this
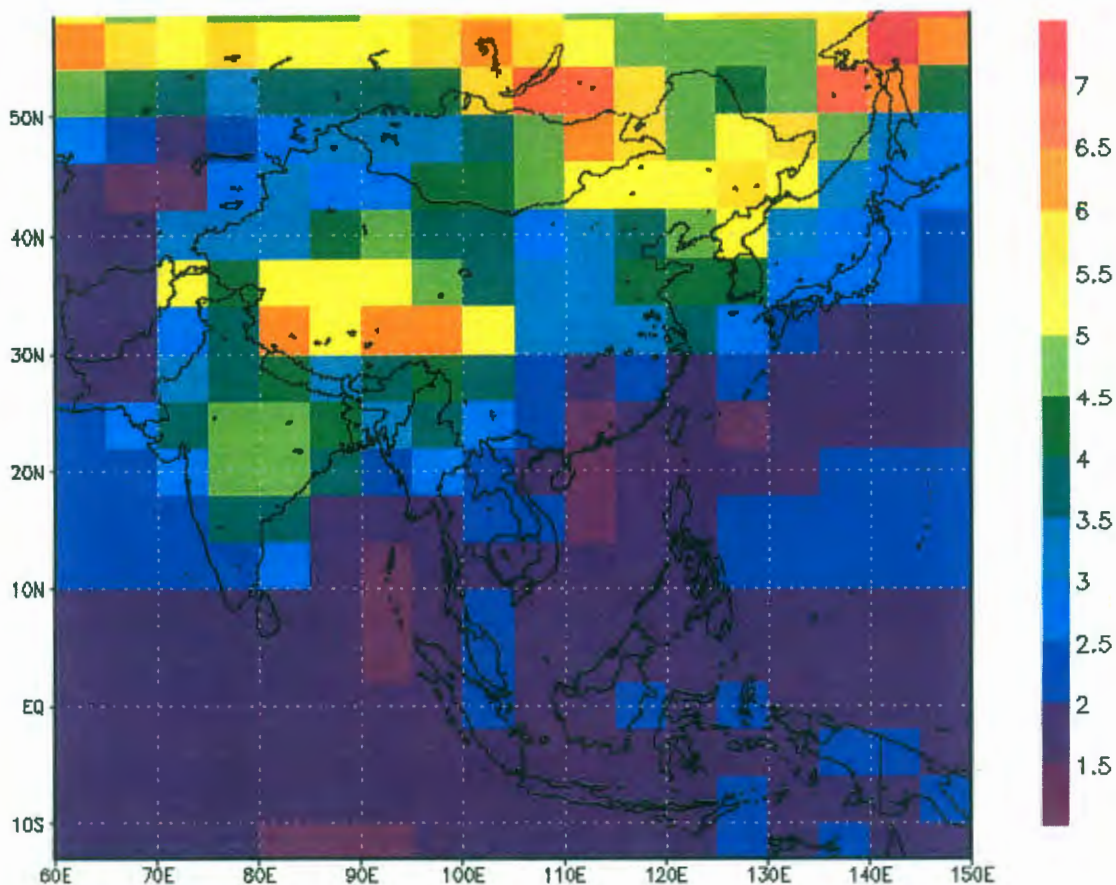
Figure 7.6. Ensemble of multi-model temperature predictions, ΔT (°C) 2100-2000.

section we consider only the effect of two drivers, temperature and water management, on future emissions and the mitigation potential of rice agriculture.

We used multi-model predictions of future surface temperature change for the year 2100 to drive our soil temperature calculations and force the model emissions. Fig. 7.6 shows ensemble deviations of predicted temperature in the year 2100 relative to base temperatures in 2000 for monsoon Asia. For island nations and coastal regions, predicted temperature increases are modest, less than 2 or 3°C. In the continental

interiors however, temperatures are expected to increase significantly. On the Indian

sub-continent, modeled temperature deviations exceed 4-5 °C.
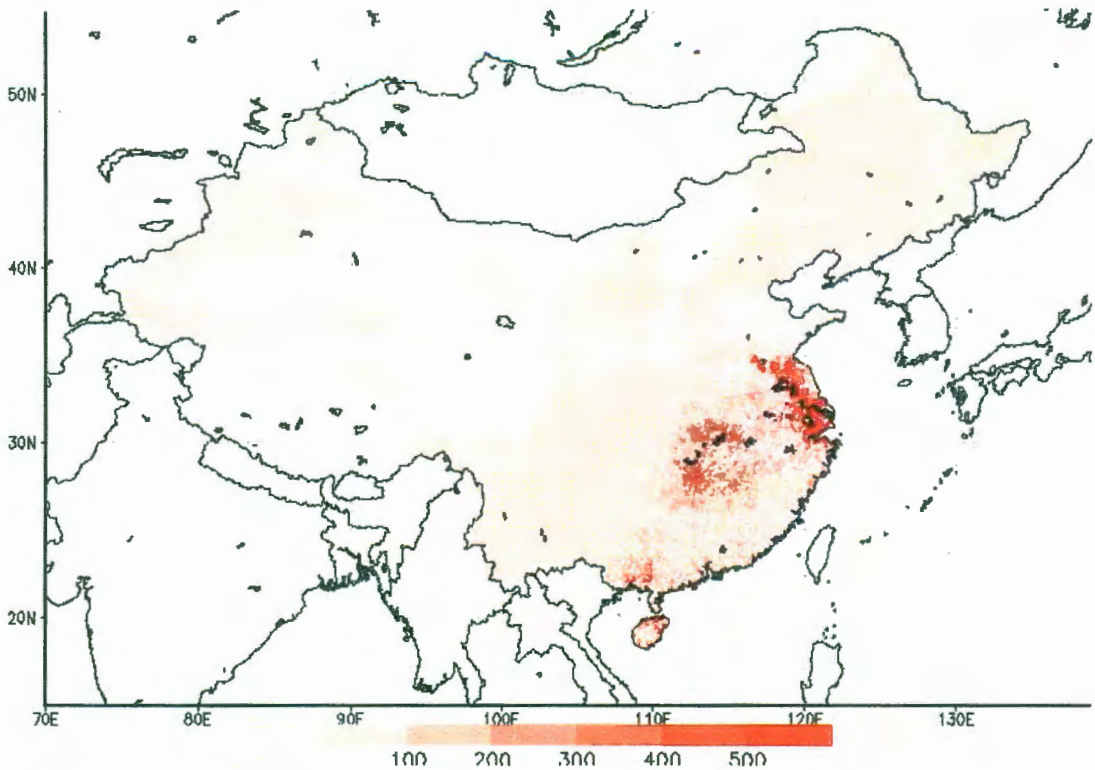
Figure 7.7. Predicted deviations in CH_4 emissions from rice agriculture using an ensemble average of temperature anomalies for year 2100. Units are t CH_4 y^{-1}. Deviations are relative to base temperatures from year 2000. Total increase in emissions over this period for China is 2.5 Tg y^{-1}.

These temperature deviations increased paddy CH_4 emissions from China to 7.6

Tg y^{-1}, an increase of 50%. Though these results are reasonable, we recognize that the

field and greenhouse flux measurements from which our model is based did not include

systems where temperatures were as high as reached in these ensemble predictions. Our

model predicts emissions increase as seasonally averaged temperatures exceed 30°C.

We expect heat stress on plants to be important at high enough temperatures, at which

point emissions would decrease. Currently we do not know how rice plants behave at abnormally high temperatures. For this reason, we do not calculate future emissions for India, though the large temperature increases predicted here likely will lead to a Q_{10} response even greater than China's. Fortunately predicted temperature increases in southeastern China, where most rice is grown, are relatively small, and these deviations do not push absolute temperatures above 30°C for the most part.

We discuss one perspective of this increase. Though 2.5 Tg y^{-1} is only a small fraction of the total methane budget and will not contribute significantly to climate change in the future, it may have significance with regards to mitigation and carbon trading policies. As we have argued elsewhere, rice agriculture is an attractive target for mitigation, since reductions in emissions are possible without added expense or damage to crop yields. For example, midseason drainage is known to decrease emissions at the same time increasing yields. Methane emission of 2.5 Tg is equivalent to 50 million tons of carbon dioxide. Currently, one ton of carbon dioxide sells for 22 $US on the European Union's Emission Trading System. In current dollars this climate-triggered CH_4 would potentially mean one billion dollars of lost revenue for China. Though small for an economy the size of China's, globally the economic impact would be significant.

7.6   Mitigation potential of rice agriculture

In this last section we estimate the potential emissions that could be mitigated from rice agriculture. Here we expand our scope to global rice production. These estimates are not predictions of future events, rather they simply provide upper limits to possible reductions.

Rice fields are generally grouped into four different ecosystems, irrigated rice where complete control over water and inundation levels is possible, rainfed rice which may be subject to either drought or flood conditions, deepwater rice grown under deep water conditions (i.e. > 1 m inundation), and upland rice which is never flooded and produces little methane emission.

When irrigated rice fields are continuously flooded, CH_4 emission is the highest of the four ecosystems (e.g. in units of kg CH_4 m^{-2}) (*Wassmann et al., 2000*). On average, seasonal emission from permanently flooded irrigated rice is about double the emission from rainfed rice, and 20% higher than deepwater rice (*Wassmann et al., 2000*). When irrigated fields are managed under mid-season drainage, emission is comparable to rainfed rice. Since 1980 China has largely eliminated the practice of permanently flooding rice fields, and now only 20% of rice fields are managed in this manner (*Li et al., 2006*). As we discussed above, this change in water management has reduced emissions drastically.

Irrigated rice is an attractive target for mitigating methane emissions. Though only 55% of global rice is irrigated, irrigated rice emits 97% of all paddy CH_4 from East Asia (e.g. China, Japan, Korea, etc.), 60% of CH_4 from South and Southeast Asia, and 70-80% of Asian paddy CH_4 overall (*Wassmann et al., 2000*). China shows that a large scale conversion to midseason drainage is possible.

We estimated the reduction of global methane emissions if all irrigated rice were converted to intermittent flooding practice. We assumed that all deepwater rice and some fraction of rainfed rice remain permanently flooded since in those systems water

249

is controlled by precipitation. Rainfed and deepwater rice make up 32% and 6% of total harvested rice area, respectively. Rainfed rice is prone to both drought and flood conditions. There is little information about the fraction of rainfed rice that remains flooded through the entire season, though it is likely small. We estimated this fraction using a summary of published fluxes by *Yan et al. (2005)*. The authors reported fluxes (RF) from rainfed rice during both the wet season (RF=0.28) and the dry season (RF=0.25) relative to fluxes from continuously flooded fields. We assumed that the slight increase in relative flux during the wet season is due to some fraction of paddies during the wet season that remained flooded and thus have a higher flux value. If we use the factor of two difference reported by *Wassmann et al. (2000)* between intermittently drained and continuously flooded rainfed rice, we calculated that about 12% of all rainfed rice remains flooded. For our mitigation calculation, we assumed that 12% of rainfed rice area remains flooded, and it is assigned the flux for continuously flooded fields.
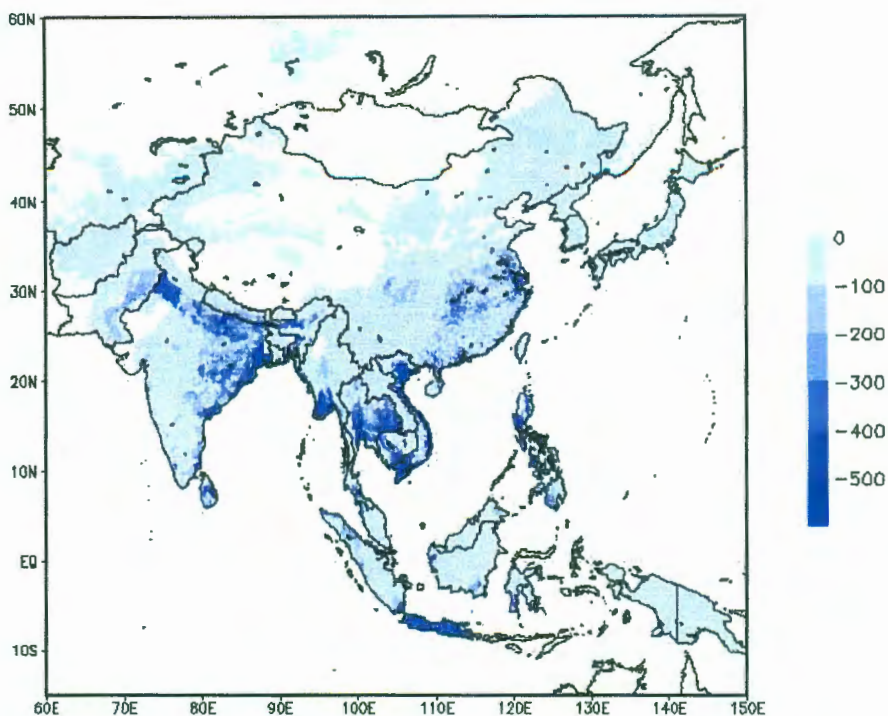
Figure 7.8. Mitigation of CH_4 emissions from rice paddies. Units are Gg CH_4 y^{-1}. Emission reductions were calculated under a future scenario in which all countries transition irrigated rice fields to midseason drainage.

We used rice ecosystem areas for each country and calculated the fraction of total harvested rice area that would remain flooded after mitigation, assuming that all irrigated rice is transitioned over to midseason drainage practice. This fraction ranged from zero in many of the interior continental countries like the former Soviet republics to 19% in Bangladesh due to its large delta regions. Results are given in Fig. 7.8. We estimated global emissions decrease by 23 Tg y^{-1} relative to current emissions following this mitigation scenario. Large decreases occur in India and Southeast Asia. Since China

251

has already largely transitioned to midseason drainage, mitigation benefits are modest there.

There is sparse literature on the mitigation potential of rice agriculture to which we can compare our value. In the 2007 IPCC report, *Smith et al. (2007)* estimated the mitigation potential of rice management is 250 Mt CO_2-eq y^{-1}. This is equivalent to 12.5 Tg CH_4 y^{-1}, or about half our estimate. However, this estimate also includes contributions from N_2O and CO_2 emissions, and mitigation options in addition to water management. *Yan et al. (2009)* estimated that if continuously flooded fields were drained, emissions would decrease by 4.1 Tg CH_4 y^{-1}. Though this estimate is much smaller, it is not surprising since the authors estimated global emissions to be only 25.6 Tg CH_4 y^{-1}, thus any reductions will be correspondingly smaller as well. The difference in global estimates is believed to be a result of temperature effects (see previous chapter).

Our estimate is uncertain due to a number of factors, not least of which is the rather poor information available about current water management and the breakdown of rice production by ecosystem. Also, intermittently draining fields is known to increase N_2O emissions (*Cai et al, 1997; Akiyama et al., 2005; Khalil et al., 2008*). We estimated that mitigating CH_4 emissions would increase global N_2O emission by 12 Gg N_2O y^{-1}, which is consistent with *Yan et al. (2009)* who estimated an increase of 9.5 Gg N_2O y^{-1}. Since 12 Gg N_2O y^{-1} is equivalent to 0.2 Tg CH_4 y^{-1}, the net effect is still to reduce GHG emissions.

One of the flexibility mechanisms built into the Kyoto Protocol to reduce costs of mitigation for emitters is the option to invest in clean technologies in developing countries. These Clean Development Mechanisms (CDMs) allow parties to offset their own emissions by paying to reduce emissions elsewhere where costs are lower. At current exchange rates and carbon market prices, our estimated mitigation potential of 23 Tg CH_4 y^{-1} is worth ten billion US dollars. Therefore Asian rice agriculture could potentially be an important target for CDMs.

Chapter 8 — Global Modeling Of Aerobic Methane Emissions From Terrestrial Plants

8.1 Introduction

Recent reports have challenged the conventional view that methane is produced primarily from decaying material under anaerobic conditions and not from living plants (*Frankenberg et al. 2005, Carmo et al. 2006, Crützen et al. 2006, Keppler et al. 2006, Miller et al. 2007; Cao et al. 2008, McLeod et al. 2008; Vigano et al. 2008, Vigano et al. 2009, Wang et al. 2009, Wang et al. 2009*). These studies include findings that methane concentrations are elevated over upland vegetation (*Frankenberg et al. 2005, Carmo et al. 2006, Miller et al. 2007, Sinha et al. 2007*), and that methane is directly emitted from intact plants and leaves under aerobic conditions (*Keppler et al. 2006; Cao et al. 2008; McLeod et al. 2008; Vigano et al. 2008; Vigano et al. 2009, Wang et al. 2009, Wang et al. 2009*).

Methane has been found to accumulate in the nighttime boundary layer of tropical forests (*Carmo et al 2006; Crutzen et al. 2006*), boreal forests (*Sinha et al. 2007*), and savannas (*Crutzen et al. 2006*) which, in the absence of soil or other emissions (e.g. *Scharffe et al. 1990*), suggests that vegetation is the source of emissions (*Crutzen et al., 2006*). Direct sampling of air from aircraft flights over eastern Amazonia has also revealed an enhancement of methane over forested lands (*Miller et al, 2007*). In addition to in situ measurements, global methane concentrations retrieved

254

from space-borne instruments are elevated over tropical forests and suggest that current methane inventories underestimate the emissions from these regions by about 70 Tg CH_4 per year *(Frankenberg et al. 2008)*. It is possible however, this imbalance is from underestimation of known sources such as tropical wetlands, biomass burning, or termites, as the measurements cannot distinguish sources.

More surprising was the *Keppler et al. (2006)* report that both C3 and C4 plants emitted and produced methane in situ under aerobic conditions, which increased with sunlight and temperature. The standard view holds that Archeaen bacteria produce methane biotically as a respiratory end-product of either H_2 oxidation and CO_2 reduction, or acetate fermentation in anaerobic zones of soils *(Schlesinger, 1997)*. Plants, if they emit methane at all, provide only a means for the methane to escape to the atmosphere, either through aerenchymal tissues or possibly by transpiration *(Nouchi et al., 1990; McGonigal and Guenther, 2008)*. *Keppler et al. (2006)* ruled out the possibility that their plant CH_4 was produced from microbial activity by isotopically labeling acetate substrate and sterilizing plant tissues with γ-radiation. Under these conditions methane release was still observed with no enrichment of $^{13}CH_4$.

Keppler et al (2006) measured plant fluxes with closed cuvettes, the use of which may stress plants since throughout the measurement CO_2 concentrations decrease while humidity and temperature increase. This concern motivated *Dueck et al (2007)* to use a flow-through chamber along with ^{13}C-labeled plants. Methane produced directly from the labeled plants should be isotopically distinct from the background, improving measurement sensitivity, which is important due to presumed low emission rates. With

this set-up *Dueck et al (2007)* found no detectable emissions from the six plant species tested.

This null result could be explained if the proposed mechanism is sensitive to [13]C *(Hopkin, 2007)*. To avoid this possible artifact, *Beerling et al. (2008)* tested normal maize and tobacco plants for emissions, and to improve sensitivity, used a large flow-through cuvette. When the plants were exposed to photosynthetically active radiation (λ=400–700 nm) no methane emissions were detected. The authors cautioned that no emissions would be expected if the action spectrum of the potential reaction fell outside the PAR range *(Beerling et al., 2008)*. In fact, later experiments showed that when plant matter is exposed to ultraviolet light, plants do produce methane *(McLeod et al., 2008; Vigano et al., 2008; Vigano et al., 2009)*. Emissions were found to increase linearly with the amount of plant material, light intensity, and temperature when plants were irradiated with UVb *(Vigano et al. 2008)* but were not detected with no UV irridation. Like *Keppler et al. (2006)* emissions roughly doubled for every 10°C increase over the range 0–50°C, suggesting a non-enzymic process *(Keppler et al., 2006; Vigano et al., 2008)*. Under UVb intensities similar to ambient surface values in the tropics (5 W m^{-2}), CH_4 emissions from detached grass leaves were 10 to 100 times larger than measured by *Keppler et al (2006)*, who themselves used solar radiation (mid-day, Heidelberg, Germany) as the light source. For twenty other plant species tested by *Vigano et al. (2008)*, emission strengths varied with UVb strength and temperature and ranged from 4 – 393 ng CH_4 per gDW h^{-1}, which is consistent with, but on the low end of the flux range reported by *Keppler et al. (2006)*.

Finally, in addition to the boundary layer accumulation studies discussed above, methane flux has also been measured from vegetation in the field using standard static chamber techniques. *Cao et al. (2008)* measured emissions from an upland alpine plant community on the Qinghai-Tibetan Plateau over three years (2003-2006). Average methane fluxes from grasses here ranged from 23 to 68 ng CH_4 per gDW h^{-1} and peaked during the growing season. *Wang et al. (2008)* also reported methane flux from several species of shrub from the Inner Mongolia steppe

The growing body of evidence strongly suggests that some plants can produce and emit methane under aerobic conditions. The responsible mechanism has yet been identified but it appears connected to plant pectins *(Keppler et al., 2006; Keppler et al., 2008, Messinger et al., 2009; Vigano et al., 2009)*, which are important polysaccharide components of cell walls. Some of the methane enhancement over vegetated regions may also be due to an underappreciated role of transpiration in moving methane from soil to atmosphere by woody and non-woody plants *(Rusch and Rennenberg, 1998; Terazawa et al., 2007; Megonigal and Guenther, 2008; Nisbet et al., 2009; Rice et al., 2010)*.

Since emissions have been observed from a wide variety of plant species, global aerobic plant source strength is potentially large. If worldwide emissions are as high as 236 Tg y^{-1} as first reported *(Keppler et al., 2006)*, the global budget of methane needs to be reconsidered. The main goal in this study was to assess this possibility. In this work, we developed a global vegetation emissions model to assess the magnitude and distribution of emissions and used ice core records of atmospheric methane and $^{13}CH_4$

to place additional constraints on emissions. We also examined the possibility that some fraction of global aerobic emissions may already be captured in wetland inventories. To our knowledge, the model developed here is the most comprehensive to date in estimating plant methane emissions. We note that although measured flux values may change in the future, the modeling framework can be adapted and modified as new information about the processes and magnitudes becomes known. The model described here will continue to provide a useful framework to assess emissions in the future. We begin by critically analyzing previous attempts to model these emissions.

8.2   Previous emission estimates

As a first attempt to estimate the global flux, *Keppler et al. (2006)* extrapolated the laboratory results using annual net primary production as their scaling proxy and estimated global CH_4 emissions to $62 - 236$ Tg y^{-1}. However, this is not an appropriate method to use for a number of reasons. First, net primary production (NPP) is the rate of organic carbon accumulation in plant tissues, i.e. the balance of the carbon fixed (photosynthesis) and that metabolized by the plant (respiration). Since the reported flux is based on biomass of *leaf matter*, the relevant parameter is the standing foliage biomass. Net primary production however, includes the accumulated carbon content in all compartments of the plant -- roots, woody tissues, foliage, etc. The fraction of NPP in the below-ground compartments can be as high as 70% in grasslands and typically around 40% in forestlands (*Saugier et al., 2001*). The standing foliage biomass also depends on the rate of loss to litterfall and herbivores. Based on these considerations, methane emissions would be overestimated based on NPP.

Secondly, plants may have significant standing foliage at the same time their net primary production is small or zero. Such is the case during the dormant season of evergreen species when cold or arid conditions limit photosynthesis. Emissions based on NPP during these times would be underestimated.

Third, even if NPP represented foliage biomass, the use of *annual* NPP by *Keppler et al. (2006)* overestimates the emissions, since their calculation assumes that the entire annual production of biomass is available during all hours of the growing season as a source of emissions, when actually the biomass slowly builds up over the growing season and the biomass available for most hours of the growing season will be much less than the annual sum. That is, if f is the factor that converts NPP to methane flux, the method of *Keppler et al.* finds the annual emissions by:

$$S = \Delta t_{grow} \times \left(f \times NPP_{annual} \right) = f \times \Delta t_{grow} \int_{\Delta t_{grow}} NPP(t)dt, \qquad (8.1)$$

where Δt_{grow} is the length of the growing season, and *NPP(t)* describes how NPP changes throughout the growing season. More appropriately, if we assume no loss of biomass throughout the season the annual source should be found by:

$$S' = f \times \int_{t'=t_o}^{t'=t_{end}} \int_{t=t_o}^{t=t'} NPP(t)dtdt', \qquad (8.2)$$

259

where t_o and t_{end} are the beginning and end times of the growing season. We estimated the difference between S and S' by using as an example the average seasonal cycle of NPP from Brasilia, Brazil, as the function $NPP(t)$ in the equations above. This site is chosen as representative of the region that dominates the global NPP. We found that emissions calculated using equation 10 are nearly 1.75 times larger than those using the correct procedure in equation 11. Clearly the large methane source predicted *Keppler et al (2006)* is suspect and is partly due to this miscalculation.

Other efforts to model global emissions used leaf biomass to scale fluxes (*Kirschbaum et al.; 2006; Parsons et al. 2006*), which is a correct method, but categorized the world's vegetation into eight biomes which grossly simplifies the inter- and intra-heterogeneity of biome leaf area indices. In the current work, we spatially resolved the vegetated lands into half-degree grid cells and determined leaf biomass in each, providing greater sensitivity to local and regional differences both spatially and throughout the year.

8.3 Vegetation emissions model

The experimental results from plant emissions studies relevant to the current work are the following. First, emissions were detected from both detached and intact leaves, though emissions from the former appeared to be insignificant compared to the latter (8.7 vs. 374 ng CH_4 per g (dry leaf matter) h^{-1}, mean values reported here). Since emissions from detached leaves were marginal, we ignored emissions from the leaf litter in our calculation below. Second, emissions were sensitive to daylight. When intact leaves were exposed to sunlight they released on average three times more

methane than when kept in the dark (*Keppler et al. 2006*). Finally, emissions from the detached leaves were strongly temperature dependent, roughly doubling for every 10°C increase in temperature (*Keppler et al., 2006; Vigano et al., 2008*). It is speculative to extend this conclusion to intact leaves since all experiments performed on live plants were at ambient temperatures near 21°C. Nonetheless, the detached leaf measurements suggest that methane emissions diminish with decreasing temperature and we assumed a threshold temperature of 20°C, consistent with the original study. In the work below, we found that global emissions are sensitive to the threshold temperature over a moderate range of values.

The primary driver of the proposed vegetation source is the magnitude of the
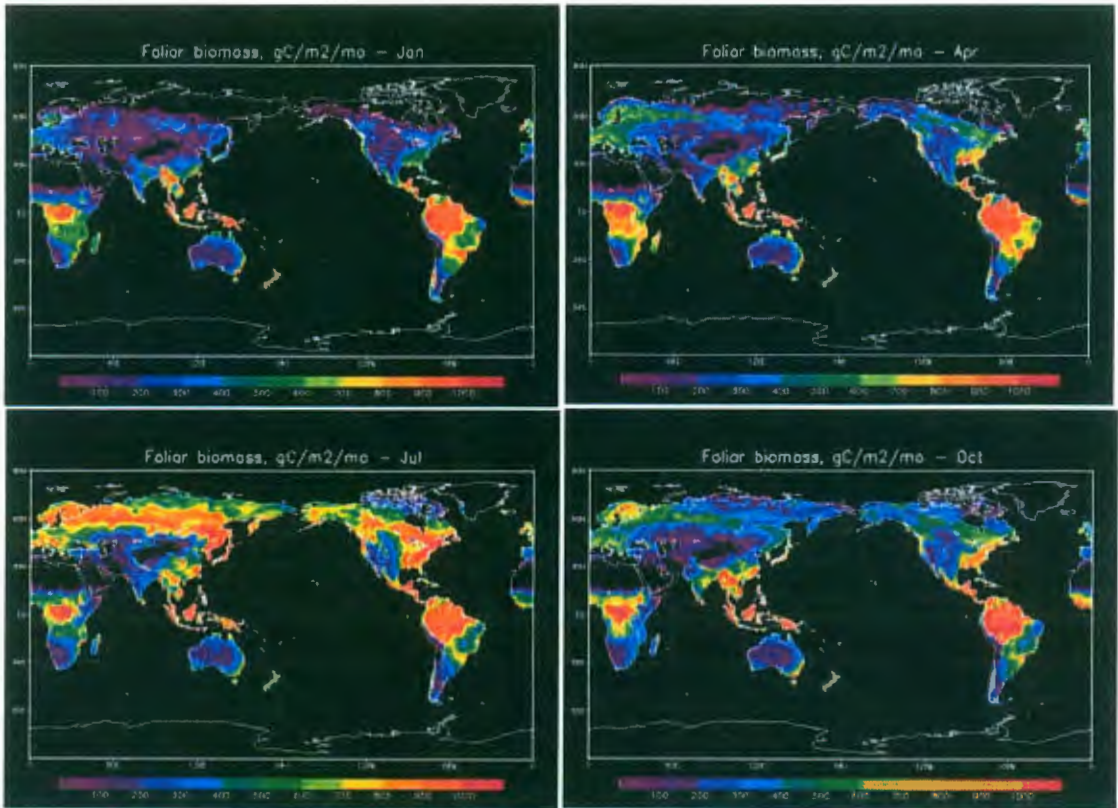
Figure 8.1. Modeled foliar biomass at half degree resolution using Method 1 (described in text). Maps have units of g C m^{-2} month^{-1}. Maps are shown for January, April, July, and October.

global reservoir of terrestrial foliage. Of secondary concern is its spatial and temporal distribution since the measurements indicate methane release from plants is sensitive to temperature and exposure to direct sunlight.

8.4   Leaf biomass maps

8.4.1   Method 1: Leaf area index

We used two independent methods to construct time and space-dependent leaf

biomass maps. In the first method we used the leaf area index (LAI) to estimate leaf biomass. The leaf area index is the ratio between the one-sided area of the leaf and the area it projects on the ground. It can be measured manually, by a hand-held instrument, or most recently by space-borne instruments. The latter is not a direct measurement of LAI, rather it is determined through the application of biophysical models of vegetation to the multi-spectral surface reflectance data measured by the space-borne instrument. In practice the leaf area index of the modeled vegetation is optimized such that the modeled reflectance is in good agreement with the observed reflectance (*Liang 2004*).

Leaf area index maps have been created using surface reflectance data taken by the Moderate Resolution Imaging Spectroradiometer (MODIS) aboard NASA's Terra satellite (*Myeni et al., 2002; Yang et al., 2006*). These globally-gridded, quarter-degree resolution maps are constructed from the 1 km, sine projection MODIS TERRA MOD15A2 product and available every eight days from the year 2000 to the present . For this work we converted them to maps of foliage biomass (*FM*) through the identity

$$FM_i = LAI_i \times A_i \times SLA_i, \qquad (8.3)$$

where A_i is the grid cell area and SLA_i is the specific leaf area given by 0.0001(6.24×LAI +19.86), with foliage biomass expressed in grams and cell area in square meters (*Pierce et al., 1994*). With this method, we calculated an annually-averaged (over years 2000 to 2006) global biomass of 49 Pg C. Our estimated global foliar biomass is plotted in Fig. 8.1.

8.4.2 Method 2: Aboveground net primary production

In our second method, we used monthly gridded maps of global net primary production (NPP). Though a plant's total NPP is a poor proxy for its foliage biomass for reasons discussed above, its aboveground net primary production (ANPP) correlates well with the plant's annual peak foliage (*Webb et al., 1983*). The ratio of ANPP to NPP varies with vegetation type but on average is close to 0.5 (*Saugier et al., 2001*). We created global maps of ANPP by scaling each grid cell in the NPP maps by the appropriate ANPP:NPP ratio determined by the vegetation type of the grid cell (*Defries and Townshend, 1994*).

For a wide range of vegetation types, the annual aboveground NPP is correlated with the annual peak foliage mass. To determine the peak foliage mass of each grid cell we annually integrated the ANPP over each cell and apply the relation (*Webb et al., 1983*)

$$PFM_i = A_i \exp(-0.76/0.93) \times \left(2 \times ANPP_i^{annual}\right)^{1/0.93}, \qquad (8.4)$$

where the peak foliage mass (*PFM*) has units of g y^{-1}. Though this calculation gives only the peak amount of foliage mass, we created a seasonal time series of foliage mass by assuming that foliage mass scales with LAI. We averaged the seasonality of LAI over all years of data and scaled it by the factor PFM_i:LAI_{max}, which is the ratio between a cell's peak foliage mass and the maximum value of LAI through the average seasonal cycle. This is based on the assumption that the peak leaf mass coincides with the peak leaf area. This is reasonable since when plant leaf area is large, so in general will be the leaf biomass. We averaged the seasonality of LAI over all years of data and scale it by the factor PFM_i:LAI_{max}, which is the ratio between the peak foliage mass and

the maximum value of LAI through the average seasonal cycle. This is based on the assumption that the peak leaf mass coincides with the peak leaf area.

The global foliage biomass calculated using this method is sensitive to the input NPP. Though NPP can be measured directly in field studies on small scales, global NPP is routinely estimated in carbon cycle and terrestrial ecosystem models. Annual global NPP from such models typically ranges from 40 to 70 Pg C y^{-1} (*Cramer et al., 1999*). For the current work we used a model that produced an annual NPP of 60 Pg C y^{-1} (*Foley et al., 1996*). This is at the upper end of the global NPP range and is chosen to produce the highest reasonable emissions of methane using this method. According to Eq. 8.3 we estimate that global foliage mass is 26 Pg C y^{-1}.

8.5 Methane emissions from foliage biomass

We transformed the leaf biomass into methane emissions using the emission rates measured by *Keppler et al.* (2006). There are two important results of their work that we considered in our simulation. First, the authors found that emissions nearly tripled when plant leaves were exposed to direct sunlight, and second there appeared to be a threshold temperature below which the plants did not produce emissions. To take into account the first observation we separated each 24-hr day into nighttime and daylight hours and additionally separated daylight hours into overcast (i.e. indirect sunlight) and cloud-free (direct sunlight) hours. We also differentiated the fraction of the leaf canopy that is in direct sunlight from the fraction that is shaded during daylight hours using a time-dependent vegetation canopy model and applied the appropriate methane emission rate to each fraction.
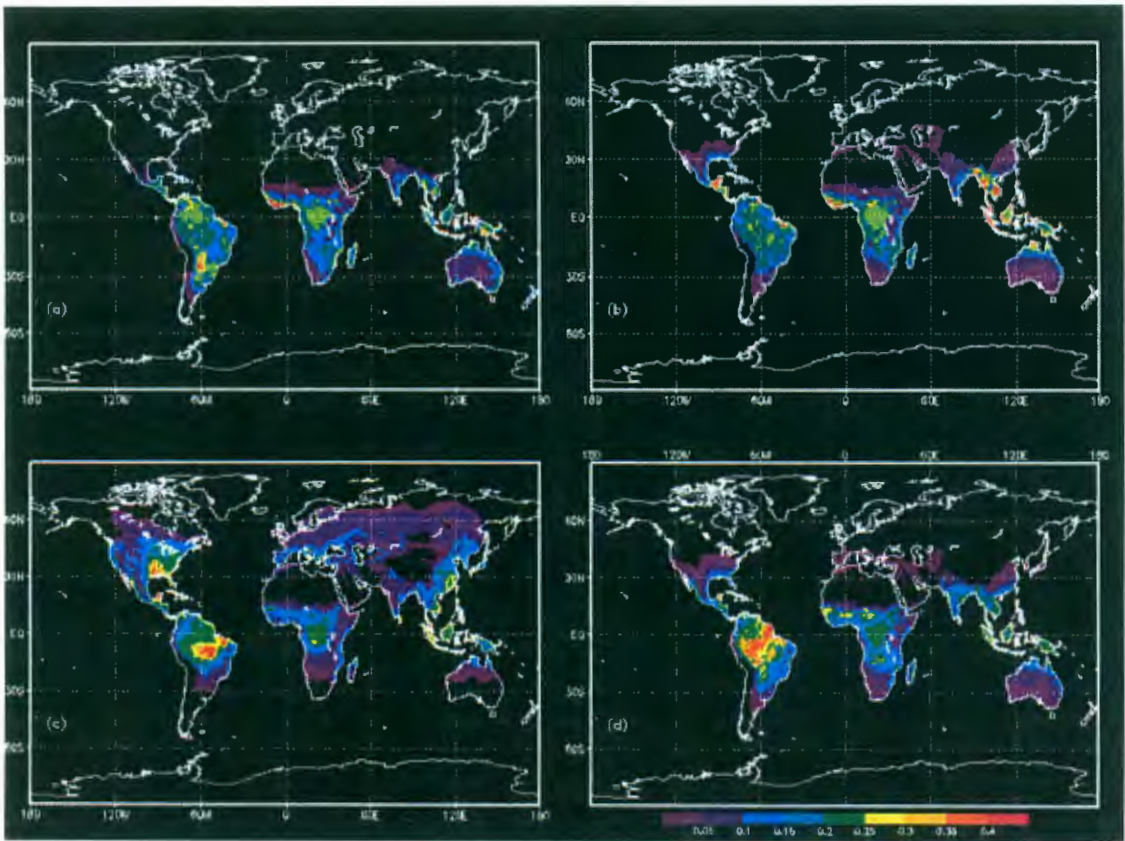
Figure 8.2. Methane emissions from oxic vegetation source using method (1). Units are Gg CH, month^{-1}.
(a) January; (b) April; (c) July; (d) October.

Though the minimum temperature required for emissions to occur is perhaps unknown,
it seems reasonable to assess the sensitivity of the global emissions to temperature as
the responsible emission mechanism, be it biological, chemical, or physical, is likely
temperature-dependent.

8.6 Results

Applying the considerations above, we calculated daily plant emissions over a
0.5×0.5° grid for all terrestrial land surfaces. The respective integrated annual emissions
are 36 and 20 Tg y^{-1} from Methods 1 and 2 when we used the mean sunlit and shaded

266

emission rates of 374 and 119 ng CH_4 per g (dry weight) h^{-1} reported in *Keppler et al., (2006)*. Our annual emissions are considerably lower than those found by the original study (149 Tg y^{-1}). If we include the reported uncertainties in the emission rates, the respective emission ranges are 14-60 Tg y^{-1} and 8-34 Tg y^{-1}. These ranges are similar to the range of 10-60 Tg y^{-1} reported by a recent study (*Kirschbaum et al., 2006*).

The spatial and temporal patterns of emissions are shown for Method 1 in Figs. 8.2 and 8.3. The pattern of emissions estimated using Method 2 is similar differing only quantitatively.

We see immediately from Fig. 8.2 that the bulk of the emissions occurs in the tropics, with concentrations in the Amazonian Basin, equatorial Africa, and the Indonesian archipelago. We estimate that nearly 90% of all emissions occur between latitudes of ±30°. Global emissions peak during the northern hemisphere summer months due to the greater landmass. During the months of June, July, and August, the
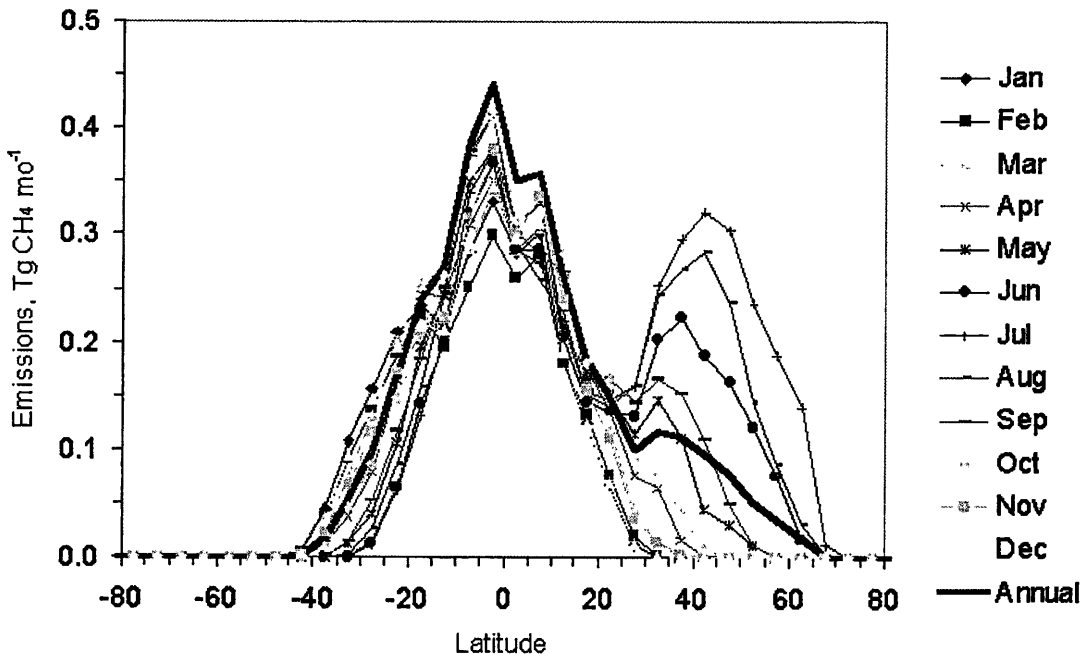
Figure 8.3. Latitudinal distribution of monthly methane emissions from vegetation based on leaf biomass distributions from Method 1.

northern hemisphere's continental landmasses (>30°N) contribute nearly 40% of the global emissions, but they contribute less than 15% of the world's annual emissions. During the winter months in each hemisphere, emissions are restricted to latitudes lower than 30°, while in the summer, emissions in the northern hemisphere extend northwards

268

of 60°. The latitudinal cut-off in emissions is largely a consequence of our choice to define a minimum temperature, below which we assume plant emissions do not occur. The smaller leaf biomass during the winter months also limits the latitudinal extent of the emissions, but this plays only a secondary role since the evergreen coniferous forest prevalent at high latitudes still contributes leaf matter during the winter months. Thus the choice of the minimum temperature is important and significantly impacts the global emissions. If we lower the threshold temperature to 15, 10, and 5°C, the global emissions are 52, 60, and 66 Tg y^{-1}, respectively. If we further reduce the temperature to 0°C --- perhaps a less controversial minimum temperature, global emissions increase only slightly more to 69 Tg y^{-1}. Using our extrapolation scheme, this then appears to be the maximum emissions we can expect from this source. When we used 0°C as the minimum temperature in Method 2, emissions increased from 20 Tg y^{-1} to 36 Tg y^{-1}. Whether such a minimum temperature exists and what its value may be is one of the largest sources of uncertainty in our extrapolation process. The sensitivity of the emissions to this temperature indicates that this needs to be a major focus of forthcoming work in this field. In the remainder of the chapter we took the minimum temperature to be 20°C.

If we categorize the emissions based on land cover type (Fig. 8.4), 41% of the total are from grasslands and wooded grasslands, while another 32% are from broadleaf evergreen forests. The only other land type of major significance is croplands, which contributes 10% of the global emissions. There are small differences between these values and those calculated using Method 2; 31%, 42%, and 12%, respectively. These
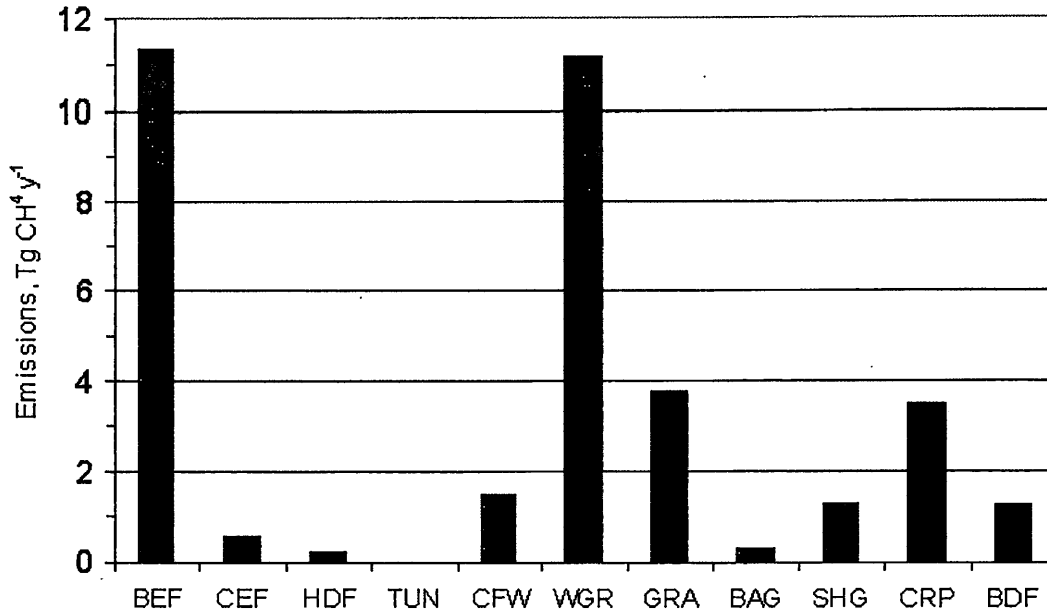
Figure 8.4. Distribution of oxic methane emissions according to vegetation type. BEF=broadleaf evergreen forest; CEF=coniferous evergreen forest; HDF=high-latitude deciduous forest; CFW=coniferous evergreen forest and woodland; WGR=wooded grassland; GRA=grassland; BAG=bare ground; SHG=shrubs and bare ground; CRP=cultivated crops; BDF=broadleaf deciduous forest and woodland.

distributions are comparable to *Keppler et al. (2006)*, who estimated tropical forests (roughly equal to our broadleaf evergreen forests) and grasslands respectively contribute about 50% and 26% to the total.

8.7   Emissions from non-wetlands

The possibility exists that if this plant source is real, it may already be partly counted as a component of the flux measured from wetlands and rice paddies.

270

According to this thought, only a fraction of the aerobic plant emissions would be considered new, with the remaining fraction folded into the previously known wetland emissions. We estimated what the upper limit to this latter fraction is by tallying the plant emissions that occur on land areas designated as either wetlands or rice paddies. For this purpose we used the global distribution of wetlands by *Matthews and Fung, (1987)* and a distribution of rice paddy areas by *Matthews et al. (1991),* both mapped on a one-degree grid. Using the emissions from Method 1 we found that 8.8 Tg out of the annual 36 Tg are from these land areas, which leaves a minimum of 27 Tg or 76% of the total oxic source that would be construed as a new source to be added to the global budget. This percentage increased to 78% when we used the set of oxic emissions estimated using a minimum temperature of 0°C as only 15 Tg out of 69 Tg lie within these regions. Thus even if the measured methane release from rice fields and wetlands already includes flux from the oxic source, the majority of this source is still unaccounted for in the present methane budget as it is released from non-flooded regions.

8.8 Top-down constraints on plant emissions

We also investigated whether our estimates of plant emissions were consistent with the known global methane and isotopic budget. Global fluxes from individual methane sources are widely uncertain due to the spatial and temporal variations of the sources. Collective emissions from all sources vary according to budget but typically lie between 500 and 600 Tg y^{-1} (*Denman et al., 2007*). Better constraints on the global rate are found through inverse techniques that deconvolve the source from the record of

atmospheric methane. From these techniques the global emission rate is found to be

around 550 Tg y^{-1} (*Dlugokencky et al., 1998; Khalil and Butenhoff, 2007*).
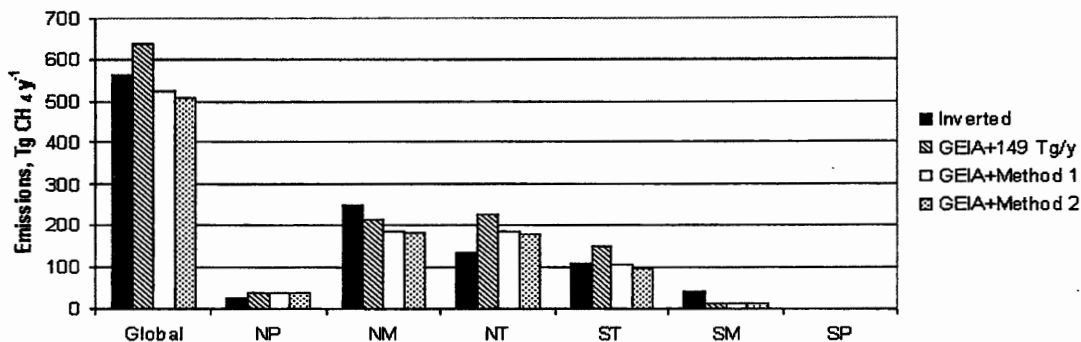
Figure 8.5. Distribution of amended-methane budget against sources derived from an inversion of the atmospheric methane record. To the base methane budget (global source = 487 Tg CH$_4$ y^{-1}) estimates of the oxic source were added. Solid black = inverted sources; diagonal pattern = base budget plus mean *Keppler et al. (2006)* vegetation estimates; no pattern=base budget plus method 1 estimates; dappled pattern=base budget plus method 2 estimates.

The geographical distribution of the source can be found by inverting the

twenty-year record of methane (see Chapter 2). Results from such an inversion using a

low-resolution model are shown in Fig. 8.5 for the major atmospheric compartments.

Alongside the inverted emissions we place bottom-up estimates of the methane

distribution using the emissions calculated in this work and those from *Keppler et al*

(2006). As the oxic source is just one of many sources, we added the oxic emissions to a

gridded global methane budget (*Fung et al., 1991*) which included contributions from

nearly all other methane sources and totals 487 Tg y^{-1}. Total emissions using the

respective estimates from Methods 1, 2, and *Keppler et al (2006)*, are 507, 523, and 639 Tg y^{-1}, while the total inverted source is 554 Tg y^{-1}. Although the geographical distribution of each data set is similar, the sources computed from Methods 1 and 2 are arguably in better agreement with the inverted sources, though all three data sets overestimate the tropical source and underestimate the middle latitude source.

8.8.1   Historical constraints from ice-core record

A more rigid constraint on plant emissions comes from the methane budget during the pre-industrial era when emissions from anthropogenic sources were minimal. Measurements of $\delta^{13}CH_4$ in the Law Dome ice-core of Antarctica have recently been used to constrain the pyrogenic and biogenic sources of methane during the late preindustrial Holocene (0 to 1700 A.D) (*Ferretti et al., 2005*). Based on these isotope measurements and the cotemporaneous atmospheric methane record, pyrogenic and biogenic emissions were estimated to be 25 and 195 Tg y^{-1}, respectively, during the period 0 to 1000 A.D. The strength of the pyrogenic emissions was somewhat surprising as it is nearly twice the size of previous estimates (*Chappellaz et al., 1993; Houweling et al., 2000*) but falls to 10 Tg y^{-1} by the year 1700 A.D.
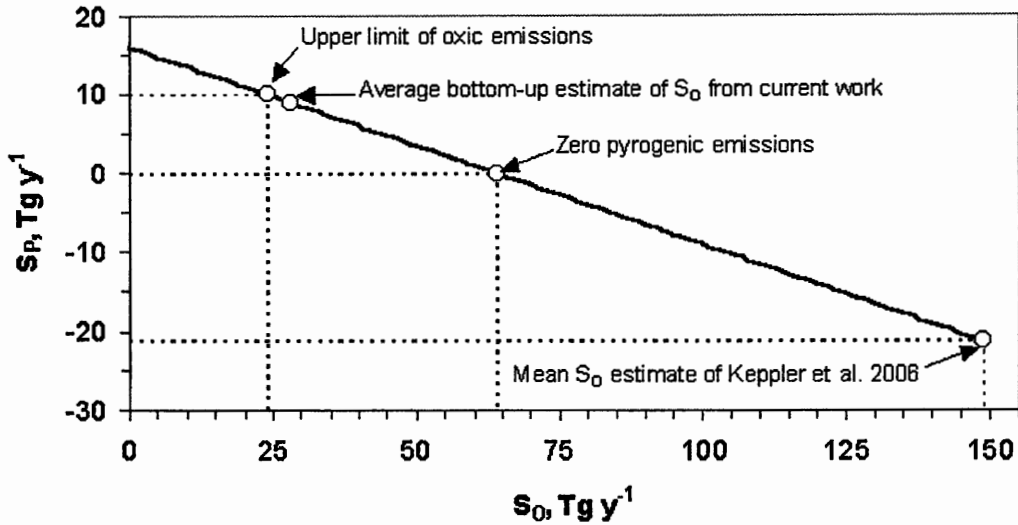
Figure 8.6. Sensitivity of the historic pyrogenic source (S_p) to the strength of the oxic source flux (S_o). Pyrogenic sources are calculated for the time period 1700-1800 A.D. from the ice-core isotope record and assuming difference source strengths for the oxic source. If oxic emissions exceed 64 Tg CH_4 y^{-1}, pyrogenic emissions are forced below zero. Likely, pyrogenic emissions are near 10 Tg CH_4 y^{-1} during this time, which constrains the oxic source to be no greater than 25 Tg CH_4 y^{-1}. This agrees with our bottom-up estimates from Methods 1 and 2.

How do these emissions change if we now consider the terrestrial vegetation source and include it in the source reconstruction during this time? Following *Ferretti et al. (2005)* we use a one-box non-equilibrium atmosphere model (*Lassey et al., 2000*) to estimate $\delta^{13}C$ of the global methane source from the ice-core measurements. The model includes isotopic fractionation due to differences between the reaction rates of OH with $^{12}CH_4$ and $^{13}CH_4$. To ensure that differences between the pyrogenic and biogenic

274

emissions computed here and those reported above are due only to the inclusion of the oxic methane source, we adopted model parameter values from *Ferretti et al. (2005):* $k_{13}/k_{12}=0.9926$, $\tau = 7.6$ y, $S_F=20$ Tg y^{-1}, $\delta^{13}C_{biogenic}= -60\%o$, $\delta^{13}C_{pyrogenic}= -20\%o$, and $\delta^{13}C_{fossil}= -40\%o$, where k_n is the rate coefficient between OH and isotope $^nCH_4$, τ is the methane atmospheric lifetime, S_F is the late pre-industrial Holocene rate of methane emissions from fossil fuels, and $\delta^{13}C_x$ is the $\delta^{13}C$ value for source x. We added to this mix $\delta^{13}C_{vegetation}=-50\%o$, which is the reported weighted $\delta^{13}C$ value for oxic vegetation emissions assuming a C3:C4 plant ratio of 60:40 (*Keppler et al., 2006*). We parameterized the isotope and atmospheric methane ice-core records with fits that produce correlation coefficients better than 0.99 and use these as inputs to the model. Over the period 0 to 1000 A.D., the fit to the isotope record is near constant at $\delta^{13}C$=-47.3%o.

When we set the plant emissions to zero and ran the model, the respective pyrogenic and biogenic emissions were 24 and 192 Tg y^{-1} (during 0 to 1000 A.D.), nearly identical to the above emissions as required. As we increased the plant emissions from zero, the pyrogenic and biogenic emissions decreased as necessary to balance the source and isotope budget. In fact, as we continued to increase plant emissions, the isotope budget was only satisfied if the pyrogenic emissions fell to below zero. This is so since plant emissions are enriched relative to the $\delta^{13}C$ value of the global source, which requires a reduced contribution from the even more enriched pyrogenic source. We found that if the pyrogenic emissions are to remain positive throughout the length of the isotope ice core record, the plant emissions cannot exceed 64 Tg y^{-1} to

accommodate the dip in $\delta^{13}C$ that occurs around 1800 (Fig. 8.6). Furthermore, it is more reasonable to constrain plant emissions to rates that produce pyrogenic emissions of at least 10 Tg y^{-1} and not zero, since pre-industrial biomass burning and wildfires are thought to contribute at least this amount (*Chapellaz et al., 1993; Houweling et al., 2000*). With this new constraint, we calculated that annual plant emissions can not exceed 25 Tg y^{-1} and certainly must be much lower than the original estimate of 149 Tg y^{-1}. When we assigned this latter value to the plant source we found that the predicted pyrogenic flux is -21 Tg y^{-1}, which turned the pyrogenic source to a sink, which is clearly unphysical. Our limit is somewhat lower than a recent estimate by *Ferretti et al. (2006)* who estimated an upper limit of 46 Tg y^{-1}

The results of our ice core analysis also corroborates the bottom-up estimates (36 and 20 Tg y^{-1}, Method 1 and 2) from above, as the mean of these two estimates (28 Tg y^{-1}) is very close to the threshold estimate of 25 Tg y^{-1}. In addition, a methane budget that includes plant emissions of this order is in better agreement with the expected pyrogenic source than a budget without. When we ran the atmospheric model with our mean estimate of 28 Tg y^{-1} over the steady-state years of 0 to 1000 A.D., the predicted pyrogenic flux during this time is 16 Tg y^{-1}. This agrees better with the expected value of 15 Tg y^{-1} (*Houweling et al., 2000*) relative to the predicted flux from a model run with no plant source (24 Tg y^{-1}). The magnitude of the plant source is not only consistent then with the known methane budget, but it brings the budget into better agreement with expectations. The predicted biogenic emissions, which include contributions from wetlands, termites, ruminants, and rice agriculture, are 170 Tg y^{-1},

which is consistent with estimates of this source, (*Chappellaz et al., 1993; Houweling et al., 2000*). Thus these results combined with those from our extrapolations support the view that emissions from terrestrial plants are modest and can be readily accommodated within the methane budget.

Chapter 9 — Conclusion

9.1 Summary

The work presented in these chapters represents an attempt to better understand the changing source and sink strengths of atmospheric methane. To do so we used measurements of trace gases at remote background stations from four different sampling networks. These networks include the Oregon Graduate Institute (OGI), the National Oceanic and Atmospheric Administration's Global Monitoring Division (NOAA-GMD), the Atmospheric Lifetime Experiment/Global Atmospheric Gas Experiment/Advanced Global Atmospheric Gas Experiment (ALE/GAGE/AGAGE), and the Gas …. of the Commonwealth Scientific Institute of Research Organization (CSIRO-GASLAB). In most cases the measurement time series extended back to the early 1980's. In many cases we joined measurements from different networks. In this way not only were we able to create longer time series than exists for a single network, we were also able to test how differences between networks influenced the results of our modeling simulations. In this manner we could assess the robustness of the modeled features.

As a starting point for our investigation we inverted the recent atmospheric history of CH_4. For this we created a time series of measurements that stretched back to 1981 and continued to recent years. The composite record was produced by joining the

OGI and NOAA data sets at the monitoring sites common to both networks. The trend of CH_4 drops rapidly over this period. To explain this behavior we used a chemical-transport model and ran it in inverse mode. In this configuration, the model uses as inputs the time series of CH_4 measurements in each of the six major latitudinal air masses (i.e. north and south polar latitudes (65-90 N,S), north and south mid-latitudes (30-65 N,S), and north and south tropics(0-30 N,S). We found that with OH levels constant, the declining trend of CH_4 is consistent with stable emissions over the 23-year period of study. Emissions were constant at ~ 550 Tg y^{-1}. This behavior of CH_4 can be explained by the approach of atmospheric CH_4 to steady state. That is the sink of CH_4, primarily the CH_4+OH reaction, is coming into balance with emissions. We showed using the global average methane record and a simple one-box model, that the recent history of atmospheric CH_4 is consistent with a constant global CH_4 source strength of 550 Tg y^{-1} and a total lifetime of 8.9 yr.

However, an alternate scenario is that both CH_4 sources and lifetime are changing simultaneously. Under this scenario, if the lifetime of CH_4 were increasing over this time period, the global source strength of CH_4 would be decreasing to maintain the trends observed in the atmospheric record. Thus an independent analysis of the trends of CH_4's sources and sinks is required to assess whether atmospheric CH_4 is indeed in steady state. This was the task of the remainder of the dissertation.

We first examined the possibility that the main sink of atmospheric CH_4, its reaction with the hydroxyl radical OH, is changing. Since the atmospheric lifetime of OH is so short, direct measurements of OH provide only local information about its

atmospheric abundance. Furthermore, no long-term systematic record of atmospheric OH is available globally. And while it is possible to model the long-term trends of atmospheric OH based on its chemical production and removal pathways, this requires additional information about the trends and abundances of any number of chemical species over large spatial and temporal scales. Thus any such effort suffers from large uncertainties.

In this work we inferred the history of OH using a proxy gas, the chlorinated solvent, methylchloroform (CH_3CCl_3). The useful properties of this gas include, it is nearly entirely anthropogenically produced through industrial processes, which has the advantage that good records exist on its production history. Secondly, it is removed almost entirely by OH. And finally, it has a relatively short lifetime (~5 yr) so its atmospheric abundance should reflect changes in OH levels. We again used our chemical-transport model. We used as inputs, the emissions record of CH_3CCl_3 based on a release history of the solvent, and the long-term ALE/GAGE/AGAGE CH_3CCl_3 measurements. Over the time period 1978 – 2008, we found that OH was not constant but had strong interannual variability. We estimated the average trend of OH over this period to be –0.43 pm 0.21 % y^{-1}. The history of OH we derived however is more complex than this single trend suggests. OH levels were mainly flat or even slightly rising from the beginning of the model period to 1990. From 1990 to 1999, OH levels drop by about 10%. This drop is simulated using not just the ALE/AGAGE/AGAGE measurements, but also the OGI and NOAA-GMD records, though trends estimated

from the latter records were not significant due to the shorter time series of MCF measurements available.

We tested to see how sensitive the OH trend is to factors such as modeling/inversion scheme, temperature, calibration, and emissions history. Within known trends and uncertainties in these drivers, the negative OH trend remains. We found that the OH trend disappears if the MCF calibration scales was in error by 10% or more. Quoted uncertainty in the AGAGE calibration is 3%, and within this range, the trend is still statistically significant. Besides the calibration, the largest uncertainty that would affect our calculation is the timing of MCF release from production. To the extent that the uncertainty of this timing was factored into the error estimates of the *McCulloch and Midgley (2001)* emission record, the OH trend remains within this uncertainty. We also conducted additional experiments on the sensitivity of emission release by constructing alternative release histories using an exponential release function. In these scenerios the delay between production and release is determined by a decay constant. We increasing the decay constant for example, we can increase the lag between production and release. Our experiments showed that no single decay constant was able to simulate emissions that were consistent with inverted emissions from a zero-OH trend modeling run. However this does not rule out the possibility that the decay constant changes over the years. Future work needs to investigate this possibility.

If the lifetime of atmospheric CH_4 is changing due to a trend in atmospheric OH, then individual CH_4 sources must change to compensate. In particular, some

sources must be decreasing in time. The next chapters of the dissertation investigated individual sources.

We used a novel technique to study emissions from biomass burning. Biomass burning is a major source of atmospheric carbon monoxide and hydrogen. In fact this pair of gases share common sources, and yet are principally removed by different mechanisms, oxidation by OH for CO, and soil deposition for H_2. We found that when we inverted the long-term time series of atmospheric measurements for both gases, the simulated emission history of each coincided to a high degree, both peaking and falling at the same time. We limited our analysis to the tropics where biomass burning is strongest and the dominant source of both gases. Here we found that our simulated CO and H_2 emissions had seasonal cycles that peaked in the dry seasons of both hemispheres, consistent when emissions from biomass burning occur. Also, a comparison between our inverted emissions and satellite-derived fire counts, showed that the seasonal cycles and cycle strength were consistent with fire activity. We integrated emissions from both the CO and H_2 record over the seasonal peaks of each year. This we took as the estimate of annual biomass burning emissions. The time series of annual emissions shows that in the southern tropics biomass burning emissions have increased by roughly 10% over the years 1981 to 1999. This is increase is evident in both the CO and H_2 emission histories. There is no emission trend seen in the northern tropics. The biggest feature here is a large positive anomaly in 1997/98. This coincides with an especially strong El Nino event that produced droughts and wildfires in western Pacific countries such as Indonesia and Malaysia.

One of the largest uncertainties in our biomass burning emission estimates is, that they rely upon consideration of other CO and H_2 emissions in the tropics. These we must account for. The source with the largest uncertainty is the production of CO and H_2 from the oxidation of isoprene and terpenes. Both of these gases are emitted by vegetation. The literature includes estimates of global source strengths that vary by a factor of two. In the tropics, isoprene and terpenes are emitted throughout the year but emissions peak during the wet season of each hemisphere, which is anti-correlated with the cycle of biomass burning. Because the impact of uncertainty on our conclusions is mitigated. However, we recognize that reducing the uncertainty in isoprene and terpene emissions is an area that needs considerable effort in the future.

We next investigated the global source strength of methane emission from rice agriculture. Recent estimates of this source vary widely, by nearly a factor of five in the latest IPCC report. We used experimental results from our greenhouse and field studies on factors controlling paddy flux, to create global gridded inventories of CH_4 emissions. Using a wide variety of geospatial agricultural, environmental, and vegetation data, we constructed gridded input maps and from these estimated methane flux for all areas of global rice production. Based on harvested area and crop phenology we estimated annual emissions from these fluxes. Our global estimate of 50 Tg y^{-1} is consistent with past work and continues the trend of decreasing estimates of methane from rice agriculture. One notable result is that emissions in India are more than twice as high as those in China. This is due to a number of reasons including higher seasonal temperature averages in India, a larger fraction of rice production managed under

continuously flooded conditions, and smaller rate of synthetic fertilizer usage, which we found in our field studies to retard methane flux.

We next used China as a test case to study how emissions from rice agriculture have changed over the past few decades. In China, a number of important changes have occurred that influenced paddy emissions. Starting in the 1970s, synthetic fertilizers became favored over organic fertilizes which would reduce CH_4 emissions (though increase N_2O emissions). To improve crop yields and conserve water, the practice of mid-season drainage was started in the early 1980s and spread widely throughout China to the present. We considered these changes and others on paddy emissions. We found that methane emissions decreased by about 15 Tg y^{-1} from 1980 to the present. This would contribute to the general reduction in methane emissions required if OH levels decreased as predicted here.

Finally we considered the potential of vegetation as a source of methane. Direct measurements of CH_4 flux from plants are limited. Here we used the reported fluxes from *Keppler et al. (2006)* to assess whether global vegetation could be an important component of the global CH_4 budget. We found through bottom-up methods that global emissions ranged from 20 to 36 Tg y^{-1}. We tested these estimates using the pre-industrial atmospheric record of CH_4 and $\delta^{13}CH_4$ measured from ice cores. The ice core records constrain the natural source strength of CH_4. We estimate an upper limit on vegetation emissions of 25 Tg y^{-1} assuming that natural biomass burning emissions were 10 Tg y^{-1}. This upper limit is consistent with our bottom-up estimates. We conclude that terrestrial plants may be a significant source of methane, though not as

large as previous studies indicate. We note that recent studies found a strong correlation between UV radiation and methane flux. This will be an important connection to model in future work.

9.2 Closing thoughts

The picture that emerges from this work dispels the notion that the sources and sinks of atmospheric methane have been constant over the past couple decades despite the fact that the recent behavior of atmospheric CH_4 is consistent with steady state conditions. There appears to be changes on the order of 10% that have occurred in the major sink of CH4 and some of its important anthropogenic sources. In the south tropics, where we estimate emissions from biomass burning are increasing, there must be some offsetting decreasing emissions there as well , as our inverse modeling of CH_4 shows that emissions must be constant in the southern hemisphere. If vegetation does emit CH_4 at rates suggested by this work, then the reduction in CH_4 emissions due to the deforestation of tropical forests could produce the required balance.

In closing, we offer the following perspective. Oftentimes, we miss the proverbial forest for the trees. We miss the bigger picture while seeing only the smaller components that compose it. Here the reverse may be true. The bigger story is that atmospheric methane is stabilizing. We may erroneously take this to mean that the component sources and sinks are doing the same. In so doing, not only might we miss a rich underlying story of sources and sinks that are bubbling underneath a smooth surface, but in the future these sources (or sinks) may break through and again push atmospheric levels of methane upwards. Here, the details are important, it is important

to see the trees for the forest. This investigation of the sources and sinks of atmospheric methane hopefully will remind us of the complexity of Earth's atmosphere and the relations that bind it to our own activities.

References

AFEAS, 2001. Production, Sales, and Atmospheric Release of Flurocarbon through 2000. AFEAS, Arlington, VA (see www.afeas.org).

Akiyama, H., K. Yagi, and X.Y. Yan, 2005. Direct N2O emissions from rice paddy fields: Summary of available data, *Global Biogeochem. Cycles*, 19, GB1005, doi:10.1029/2004GB002378.

Alexander, R., and A.C. Millington, 2000. *Vegetation Mapping*. Chichester, England: John Wiley.

Allan, W., et al., 2005. Interannual variations of ^{13}C in tropospheric methane: Implications for a possible atomic chlorine sink in the marine boundary layer. *J. Geophys. Res.*, 110, doi:10.1029/2004JD005650.

Andreae, M.O., 1991. Biomass burning: Its history, use, and distribution and its impact on environmental quality and global climate, in *Global Biomass Burning: Atmospheric, Climatic, and Biospheric Implications*, J.S. Levine, ed., MIT Press, Cambridge, Mass. 1991.

Andreae, M.O., and P. Merlet, 2001. Emission of trace gases and aerosols from biomass burning, *Global Biogeochem. Cycles, 15*, 955-966.

Angell, J. K. ,2000. Difference in radiosonde temperature trend for the period 1979–1998 of MSU data and the period 1959–1998 twice as long, *Geophys. Res. Lett.*, 27, 2177-2180.

Arellano Jr., A.F., P.S. Kasibhatla, L. Giglio, G.R. van der Werf, J.T. Randerson, and G.J. Collatz, 2006. Time-dependent inversion estimates of global biomass-burning CO emissions using Measurement of Pollution in the Troposphere (MOPITT) measurements, *J. Geophys. Res., 111*, D09303, doi:10.1029/2005JD006613.

Arino, O., and J.-M. Rosaz, 1999. 1997 and 1998 World ATSR Fire Atlas using ERS-2 ATSR-2 data, in *Proceedings of the Joint Fire Science Conference*, Boise, Idaho, p. 177-182, University of Idaho and the International Association of Wildland Fire.

Aslemann I, and P.J. Crutzen, 1989. Distribution of natural freshwater wetlands, *J. Atm. Chem., 8*, 307-358.

Aucott, M.L, A. McCulloch, T.E. Graedel, G. Kleiman, P.M. Midgley, Y.-F. Li, 1992. Anthropogenic emissions of trichloromethane (chloroform, CHCl$_3$) and

chlorodifluoromethane (HCFC-22): Reactive Chlorine Emissions Inventory, *J. Geophys. Res.* 104, 8405-8416, 1999

Bauer, K., W. Seiler, and H. Giehl, 1979. CO Produktion hoherer Pflanzen an naturlichen Standorten, *Z. Pflanzenphysiol.*, 94, 219-230.

Bergamaschi, P., R. Hein, M. Heimann, and P.J. Crutzen, 2000a. Inverse modeling of the global CO cycle. 1. Inversion of CO mixing ratios, *J. Geophys. Res., 105*, 1909-1927.

Bergamaschi, P., R. Hein, C.A.M. Brenninkmeijer, and P.J. Crutzen, 2000b. Inverse modeling of the global CO cycle 2. Inversion of $^{13}C/^{12}C$ and $^{18}O/^{16}O$ isotope ratios, *J. Geophys. Res., 105*, 1929-1945.

Bousquet, P., D.A. Hauglustaine, P. Peylin, C. Carouge, and P. Ciais, 2005. Two decades of OH variability as inferred by an inversion of atmospheric transport and chemistry of methyl chloroform, Atmos. Chem. Phys., 5, 2635-2656.

Bouman, A. F., 1990. *Soils and the Greenhouse Effect*, 575 pp., Wiley, Chichester, U.K.

Bruhl, C., S. R. Drayson, J. M. Russell III, P. J. Crutzen, J. M. McInerney, P. N. Purcell, H. Clande,, H. Gernandt, T. J. McGee, I. S. McDermid, and M. R. Gunson, 1996. Halogen Occulatation Experiment ozone channel validation, *J. Geophys. Res.*, 10217-10240.

Butenhoff, C.L., 2002. Development and application of a two-dimensional atmosphere-ocean transport box model to CCl_3F and CCl_2F_2, *Master's Thesis*, Portland State University, Portland, OR.

Butler, J.H., M. Battle, M. L. Bender, S. A. Montzka, A.D. Clarke, E. S. Saltzman, C. M. Sucher, J. P. Severinghaus, and J. W. Elkin, 1999. A record of atmospheric halocarbons during the twentieth century from polar firn air, *Nature*, 399, 749.

Cai, Z.C, G.X. Xing, X.Y. Yan, H. Xu, H. Tsuruta, K. Yagi, and K. Minami, 1997. Methane and nitrous oxide emissions from paddy fields as affected by nitrogen fertilizers and water management, *Plant Soil*, 196, 7-14.

Cao, M., J.B. Dent, and O.W. Heal, 1995. Modelling methane emissions from rice paddies, *Global. Biogeochem. Cycles*, 9, 183-195.

Carmo, J.G., M. Keller, J.D. Dias, P.B. Carmargo and P. Crill. 2006. A source of methane from upland forests in the Brazilian Amazon, *Geophys. Res. Lett.*, 33, L04809.

Cramer, W., D.W. Kicklighter, A. Bondeau, B. Moore III, G. Churkina, B. Nemry, A. Ruimy, and A.L. Schloss, 1999. Comparing global models of terrestrial net primary production (NPP): overview and key results, *Global Change Biol., 5*, 1-15.

Cheng W., H. Sakai, A. Hartley, K. Yagi, and T. Hasegawa, 2008. Increased night temperature reduces the stimulatory effect of evelevated carbon dioxide concentration on methane emission from paddy soil, *Glob. Change. Bio.*, 14, 644-656.

Christy, J.R., R.W. Spencer, and W.D. Braswell, 2000: MSU tropospheric temperatures: Dataset construction and radiosonde comparisons. J. Atmos. Ocean. Technol., 17, 1153–1170.

Cicerone, R.J., and J.D. Shetter, 1981. Sources of atmospheric methane: Measurements in rice paddies and a discussion, *J. Geophys. Res.,* 86, 7203-7209.

Conrad, R., W. Seiler, G, Bunse, and H. Giehl, 1982. Carbon monoxide in sea water (Atlantic Ocean), *J. Geophys. Res.,* 87, 8839-8852.

Cooper, L.N., L.P. Steele, R.L. Langenfelds, D.A. Spencer and M.P. Lucarelli, 1999. Atmospheric methane, carbon dioxide, hydrogen, carbon monoxide and nitrous oxide from Cape Grim flask air samples analysed by gas chromatography. *Baseline Atmospheric Program (Australia)* 1996, edited by J.L. Gras, N. Derek, N.W. Tindale and A.L. Dick, pp 98 - 102, Bureau of Meteorology and CSIRO Atmospheric Research, Melbourne, Australia, 1999

Crutzen, P.J., and M.O. Andreae, 1990. Biomass burning in the tropics: Impact on atmospheric chemistry and biogeochemical cycles, *Science, 250*, 1669-1678.

Crutzen, P.J., and J. Lelieveld, 2001. Human impacts on atmospheric chemistry, *Annu. Rev. Earth Planet Sci.*, 29, 17-45.

Crutzen, P.J., A.C. Delany, J. Greenberg, P. Haagenson, L. Heidt, R. Leub, W. Pollock, W. Seiler, A. Wartburg, and P. Zimmerman, 1985. Tropospheric chemical composition measurements in Brazil during the dry season, *J. Atmos. Chem.*, 2, 233-256, 1985.

Crutzen, P.J., E. Sanhueza and C.A.M. Brenninkmeijer. 2006. Methane production from mixed tropical savanna and forest vegetation in Venezuela. *Atmos. Chem. Phys. Discuss.*, 6, 3093–3097.

Defries, R. S. and J.R.G. Townshend, 1994. NDVI-derived land cover classification at a global scale, *Int. J. Remote. Sens., 15*, 3567-3586.

Denman, K.L., G. Brasseur, A. Chidthaisong, P. Ciais, P.M. Cox, R.E. Dickinson, D. Hauglustaine, C. Heinze, E. Holland, D. Jacob, U. Lohmann, S Ramachandran, P.L. da

Silva Dias, S.C. Wofsy and X. Zhang, 2007: Couplings Between Changes in the Climate System
and Biogeochemistry. In: *Climate Change 2007: The Physical Science Basis. Contribution of Working Group I to the Fourth Assessment Report of the Intergovernmental Panel on Climate Change* [Solomon, S., D. Qin, M. Manning, Z. Chen, M. Marquis, K.B. Averyt, M.Tignor
and H.L. Miller (eds.)]. Cambridge University Press, Cambridge, United Kingdom and New York, NY, USA.

Ding,A., C.R.Willis, R.L. Sass, and F.M. Fisher,1999. Methane emissions from rice fields: Effect of plant height among several rice, *Glob. Biogeochem. Cycles*, 13, 1045.

Dlugokencky, E.J., E.G. Dutton, P.C. Novelli, P.P. Tans, K.A. Masarie, K.O. Lantz, and S. Madronich, 1996.Changes in CH4 and CO growth rates after the eruption of Mt. Pinatubo and their link with changes in tropical tropospheric UV flux, *Geophys. Res. Lett.*, 23, 2761-2764.

Dlugokencky, E.J., K.A. Masarie, P.M. Lang, and P.P. Tans, 1998. Continuing decline in the growth rate of the atmospheric methane burden, *Nature*, 393, 447-450.

Dlugokencky, E.J., B.P. Walter, K.A. Masarie, P.M. Lang, and E.S. Kasischke, Measurements of an anomalous global methane increase during 1998, *Geophys. Res. Lett.*, 28, 499-502.

Dlugokencky, E.J., S. Houweling, L. Bruhwiler, K.A. Masarie, P.M. Lang, J.B. Miller, and P.P. Tans, 2003. Atmospheric methane levels off: Temporary pause or a new steady-state?, *Geophys. Res. Lett.*, 30, doi.1029/2003GL018126.

Dlugokencky, E.J., P.M. Lang, and K.A. Masarie, 2009. Atmospheric Methane Dry Air Mole Fractions from the NOAA ESRL Carbon Cycle Cooperative Global Air Sampling Network, 1983-2008, Version: 2009-06-18, Path: ftp://ftp.cmdl.noaa.gov/ccg/ch4/flask/event/.

Duncan, B.N., R.V. Martin, A.C. Staudt, R. Yevich, and J. A. Logan, 2003. Interannual and seasonal variability of biomass burning emissions constrained by satellite observations, *J. Geophys. Res., 108,* 4100, doi:10.1029/2002JD002378.

Emmons, L.K., M.N. Deeter, and J.C. Gille, 2004. Validation of measurements of pollution in the troposphere (MOPITT) CO retrievals with aircraft in situ profiles, *J. Geophys. Res., 109*, D03309, doi:10.1029/2003JD004101.

FAO (2005) *FAOSTAT Agricultural Data*

Ferretti, D.F., J.B. Miller, J.W.C. White et al., 2005. Unexpected changes to the global methane budget over the past 2000 years, *Science, 309,* 1714-1717.

Fleming, E.L, S. Chandra, M.R. Shoeberl, and J.j. Barnett, 1988. Monthly mean global climatology of temperature, wind, geopotential height, and pressure for0-120 km, NASA Technical Memorandum 100697.

Foley, J.A., I.C. Prentice, N. Ramankutty, S. Levis, D. Pollard, S. Stich, and A. Hazeltine, 1996. An integrated biosphere model of the land surface process, terrestrial carbon balance, and vegetation dynamics, *Global Biogeochem. Cycles*, 10, 603-628.

Forster, P., V. Ramaswamy, P. Artaxo, T. Berntsen, R. Betts, D.W. Fahey, J. Haywood, J. Lean, D.C. Lowe, G. Myhre, J. Nganga, R. Prinn, G. Raga, M. Schulz and R. Van Dorland, 2007. Changes in Atmospheric Constituents and in Radiative Forcing. *In: Climate Change 2007: The Physical Science Basis. Contribution of Working Group I to the Fourth Assessment Report of the Intergovernmental Panel on Climate Change* [Solomon, S., D. Qin, M. Manning, Z. Chen, M. Marquis, K.B. Averyt, M.Tignor and H.L. Miller (eds.)]. Cambridge University.

Francey, R.J., L.P. Steele, R.L. Langenfelds and B.C. Pak, High precision long-term monitoring of radiatively-active trace gases at surface sites and from ships and aircraft in the Southern Hemisphere atmosphere. J. Atmos. Science., 56, 279-285, 1999.

Frankenberg, C., J.F. Meirink, M. vanWeele, U. Platt and T.Wagner. 2005. Assessing methane emissions from global space-borne observations. *Science*, 308:1010–1014

Galanter, M., H. Levy II, and G.R. Carmichael, 2000. Impacts of biomass burning on tropospheric CO, NO_x and O_3, *J. Geophys. Res., 105*, 6633-6653.

Gregoire, J.-M., K. Tansey, and J.M.N Silva, 2003. The GBA2000 initiative: Developing a global burned areas database from SPOT-VEGETATION imagery, *Int. J. Remote Sens.*, 24, 1369-1376.

Guenther A, Hewitt CN, Erickson D, Fall R, Geron C, Graedel T, Harley P, Klinger L, Lerdau M, McKay Wa, Pierce T, Scholes B, Steinbrecher R, Tallamraju R, Taylor J, Zimmerman P 1995. A Global-Model of Natural Volatile Organic-Compound Emissions, *J. Geophys. Res.,* 100 (D5): 8873-8892.

Gupta, M., et al., 1997. $^{12}C/^{13}C$ kinetic isotope effects in the reactions of CH_4 with OH and Cl. *Geophys. Res. Lett.*, **24**, 2761–2764.

Hamburger, J. 2002. Pesticides in China: a growing threat to food safety, public health, and the environment. *China Environment Series* **5**: 29-44.

Hansen, J., M. Sato, R. Ruedy, A. Lacis, and V. Oinas, 2000. Global warming in the twenty-first century: An alternative scenario, *Proc. Natl. Acad. Sci.*, 97, 9875-9880.

Hanst, P.L., J.W. Spence, and O. Edney, 1980. Carbon monoxide production in photooxidation of organic molecules in the air. *Atmos. Environ.* 14, 1077-1088.

Hao, W.M., and M-H Liu, 1994. Spatial and temporal distribution of tropical biomass burning, *Global Biogeochem. Cycles, 8*, 495-503.

Hauglustaine, D. A. et al., 1998. MOZART, a global chemical transport model for ozone and related chemical tracers 2. Model results and evaluation, *J. Geophys. Res.*, 103, 28,291-28,335.

Hauglustaine D.A. and D.H. Ehhalt, 2002. A three-dimensional model of molecular hydrogen in the troposphere, 107, 4330, doi.10.1029/2001JD001156.

Hoelzemann, J.J., M.G. Schultz, G.P. Brasseur, and C. Granier, 2004. Global Wildland Fire Emission Model (GWEN): Evaluating the use of global area burnt satellite data, *J. Geophys. Res., 109*, D14S04, doi:1029/2003JD003666.

Holzapfel-Pschorn, A., and W. Seiler, 1986. Methane emission during a cultivation period from an Italian rice paddy, *J. Geophys. Res.*, 91(D11), 11,803-11,814.

Houweling, S., F. Dentener, F., and J. Lelieveld, 2000. Simulation of pre-industrial atmospheric methane to constrain the global source strength of natural wetlands, *J. Geophys. Res.*, 105, 17243-17255.

Huang, Y., Z. Wen, Z. Xunhua, H. Shenghui, and Y. Yongqiang, 2006. Estimates of methane emissions from Chinese rice paddies by linking a model to GIS database, *Acta Ecol. Sinica, 26*, 980-988.

Huang, Y., W. Zhang, Z Zheng, J. Li, and Y. Yu, 2004. Modeling methane emission from rice paddies with various agricultural practices, J. Geophys. Res., 109, D08113, doi:10.1029/2003JD004401.

Horowitz, L.W., S. Walters, D.L, Mauzerall, et al., 2003. A global simulation of tropospheric ozone and related tracers: Description and evaluation of MOZART, version 2, *J. Geophys. Res., 108(D24),* 4784, doi:10.1029/2002JD002853.

Intergovernmental Panel on Climate Change (IPCC), 1990. *Climate Change-Scientific Assessment*, 365 pp., Cambridge Univ. Press, Cambridge, UK.

Intergovernmental Panel on Climate Change (IPCC), 1994. Radiative forcing of climate change and an evaluation of the IPCC IS92 emission scenarios, in *Climate Change 1994, edited by J.T. Houghton et al.,* Cambridge Univ. Press, New York.

Intergovernmental Panel on Climate Change (IPCC), 2007. *2006 IPCC Guidelines for National Greenhouse Gas Inventories, Inst. For Global Environ. Strategies*, Hayama, Japan.

Ito, A., and J.E. Penner, 2004. Global estimates of biomass burning emissions based on satellite imagery for the year 2000, J. Geophys. Res., 109, D14S05, doi:10.1029/2003JD004423.

Jacob, D.J., and S.C. Wofsy, 1990. Budgets of reacdtive nitrogen, hydrocarbons, and ozone over the Amazon forest during the wet season, *J. Geophys. Res.*, 95, 16,737-16754.

Kalnay et al.,1996. The NCEP/NCAR 40-year reanalysis project, *Bull. Amer. Meteor. Soc.*, 77, 437-470.

Kanakidou, M., and P.J. Crutzen, 1999. The photochemical source of carbon monoxide: Importance, uncertainties, and feedbacks, *Chemosphere: Global Change Science*, 1, 91-109.

Karl, T, A. Hansel, T. Märk, W. Lindinger, and D. Hoffmann, 2003. Trace gas monitoring at the Mauna Loa Baseline Observatory using proton-transfer reaction mass spectrometry, *Internat. J. of Mass Spectromet.*, 223-224, 527-538,.

Karlsdottir, S., and I.S.A. Isaksen, 2000. Changing methane lifetime: Possible cause for reduced growth, *Geophys. Res. Lett.*, 27, 93-96.

Keeling, C.D., R.B. Bacastow, A.E. Bainbridge, C.A. Ekdahl, P.R. Guenther, and L.S. Waterman, 1976. Atmospheric carbon dioxide variations at Mauna Loa Observatory, Hawaii, *Tellus*, vol. 28, 538-551.

Keppler, F., J.T.G. Hamilton, M. Brass, and T. Rockmann, 2006. Methane emissions from terrestrial plants under aerobic conditions, *Nature, 439*, doi:10.1038..

Khalil, M.A.K., and R.A. Rasmussen, 1984. Carbon monoxide in the earth's atmosphere: Increasing trend, *Science*, 224, 54-56.

Khalil, M.A.K., and R.A. Rasmussen, 1988. Carbon monoxide in the earth's atmosphere: Indications of a global increase, *Nature*, 332, 242-245.

Khalil, M.A.K., and R.A. Rasmussen, 1990. Atmospheric methane: Recent global trends, *Environ. Sci. Technol.,* 24, 549-553..

Khalil, M.A.K., and R.A. Rasmussen, 1991. Methane emissions from rice fields in China, *Environ. Sci. Tech.,* 25, 979-981.

Khalil, M.A.K., and R.A. Rasmussen, 1993. Decreasing trend of methane: Unpredictability of future concentrations, *Chemosphere,* 26, 803-814.

Khalil, M.A.K., and R.A. Rasmussen, 1994. Global decrease in atmospheric carbon monoxide concentration, *Nature,* 370, 639-641.

Khalil, M.A.K., and M.J.Shearer, 2000. Sources of methane: An overview, in *Atmospheric Methane: Its Role in the Global Environment,* edited by M.A.K. Khalil, pp 98-111, Springer, Berlin.

Khalil, M.A.K., R.A. Rasmussen, and M.J. Shearer, 1998a. Effects of production and oxidation processes on methane emissions from rice fields, *J. Geophys. Res.,* 103, 25,233-25,239.

Khalil, M. A. K., R. A. Rasmussen, M. J. Shearer, Z. L. Chen, H. Yao, and Y. Jun , 1998b. Emissions of methane, nitrous oxide, and other trace gases from rice fields in China, *J. Geophys. Res.,* 103(D19), 25,241–25,250.

Khalil, M.A.K., R.A. Rasmussen, M.J. Shearer, R.W. Dalluge, L.X. Ren, and C.-L. Duan, 1998c. Measurements of methane emissions from rice fields in China, *J. Geophys. Res.,* 103, 25,181-25210.

Khalil, M. A. K., M. J. Shearer, R. A. Rasmussen, C. L. Duan, and L. X. Ren, 2008a. Production, oxidation, and emissions of methane from rice fields in China, *J. Geophys. Res.,* 113, G00A04, doi:10.1029/2007JG000461.

Khalil, M. A. K., M. J. Shearer, R. A. Rasmussen, L. Xu, and J.-L. Liu, 2008b. Methane and nitrous oxide emissions from subtropical rice agriculture in China, *J. Geophys. Res.,* 113, G00A05, doi:10.1029/2007JG000462.

Krol., M. P.J. van Leeuwen, and J. Lelieveld, 1998. Global OH trend inferred from methylchloroform measurements, *J. Geophys. Res., 103,* 10697-10711.

Krol, M., and J. Lelieveld, 2003. Can the variability in tropospheric OH be deduced from measurements of 1,1,1-trichloroethane (methyl chloroform)?, J. Geophys. Res., 108, 4125, doi:10.1029/2002JD002423.

Koyama, T., 1963. Gaseous metabolism in lake sediments and paddy soils and the production of hydrogen and methane, *J. Geophys. Res.*, 68, 3971-3973.

Kurylo, M. J, J.M. Rodriguez, M.O. Andreae, E.L. Atlas, D.R. Blake, J.H. Butler, S. Lal, D.J. Lary, P.M. Midgley, S.A. Montzka, P.C. Novelli, C.E. Reeves, P.G. Simmonds, L.P. Steele, W.T. Sturges, R.F. Weiss, and Y. Yokouchi, 1998. *Short-Lived Ozone-Related Compounds*, World Meteorological Organization, Geneva.

Lamontagne, R.A., J.W. Swinnerton, and V.J. Linnenboom, 1974. C1-C4 hydrocarbons in the north and south Pacific, *Tellus*, 26, 71-77.

Lassey, K.R., D.M. Etheridge, D.C. Lowe, A.M. Smith, and D.F. Ferretti, 2007. Centennial evolution of the atmospheric methane budget: what do the carbon isotopes tell us?, *Atmos. Chem. Phys.*, 7, 2119-2139.

Lassey, K.R., D.C. Lowe, and M.R. Manning, 2000. The trend in atmospheric methane $\delta^{13}C$ and implications for isotopic constraints on the global methane budget, *Global Biogeochem. Cycles, 14*, 41-49.

Leff, B., N. Ramankutty, and J.A. Foley, 2004. Geographic distribution of major crops across the world, *Global Biogeochem. Cycles, 18*, GB1009, doi:10.1029/2003GB002108.

Levine, J.S., 1999. The 1997 fires in Kalimantan and Sumatra, Indonesia: Gaseous and particulate emissions, *Geophys. Res. Lett.,* 7, 815-818.

Levine, J.S., and W.R. Cofer, 1999. *Boreal forest fire emissions and the chemistry of the atmosphere. Fire, Climate Change and Carbon Cycling in the North American Boreal*, Ecological Studies Series, Springer-Verlag, New York.

Li, C., A. Mosier, R. Wassman, Z. Cai, X. Zheng, Y. Huang, H. Tsuruta, J. Boonjawat, and R. Lantin, *Global Biogeochem. Cycles, 18*, GB1043, doi:1029/2003GB002045.

Li. C., J. Qiu, S. Frolking, X. Xiao, W. Salas, B. Moore III., S. Boles, Y. Huang, and R. Sass, 2002. Reduced methane emissions from large-scale changes in water management of China's rice paddies during 1980-2000, *Geophys. Res. Lett.*, 29, 1972, doi:10.1029/2002GL015370.

Liang, S. 2004. *Quantitative remote sensing of land surfaces*. Hoboken, NJ: Wiley-Interscience.

Liss, P.S., and P.G. Slater, 1974. Flux of gases across the air-sea interface, *Nature*, 247, 181-184.

Lobert, J. M., W. C. Keene, J. A. Logan, and R. Yevich, 1999. Global chlorine emissions from biomass burning: Reactive Chlorine Emissions Inventory, *J. Geophys. Res.*, 104(D7), 8373–8389, doi:10.1029/1998JD100077.

Logan, J.A., 1983. Nitrogen oxides in the troposphere: Global and regional budgets, *J. Geophys. Res., 88*, 10785-10807.

Lowe, D. C., 2006. Global change: A green source of surprise, *Nature*, 439, 148-149.

Madronich, S. 1993. The atmosphere and UV-B radiation at ground level, *Environmental UV Photobiology*, Plenum Press, 1–39.

Mather, P.M., 1995. *Terra 2 Understanding the Terrestrial Environment*. Chichester, England: John Wiley.

Matthews, E., and I. Fung, 1987. Methane emissions from natural wetlands: global distribution, area, and environmental characteristics of sources, *Global Biogeochem. Cycles, 1,* 61-86.

Matthews, E., I. Fung, and J. Lerner, 1991. Methane emission from rice cultivation: Geographic and seasonal distribution of cultivated areas and emissions, *Global Biogeochem. Cycles, 5,* 3-24.

Matthews, R.B., R. Wassmann, and J. Arah, 2000. Using a crop/soil simulation model and GIS techniques to assess methane emissions from rice fields in Asia. I. Model development, *Nut. Cycling Agroecosys.,* 58, 141-159.

McCulloch, A., P.M. Midgley, and D.A. Fisher, 1994. Distribution of CFCs 11, 12, 113, 114, and 115 among reporting and non-reporting countries during 1986, *Atmos. Environ.*, 28, 2567-2582.

McCulloch, A., and P.M. Midgley, 2001. The history of methylchloroform emissions: 1951-2000, *Atmos. Environ.*, 35, 5311-5319.

McCulloch, A., P.M. Midgley, and P. Ashford, 2003. Releases of refrigerant gases (CFC-12, HCFC-22, and HFC-134a) to the atmosphere, *Atmos. Environ.*, 37, 889-902.

McMillan, W. W., et al., 200. Tropospheric carbon monoxide measurements from the Scanning High-Resolution Interferometer Sounder on 7 September 2000 in southern Africa during SAFARI 2000, *J. Geophys. Res.*, 108(D13), 8492, doi:10.1029/2002JD002335.

Midgley, P.M., A. McCulloch, 1995. The production and global distribution of emissions to the atmosphere of 1,1,1 trichloroethane (methylchloroform), *Atmos. Environ.*, 14, 1601-1608.

Miller, B.R., J. Huang, R.F. Weiss, R.G. Prinn and P.J. Fraser, 1998. Atmospheric trend and lifetime of chlorodifluoromethane (HCFC-22) and the global tropospheric OH concentrations, J. Geophys. Res., 103, 13,237-13,248.

Mitra, A. P., 1992. *Greenhouse gas emissions in India: 1991 Methane Campaign.* Science Report No. 2. Council of Scientific and Industrial Research and Ministry of Environment and Forests, New Delhi.

Montzka, S.A., R. C. Myers, J. H. Butler, J. W. Elkins, and S. O. Cummings, 1993. Global tropospheric distribution and calibration scale of HCFC-22, *Geophys. Res. Lett.,* 20, 703-706.

Montzka, , S.A., J. H. Butler, R. C. Myers, T. M. Thompson, T. H. Swanson, A. D. Clarke, L. T. Lock, and J. W. Elkins, 1996. Decline in the tropospheric abundance of halogen from halocarbons: Implications for stratospheric ozone depletion, *Science*, 272, 1318-1322.

|Montzka, , S.A., J. H. Butler, J. W. Elkins, T. M. Thompson, A. D. Clarke, and L. T. Lock, 1999. Present and Future Trends in the Atmospheric Burden of Ozone-Depleting Halogens, *Nature*, 398, 690-694

Montzka, S.A., C. M. Spivakovsky, J. H. Butler, J. W. Elkins, L. T. Lock and D. J. Mondeel, 2000. New observational constraints to atmospheric hydroxyl on global and hemispheric scales, *Science*, 288, 500-503, 2000.

Mosier, A., C. Kroeze, C. Nevison, O. Oenema, S. Seitzinger, and O. van Cleemput, 1998. Closing the global N2O budget: nitrous oxide emissions through the agricultural nitrogen cycle, *Nut. Cycl. Agroecosys.*, 52, 225-248.

Moulin, S., A. Biondeau, and R. Delecolle, 1998. Combining agricultural crop models and satellite observations: from field to regional scales. *Int. J. Remote Sens.* 19 (6), 1021–1036.

Myneni, R. B., et al., 1997. Algorithm for the estimation of global land cover, LAI and FPAR based on radiative transfer models. *IEEE Trans. Geosc. Remote Sens.*, 35: 1380-1393

Myeni, R.B., S. Hoffman, Y. Knyazikhin, J.L. Privette, J. Glassy, Y. Tian, Y. Wang, X. Song, Y. Zhang, G.R. Smith, A. Lotsch, M. Friedl, J.T. Morisette, P. Votava, R.R.

Nemani, S.W. Running, 2002. Global products of vegetation leaf area and fraction absorbed PAR from year one of MODIS data, *Remote Sens. Environ.*, 83, 214-231.

Myneni, R.B., R.R., Nemani, and S.W. Running, 1997. Estimation of global leaf area index and absorbed par using radiative transfer models. *IEEE Trans. Geosci. Remote Sens.* 35, 1380–1393.

Neue, H.U., 1997. Fluxes of methane from rice fields and potential for mitigation, *Soil Use and Management*, 13, 258-267.

Neue, H.U., and R.L. Sass, 1998. The budget of methane from rice fields, *IG Activ. Newsl.*, 12, 3-11.

Neue, H.U., R. Wassmann, R.S. Lantin, MA C.R. Alberto, J.B. Aduna, and A.M. Javellana, 1996. Factors affecting methane emission from rice fields, *Atmos. Environ.*, 30, 1751-1754.

Nouchi, I., Mariko, S. & Aoki, K., 1990. Mechanism of methane transport from the rhizosphere to the atmosphere through rice plants. *Plant Physiol.* 94, 59–66.

Novelli, P. C., Lang, P. M.,Masarie, K. A., Hurst, D. F.,Myers, R., and Elkins, J.W., 1999: Molecular hydrogen in the troposphere: Global distribution and budget, *J. Geophys. Res.* 104, 30427–30444.

Novelli, P.C. and K.A. Masarie, 2009. Atmospheric Carbon Monoxide Dry Air Mole Fractions from the NOAA ESRL Carbon Cycle Cooperative Global Air Sampling Network, 1988-2008, Version: 2009-07-28, Path: ftp://ftp.cmdl.noaa.gov/ccg/co/flask/event/.

Olivier, J.G.J., 2002. *On the Quality of Global Emission Inventories. Approaches, Methodologies, Input Data and Uncertainties*, Thesis, Utrecht University, Utrecht, The Netherlands, 4.2, 58-90.

Olivier, J.G.J., and J.J.M. Berdowski, 2001. Global emission sources and sinks, pp. 33-37 in the Climate System, J. Berdowski, R Guichert, and B. Heij, eds. Swets and Zeitlinger B. V. Lisse.

Olivier, J.G.J, J.P.J. Bloos, J.J.M. Berdowski, A.J.H. Visschedijk and A.F. Bouwman, . A 1990 global emission inventory of anthropogenic sources of carbon monoxide on 1ox1o developed in the framework of EDGAR/GEIA. *Chemosphere: Global Change Science*, 1, 1-17.

Pacyna, J.M., and T.E. Graedel, 1995. Atmospheric emissions inventories: status and prospects, *Annu. Rev. Energy Environ.*, 20, 265-300.

Pathak, H., C. Li, and R. Wassman, 2005. Greenhouse gas emissions from Indian rice fields: calibration and upscaling using the DNDC model, *Biogeosciences, 2,* 113-123.

Petron, G., C. Granier, B. Khattatov, J-F. Lamarque, V. Yudin, J.-F. Muller, and J. Gille, 2002. Inverse modeling of carbon monoxide surface emissions using Climate Monitoring and Diagnostics Laboratory network observations, *J. Geophys. Res., 107,* 4761, doi:10.1029/2001JD001305.

Pierce, L.L., S.W. Running, J. Walker, 1994. Regional-scale relationships of leaf area index to specific leaf area and leaf nitrogen content, *Ecol. Appl., 4,* 313-321.

Platt, U., W. Allan, and D. Lowe. 2004: Hemispheric average Cl atom concentration from $^{12}C/^{13}C$ ratios in atmospheric methane. *Atmos. Chem. Phys.*, 4, 2393–2399.

Prinn, R., R. Rasmussen, P. Simmonds, F. Alyea, D. Cunnold, B. Lane, C. Cardelino, and A. Crawford, 1983. The Atmospheric Lifetime Experiment 5. Results for CH3CCl3 Based on Three Years of Data, *J. Geophys. Res.*, 88(C13), 8415-8426.

Prinn, R.G., D. Cunnold, P. Simmonds, F. Alyea, R. Boldi, A. Crawford, P. Fraser, D. Gutzler, D. Hartley, R. Rosen, and R. Rasmussen, 1992. Global average concentration and trend for hydroxyl radicals deduced from ALE/GAGE trichloroethane (methyl chloroform) data for 1978-1990, *J. Geophys. Res., 97*, 2445-2461.

Prinn, R.G., R.F. Weiss, P.J. Fraser, P.G. Simmonds, D.M. Cunnold, F.N. Alyea, S. O'Doherty, P. Salameh, B.R. Miller, J. Huang, R.H.J. Wang, D.E. Hartley, C. Harth, L.P. Steele, G. Sturrock, P.M. Midgley, and A. McCulloch, 2000. A History of Chemically and Radiatively Important Gases in Air deduced from ALE/GAGE/AGAGE, J. Geophys. Res., 105, 17,751-17,792, 2000.

Prinn , R.G., and J. Huang, 2001. Comment on "Global OH inferred from methylchloroform measurements" by Maarten Krol et al., *J. Geophys. Res., 106*, 23151-23157.

Prinn , R.G., J. Huang, R.F. Weiss et al., 2001. Evidence for substantial variations of atmospheric hydroxyl radicals in the past two decades, *Science, 292*, 1882-1888.

Prinn , R.G., J. Huang, R.F. Weiss et al., 2005. Evidence for variability of atmospheric hydroxyl radicals over the past quarter century, *Geophys. Res. Lett., 32,* L07809, doi:10.1029/2004GL022228.

Prinn, R.G., R. F. Weiss, B.R. Miller, J. Huang, F.N. Alyea, D.M. Cunnold, P.J. Fraser, D.E. Hartley, and P.G. Simmonds, 1995. Atmospheric trends and lifetime of CH_3CCl_3 and global OH concentrations, *Science, 269*, 187-192.

Rasmussen, R.A. and M.A.K. Khalil, 1980. *Proceedings of the NATO Advanced Study Institute on Atmospheric Ozone* (Editor A.C. Aitkin (U.S. Department of Transportation, Washington, D.C.), 209-231.

Rasmussen, R.A., M.A.K. Khalil, 1981. Atmospheric methane: Trends and seasonal cycles, *J. Geophys. Res.*, 86, 9826-9832.

Rasmussen, R.A., M.A.K. Khalil, R.W. Dalluge, 1981. Atmospheric trace gases in Antarctica, *Science*, 211, 285.

Rasmussen, R.A., and M.A.K. Khalil, 1981. Global atmospheric distribution and trend of methylchloroform (CH_3CCl_3), *Geophys. Res. Lett.,* 8, 1005-1007.

Rasmussen, R.A., and M.A.K. Khalil, 1986. Atmospheric trace gases: Trends and distributions over the last decade, *Science*, 232, 1623-1624.

Roy, D.P, P.E. Lewis, and C.O. Justice, 2002. Burned area mapping using multi-temporal moderate spatioal resolution data – A bi-directional reflectance model-based expectation approach, *Remote Sens. Environ.*, 83, 263-286.

Ruddiman, W.F., Z. Guo, Z. Zhou, H. Wu, and Y. Yu, 2008. Early rice farming and anomalous methane trends, *Quat. Sci. Rev.*, 27, 1291-1295.

Rudoph, J. A. Khedim, R. Koppmann, and B. Bonsan, 1995. Field study of the emissions of methyl chloride and other halocarbons from biomass burning in Western Africa, *J. Atmos. Chem.,* 22, 67-80.

Rudolph, J., K. von Czapiewski, and R. Koppmann, 2000. Emissions of methyl chloroform (CH3CCL3) from biomass burning and the tropospheric methyl chloroform budget, *Geophys. Res. Lett.*, 27, 1887-1890.

Sander, S. P., R. R. Friedel, R. E. Huie, M. J. Kurylo, C. E. Kolb, D. M.Golden, A. R. Ravishankara, and M. J. Molina, 2000. *Chemical Kinetics and Photochemical Data for Stratospheric Modeling*, JPL Publication 00-3, JPL, Pasadena, CA.

Sass, R.L, 1994. Short summary chapter for methan, in *CH4 and N2O: Global Emissions and Controls From Rice Fields and Other Agricultural and Industrial Sources*, edited by K. Minami, A. Mosier, and R.L. Sass, pp. 1-7, Natl. Inst. Of Agro-Environ. Sci., Tsukuba, Japan.

Saugier, B., J. Roy, H.A. Mooney, 2001. Estimations of global terrestrial productivity: converging toward a single number? In *Terrestrial Global Productivity*; Roy, J., Saugier, B., Mooney, H.A., Eds., Academic Press, San Diego, CA, 2001.

Schule, W., 1990. Landscapes and climate in prehistory: Interactions of wildlife, man and fire, in *Fire in the Tropical Biota: Ecosystem Processes and Global Challenges*, J. Goldammer, ed., Springer-Verlag, New York.

Schultz, M.G., 2002. On the use of ATSR fire count data to estimate the seasonal and interannual variability of vegetation fire emissions, *Atmos. Chem. and Phys.*, 2, 387-395.

Schutz, H. A., Holzapfel-Pschorn, R. Conrad, H. Rennenberg, and W. Seiler, 1989. A 3-year continuous record on the influence of daytime, season, and fertilizer treatment on methane emission rates from an Italian rice paddy, *J. Geophys. Res.*, 94, 16,405-16,416.

Seiler, W., 1974. The cycle of atmospheric CO. *Tellus*, 26, 116-135.

Seiler, W., H. Giehl, and G. Bunse, 1978. Influence of plants on atmospheric carbon monoxide and dinitrogen oxide, *Pure Appl. Geophs.*, 116, 439-451.

Seiler, W., and P.J. Crutzen, 1980. Estimates of gross and net fluxes of carbon between the biosphere and the atmosphere from biomass burning, *Clim. Change, 2*, 207-247.

Seiler, W., and U. Schmidt, 1974. Dissolved non-conservative gases in sea water. In *The Sea*, ed. E. P. Goldberg et al., Vol 5, Wiley Interscience, New York.

Seiler, W., A. Holzapfel-Pschorn, R. Conrad, and D. Scharffe, 1983. Methane emission from rice paddies, *J. Atmos. Chem.*, 1, 241-268.

Shabanov, N.V., D. H.uang, W. Yang, B. Tan, Y. Knyazikhin, R. B. Myneni, D. E. Ahl,, S. T. Gower, A.R. Huete, L.E. O. C. Aragão, and Y. E. Shimabukuro, 2005. Analysis and Optimization of the MODIS Leaf Area Index Algorithm Retrievals Over Broadleaf Forests, *IEEE Trans. Geosci. Remote Sens.*, 43, 1855-1865.

Sharman, M., Boissezon, H., de Gonzales, G., Pous, B., 1992. Rapid estimates of acreages and potential yield at a European scale. In: *Proceedings of the 43rd Congress of the International Astronautical Federation*, Washington, DC, August 28–September 5.

Shuler, S., and R. Conrad, 1991. Hydrogen oxidation activities in soil as influenced by pH, temperature, moisture, and season, *Biol. Fertil. Soils*, 12, 127-130, 1991.

Simon, M., 2002. GLOBSCAR products qualification report, Tech. Note, *Euro. Space Ag.*, Paris.

Simon, M., S. Plummer, F. Fierli, J. Hoelzemann, and O. Arino, 2004. Burnt area detection at global scale using ATSR-2: The GLOBSCAR products and their qualification, *J. Geophys. Res., 109*, D14S02, doi:10.1029/2003JD003622.

Smith, P., D. Martino, Z. Cai, D. Gwary, H. Janzen, P. Kumar, B. McCarl, S. Ogle, F. O'Mara, C. Rice, B. Scholes, O. Sirotenko, 2007: Agriculture. *In Climate Change 2007: Mitigation. Contribution of Working Group III to the Fourth Assessment Report of the Intergovernmental Panel on Climate Change* [B. Metz, O.R. Davidson, P.R. Bosch, R. Dave, L.A. Meyer (eds)], Cambridge University Press, Cambridge, United Kingdom and New York, NY, USA.

Strahler, A., D. Muchoney, J. Borak, F. Gao, M. Friedl, S. Gopal, J. Hodges, E. Lambin, D. McIver, A. Moody, C. Schaaf, and C. Woodcock, 1999. *MODIS Land Cover Product, Algorithm Theoretical Basis Document (ATBD), Version 5.0*, Center for Remote Sensing, Department of Geography, Boston University, Boston, MA.

Steele, L. P., P. B. Krummel and R. L. Langenfelds. 2007. Atmospheric CO_2 concentrations from sites in the CSIRO Atmospheric Research GASLAB air sampling network (August 2007 version). In Trends: A Compendium of Data on Global Change, Carbon Dioxide Information Analysis Center, Oak Ridge National Laboratory, U.S. Department of Energy, Oak Ridge, TN, U.S.A.

Summers, M.D., B.M. Jenkins, P.R. Hyde, J.F. Williams, R.G. Mutters, S.C. Scardacci, and M.W. Hair, 2003. Biomass production and allocation in rice with implications for straw harvesting and utilization, *Biomass and Bioenergy*, 24, 163-173.

Tan, B., J. Hu, D. Huang, W. Yang, P. Zhang, N.V. Shabanov, Y. Knyazikhin, R.R. Nemani, and R.B. Myneni, 2005. Assessment of the broadleaf crops leaf area index product from the Terra MODIS instrument, *Agri. Forest. Met.,* 135, 124-134.

Tan, B., J. Hu, P. Zhang, D. Huang, N. Shabanov, M. Weiss, Y. Knyazikhin, and R. B. Myneni, 2005. Validation of Moderate Resolution Imaging Spectroradiometer leaf area index product in croplands of Alpilles, France, *J. Geophys. Res.*, 110, D01107, doi:10.1029/2004JD004860.

Tucker, C.T., B.N. Holben, J.H. Elgin, and J.E. McMurtery, 1980. Relationship of spectral data to grain yield variation. *Photogram. Eng. Remote Sens.* 46 (5), 657–666.

Troxler, R. F., and J. M. Dokos, 1973. Formation of carbon monoxide and bile pigment in red and green algae, *Plant Physiol.,* 51, 72-75.

Tyler, P., 1995. On the farms, China could be sowing disaster. *The New York Times*, 10 April 1995.

Tyler, S.C., et al., 2000. Experimentally determined kinetic isotope effects in the reaction of CH_4 with Cl: Implications for atmospheric CH4. *Geophys. Res. Lett.*, 27, 1715–1718.

UNEP (United Nations Environment Program), 2002. Production and Consumption fo Ozone Depleting Substances Under the Montreal Protocol 1986-2000. Ozone Secretariat, UNEP, Nairobi, Kenya (see www.unep.org/ozone).

van Bodegom, P.M., R. Wassman, and T.M. Metra-Corton, 2001. A process-based model for methane emission predictions from flooded rice paddies, *Global Biogeochem. Cycles, 15,* 247-263.

van der Werf, G.R., J.T. Randerson, G.J. Collatz, and L. Giglio, 2003. Carbon emissions from fires in tropical and subtropical ecosystems, *Global Change Bio., 9,* 547-562.

Wang M. K., A. Mosier, R. Sass eds. 1994. *CH4 and N2O: Global Emissions and Controls from Rice Fields and Other Agricultural and Industrial Sources*, Tokyo, Yokendo Publishers, 9-26.

Wang Q.B., C. Halbrendt, and S.R. Johnson. 1996. Grain production and environmental management in China's fertilizer economy. *Journal of Environmental Management* **47**: 283-296

Wassmann, R., H.-U. Neue, R.S. Lantin, L.V. Buendia, and H. Rennenberg, 2000a. Characterization of methane emissions from rice fields in Asia. I. Comparison among field sites in five countries, *Nutrient Cycling in Agroecosys.*, 58, 1-12.

Wassmann, R., H.-U. Neue, R.S. Lantin, K. Makarim, N. Chareonsilp, L.V. Buendia, and H. Rennenberg, 2000b. Characterization of methane emissions from rice fields in Asia. II. Differences among irrigated, rainfed, and deepwater rice, *Nutrient Cycling in Agroecosys.*, 58, 13-22.

Wassman, R., X.J. Shangguan, M. Tolg, D.X. Cheng, M.X. Wang, H. Papen, H. Rennenberg, W. Seiler, 1996. Spatial and seasonal distribution of organic amendements affecting methane emission from Chinese rice fields, *Biol. Fertil. Soils*, 22, 191-195.

Webb, W.L, W.K. Lauenroth, S.R., Szarek, R.S. Kinerson, 1983. Primary production and abiotic controls in forests, grasslands, and desert ecosystems in the United States, *Ecology, 64*, 134-151.

Wen, Q.-X., 1984. Utilization of organic materials in rice production in China, *Organic Matter and Rice*, International Rice Research Institute, Los Banos, Philippines.

Willats WG, McCartney L, Mackie W, Knox JP, 2001. Pectin: cell biology and prospects for functional analysis, Plant Mol Biol., 47, 9-27.

Yagi, K., and K. Minami, 1990. Effects of organic matter application on methane emission from Japanese paddy fields. In: *Soil and the Greenhouse Effects* (A.F. Bouwman, ed.), John Wiley, p 467-473.

Yan, X., Y. Kazuyuki, H. Akiyama, and H. Akimoto, 2005. Statistical analysis of the major variables controlling methane emission from rice fields, *Global Change Bio., 11*, doi: 10.1111/j.1365-2486.2005.00976.x.

Yan, X., H. Akiyama, K. Yagi, and H. Akimoto, 2009. Global estimations of the inventory and mitigation potential of methane emissions from rice cultivation conducted using the 2006 Intergovernmental Panel on Climate Change Guidelines, *Global Biogeochem. Cycles, 23*, GB2002, doi:1029/2008GB003299.

Yang, W., D. Huang, B. Tan, J.C. Stroeve, N.V. Shabanov, N.V., Y. Knyazikhin, R. R. Nemani, R.B. Myneni., 2006. Analysis of leaf area index and fraction of PAR absorbed by vegetation products from the Terra MODIS Sensor: 2000-2005, *IEEE Trans. Geosci. Remote Sensing, 44*, 1829-1842.

Yonemura, S., S. Kawashima, and H. Tsuruta, 2000. Continuous measurements of CO and H_2 deposition velocities onto an andisol: Uptake control by soil moisture,*Tellus, Ser. B. 51,* 688-700.

Yonemura, S., S. Kawashima, and H. Tsuruta, 2000. Carbon monoxide, hydrogen, and methane uptake by soils in a temperate arable field and a forest, *J. Geophys. Res. 105,* 14347-14362.

Yuan, C-Y., 1984. The utilization of animal and human wastes in rice production in China, *Organic Matter and Rice*, International Rice Research Institute, Los Banos, Philippines.

Zhang, P., B.T. Anderson, and R. Myneni, 2006. Monitoring of the 2005 U.S. Corn-belt Yield using Satellite Data, *Eos*, Vol. 87, No. 15, 150.